UNIVERSITY OF Southampton

University of Southampton Research Repository
ePrints Soton

Copyright © and Moral Rights for this thesis are retained by the author and/or other copyright owners. A copy can be downloaded for personal non-commercial research or study, without prior permission or charge. This thesis cannot be reproduced or quoted extensively from without first obtaining permission in writing from the copyright holder/s. The content must not be changed in any way or sold commercially in any format or medium without the formal permission of the copyright holders.

When referring to this work, full bibliographic details including the author, title, awarding institution and date of the thesis must be given e.g.

AUTHOR (year of submission) "Full thesis title", University of Southampton, name of the University School or Department, PhD Thesis, pagination

http://eprints.soton.ac.uk

UNIVERSITY OF SOUTHAMPTON

FACULTY OF SCIENCE

SCHOOL OF OCEAN AND EARTH SCIENCE

FRACTAL ANALYSIS OF TOPOGRAPHY AND REFLECTANCE SURFACES

BY

XINXIA JIANG

A thesis submitted for the degree of Doctor of Philosophy

August 1998

TO MY WIFE, MY PARENTS, AND THE PEOPLE

I LOVE AND WHO LOVE

CORRECTION SHEET

UNIVERSITY OF SOUTHAMPTON

ABSTRACT

FACULTY OF SCIENCE

GEOLOGY

Doctor of Philosophy

FRACTAL ANALYSIS OF TOPOGRAPHY AND REFLECTANCE SURFACES

by Xinxia Jiang

Key words: *fractal dimension; topography; topographic contour; coastline, scaling behaviour; profile; surface; simulation; DEM; TM imagery.*

The definition of a fractal has been successfully deduced from constructing the Koch curve and the Cantor set. Principles of seven methods (the ruler, box-counting, spectral, structure function, intersection methods, cube-counting, and triangular prism methods) for determining the fractal dimensions are illustrated and verified by the Koch curve, Cantor set, and the simulated 1-dimensional and 2-dimensional fBm samples by comparing the calculated with the theoretical D values of the theoretical fractal models. The application of appropriate methods to self-similar or self-affine fractals is essential due to different theoretical assumptions of the methodologies. The ruler dimension is different from the spectral dimension. The application of Hanning window to the synthetic fBm samples (Hanning window weighted) is important to obtain correct fractal dimensions for the spectral method and structure function methods. The multi-scaling behaviour of a fractal can be unveiled by revealing the difference between the 1^{st} and 2^{nd} order structure function methods. The zeroset theory is used to relate the D values of 1-d contour set with 2-d surface by analyzing the DEM data.

The results of fractal analysing 132 topographic contours digitized from different

scales (1:200,000, 1:50,000, 1:20,000) of maps of the border area between Spain and Portugal show that contours are self-similar, and have a fractal dimension of about D = 1.23 over length scales ranging from 30 m to 13 km scale (3 orders of magnitude). The thirteen filed and map profiles from Dorset area of southern England has a D value of 1.03 derived from the ruler method. The variations in D values are controlled by three geological factors: erosive processes, lithologies, and fractures. The dominant control is the erosive process and fractures, and lithologies can either result in significant difference or produce more subtle variation in D values of coastlines and contours. For example, the river down-cutting produces higher D value (1.1 ~ 1.5) than the wave action or cliff retreat erosive processes (1.01 ~ 1.10).

The results of the fractal analysis of the five TM sub-image of Qatar have shown that D values of the TM images range from 2.10 to 2.96. The variations in D values are controlled by different types of surface, band variations, and methodologies. The study area B of a single rock type has the lowest D value (D is about 2.25) and is significant different from the other four study areas, whilst the urban area E yields the highest fractal dimension (about D = 2.6). Band 3 yields the highest fractal dimensions, followed by bands 4, 5, 1, and 6, and band 2 has the lowest D value. The difference between the D values derived from the 2^{nd} and 1^{st} order structure function methods for all the six bands of five study areas is $D_{2s}(q=2) - D_{2s}(q=1) = 0.16 \pm 0.13$ (the uncertainty is the standard deviation), and suggests that the TM imagery has a multi-scaling property.

TABLE OF CONTENTS

LIST OF TABLES

LIST OF FIGURES

ACKNOWLEDGEMENTS

This research is founded by the TC (Technical Co-operation between Britain and China) scheme. The author wishes to thank the officers of the British Council and the Education Section of the Chinese Embassy in the UK. Among these are Sandra Bance, Berthan Roberts, Xueyi Yang, and Li Xie.

The author is very grateful for the supervisors, Professor David J. Sanderson (the head of the geology department) and Dr Clive A. Boulter. Without their outstanding guidance and advice, their encouragement, their patience, and their kindness through the past years, the successful accomplishment of this thesis is impossible. The author also wishes to thank the chairman Prof. J. W. Murray and the member Dr. D. A. V. Stow of the advisory group. Uncountable assistance and advice from nearly all the staffs of the Geology Department and the goemechanics research group are greatly appreciated. In particular, I would like to thank Giles Pickerling for providing some of his programs, to Charles Kerr for helping me in the use of the Sun workstation, to Ali for providing the TM imagery.

The completion of the thesis would not be possible without the assistance of the Guilin Institute of Technology (was Guilin College of Geology), Guilin, Guangxi, P. R. China, for providing me the opportunity to pursue a higher education degree. Especially, I am very grateful for the help and advice provided by Professor Kuirong Yuan (the former president of the college) and Professor Jincheng Liang (the president of the college).

Finally, but not least, I wish to present very special thanks and love to my wife, Hui Li, for her selfless accompanying my staying in the UK and her enduring moral and financial supports throughout the past years. Special thanks and love are also presented to my parents (Shizhong Jiang and Xiayu Zhou), my uncles (Shijun Jiang, Shibiao Jiang, and Shixun Jiang), and my sisters (Shuijuan Jiang and Lijuan Jiang), for their outstanding support for my fulfilling the high school and university education. Special thanks also go to my sister Lixia Jiang for her important moral help when I started my university education.

ABBREVIATIONS USED

1-d 1-dimensional

2-d 2-dimensional

α confidential level as 95% as $\alpha = 0.05$

AOV analysis of variance

avg average

β slope of the regression line on a log-log plot

C intercept of the regression line on a log-log plot

The subscripts $_{r, 1b, 1f, 1s, 1i, 2b, 2f, 2s, 2i,}$ and $_t$ under C are the intercepts derived from the ruler, box-counting, 1-d spectral, 1-d structure function, 1-d intersection, cube-counting, 2-d spectral, 2-d structure function, 2-d intersection, and triangular prism methods.

CE contour elevation

D fractal dimension

The subscripts $_{r, 1b, 1f, 1s, 1i, 2b, 2f, 2s, 2i,}$ and $_t$ under D are the intercepts derived from the ruler, box-counting, 1-d spectral, 1-d structure function, 1-d intersection, cube-counting, 2-d spectral, 2-d structure function, 2-d intersection, and triangular prism methods.

DEM digital elevation model

DN digital number in TM

$\mathbf{N_{dp}}$ the number of digitized points

E Euclidean dimension

fBm fractional Brownian motion

M(h) absolute mean relief at lag h

γ**(h)** semivariance at lag h

H Hausdorff measure ($0 < H < 1$)

h lag

$\mathbf{L_0}$ profile length

λ wavelength

k radius wave number $k = 2\pi/\lambda$

P(λ) power spectral density at λ

P(k) power spectral density at k

q order of structure function (or order of moment)

r ruler length (or scaling factor)

$\mathbf{R^2}$ correlation coefficient for the regression line ($0 \leq R^2 \leq 1$)

$\mathbf{R_a}$ **(CLA)** centre line average

$\mathbf{r_L}$ the lower fractal limit

$\mathbf{R_q}$ **(RMS)** root mean square

RSS residual sum of square (%)

$\mathbf{r_U}$ the upper fractal limit

$\mathbf{s}$, $\mathbf{s_0}$ average sampling interval

S surface area

$\mathbf{s^2}$ resolution area

σ^2 variance

std standard deviation

TM Thematic Mapper TM imagery

INFORMATION OF THE THESIS

Key words	*fractal dimension; topography; topographic contour; coastline, scaling behaviour; profile; surface; simulation; DEM; TM imagery.*
Word processing	*Microsoft Word 7.0 (Win 95)*
Diagrams processing	*DrawPecfect 1.1 and CorelDraw 5.0*
Fonts used in the thesis:	
Main body	Times New Roman, 12 pt
Header	**Times New Roman, Italic, Bold, 12 pt**
Text in Tables	Times New Roman, 10 pt
Illustration of figures	Times New Roman, 10 pt
Text layout	*Flush left*
Margins:	
Left	*3.81 cm*
Right	*1.52 cm*
Top	*2.54 cm*
Bottom	*1.52 cm*
Line space	*1.5 Lines*
Total number of words	*=58,000 approximately*
Total number of pages	*278 (Main body of the thesis 213)*
Total number of tables	*50*
Total number of figures	*71*

CHAPTER 1

INTRODUCTION TO THE FRACTAL CONCEPT

CHAPTER 1

INTRODUCTION TO THE FRACTAL CONCEPT

1. INTRODUCTION TO THE FRACTAL CONCEPT

1.1. INTRODUCTION

Traditionally, the Euclidean dimension is always integer. For example, the Euclidean dimension of a point is zero, a line is one, a square is two, and a cube is three. However, considering the dimensions of sets of points, lines, squares, or cubes is often beyond the capacity of Euclidean dimension theory, therefore the concept of fractional dimensions has been developed.

The concept of a fractal set was introduced by Mandelbrot (1967) in his famous article entitled "How long is the coast of Britain", following the earlier work of Richardson (1961). In his subsequent book of "The Fractal Geometry of Nature", Mandelbrot (1983) refined and extended his fractal theory. Since then, it has been widely used in a range of areas, from pure mathematics to engineering.

Many phenomena in nature are independent of the observation scale. For example, a topographic contour of a 1:200,000 map may be indistinguishable from that of a 1:50,000 map. Therefore, a contour needs either to be specified at a certain length scale or to be generalized over all scale lengths. The fractal concept provides an essential tool to study these scale-independent natural phenomena.

Many geological phenomena have been characterized by the fractal concept. Fractal analysis, as well as methods for calculating the fractal dimension, has been reported in the

disciplines of **rock profiles and surfaces** (Goodchild, 1980; Shelberg *et. al.*, 1983; Mark and Aronson, 1984; Brown and Scholz, 1985; Brown, 1987; Roy *et. al.*, 1987; Turcotte, 1987; Dubuc *et. al.*, 1989a, b; Gilbert, 1989; Aharonov and Rothman, 1996; Glover *et. al.*, 1994; Kopaskamerkel, 1994; Poliakov and Herrmann, 1994), **earthquake studies** (Aki, 1984; Allègre *et. al.*, 1982; Smalley *et. al.*, 1987; Bak and Tang, 1989; Hirata, 1989b; Huang and Turcotte, 1990a; Scholz, 1990; Arab *et. al.*, 1994; Volant and Grasso, 1994; Wang, 1993, 1995, 1996; Godano and Caruso, 1995; Khattri, 1995; Robertson *et. al.*, 1995; Turcotte, 1995; Yin and Ranalli, 1995; Godano *et. al.*, 1996; Srivastava *et. al.* 1996; Steacy *et. al.*, 1996; Varnes and Bufe, 1996; Wang and Lee, 1996), **fault distributions** (King, 1983; Aviles *et. al.*, 1987; Sammis and Biegel, 1989; Hirata, 1989a; Jackson and Sanderson, 1992; Pickering *et. al.*, 1994; An and Sammis, 1994; Carter and Winter, 1995; Lee and Schwarcz, 1995; Idziak and Teper, 1996; Lee and Bruhn, 1996; Oncel *et. al.*, 1996), **rock fractures** (Byerlee, 1978; Madden, 1983; Brown and Scholz, 1986; Barton, 1986; Okubo and Aki, 1987; Hirata *et. al.*, 1987; Atkinson, 1987; Velde *et. al.*, 1990; Gillespie *et. al.*, 1993; Zhang and Sanderson, 1994; Xie and Sanderson, 1994, 1995; Gillespie *et. al.*, 1993; Zhao *et. al.*, 1993; Borodich, 1994; Caldarelli *et. al.*, 1994; Hammad and Issa, 1994; Hao *et. al.*, 1994; Mishnaevsky, 1994; Odling, 1994; Weinstein and Majumdar, 1994; Lee *et. al.*, 1994; Lyu *et. al.*, 1994; Saouma and Barton, 1994; Silberschmidt, 1994; Zhang *et. al.*, 1994; Carpinteri and Chiaia, 1995; Frantziskonis, 1995; Djordjevic *et. al.*, 1995; Hooke and Iverson, 1995; Lu, 1995; Perfect and Kay, 1995; Pezzotti *et. al.*, 1995; Thompson *et. al.* 1995a; Kulatilake *et. al.*, 1995; Podsiadlo and Stachowiak, 1995; Thompson *et. al.*, 1995b; Watanabe and Takahashi, 1995; Carpinteri and Chiaia, 1996), **river networks** (Gan *et. al.*, 1992), **landscape** (Mandelbrot, 1975; Goodchild, 1980; Shelberg *et. al.*, 1983; Mark and Aronson, 1984; Brown and Scholz, 1985; Brown, 1987; Turcotte, 1987; Milne, 1988; Gilbert, 1989; Mandelbrot, 1989; Devries *et. al.*, 1994; Sun *et. al.*, 1994; Beauvais and Montgomery, 1996; Claps and Oliveto, 1996; Manna and Subramanian, 1996; Maritan *et. al.*, 1996), **ocean-bottom relief** (Berkson and Mathews, 1983; Barenblatt *et. al.*, 1985; Fox and Hayes, 1985; Gilbert and Malinverno, 1988; Goff and Jordan, 1988; Mareschal, 1989; Raizer *et. al.*, 1994; Magde *et. al.*, 1995; Fox, 1996), **lithology** (Katz and Thompson, 1985; Plotnick, 1986; Kronhn, 1988a, b; Velde *et. al.*, 1991; Malinverno, 1989b; 1995; Leonardi *et. al.*, 1994; Ringrose, 1994), **oil field** (Hewett, 1986; Holliger and Levander, 1994; Dolan *et. al.*, 1998), **seismicity** (Anderson, 1986; Cao and Aki, 1984; 1986; Main and Burton,

1986; Turcotte, 1989; Levander *et. al.*, 1994; Saleur *et. al.*, 1996; Costain and Bollinger, 1996), and **image analysis** (Kronhn, 1986; Yokoya *et. al.*, 1989; Huang and Turcotte, 1989; 1990b; Lam, 1990; Polidori *et. al.*, 1991; Sarkar and Chaudhuri, 1994; Vasselle and Giraudon, 1994; Bandrivskii *et. al.*, 1995; Bower *et. al.*, 1995; Chan, 1995; Dejong and Burrough, 1995; Donnelly *et. al.*, 1995; Sarkar and Chaudhuri, 1995; Wu and Wu, 1995; Carmichael *et. al.*, 1996; Krueger *et. al.*, 1996; Lawrence and Ripple, 1996; Soille and Rivest, 1996).

In this Chapter, the definition of a fractal concept is deduced from demonstrating the construction of the Koch curve and the Cantor set. Then the ruler and box-counting methods are used to determinate the fractal dimension. After that, the self-similarity and self-affinity of fractals are discussed and the concept of fractal dimensions and fractal limits, introduced. Finally, the objectives and organization of the thesis are presented.

1.2. DEFINITION OF A FRACTAL SET

The definition of a fractal can be deduced through using two traditional examples called the 'Koch curve' and the 'Cantor set'. These two theoretical examples illustrate many features of fractals and the methods needed to define the fractal dimension (D).

1.2.1. Koch curve

The Koch curve was introduced by Hedge von Koch in 1904. Fig. 1.1(a) illustrates the first four steps of the construction of the Koch curve. In the diagrams of (b), (c), and (d), r stands for the length of line segment(s), N is the number of the line segments, and L is the total length of the curve. The construction of the Koch curve starts with a line of unit length (r = 1) which is called the initiator. Firstly, the initiator is divided into three equal parts and the middle part is replaced by two sides of an equilateral triangle. Therefore the line of unit length becomes a curve consisting of four straight lines, and this curve is called the generator or motif. Then each of the four line segments is taken as the base and replaced by the corresponding scaled-down generator. Recursion of this process leads to the Koch curve at a certain order. Thus at each step, a line is replaced by four lines of each of length 1/3. Generally, each part of the 4 line segments in the k^{th} step is a scaled-down version, by a factor of 3, of the entire curve in the previous $(k-1)^{th}$ step.

The Koch curve has some significant features as described in Fig. 1.1(a) and (b).

- Firstly, the total length, L, and the number of the line segments, N, of the curve consistently increases as the length of the line segments (r) decreases at higher order. The recursion itself is infinite, but the area which the curve covers is finite. Thus, the Koch curve has an infinite length (L) in a finite area (S) of the plane without intersecting itself, i.e., as $r \to 0$, then $L \to \infty$, and $S = \sqrt{3}/20$. They can be given by,

$$L = \underset{n\to\infty}{Lim}\left(\frac{4}{3}\right)^{n} = \infty$$

$$S = \frac{\sqrt{3}}{4}\frac{1}{9}\underset{n\to\infty}{Lim}\left[1+\frac{4}{9}+\left(\frac{4}{9}\right)^{2}+\left(\frac{4}{9}\right)^{3}+\ldots+\left(\frac{4}{9}\right)^{n-1}+\ldots\right] = \frac{\sqrt{3}}{20}$$

- Secondly, any part of the curve, when magnified isotropically with a proper scale factor, is identical to the whole curve, i.e. its geometry is self-similar or scale invariant.
- Thirdly, there is a power-law relationship between the number of line segments N (or the total length L) of the curve and the length of the line segments r as shown in Fig. 1.1(c) and (d).

The relationship between N and r can be revealed by their log-log plot as shown in Fig. 1.1(c) for the first 10 orders. The points fall on a straight line of slope β_1 = Log(4)/Log(3) = 1.261858.... This indicates that there is a power-law relationship between N and r. The line can be mathematically given by,

$$Log(N) = -1.261518\ Log(r)$$

More generally,

$$Log(N) = Log(C) - D\ Log(r)$$

Therefore,

$$N = C\, r^{-D} \tag{1.1}$$

where N is the number of objects (i.e. fragments) with a characteristic length r, C is a constant of proportionality, and D is termed the **FRACTAL DIMENSION**. For the Koch curve D = *Log(4)/Log(3)* = 1.261858 and C = 1.

As shown in Fig. 1.1(d), the power-law relationship between the length of the Koch curve (L) and r can be easily obtained since L = N r and from equation (1.1),

$$L = C\, r^{1-D} \tag{1.2}$$

1.2.2. Cantor set

The Cantor set was first published by Georg Cantor in 1883. It is constructed by the

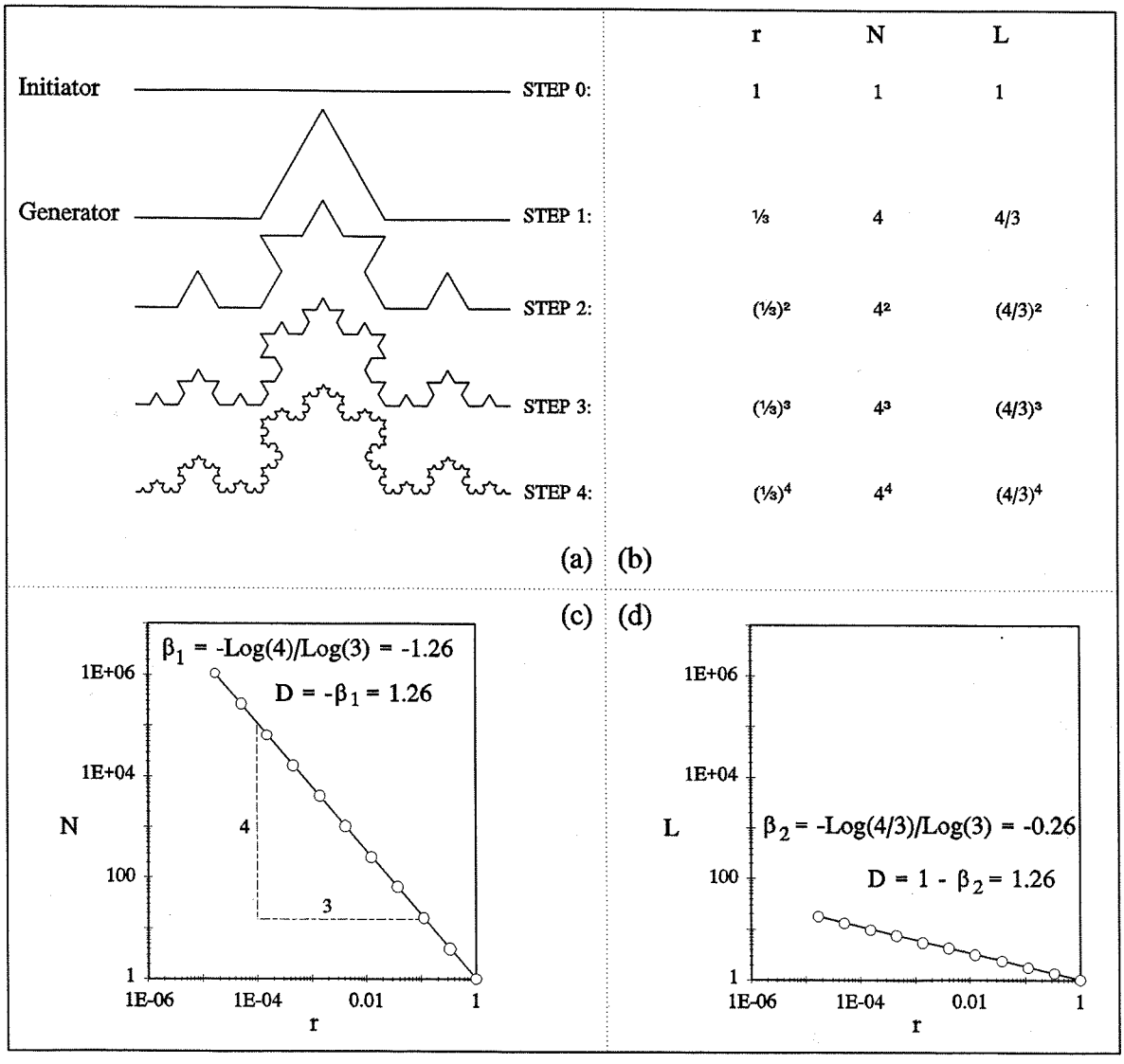

Fig. 1.1. Construction of the Koch curve and illustration of the fractal concept derived from the curve, where β is the slope of the fitted lines. **(a)** Construction of the Koch curve for the first 4 orders. **(b)** A list of length (r) and the number (N) of the line segments, and the total length of the curve (L) at different orders. **(c)** Double logarithm diagram of N against r shows a power-law relationship of the form $N = C r^{\beta_1}$, where the fractal dimension of the Koch curve D = $-\beta_1$ = 1.26. **(d)** The perfect fitted line of Log-log plot of L against r also leads to a power-law relationship of the form $L = C r^{\beta_2}$, i.e., the fractal dimension of the Koch curve D = 1 - β_2 = 1.26. Therefore, the Koch curve has a fractal dimension D = 1.26 and a proportional constant C = 1.

sequential removal of the middle one-third of a line segment based on a unit length line as shown in Fig. 1.2(a).

In Fig. 1.2(a), the unit length line, $r_0 = 1$, is firstly divided into three equal parts so

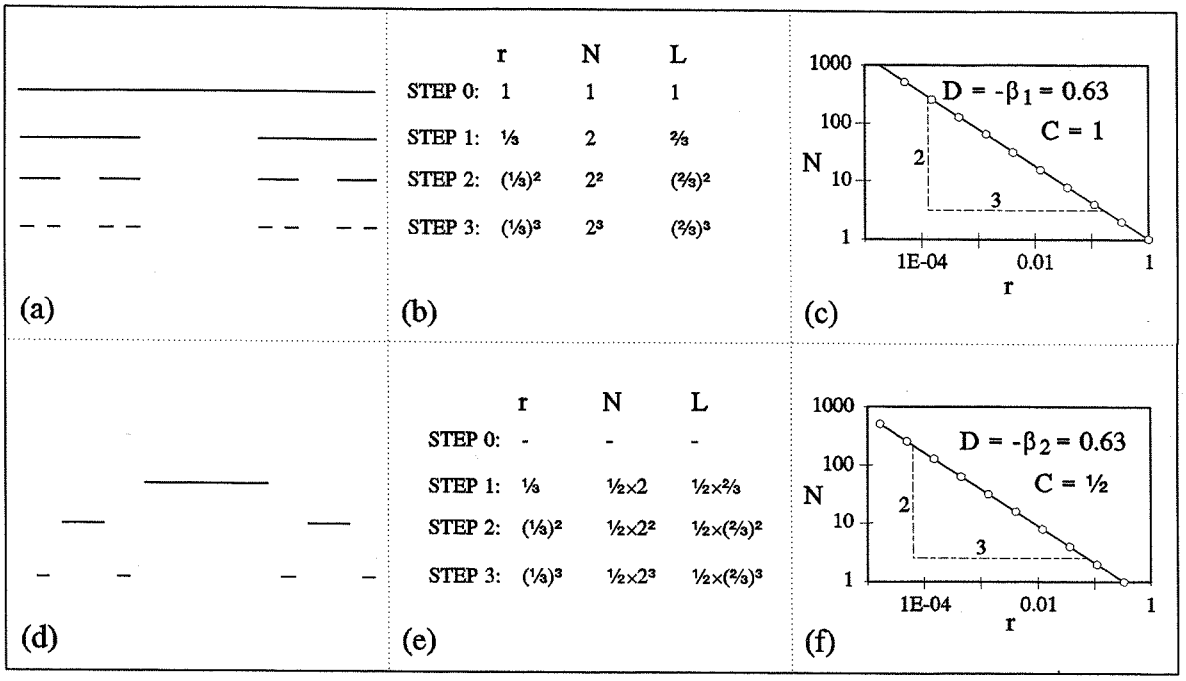

Fig. 1.2. Construction of the Cantor set and its derived fractal concept as shown in (a), (b), and (c). Construction of a fractal set from those removed parts during the construction of the Cantor set and its derived fractal concept as shown in (d), (e), and (f). **(a)** The first three orders in the construction of the Cantor set. **(b)** A list of lengths (r) and numbers (N) of the line segments, and the length of the Cantor set (L) at different orders. **(c)** Log-log plot of N against r where the plotted points link a perfect power-law of the form $N = C r^{\beta_1}$. Hence the fractal dimension of the Cantor set is D = Log(2) / Log(3) = 0.630929 and the proportional constant is C = 1. **(d)** All those removed line segments during the construction of the Cantor set as shown in (a) leads to another fractal structure. **(e)** A list of lengths (r) and numbers (N) of the line segments, and the length of the new-formed fractal set (L) at different orders. **(f)** Log-log plot of N against r for the construction of fractal shown in (d). Its fractal dimension is D = Log(2) / Log(3) = 0.630929 and the proportional constant is C = 0.5

that the length of each line segment is $r_1 = 1/3$. The two end-line segments of the same length 1/3 are retained so that the number of line segments $N_1 = 2$. Subsequently, these two retained line segments are each further divided into three equal parts so that the length of every line segment $r_2 = (1/3)^2$. The four end-line segments of the same length of $(1/3)^2$ are retained so that the number of line segments is $N_2 = 2^2$. This recursion, theoretically, is endless and as the number of recursion goes to infinity, the Cantor set comprises an infinite number of points (or a infinite number of lines which have infinitesimal lengths). The length (r), number (N), and total length (L) of retained line segments for the first three orders of the construction of the Cantor set are shown in Fig. 1.2(b).

To reveal the relationship for the number (N) and length (r) of retained line segments, the first ten orders in the construction of the Cantor set is taken as an example. As the recursion process is repeated ten times, then a set of lines (2^{10} line segments, $(1/3)^{10}$ in length at order 10) is obtained. The log-log plot of N against r, as shown in Fig. 1.2(c), reveals their power-law relationship. All the plotted points fall on a straight line where,

$$Log(N) = -0.630929\ Log(r)$$

The equation, again, can be written as,

$$N = C\, r^{-D}$$

where N is the number of objects (i.e. line segments here) with a characteristic criteria r (here r is the length of line segments), C is a constant of proportionality, and D is the fractal (fractional) dimension (Turcotte, 1992). For the Cantor set D = 0.630929, and C = 1.

Let us investigate the fractal behaviour of the removed parts during the procedure of construction of the Cantor set, they form another fractal structure as shown in Fig. 1.2(b). There is a power-law relationship between N and r as shown in Fig. 1.2(e), and (f), where,

$$Log(N) = Log(0.5) - 0.630929\ Log(r)$$

It has the same fractal dimension D = *Log(2)/Log(3)* = 0.630929 as the Cantor set, but with C = 0.5.

1.2.3. Extension to the higher dimensions

The fractal concept could be extended to 2-dimensions, 3-dimensions, and even higher dimensions. The Koch curve and the Cantor set are both examples of fractals generated from 1-dimensional lines. The Koch curve is constructed by removing less, but adding more line segments to the initiator, hence the Koch curve has fractal dimension of D = 1.26 rather than a simply integer D =1 of initiator. The Cantor set, however, is the result of constantly removal of line segments, and has a fractal dimension of D =0.63. The principles of removing line segments could be easily extended to higher dimensional

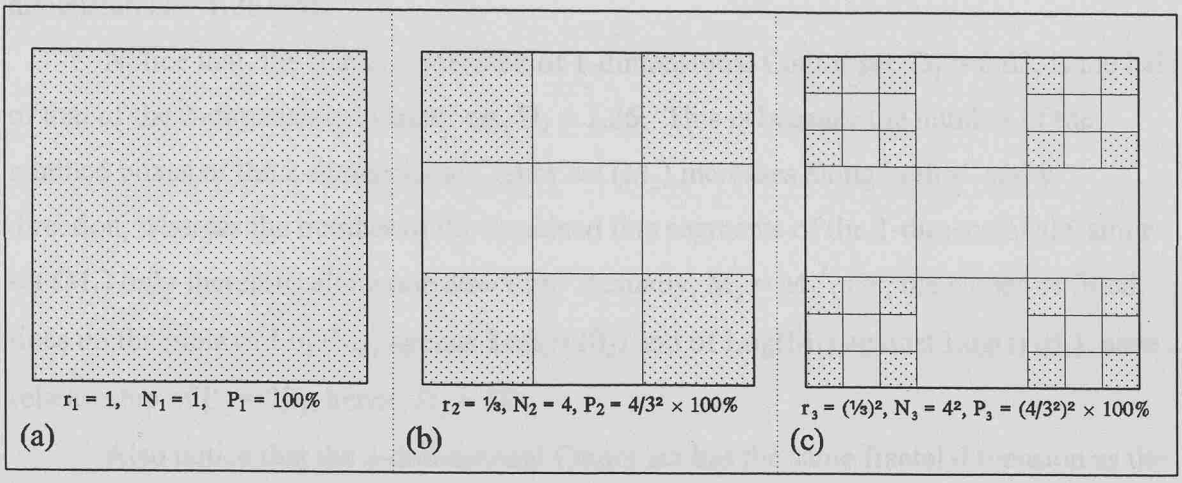

Fig. 1.3. Construction of a 2-dimensional Cantor set for the first two orders. **(a)** A square of a unit side-length $r_1 = 1$, hence the number of boxes is $N_1 = 1$ and percentage of retained boxes is $P_1 = 100\%$. **(b)** The square is firstly divided into nine equal small boxes and the four corner boxes are retained so that the side-length of the small boxes $r_2 = 1/3$, the number of retained boxes is $N_2 = 4$, and percentage of retained boxes is $P_2 = 4/9 \times 100\%$. **(c)** The four retained boxes are further equally divided into nine boxes respectively, and from which four corner boxes are retained so that $r_3 = (1/3)^2$, $N_3 = 4^2$, and $P_3 = (4/9)^2 \times 100\%$. This procedure can be carried out to any finer resolution required

geometry. For example, 2-dimensional boxes and 3-dimensional cubes can be removed from a square or a cube initiators to construct 2-dimensional or 3-dimensional fractals.

Fig. 1.3 demonstrates a 2-dimensional fractal construction procedure. This fractal could be termed the "2-dimensional Cantor set" because its construction procedure is similar to a Cantor set. A square of unit area, which has a side-length of $r_1 = 1$, is initially divided into nine small squares with a side length of $r_2 = 1/3$, and the four corner small squares are retained and the others are discarded. Recursion of this procedure (e.g. Fig. 1.3(c)) can be performed so forth on the remaining boxes until a satisfied resolution is reached.

A log-log plot of the number of the retained squares (N) against their side-length (r) at each step is exactly the same as Fig. 1.1(c). This is because the numbers of the retained squares of the 2-dimensional Cantor set (Fig. 1.3) are same as those of line segments of the Koch curve. Therefore, Fig. 1.1(c) could be used to demonstrate the power-law relationship between N and r for the 2-dimensional Cantor set. The slope of fitted line is $\beta = -Log(4)/Log(3) = -1.261858$, and hence the fractal dimension $D = 1.261858$ and $C = 1$. Similarly, the log-log plot of the percentage of the retained boxes (P) against the side-length of the retained boxes (r) also shows a perfect fitted line which also results in the same fractal

dimension D = 1.261858.

Notice that, the fractal dimension of 1-dimensional Cantor set, $D_1 = 0.63$, is the half of that of the 2-dimensional Cantor set, $D_2 = 1.26$. This is because the number of the retained boxes of the 2-dimensional Cantor set (M_2) increases along both x- and y-direction, whereas the number of the remained line segments of the 1-dimensional Cantor set (M_1) only increases along one direction. Actually, $M_2 = M_1^2$, i.e., the slopes of fitted lines on the plots of Log(M_2) against Log(r) (β_2) and of Log(M_1) against Log(r) (β_1) have a relationship of $\beta_2 = 2\beta_1$, hence, $D_2 = 2D_1$.

Also notice that the 2-dimensional Cantor set has the same fractal dimension as the Koch curve, both are D = 1.26. The 2-dimensional Cantor can be regarded as an infinite set of infinite small areas or points in the unit area between (0, 0) and (1, 1). Therefore, a set of points could have same fractal dimension as a curve if the quantitative power-law relationship between the number of objects (N) with a characteristic size (r) is the same.

1.2.4. Summary

The Koch curve and the Cantor set illustrate the fractal concept applied to sets of line segments, points, areas, curves; similar constructions can also be extended to higher dimensions. In summary, the dimension of a set of points, lines, curves, areas, or volumes is not always an integer, but a fractional value, such sets are termed **FRACTAL** and the fractal dimension is defined by equation (1.1).

Generally speaking, a set of points on a line (e.g., Cantor set) has a fractal dimension between 0 (point) < D < 1 (line); a set of points in a plane (e.g., 2-d Cantor) has a fractal dimension between 0 (point) < D < 2(plane); a set of lines (Koch curve) on a plane has a fractal dimension between 1 (line) < D < 2(plane); and a surface should have a fractal dimension of 2 < D < 3.

1.3. DETERMINATION OF FRACTAL DIMENSIONS

The definition of a fractal concept, as demonstrated by the Koch curve and the Cantor set, leads to a power-law equation (1.1) as,

$$N = C\,r^{-D}$$

where N is the number of objects (i.e. fragments) with a characteristic length r, C is a constant of proportionality, and D is termed the fractal dimension. It is from this power-law relationship that the fractal dimensions of natural phenomena can be determined. The ruler and box-counting methods are two of the simplest methods for determining fractal dimensions using equation (1.1). All the other methods for determining fractal dimensions are more or less derived from this equation. A brief discussion of the ruler and box-counting methods is introduced here.

1.3.1. The ruler method

The ruler method is also called the divider method or the compass method. The Koch curve may be used as an appropriate mathematical model on which to illustrate the determination of the fractal dimension by the ruler method.

The power-law relationship between the number of line segments (N) and the ruler length (r) of the Koch curve, as shown in Section 1.2.1, is given by equation 1.1. If the Koch curve (Fig. 1.4a) is measured using two different yardsticks (ruler length) r_1 and r_2 from the left-hand side as shown in Fig. 1.4(b) and (c), we have,

$$N_1 = C\,r_1^{-D}$$

$$N_2 = C\,r_2^{-D}$$

Then,

$$\frac{N_2}{N_1} = \left(\frac{r_2}{r_1}\right)^{-D}$$

Thus the fractal dimension D can be given directly by,

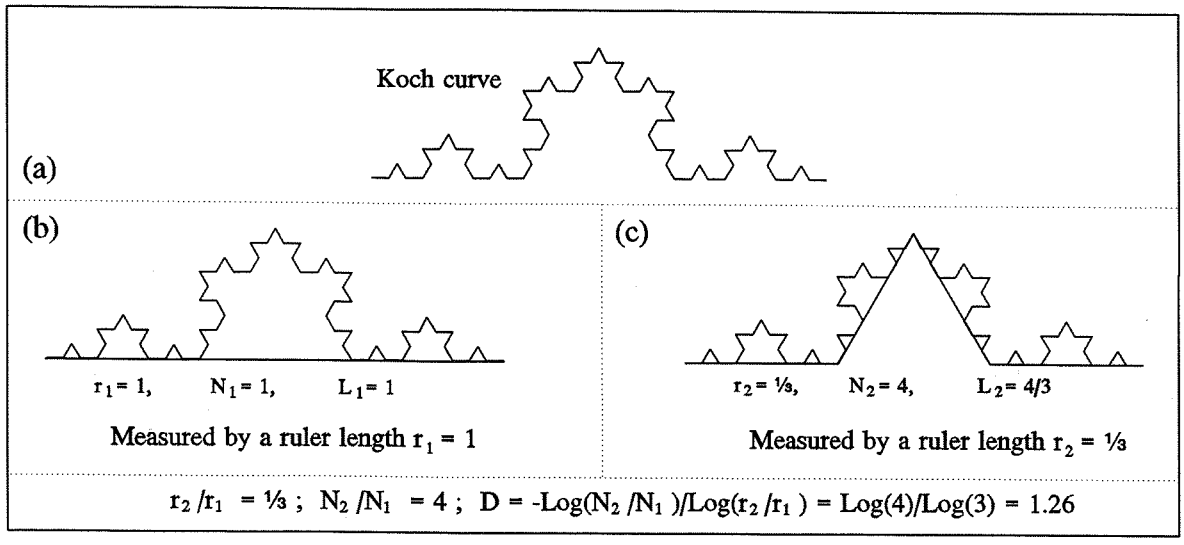

Fig. 1.4. Illustrations of the principles of the ruler method. The Koch curve has different lengths (L) and different numbers (N) of rulers when it is measured using different ruler lengths (r). **(a)** Koch curve at order 3. As the Koch curve is measured by a ruler $r_1 = 1$, then one measurement is needed ($N_1 = 1$), and the curve has a length $L_1 = 1$ as shown in Fig. 1.4(b). As the Koch curve is measured by a ruler $r_2 = 1/3$, then $N_2 = 4$ and $L_2 = 4/3$ as shown in Fig. 1.4(c).

$$D = -\frac{Log\left(\frac{N_2}{N_1}\right)}{Log\left(\frac{r_2}{r_1}\right)}$$

The Koch curve has a fractal dimension of $D = Log(4)/Log(3) = 1.26$ and $C = 1$ (Fig. 1.4).

The fractal dimension can also be derived from the power-law relationship between the length (L) and the ruler length (r) of the Koch curve by,

$$L = C\, r^{1-D}$$

since $L = N\, r$, then,

$$D = 1 - \frac{Log(L)}{Log(r)}$$

For the different yardsticks r_1 and r_2, we have,

$$D = 1 - \frac{Log(\frac{L_2}{L_1})}{Log(\frac{r_2}{r_1})}$$

Thus a plot of Log(L) against Log(r) as shown in Fig. 1.2(c) should be a straight line of slope 1 - D. For the Koch curve, D = 1.261858 and C = 1.

1.3.2. The box-counting method

The Cantor set is an infinite set of points in the unit interval [0,1]. It is an "ideal fractal", which forms a suitable basis for discussion of the interval counting method. When extended to 2-dimensions it becomes the widely used box-counting method for determining the fractal dimension.

Supposed that N_1 and N_2 are the numbers of boxes, of side lengths of r_1 and r_2 respectively, needed to cover the retained squares in Fig. 1.3b, then N_1 and N_2 are, from equation (1.1), given by,

$$N_1 = C\, r_1^{-D}$$
$$N_2 = C\, r_2^{-D}$$

Thus,

$$\frac{N_2}{N_1} = \left(\frac{r_2}{r_1}\right)^{-D}$$

or,

$$D = -\frac{Log\left(\frac{N_2}{N_1}\right)}{Log\left(\frac{r_2}{r_1}\right)} \qquad (1.3)$$

To cover four retained corner squares, one square of side length $r_1 = 1$ is needed,

hence $N_1 = 1$; four boxes of side length $r_2 = 1/3$, however, are needed, hence $N_2 = 4$. Therefore, the fractal dimension can be easily determined; $D = Log(4)/Log(1/3) = 1.261858$.

Alternatively, the box-counting dimension can be determined by revealing the power-law relationship between P and r, where P is the ratio of the number (N) of boxes needed to cover the retained squares and the total number of squares ($N_t = (1/r)^2$), and r is the side length of each square. For box sizes of r_1 and r_2, P_1 and P_2 are given by,

$$P_1 = N_1\left(\frac{1}{r_1}\right)^2 = \frac{N_1}{r_1^2}$$

$$P_2 = N_2\left(\frac{1}{r_2}\right)^2 = \frac{N_2}{r_2^2}$$

Thus,

$$\frac{P_2}{P_1} = \left(\frac{N_2}{N_1}\right)\left(\frac{r_2}{r_1}\right)^2$$

or,

$$Log\left(\frac{P_2}{P_1}\right) = Log\left(\frac{N_2}{N_1}\right) + 2\,Log\left(\frac{r_2}{r_1}\right)$$

Combining the equation with (1.2) gives,

$$D = 2 - \frac{Log\left(\frac{P_2}{P_1}\right)}{Log\left(\frac{r_2}{r_1}\right)} \qquad \textbf{(1.4)}$$

For the example shown in Fig. 1.3, $D = 2 - Log(4/9) / Log(1/3) = Log(4)/Log(3) = 1.261858$, which is equal to the fractal dimension of the Koch curve.

1.4. SELF-SIMILARITY AND SELF-AFFINITY

Theoretically, a fractal is defined as self-similar if any small portion is similar to the entire object when the portion is magnified isotropically by any factor r. For a self-affine fractal, however, similarity exists only when the portion is magnified by different scales along x- and y- axes.

Natural fractals can be characterized by these two fractal concepts, self-similarity and self-affinity in a statistical sense, as defined by Mandelbrot (1983). The term "statistical sense" of natural fractals implies:

- The similarity between the portion and its magnified one is statistically similar, not exactly the same. The Koch curve and the Cantor set discussed above are pure mathematical fractal models – theoretical fractals. Its magnified portion is exactly as same as the entire curve.
- The theoretical fractals can be generated at all scales, from 0 to ∞, however, the natural phenomena are usually only fractal within a certain range which is termed the fractal limits. This will be discussed in the Section 1.5.

1.4.1. Self-similarity

The self-similar fractal is illustrated by the Koch curve (Fig. 1.5(a)) and an example contour (Fig. 1.5(b)). When the portion in the smaller ellipse is magnified isotropically, the enlarged one (in the bigger ellipse) is similar to the entire object. In general, if a profile or a surface is statistically self-similar, a portion of the profile will appear similar to the entire profile when it is magnified isotropically. A formal definition of a self-similar fractal, in a two-dimensional (xy) space, is that f(rx, ry) is statistically similar to f(x, y), where r is a scale factor (Turcotte, 1992).

1.4.2. Self-affinity

The self-affinity of a profile is shown in Fig. 1.5(c). If a profile is a statistical self-affine fractal then any portion of the profile appears similar to the entire profile, only if different scaling factors are used for the directions parallel and perpendicular to the surface. A formal definition of a self-affine fractal, in a two-dimensional xy-space, is that f(rx, r^Hy) is statistically similar to f(x, y), where r is a scaling factor and H is known as the

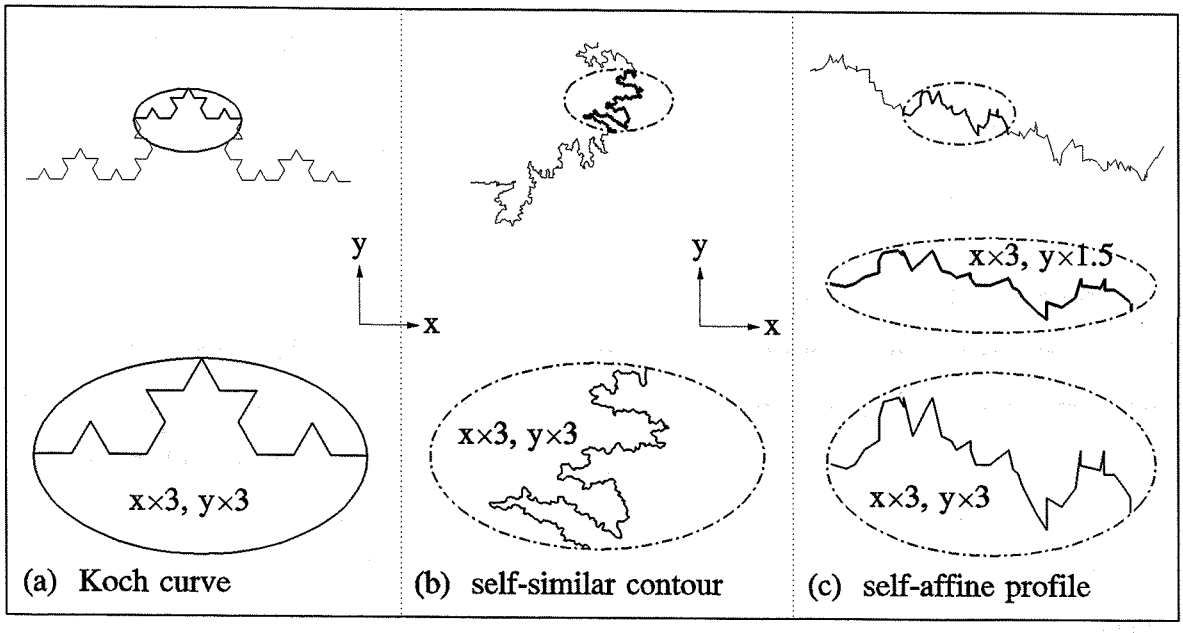

Fig. 1.5. Illustrations of the self-similarity and the self-affinity. Three bold curves in small ellipses are isotropically magnified by a factor of 3 in **(a)** the Koch curve, the pure mathematical fractal model and in **(b)** a topographic contour; **(c)** is a topographic profile. Two pieces of isotropically magnified portion shown in (a) and (b) are similar to the original curves. This is called statistically self-similar fractal. However, the isotropically magnified portion (lower part in c) by a factor of 3 has much more vertical variation than the original curve. In order to preserve the statistical characters, different scaling factor along x- and y- directions are needed (middle portion of c). This curve is a statistically self-affine fractal.

Hausdorff measure. Clearly, the self-similar fractal is one specific case of the more general self-affine fractal where H = 1.

Topography is a good example of both self-similar and self-affine fractals and can be used to illustrate the differences between them. The topographic contours are usually self-similar fractals, since the two horizontal coordinates (x, y) involved in a contour are statistically indistinguishable if the erosive processes do not vary with directions of (x, y). A vertical cross-section (a profile) of topography, however, is more likely a self-affine fractal. This kind of profile involves two coordinates, horizontal distance and vertical height, and has different magnitudes along the two coordinates. The processes modifying topography general lead to different scaling in the horizontal and vertical (height) direction, hence the two coordinates are statistically distinguishable.

1.5. FRACTAL LIMITS

Theoretical fractal models, such as the Koch curve and Cantor set, can be generated at all scales, essentially from 0 to ∞. Natural phenomena, on the other hand, are usually only fractal between a certain range in a statistical sense (Mandelbrot 1977); the upper and lower fractal limits. The range between these fractal limits is termed the fractal range. Considering topography, the lower fractal limit may be imposed by grain size, bed thickness, joint spacing etc. The upper fractal limit may be imposed by local limits to the size of the study area.

A number of studies have noted that the upper fractal limit plays an important role in characterizing surfaces' geography, and it can not be imposed to any scales observed on the Earth. For example, Nye (1973) noted sea ice spectra for wavelengths longer than 100 m tends to be flat, i.e., sea ice is smooth over the large scale. Bell (1975, 1979) shown the spectra for abyssal hills seem to flatten over a wavelength longer than 40 km because of a lack of large scale hills; later he pointed out that a profile length should not be longer than a few tens of kilometres since the size of abyssal hills are usually less than 10 km. Malinverno (1989b) studied the spectra of abyssal hills over the ranges of 300 m and 50 km, and found that the spectra over long wavelengths had to flatten because his extrapolating power spectra at longer wavelength (>50 km) gave unrealistic amplitude (4 km for a wavelength of 1000 km). Similar results also concluded by Gilbert (1989) and Malinverno (1988), and Gilbert and Courtillot (1987).

Whilst the lower fractal limit maybe deformed by process, it is often controlled by the resolution of measurement, such as map scales, sampling intervals, the digitizing steps etc. This will be discussed in more detail in Chapter 3.

1.6. OBJECTIVES AND ORGANIZATION OF THE THESIS

1.6.1. Objectives of the thesis

The objectives of the study are:

1. **To examine the fractal properties of topographic contours** in a statistical sense by the ruler and box-counting methods; to reveal the relationships between fractal limits and contour lengths (and digitizing steps); to investigate whether contours from different methodologies, different maps, different rock types, and different contour elevations have distinct fractal dimensions. 132 topographic contours digitized from different scales of maps (1:20,000, 1:50,000, and 1:200,000) of the border areas between Spain and Portugal are involved in this study.
2. **To study the fractal behaviours of the map and field profiles from kilometre scales (map profiles) down to centimetre (field profiles)** scales by the ruler, spectral, and first order structure function methods; to discuss the different D values resulting from the ruler method and the spectral (and/or the 1st order structure function) methods; to link the variations of D values with the geological factors, such as rock types and erosive processes. Ten field profiles measured at different intervals and three digitized map profiles from Dorset area of southern England are used in the discussion.
3. **To investigate the effects on the variation in D values of topographic contours and coastlines caused by different erosive processes, rock types, and fracture orientations**. The ruler method is deployed to determine the fractal dimensions of parts of the coastlines of Great Britain and Ireland. The determined D values are compared with those obtained from worldwide literature and from the Chapters 3 and 4.
4. **To analyze and compare the fractal dimensions of the DEM and Qatar TM data** by the spectral, 1st and 2nd order structure function methods; to examine the roles of different methodologies, different land types, and different bands played in fractal dimensions. The DEM is digitized from the 1:20,000 map of the boarder area between Spain and Portugal, and also analyzed by the cube-counting and triangular method. Five study areas which covers different rock types and geographical features (such as coast and urban areas) from the TM quadrant of Qatar, which lacks thermal band and thus covers six bands, are selected in the study.

1.6.2. Organization of the thesis

The thesis covers seven chapters.

1. Chapter 1 is devoted to the deduction of the definition of the fractal concept by constructing the Koch curve and the Cantor set.
2. Chapter 2 illustrates the principles of seven methodologies for determining the fractal dimensions of spatial 1-dimensional curves and 2-dimensional surfaces data. The programs for the calculation are developed and verified by calculating the fractal dimensions of the simulated data which have known theoretical D values.
3. Chapter 3 analyzes the fractal behaviour of topographic contours digitized from different scales of maps by the ruler and box-counting methods.
4. Chapter 4 studies the fractal behaviours of the map and filed profiles from kilometre scales (map profiles) down to centimetre (field profiles) scales.
5. Chapter 5 investigates the effects on the variation in D values of topographic contours and coastal lines caused by different erosive processes, different rock types, and different fracture orientations.
6. Chapter 6 is the fractal analysis of the DEM and Qatar TM data by the spectral, 1^{st} and 2^{nd} order structure function methods.
7. Chapter 7 is about the conclusions drawn from the whole study.

CHAPTER 2

METHODOLOGY FOR DETERMINING FRACTAL DIMENSIONS

CHAPTER 2

METHODOLOGY FOR DETERMINING FRACTAL DIMENSIONS

2. METHODOLOGY FOR DETERMINING FRACTAL DIMENSIONS

2.1. INTRODUCTION

The fractal dimension has been computed in a variety ways. The methods used to calculate the fractal dimensions of lines and surfaces can be categorised into 1-dimensional and 2-dimensional (abbreviated as 1-d and 2-d respectively in the later discussion) methods. 1-d methods are used to determine the fractal dimensions of lines. These methods include the ruler, box-counting, 1-d spectral, 1-d structure function, and 1-d intersection methods. 2-d methods are used to determine the fractal dimensions of surfaces which are equally sampled as regular grid data. These methods include the 2-d spectral, 2-d structure function, 2-d intersection, cube-counting, and triangular prism methods.

In general, methods for calculating the fractal dimensions of lines can be easily extended to handle surfaces, such as the box-counting, spectral, structure function, and intersection methods. However, there is no direct equivalent of the ruler method for determining fractal dimensions of surfaces. The fractal dimension of a surface can be related with that of a profile or a contour set, which is resulted from the intersection of the surface with a plane. This approach is based on the zeroset theory (Goodchild, 1982; Burrough, 1981; Barnsley *et. al.*, 1988), for which the dimensions of surfaces (or curves) are reduced by 1 after they are intersected by a plane.

Self-similarity or self-affinity seriously affect the suitability of applying a method.

For example, some care should be taken when applying the ruler method to self-affine fractals (Mandelbrot, 1985; Brown, 1987; Wong, 1987). It will lead the D values of the self-affine fractals to be very close to 1 (self-affine curves) or 2 (self-affine surfaces for the box-counting method).

In Chapter 1, the concept of a fractal set has been originated from the construction of the Koch curve and the Cantor set. The objectives of this chapter are;

- To generate theoretical fractals, such as the Koch curve, Cantor set, simulated 1-d and 2-d fBm profiles and surfaces, which have known theoretical D values. The 1-d and 2-d fBm are generated by the midpoint displacement and interpolation techniques with H = 0.8, 0.5, and 0.2;
- To develop programs (in *VISUAL BASIC* and *FORTRAN* codes) for determining the fractal dimensions of the generated theoretical fractals;
- To verify the programs developed and the implementation of the methods by comparing the calculated D values with the theoretical D values;
- To discuss the analysis results of applying the ruler, box-counting, spectral, structure function, and intersection methods on the generated theoretical fractals.

Chapter 2 covers ten sections. Sections 2.2 and 2.3 demonstrate the principles of the ruler and box-counting methods using a topographic contour. The methods and programs are verified by determining the fractal dimensions of the self-similar Koch curve of level 5. The 1-d and 2-d fBm self-affine profiles and surfaces are generated by the midpoint-displacement and interpolation methods using H = 0.8, 0.5, and 0.2 in Section 2.4. The principles of the spectral and structure function are demonstrated and verified by applying the methods on the simulated fBm fractals, and are shown in Sections 2.5 and 2.6. Section 2.7 deals with the intersection method which is based on the zeroset theory, and links the D values of 1-d fractals with those of 2-d fractals. Sections 2.8 and 2.9 demonstrate the principles of the cube-counting and triangular prism methods. Some discussion of the methodology for determining the fractal dimensions is shown in Section 10. Section 11 is a list of programs developed (*VISUAL BASIC* and *FORTRAN* code) to calculate the fractal dimensions and to draw nearly all the diagrams of the thesis.

2.2. THE RULER METHOD

The ruler method is also known as the compass method, or (walking) divider method. Its basis has been demonstrated in Chapter 1.2.1 using the Koch curve. In this section, the ruler method (*RULERM* program written in *VISUAL BASIC* code) will be used to analyse a Koch curve of a recursion level of 5. Thus the *RULERM* can be verified by comparing the theoretical and calculated D values of the Koch curve. The section also demonstrates the principles of the method as it is applied to a topographic contour *PC2031*, and discusses some fractal features derived from the methodology.

2.2.1. Verification of the ruler method

Prior to application of the ruler method to topographic contours, it is necessary to verify the suitability and accuracy of the method (*RULERM* program). This can be achieved by applying *RULERM* to a theoretical curve whose fractal dimension is known, and comparing the theoretical fractal dimension and the calculated fractal dimension of the curve. The Koch curve, which has much of the complexity of a coast line or topographical contour, is one of the ideal fractal curves to verify the method.

A Koch curve of level 5 was produced by the program *Koch.bas* as shown in Fig. 2.1(a). Thus the Koch curve has a number of 1025 (4^5+1) points, each single line segment was assigned to be a length of 1, and the curve has a nominal length (the horizontal length in which the profile spans over) of 243 (3^5), and a total curve length of 1024. Theoretically, the curve has a fractal dimension D = 1.262 and the intercept C = 3.01 (i.e. C = Log(1024) =3.01 since the curve has a length of 1024 as it is measured by a unit length of 1).

Fig. 2.1(b) shows the log-log plot of the curve length of L against the ruler step r as the produced Koch curve of level 5 is input into the program *RULERM*. The slope of the regression line (β) between the ranges of the ruler step r = [2, 50] is $\beta = -0.262 \pm 0.015$, and the intercept $C = 2.912 \pm 0.016$. This shows the curve has a fractal dimension of 1.262 over a range between the lower fractal limit $r_L = 2$ and the upper fractal limit $r_U = 50$. For $r < r_L$ and $r > r_U$, the slopes of the regression lines are near to 0, and $D \approx 1.0$. This is because that the length of the curve tends to be the same (constant) with the variations of the ruler length r outside the fractal limits range of $[r_L, r_U]$.

Compared with the theoretical log-log plot of the Koch curve (solid circles), the

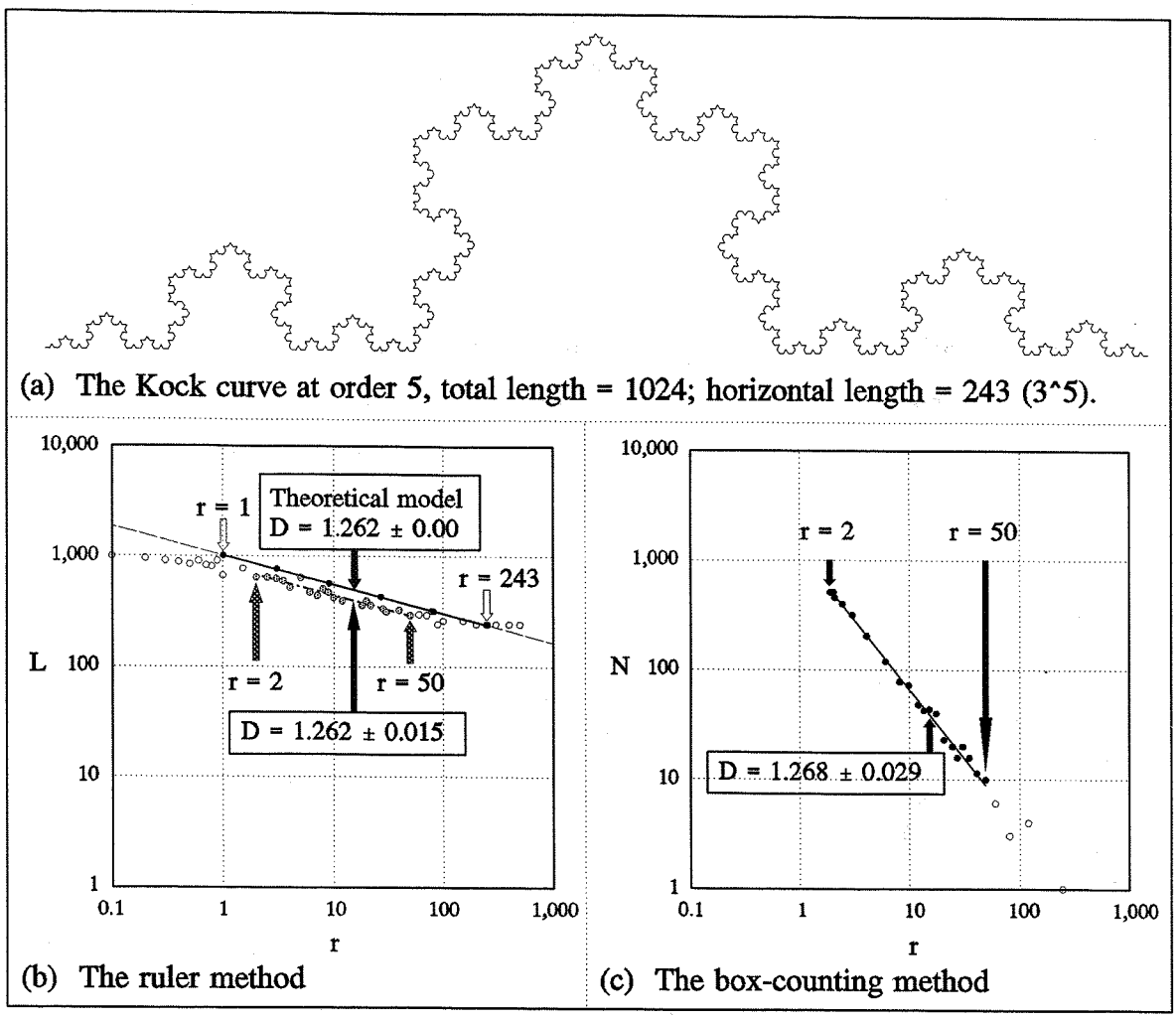

Fig. 2.1 Fractal analysis of a Koch curve by the ruler and box-counting methods. **(a)** A Koch curve of a recursion level of 5. The curve has a number of points of 1025, a nominal length of 243, a total curve length of 1024, and each line segment has a length of 1. **(b)** Log-log plot of the curve length (L) against the ruler length (r) used to measure the curve. **(c)** Log-log plot of the number of filled boxes (N) against the box size (r). Both plots of (a) and (b) show that the curve has a fractal dimension of 1.26 which is as same as the theoretical fractal dimension of the Koch curve.

practical log-log plot pattern (grey circles) differs in three ways (Fig. 2.1b):

1) The plotted points are scattered in the practical model. This is because the fractional numbers are used to deduce the theoretical length of the Koch curve at different ruler steps, hence the plotted points fit a perfect straight line. However, the Koch curve is practically recorded as a series of coordinates of decimal numbers in the practical model by the *Koch.bas*. Therefore, the lengths of the curve calculated based on these decimal numbers differ from the theoretical length at different ruler steps.
2) The power-law relationship between L and r only occurs over the fractal limits ($r_L = 2$, r_U

= 50) in the practical model, features beyond this range is out of statistical interests. In theoretical model, however, the length of the Koch curve has a perfect power-law relationship over a range between $r_1 = 1$ and $r_2 = 243$ ($r_1 = 1$ is the finest resolution of the curve, i.e., the length of each line segment; while $r_2 = 243$ is the nominal length, i.e., the longest distance between any two points of the Koch curve). Theoretically, r_1 (or r_2) can be any infinite small (or large) number.

3) Notice that the practical pattern is generally lower than the theoretical one. The intercept C = 2.912 for the practical model is lower than the theoretical intercept 3.01. This indicates, in practical term, the curve has a total length of $10^{2.912} = 816.6$, not a length of $10^{3.01} = 1024$. This can also be explained by the fact that the decimal digits of a certain length are used in the calculation of the practical model, whereas fractional numbers are used in the theoretical one.

Table 2.1 summarises the theoretical fractal dimension and the determined fractal dimension of the Koch curve by the ruler and the box-counting methods, it clearly shows that the fractal dimension of the Koch curve derived from the *RULERM* program within fractal limits between r = 2 and r = 50 is as same as the theoretical one, D = 1.26.

Table 2.1 Comparison of the theoretical and determined fractal features

	Theoretical	*RULERM* **D ± ΔD**	*BOXCM* **D ± ΔC**
D	1.262 ± 0.00	1.262 ± 0.015	1.268 ± 0.029
C	3.010 ± 0.00	2.912 ± 0.016	3.085 ± 0.032
r_L	1	2	2
r_U	243	50	50
Basic information of the curve: Recursion level = 5; Number of points = 1025 ($4^5 + 1$); Length of each line segments = 1; Total length of the curve = 1024; Nominal length of the curve = 243			

In Table 2.1, the notations r_L and r_U stand for the lower and upper fractal limits, and ΔD and ΔC are the error values for estimating the values of D and C by the least square method during fitting the regression line. Suppose there are K pairs of data points (x_i, y_i) to be used to fit the regression line, and the regression line has a slope of β and the intercept C, then the estimate errors in slope Δβ and the intercept ΔC are determined by (Bevington, 1969; Press *et. al.* 1986) by equation (2.1), where $\bar{x} = \frac{1}{K}\sum_{i=1}^{K} x_i$. Therefore, the estimate error in the fractal dimension ΔD = Δβ based on the equation (2.2). For the box-counting,

the spectral, and the 1st order structure function methods, ΔD and ΔC will be determined in the same way except $\Delta D = \Delta\beta/2$ for the 1-d and 2-d spectral and the 2nd order structure function methods as deployed in later discussions.

$$\Delta\beta = \sqrt{\frac{1}{\sum_{i=1}^{K}(x_i - \bar{x})^2} \times \frac{1}{K-2}\sum_{i=1}^{K}(y_i - (\beta x_i + C))} \qquad (2.1)$$

$$\Delta C = \sqrt{\left(\frac{1}{K} + \frac{(\bar{x})^2}{\sum_{i=1}^{K}(x_i - \bar{x})^2}\right) \times \frac{1}{K-2}\sum_{i=1}^{K}(y_i - (\beta x_i + C))}$$

2.2.2. Illustration of applying the ruler method to contours

To illustrate the application of the ruler method to contours, a topographic contour *PC2031* was taken as an example to demonstrate the principles of the methodology (Fig. 2.2). The contour was digitized from a 1:50,000 map of Spain by the *DIGICON* program, and further analyzed by *RULERM*. The digitized contour has a digitized length of L_0 = 28814.7 m, the number of digitized points is 1277, and has an average digitized interval of 22.6 m (=28814.7/1276). Refer to Chapter 3.2.2 for more details about the procedure of digitizing contours from maps. The digitized length of a curve L_0 is given by,

$$L_0 = \sum_{i=1}^{N-1}\sqrt{(x_{i+1} - x_i)^2 + (y_{i+1} - y_i)^2}, \quad i = 1,2,\ldots,N-1$$

where $[x_i, y_i]$, i = 1, 2, …, N, are a series of coordinates recorded for a topographic contour.

Firstly, the contour is displayed in a scaled down square [Fig. 2.2(a)]. The initial box size is R_0 = 6709 m, which is equal to the longest distance along x- or y-direction.

Secondly, a fixed ruler (or yardstick) of a length r is stepped out along the digitized contour from the first point of the line segment (the top of the box) [Fig. 2.2(b)].

Thirdly, different lengths of longer ruler (r) are used to repeat measuring the contour length (L) which is taken as the sum of ruler steps (r) plus any length remaining between the

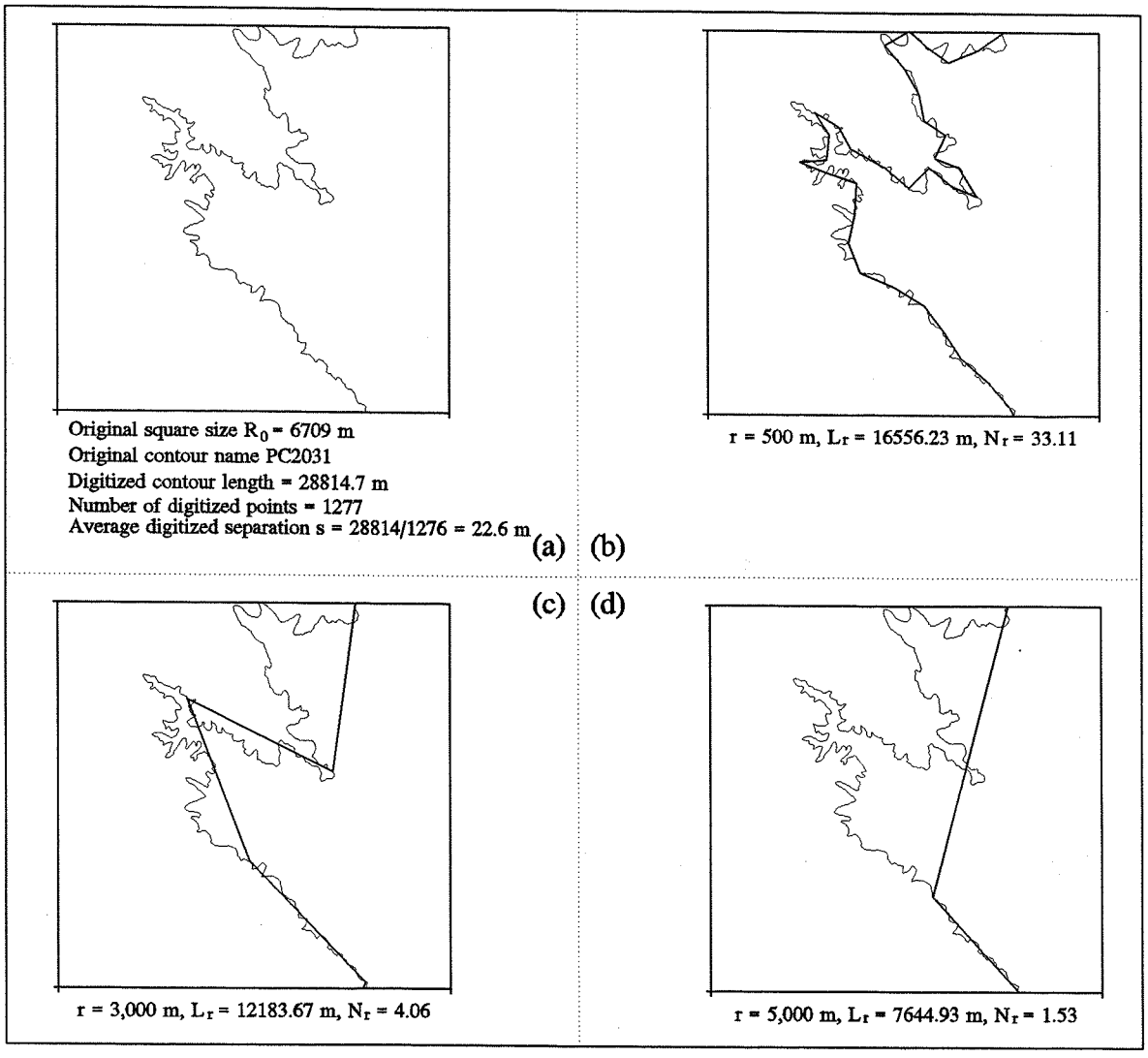

Fig. 2.2. Illustration of the principles of the ruler method. Measuring from the first point (the top-most point of the box) on the digitized contour, *PC2031*, using different ruler lengths leads to different measured lengths of the contour. **(a)** The original contour is scaled down and displayed in a square box, which has a side length of R_0 = 6709 m. **(b)** When the ruler length r = 100 m is employed to measure the contour then the length of the contour L = 16.56 km, and the number of the rulers N = 33.11. **(c)** L = 12.8 km and N = 4.06 when the contour is measured by a r = 3000 m. **(d)** If the contour is measured by a r = 5000 m, then L = 7.65 km and N = 1.53.

last step and the end of the digitized line [Fig. 2.2(c) and (d)]. On increasing the length of the ruler (r), the measured length of the contour decreases [Fig. 2.2(b) to (d)]. Refer to Table 2.2 for more details. The left side of Table 2.2 shows the results of applying the ruler method to the example contour *PC2031*. Typically, decreasing the ruler length (r) results in increasing the number of the rulers (N), as well as the length of the contour (L).

Table 2.2. Processed results of the contour *PC2031* from using the *RULERM* and *BOXCM* programs

The ruler method

r: ruler length (m);
N: Number of rulers used for r;
L: Total length of the contour;

The box-counting method

r: side length of the box (m);
N_t: total number of boxes;
N: number of the filled boxes;
P: percentage of the filled boxes (%).

r (m)	N	L (m)	Demo. Figs	r (m)	N_t	N	P (%)	Demo. Figs
6000	1.16	6966.05						
5000	1.53	7644.93	**Fig. 2.2(d)**	52.82	127^2	690	4.28	
4000	**2.41**	**9626.86**		55.91	120^2	636	4.42	
3500	2.55	8932.29		60.99	110^2	587	4.85	
3000	4.06	12183.67	**Fig. 2.2(c)**	67.09	100^2	528	5.28	
2500	4.67	11682.95		**74.54**	**90^2**	**474**	**5.85**	
2000	6.19	12373.37		83.86	80^2	408	6.38	
1750	6.32	11057.24		95.84	70^2	350	7.14	
1500	9.23	13843.57		111.81	60^2	293	8.14	
1250	10.25	12808.44		134.18	50^2	237	9.48	
1000	15.06	15060.78		167.72	40^2	183	11.44	
900	15.95	14354.10		223.63	30^2	129	14.33	
800	18.61	14885.03		335.44	20^2	75	18.75	**Fig. 2.4(f)**
700	23.05	16133.10		419.30	16^2	58	22.66	
600	26.20	15719.72		559.06	12^2	39	27.08	
500	33.11	16556.23	**Fig. 2.2(b)**	670.88	10^2	29	29.00	**Fig. 2.4(e)**
400	44.38	17751.79		745.42	9^2	28	34.57	
350	52.10	18233.48		838.59	8^2	24	37.50	
300	63.48	19044.07		958.39	7^2	19	38.78	
250	79.55	19886.29		1118.1	6^2	16	44.44	**Fig. 2.4(d)**
200	106.95	21390.80		1341.7	5^2	13	52.00	
175	124.88	21853.38		1677.2	4^2	11	68.75	**Fig. 2.4(c)**
150	149.93	22489.37		2236.3	3^2	8	88.89	
125	187.11	23388.30		**3354.4**	**2^2**	**4**	**100.0**	**Fig. 2.4(b)**
100	243.79	24379.15		6708.8	1^2	1	100.0	**Fig. 2.4(a)**
90	276.84	24915.78						
80	319.91	25593.19		***NOTE:***				
70	375.71	26299.73		*Input file name:*				*PC2031.CON;*
60	438.03	26281.62		*Output file name:*				*PC2031.DAT;*
50	**537.06**	**26852.90**		*Map scale:*				*1:50000;*
40	687.72	27508.69		*Contour level:*				*320 (m);*
30	928.61	27858.37		*Number of digitized points:*				*1277;*
20	1408.9	28178.94						
15	1890.6	28358.36		*Digitized length:*				*28814.7 (m);*
10	2852.8	28527.95		*Average digitized interval:*				*22.6 (m).*
5	5730.1	28650.69						

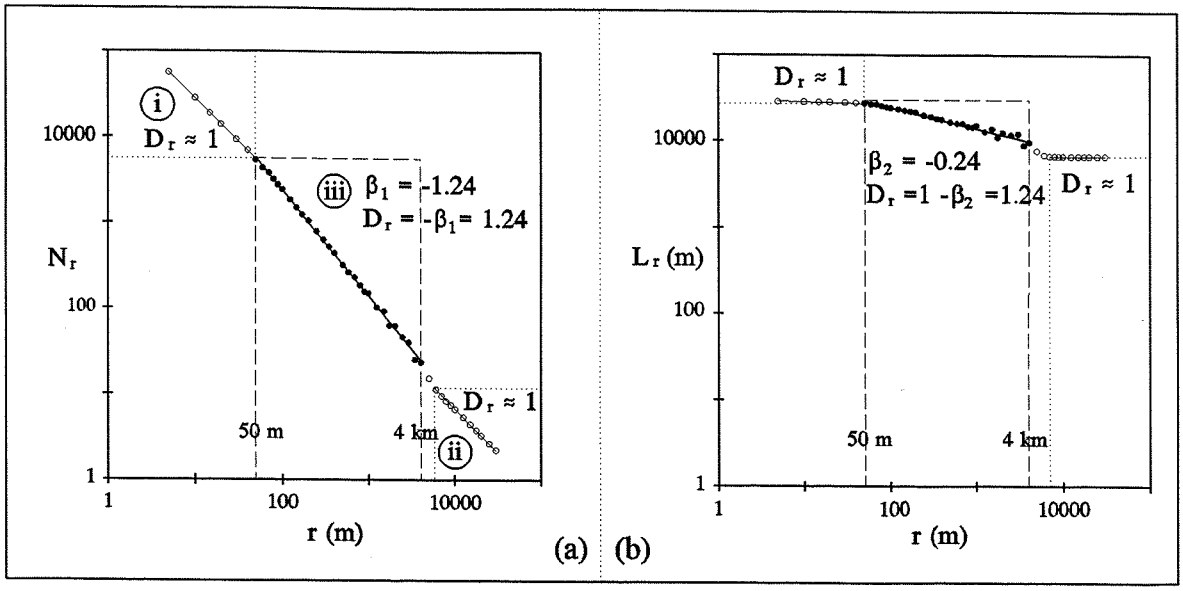

Fig. 2.3. Log-log plots of the ruler method to determine the fractal dimension of a contour. **(a)** shows a power-law relationship between the number of rulers (N) and the ruler length r, where $\beta_1 = -1.24$ is the slope of the regression line. Therefore, the contour is statistically a fractal over fractal limits between $r_L = 50$ m and $r_U = 4$ km with a fractal dimension $D_r = -\beta_1 = 1.24$. **(b)** shows a log-log plot of the contour length (L) against the ruler length (r), where $\beta_2 = -0.24$ is the slope of fitted regression line. The power-law relationship between L and r again reveals that the contour has a fractal dimension $D_r = 1 - \beta_2 = 1.24$ over the fractal limits between $r_L = 50$ m and $r_U = 4$ km.

Fourthly, the length of the contour (L) and the ruler length (r) are plotted on a log-log scale paper [Fig. 2.3(a)]. The plotted points over a range between 50 m and 4 km can be fitted by a regression line. This range is the fractal limits termed lower fractal limit (r_L) and upper fractal limit (r_U) respectively. This regression line shows a power-law relationship between L and r, and has a slope of $\beta_1 = -1.24$.

Finally, recalling the definition of a fractal set described in Chapter 1, equation (1.1) can be rewritten as,

$$N = C_r \, r^{-D_r} \tag{2.2}$$

where D_r is defined as the fractal dimension. Hence the fractal dimension of the contour *PC2031* is $D_r = -\beta_1 = 1.24$.

Alternatively, the fractal dimension of the contour can be derived from the plot of Log(L) against Log(r) as shown in Fig. 2.3(b). Based on equation (1.2), the power-law

relationship between L and r can be rewritten as,

$$L = C_r \, r^{1-D_r}$$

since the length of the curve L = N r. The slope of the fitted regression line (β_2), over the fractal limits between 50 m and 4 km, is -0.24, therefore, the fractal dimension of the contour is $D_r = 1 - \beta_2 = 1.24$. Refer to the left side of Table 2.2 for more details about the variations of the lengths of the contour (L) with changing the ruler length r

The power-law relationships between (N) and (L) against (r) in the range of about r_L = 50 m and r_U = 4 km as shown in Fig. 2.3(a) and (b) satisfy the definition of a fractal set. The example contour, *PC2031*, has a fractal dimension $D_r = 1.24$ in the fractal limits of about r_L = 50 m and r_U = 4 km, i.e., about three orders of magnitude.

2.2.3. Discussion of the log-log plot pattern of the ruler method

Both plots shown in Fig. 2.3 share similar features, the patterns of the plotted points can be categorized into three groups based on the r ranges. The distribution pattern between r_L and r_U reveals the scaling behaviours of the topographic contour, whilst for r range beyond [r_L, r_U] the distribution patterns unveil little. Fig. 2.3(b) is taken as an example to demonstrate the general patterns of the log-log plots for the ruler and box-counting methods.

- For r < 50 m, the plotted points fit a straight line which has a slope of about 0. Thus, the fractal dimension of the contour over this range is $D_r = 1$. The average digitized interval of the contour is 22.6 m, as shown in Table 2.2. Based on the Nyquist theory, the information retained in a contour should not be less than twice the average sampling (digitized) interval (≈ 50 m) when the contour is digitized from a map.
- For r > 4 km, the plotted points again fit a straight line of a slope of about 0, implying $D_r = 1$. This is because the length of the contour reaches a constant value when the ruler length exceeds a maximum length which is the maximum distance between the start and any other points of the digitized contour.
- The ruler range between 50 m and 4 km reveals most details of the contour. The slope of the fitted line (β_2), which is determined by the least squares regression method is -0.24, i.e., $D_r = 1 - \beta_2 = 1.24$ (Fig. 2.3b).

2.3. THE BOX-COUNTING METHOD

The box-counting method, as well as the ruler method, is suitable for determining the fractal dimensions of 1-d self-similar fractals, such as topographic contours. Its concept has also been deduced and illustrated in Chapter 1.2.3. In this section, the box-counting method (program *BOXCM* code written in *VISUAL BASIC*) is verified by comparing the calculated and theoretical fractal dimensions of the Koch curve generated in Section 2.2.1, and the principles of the methodology is demonstrated by applying the method to the example topographic contour *PC2031*.

2.3.1. Verification of the box-counting method

The box-counting method (*BOXCM* program) can also be tested by applying the method to the Koch curve generated in Section 2.2.1. Fig. 2.1(c) shows the log-log plot of the number of the filled boxes (N) against the box size (r). The slope of the regression line (β) over r ranges between $r_L = 2$ and $r_U = 50$ is $\beta = -1.268 \pm 0.029$, and the intercept $C = 3.085 \pm 0.032$ (i.e., the number of boxes of size r = 1 to cover the Koch curve is $10^{3.085} = 1216$). It indicates that the curve has a fractal dimension of 1.268 over a range of [2, 50]. This indicates that the D value of the Koch curve (of 5 level recursion) derived from the box-counting method is roughly the same as that determined by the ruler method, and both are consistent with the theoretical D value of the Koch curve (Table 2.1).

2.3.2. Illustration of applying the box-counting method to contours

Similarly, the example contour *PC2031* is taken as an example to illustrate the principles of the box-counting method (Fig. 2.4).

Firstly, the contour *PC2031* is displayed in a scaled down square box of size R_0 =6,709 m as shown in Fig. 2.4(a), i.e., the contour is contained in an initial box of a side length of r = 6709 m [Fig. 2.4(a)]..

Secondly, the initial box is subdivided into 2^2 equal-sized square boxes of side length $r = R_0/2$ [Fig. 2.4(b)]. Those boxes in which any portion of the contour occurs are named as filled boxes (shaded), and the number of filled boxes is recorded as N. The ratio of N and the total number of boxes (N_t) is recorded P as percentage of the filled boxes. At this stage, r = 3354 m, N = 4, and P = 100%.

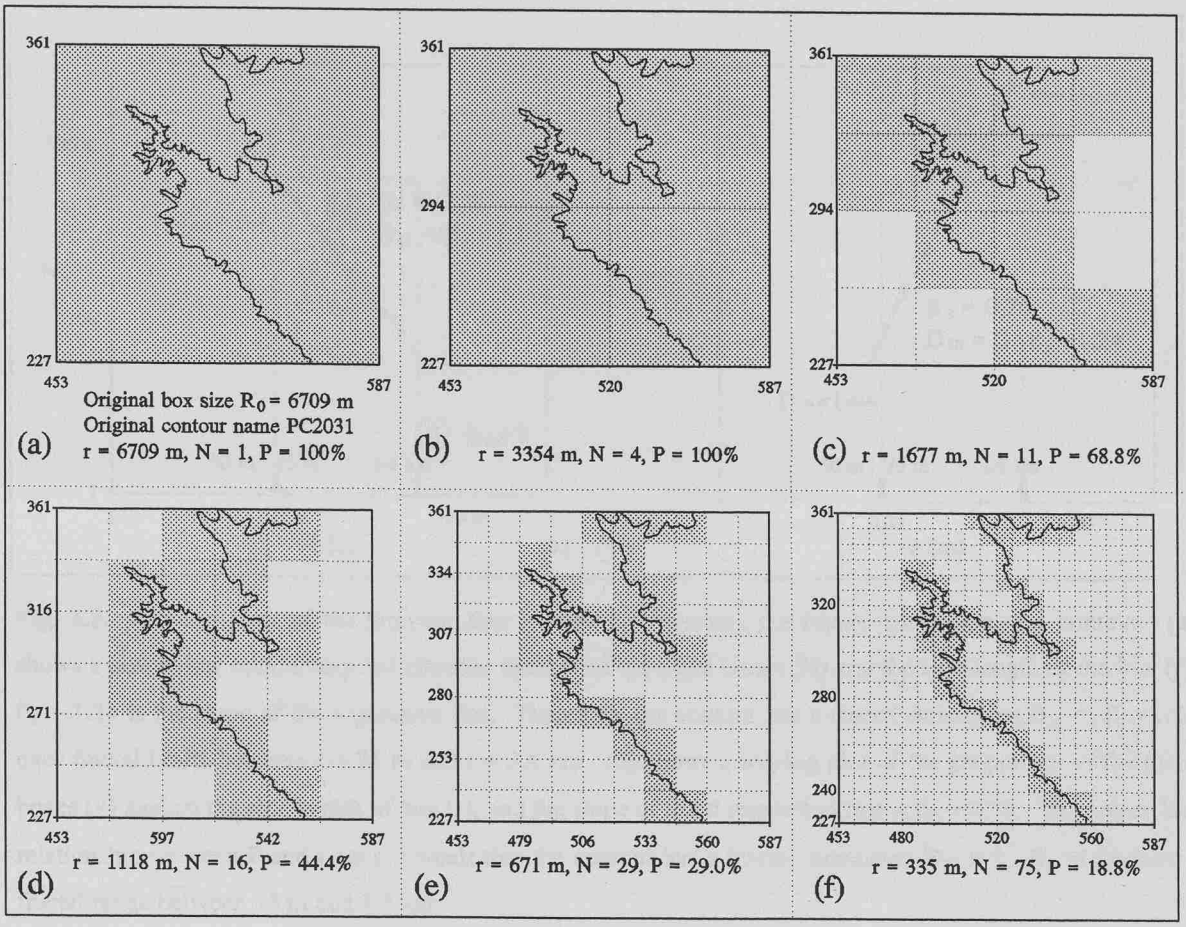

Fig. 2.4. Illustration of the principles of the box-counting method. The curve is the topographic contour *PC2031*. Those boxes in which any portion of the contour occurs are named as filled boxes, the number of filled boxes is recorded as N, and the ratio of N and the total number of boxes (N_t) as percentage of the filled boxes P. Refer to Table 2.2 for more details. **(a)** shows the original contour scaled down and displayed in the square box of a side length R_0 = 6.7 km. If the contour is measured by a box sized r = 6.7 km, then the number of filled boxes N = 1, and the proportion of filled boxes P = 100%. **(b)** If the contour is covered by 4 smaller boxes of size r = 3.35 km, then N = 4 and P = 100%. **(c)** When 16 boxes sized r = 1.68 km are used to cover the contour, then N = 11 and P = 68.8%. **(d)** When r = 1.12 km, then N = 16 and P = 44.4%. **(e)** For r = 0.671 km, then N = 29 and P = 29.00%. **(f)** when r = 0.34 km, then N = 75 and P = 18.8%

Thirdly, the initial box can be divided into smaller and smaller boxes, such as $r = R_0/n$, where n^2 is the total number of boxes divided from the initial square box. Therefore, a series of the number (N) and proportion (P) of filled boxes are obtained for different box sizes (r), and are listed in the right column of Table 2.2.

Fourthly, the number of the filled boxes (N) and the side length of the box (r) are plotted on a log-log scale paper as shown in Fig. 2.5(a). For these plotted points over the r range between 75 m and 3.4 km, a regression can be obtained. This regression line reveals

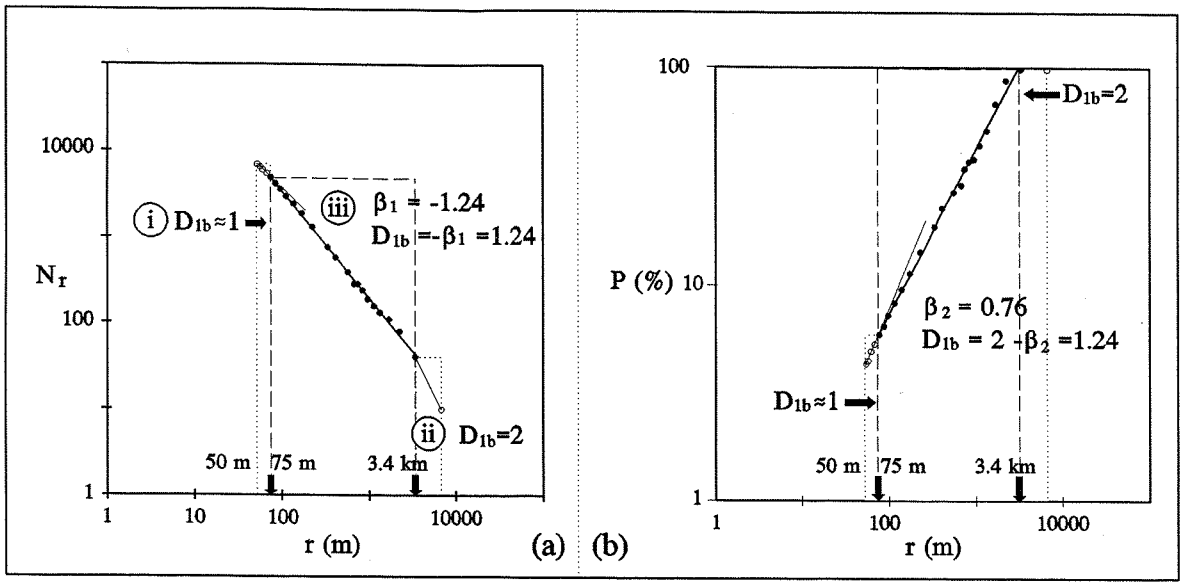

Fig. 2.5. Log-log plots of the box-counting method to determine the fractal dimension of a contour. **(a)** shows a power-law relationship between the number of the filled boxes (N) and the side length of the box (r), $\beta_1 = 1.24$ is the slope of the regression line. Therefore, the contour has a fractal dimension $D_{1b} = -\beta_1 = 1.24$ over fractal limits between r = 75 m and r = 3.4 km. **(b)** shows a log-log plot of the proportion of the filled boxes (P) against the side length of box (r), and the slope of fitted regression line is $\beta_2 = 0.76$. The power-law relationship between P and r again reveals that the contour has a fractal dimension $D_{1b} = 2 - \beta_2 = 1.24$ over a fractal range between 75 m and 3.4 km.

a power-law relationship between N and r, and has a slope of $\beta_1 = -1.24$.

Finally, the fractal dimension of the contour is derived from the definition of a fractal set described in equation (1.1) as $D_{1b} = -\beta_1 = 1.24$ over a fractal range 75 m < r < 3.4 km. Alternatively, the log-log plot of the proportion of the filled boxes (P) against the side length of box (r) [Fig. 2.5(b)] reveals that the contour has a fractal dimension of $D_{1b} = 2 - \beta_2 = 1.24$ over a fractal range from r = 75 m to r = 3.4 km based on the equation (1.4). The fractal dimension is the same as that derived from Fig. 2.5(a) using N and r.

For the side length of box r < 75 m and r > 3.4 km, the power-law relationship of the log-log plot deduce the fractal dimension of the contour $D_{1b} = 1$, and 2, respectively. This is because the contour is initially a line if the contour is observed at a fine scale of resolution (< 75 m) hence $D_{1b} = 1$, or fills an area if the contour is observed at a coarse resolution (> 3.4 km) hence $D_{1b} = 2$.

2.4. SIMULATION OF RANDOM FRACTALS – fBm

In this Section, six 1-d (mp12, mp15, mp18; int12, int15, int18) and six 2-d (mp22, mp25, mp28; int22, int25, int28) random fractals of known fractal dimensions are generated by using midpoint displacement and interpolation techniques using H = 0.8, 0.5, and 0.2. The generation of the random fractals are for the purpose of verifying the spectral and structure function methods. By comparing the calculated with the theoretical D values of these random fractals, the applicability of the spectral and structure function methods can then be verified when they are applied to the natural profiles or surfaces in the world.

The generation of random fractals relies on the integration of Brownian motion with the fractal concept (thus termed fractional Brownian motion, fBm). Barnsley *et. al.* (1988) provided a lot of methods to generate the random fractals, the midpoint displacement and the interpolation methods are used in the study (Refer to Appendix 1 for more details).

2.4.1. The midpoint displacement technique

The midpoint displacement method was firstly used to approximate the normal Brownian motion in 1920's by N. Wiener. Promoted by Carpenter, Fournier, and Fussell (Carpenter, 1980; Fournier *et. al.*, 1982), it has become widely popular in areas of surfaces simulation and computer graphics (Hearn and Baker, 1986; Harrington, 1987). Fig. A1.2 demonstrates the principle of the midpoint displacement method for the first two levels. Briefly, the method is a recursive generating, or midpoint interpolating technique with a scaling factor of r = 0.5. Given a time interval [0, 1], a parameter $1 > H > 0$, and $V_H(0) = 0$ and $V_H(1)$ a sample of Gaussian random variable of zero mean and variance of σ^2. At a recursive level n, the values of midpoints are averaged by their nearby two points plus a random Gaussian offset D_n, i.e.,

$$V_H(x_{mid}) = \frac{1}{2}\left(V_H(x_0) + V_H(x_1)\right) + D_n$$

The offset D_n has a zero mean and variance Δ_n^2 which is given by,

$$Var(D_n) = \Delta_n^2 = \frac{1}{(2^n)^{2H}}\left(1 - 2^{2H-2}\right)\ \sigma^2$$

where σ^2 is the initial variance. Thus the length scale has decreased to 2^{-n}.

The principles of 1-d midpoint displacement method can be easily extended to 2-dimension as shown in Section A1.4.3.1 and Fig. A1.6. Suppose a unit square has four corner points (x_0, y_0), (x_1, y_0), (x_1, y_1), and (x_0, y_1), and their corresponding values are given as random Gaussian samples $V(x_0, y_0)$, $V(x_1, y_0)$, $V(x_1, y_1)$, and $V(x_0, y_1)$ with zero mean and an initial variance of σ^2. Then, at recursion level n, the value of a displaced point at a scale factor $r = 1/\sqrt{2}$ is averaged by its nearby 3 (for the displaced points located at the edges of the unit square) or 4 (for the displaced points located in the unit square) data points plus a random Gaussian offset D_n, of a variance Δ_n^2 is given by,

$$Var(D_n) = \Delta_n^2 = \left[\left(\frac{1}{\sqrt{2}}\right)^n\right]^{2H} \sigma^2 = \left(\frac{1}{2}\right)^{nH} \sigma^2$$

In this study, the midpoint displacement was used to generate 1-d fBm profiles as mp12 (H = 0.8, D = 1.2), mp15 (H = 0.5, D = 1.5), and mp18 (H = 0.2, D = 1.8) and 2-d fBm surfaces as mp22 (H = 0.8, D = 2.2), mp25 (H = 0.5, D = 2.5), and mp28 (H = 0.2, D = 2.8). They have non-stationary increments characteristics when $H \neq 1$ (Refer to Section A1.3.3.1 of Appendix 1). In later discussion, they are abbreviated as mp profiles and mp surfaces respectively.

2.4.2. The interpolation technique

The midpoint displacement is a special case of the interpolation method, where interpolated midpoints at each level have the same interpolating ratio of r = ½, i.e., the resolution is improved by a factor of r = ½ each time further. The interpolation method deals with the situations that different interpolating ratios $0 < r < 1$ are evoked. If there are N_n points with a resolution of Δt at level n, then there will be $N_{n+1} = N_n / r$ new points with a new resolution of $r\Delta t$ at level (n + 1). The values of these new points are set through using the linear interpolation which is a kind of distance weighted average method as shown in Fig. A1.5(a). If the weighted index to the end point x_1, say u, is defined as,

$$u = \frac{(x - x_0)}{(x_1 - x_0)}$$

then the value of the interpolated point at x, $V_H(x)$, is determined by,

$$V_H(x) = (1-u)V_H(x_0) + u\,V_H(x_1) + D_n$$

A random offset D_n of Gaussian random variable with variance of Δ_n^2 is added to all points, including the original and new interpolated points for the purpose of stationary increments. Δ_n^2 is given by,

$$\Delta_n^2 = \frac{1}{2}(r^n)^{2H}(1 - r^{2-2H})\ \sigma^2$$

where r is a scaling factor ($0 < r < 1$). Different r values will change the appearance of the generated fractals, but not the D value which is only controlled by H ($0 < H < 1$).

The scaling factor discussed in the 2-d displacement method is $r = 1/\sqrt{2}$, it can be easily extended to approximate a 2-d fBm using different scaling factors $0 < r < 1$. Suppose a unit square has random values of its four corners selected from a Gaussian distribution with variance σ^2. In order to interpolate the data size to be N^2, then the final resolution is to be 1/(N-1). As can be deduced easily that there will be $[(r)^{-n} + 1] - 4$ new points to be generated at stage n. The values of these new points are firstly bilinearly interpolated from their nearby four corner points, then an offset D_n is added to ALL the new generated points. D_n is, again, a Gaussian random variable with a variance σ_n^2 which is given by,

$$\Delta_n^2 = \frac{1}{2}(r^n)^{2H}(1 - r^{2-2H})\ \sigma^2$$

The bilinear interpolation method is demonstrated in Fig. A1.8 (Press *et. al.*, 1986). The unit square has four corner points (x_0, y_0), (x_1, y_0), (x_1, y_1), and (x_0, y_1), and their values are given as $V(x_0, y_0)$, $V(x_1, y_0)$, $V(x_1, y_1)$, and $V(x_0, y_1)$ respectively. Supposing that a new point V(x, y) falls in the grid square, then the bilinear interpolation gives its value as,

$$\begin{aligned} V(x,y) = {} & (1-u)(1-v)V(x_0,y_0) + u(1-v)V(x_1,y_0) \\ & + (1-u)vV(x_0,y_1) + uvV(x_1,y_1) + D_n \end{aligned}$$

as u and v are defined as,

$$u = \frac{(x - x_0)}{(x_1 - x_0)} \quad and \quad v = \frac{(y - y_0)}{(y_1 - y_0)}$$

where $0 \leq u, v \leq 1$. A random offset D_n with a variance of Δ_n^2 is added ALL points to maintain the property of stationary increments.

The interpolation method is deployed in this study to generate six 1-d and 2-d with H = 0.8, 0.5, and 0.2. They are 1-d fBm profiles int12 (H = 0.8, D = 1.2), int15 (H = 0.5, D = 1.5), and int18 (H = 0.2, D = 1.8); and 2-d fBm surfaces int22 (H = 0.8, D = 2.2), int25 (H = 0.5, D = 2.5), and int28 (H = 0.2, D = 2.8). In later discussion, they are abbreviated as int profiles and int surfaces respectively.

It is worthwhile pointing out that the variation of scaling factor r ($0 < r < 1$) used for generating fBm by the interpolation technique will change the appearance of the generated int profiles and surfaces, but not the D values which are only controlled by the parameter H ($0 < H < 1$). The variation in fractal appearance caused by the changes of r is termed lacunarity (refer to sections A1.3.3 and A1.4.3.2 of appendix 1 for more details).

The int profiles and surfaces have stationary increments, whereas mp profiles and surfaces have non-stationary increments. The profiles and surfaces of different fractal dimensions D are characterized by the parameter H (also known as *Hausdoff* measure, $0 < H < 1$). The relationship between the fractal dimension D and the parameter H is given by (Barnsley *et. al.*, 1988),

$$D = E - H$$

where E = 2 for 1-d fBm profiles, and E =3 for 2-d fBm surfaces.

The programs for generating 1-d fBm, 2-d fBm were written both in *FORTRAN 77* and *VISUAL BASIC* codes. The programs for plotting figures and diagrams in the study was written in *VISUAL BASIC* code.

2.4.3. Generation of one-dimensional fBm profiles

Fig. 2.6(a) and (c) show the generated 1-d fBm of the parameter values of H = 0.8,

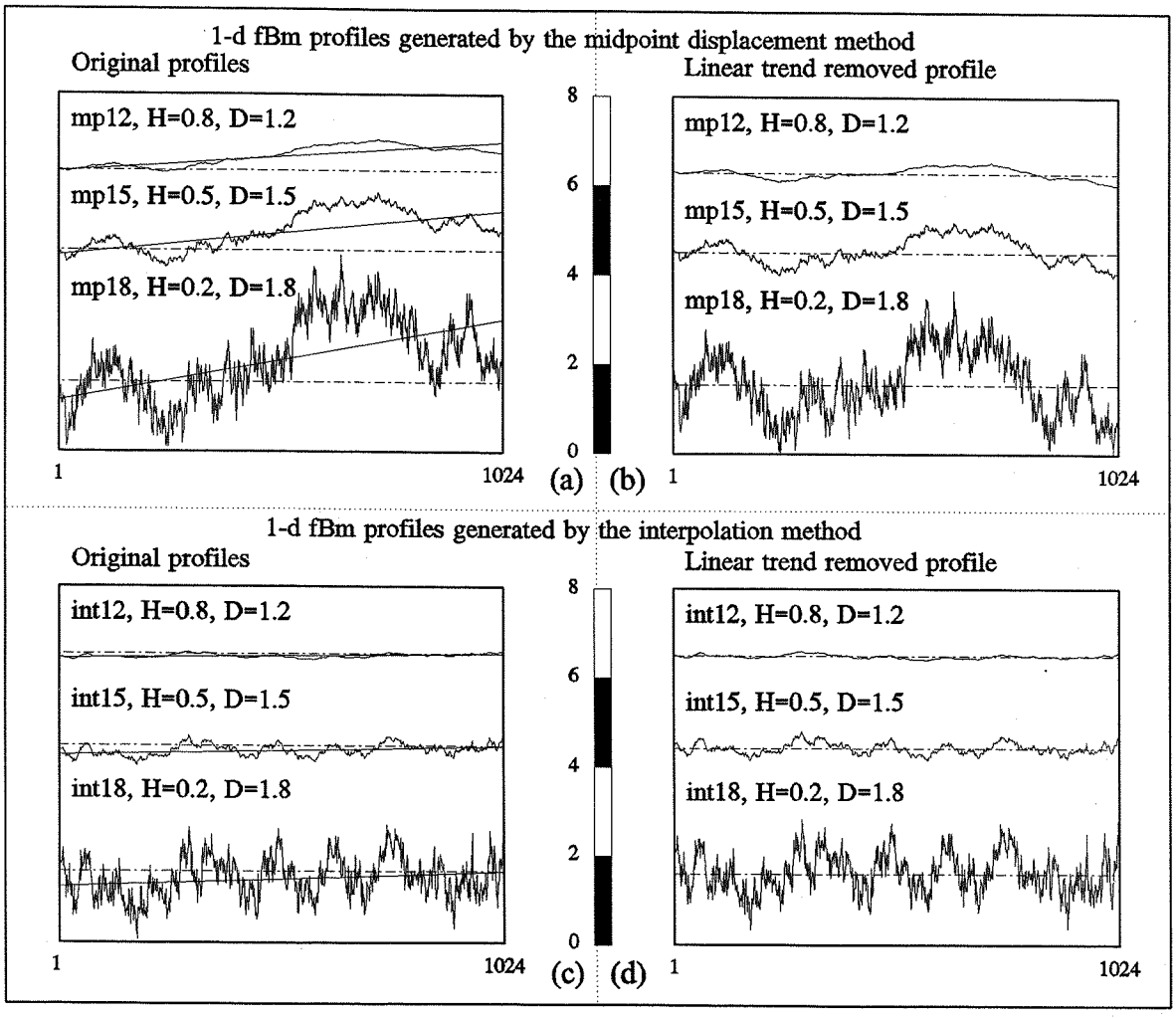

Fig. 2.6. 1-d fBm original and detrended mp and int profiles of H = 0.8, 0.5 and 0.2. All profiles have the same nominal length of 2^{10} - 1. The trend of the profile is marked by the solid line crossing the curve. **(a)** shows the original profiles of H = 0.8, 0.5 and 0.2 (hence D = 1.2,. 1.5, and D = 1.8) generated by the midpoint displacement method. Their trends removed profiles are shown in **(b)** respectively. **(c)** shows the original profiles of H = 0.8, 0.5 and 0.2 (hence D = 1.2,. 1.5, and D = 1.8) generated by the interpolation method. Their trends removed profiles are shown in **(d)** respectively.

0.5, and 0.2 by the midpoint displacement (*MP1D* program) and interpolation (*INT1D* program) methods, hence D = 1.2, 1.5, and 1.8 respectively. The generated profile is recorded as $[x_i, y_i = g(x_i)]$ where x_i, i = 1, 2, ..., 2^{10}, hence the profiles have the same nominal length of $L_n = x_N - x_1 = 1023$ (2^{10} - 1). The initial variance for generating the simulated 1-d fBm profiles and 2-d fBm surfaces was taken as $\sigma^2 = 1$, the seed value for random generator was taken as 4, and the scaling factor r = 0.6 was used for the interpolation technique. Some of the statistics information of the vertical variation $y_i = g(x_i)$

for the different profiles named in the Fig. 2.6(a) and (c) is shown in Table 2.3. Fig. 2.6(b) and (d) are linearly detrended (linear trend removed) profiles of the original profiles as shown in Fig. 2.6(a) and (c). The detrending procedure includes fitting a best-fit line y_T to the original profile by a robust line-fitting algorithm (Press *et. al.*, 1986), and the detrended (residual) profile y_R is obtained by subtracting the linear trend line from the original profile y, i.e.,

$$y_R = y - y_T$$

The original and detrended profiles have the same nominal length of $L_n = 1023$. The linear trend line can written as,

$$y_T = a\,x + b$$

where **a** is the slope and **b** is the intercept of the linear trend line.

Table 2.3. Statistics of simulated 1-d fBm profiles

	Trend line information y_T = **a** x + **b**				Original profile [x, y] information					
File name	**a**	**b**	**%RSS**	**r**	L_0	**avg**	**std**	**min**	**max**	R_q / R_a
mp12 (H = .8)	0.038	-0.033	67.2	0.86	1023.0	0.33	0.01	-0.05	0.71	1.22
mp15 (H = .5)	0.056	-0.120	42.4	0.73	1023.5	0.44	0.01	-0.39	1.31	1.20
mp18 (H = .2)	0.102	-0.411	34.4	0.60	1055.5	0.54	0.03	-1.46	2.86	1.19
int12 (H = .8)	0.006	-0.100	41.3	0.60	1023.0	-0.05	0.00	-0.15	0.13	1.26
int15 (H = .5)	0.011	-0.211	19.1	0.42	1023.4	-0.10	0.00	-0.45	0.29	1.21
int18 (H = .2)	0.018	-0.341	4.0	0.20	1049.5	-0.15	0.01	-1.54	1.19	1.19

In Table 2.3, the nominal length of all profiles is the same, $L_n = 1023$, the total length of the original profile L_0 is determined by,

$$L_0 = \sum_{i=1}^{N-1} \sqrt{(x_{i+1} - x_i)^2 + (y_{i+1} - y_i)^2}, \quad i = 1,2,\ldots,N-1$$

where $[x_i, y_i = g(x_i)]$, i = 1, 2, …, N, are a series of coordinates of the profile. The notations of avg, std, min, and max are the average value, the standard deviation, the minimum, and

maximum values of the original profile $[x_i, y_i]$. R_q and R_a are the root mean square and the centre line average values, which will be discussed in Chapter 4.3.4. The traditional description of the trend for a profile is the trend line angle degree, which very much depends on the amplitude of the profile. It is not a proper descriptor for the simulated profiles since their amplitudes can be magnified by any factor without changing the H value, hence without changing the D value. Suppose that

$$\bar{y} = \frac{1}{N}\sum_{i=1}^{N} y_i$$

and

$$\overline{y_T} = \frac{1}{N}\sum_{i=1}^{N} y_{Ti},$$

then %RSS (Residual Sum of Squares) is defined as the ratio of RSS_T and RSS_O, which are the sums of squares of the trend line $[x_i, y_{Ti}]$ and the original profile $[x_i, y_i]$, i.e.,

$$\%RSS = \frac{RSS_T}{RSS_O} \times 100\% = \frac{\sum_{i=1}^{N}\left(y_{Ti} - \overline{y_T}\right)^2}{\sum_{i=1}^{N}\left(y_i - \bar{y}\right)^2} \times 100\%$$

%RSS is a parameter to quantify the trend of the linear trend line (Chatfield, 1983), it is the ratio of the explained variance and the total variance of the profile, the higher the %RSS is, the more marked trend the profile has. Generally,

as %RSS < 4%	slight, almost negligible trend;
as %RSS 4 - 16%	low, definite but small trend;
as %RSS 17 - 49%	moderate-substantial trend;
as %RSS 50 - 80%	high, marked trend;
as %RSS 81 - 100%	very marked trend.

The coefficient value r ($1 > r > 0$) as shown in Tables 2.3 is a parameter to describe how

well the trend line fits the data, it is determined by,

$$r = \frac{\sum_{i=1}^{N}(x_i - \bar{x})(y_i - \bar{y})}{\sqrt{\sum_{i=1}^{N}(x_i - \bar{x})^2 \times \sum_{i=1}^{N}(y_i - \bar{y})^2}}$$

where $\bar{y} = \frac{1}{N}\sum_{i=1}^{N} y_i$. As r = 1, all data points should fall on the fitted line, whereas r = 0 indicates that y is independent on x. As shown in Table 2.3, int12 profile has higher trend than int15 and int18, although it looks so smooth. In fact, if the scale of y is magnified, its moderate-substantial trend will be disclose more clearly.

2.4.4. Generation of two-dimensional fBm surfaces

Fig. 2.7(a) and (c) show the generated 2-d fBm of the parameter values of H = 0.8, 0.5, and 0.2 by the midpoint displacement (*MP2D* program) and interpolation (*INT2D* program) methods, hence D = 2.2, 2.5, and 2.8 respectively. Each generated surface is recorded as $[x_i, y_i, z_i = g(x_i, y_i)]$ where i, x_i, y_i = 1, 2, …, 64, hence the data size is 64 by 64. The initial variance for generating the simulated 1-d fBm profiles and 2-d fBm surfaces was taken as σ^2 =1, the seed value for random generator was taken as 4, and the scaling factor r = 0.6 was used for the interpolation technique. Some of the statistics information of the vertical variation z_i for the different profiles named in the Fig. 2.7(a) and (c) is shown in Table 2.4.

Table 2.4. Statistics of simulated 2-d fBm surfaces

	Trend plane z_T = **m** x + **n** y + **c**				Original surface [x, y, z] information				
File name	**m**	**n**	**c**	**%RSS**	**data size**	**avg**	**std**	**min**	**max**
mp22 (H = .8)	0.017	-0.0008	-0.932	55.4	64 * 64	-0.41	0.42	-1.65	0.95
mp25 (H = .5)	-0.010	-0.003	1.669	18.1	64 * 64	1.23	0.47	-0.29	3.20
mp28 (H = .2)	0.005	-0.009	-0.280	5.7	64 * 64	-0.43	0.79	-2.98	2.11
int22 (H = .8)	-0.005	-0.004	0.018	61.1	64 * 64	-0.25	0.14	-0.80	0.27
int25 (H = .5)	-0.004	-0.002	-0.072	10.9	64 * 64	-0.24	0.22	-0.97	0.53
int28 (H = .2)	-0.003	0.0003	-0.136	1.4	64 * 64	-0.23	0.48	-1.89	1.43

To clarify the perspective views of these surfaces, only the upper half (those z values

are greater than the average value of the whole data set, refer to Table 2.4) of the surface is plotted. Fig. 2.7(b) and (d) are linearly detrending (linear trend removed) surfaces of (a) and (c). The detrending procedure includes: Firstly, a best-fit linear plane z_T was fitted to the original surface by a robust fitting algorithm (Press *et. al.*, 1986), which is written as,

$$z_T = mx + ny + c$$

where **m** and **n** are the slopes of the trend plane intersected with x and y coordinates, and **c** is the intercept of the trend plane intersected with z coordinate, i.e., $\mathbf{c} = z_T(x = 0, y = 0)$. Secondly, the detrended (residual) surface, z_R, is obtained by subtracting the linear trend plane from the original surface z, i.e.,

$$z_R = z - z_T$$

In Tables 2.4, the abbreviations of avg, std, min, max, and %RSS are the same as those of Table 2.3, but they are the values of the 2-d fBm surfaces z. %RSS is the ratio of the sum squares of the trend plane and the original surface, given by,

$$\%RSS = \frac{RSS_T}{RSS_O} \times 100\% = \frac{\sum_{i=1}^{N}\sum_{j=1}^{N}\left(z_{Tij} - \overline{z_T}\right)^2}{\sum_{i=1}^{N}\sum_{j=1}^{N}\left(z_{ij} - \bar{z}\right)^2} \times 100\%$$

where $\overline{z_T} = \frac{1}{N^2}\sum_{i=1}^{N}\sum_{j=1}^{N} z_{Tij}$ and $\bar{z} = \frac{1}{N^2}\sum_{i=1}^{N}\sum_{j=1}^{N} z_{ij}$. The higher the value of %RSS, the more significant trend the surface has. As shown in Table 2.4, the int22 and mp22 surfaces have most marked trends.

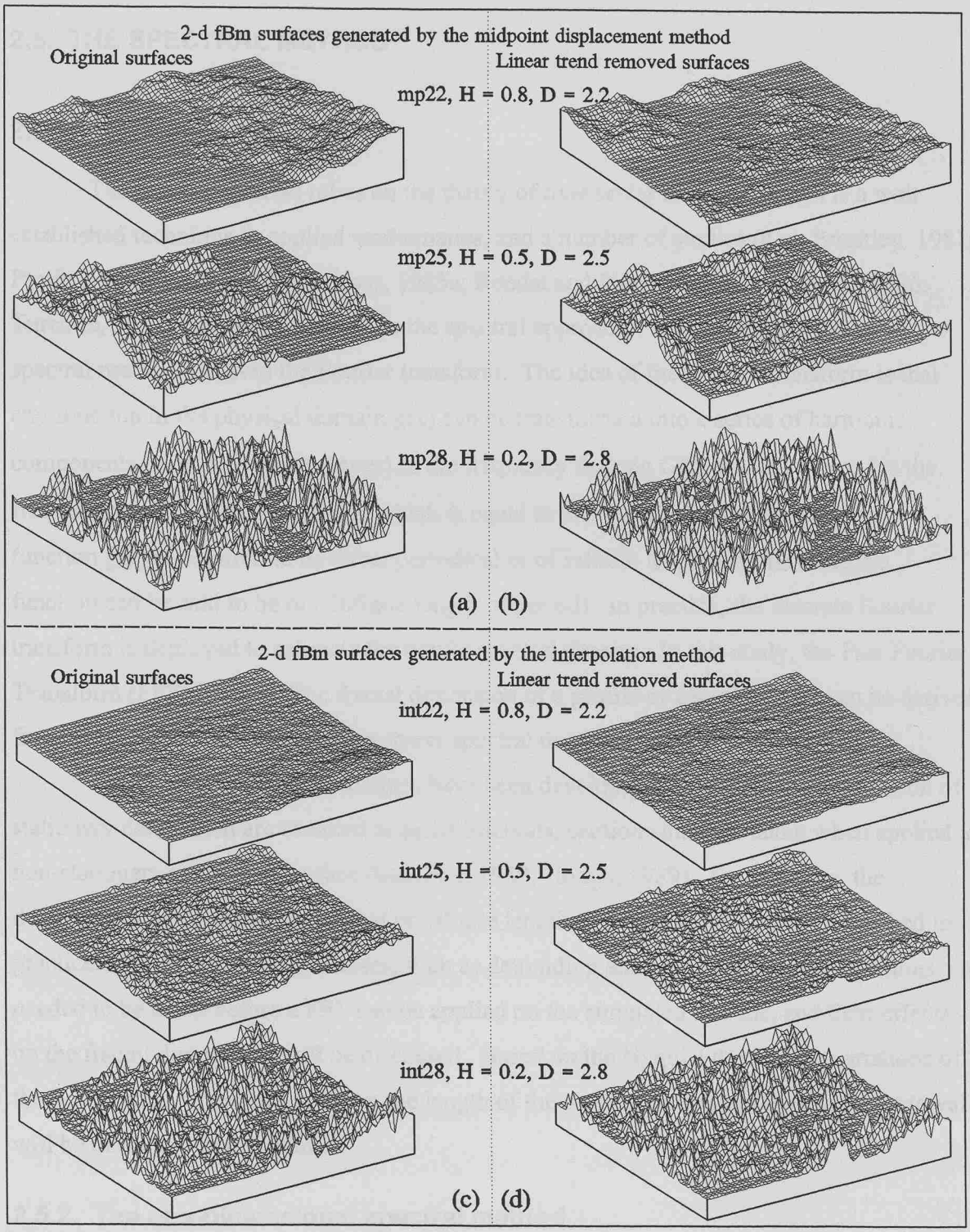

Fig. 2.7. Perspective views of 2-d fBm original and detrended surfaces generated by the midpoint displacement and interpolation techniques using H = 0.8, 0.5 and 0.2. Therefore, their D values are 2.2,. 2.5, and 2.8). The surface variation is recorded as z = g(x, y), where x, y = 1, 2, …, 64. **(a)** and **(b)** show the original surfaces generated by the midpoint displacement method and their trends removed surfaces. **(c)** and **(d)** show the original surfaces generated by the interpolation method and their trends removed surfaces.

2.5. THE SPECTRAL METHOD

2.5.1. The spectral method

The spectral method relies on the theory of *time series analysis*, which is a well established technique in applied mathematics, and a number of studies (e.g., Priestley, 1981; Pfeifer, 1984; Pentland, 1984; Voss, 1985a; Bendat and Piersol, 1986; Bracewell, 1986; Turcotte, 1987) have been devoted to the spectral approach. The underlying theory of the spectral method involves the Fourier transform. The idea of the Fourier transform is that any function in the physical domain g(x) can be transformed into a series of harmonic components (sine and cosine waves) in the frequency domain G(f) or G(λ) where f is the frequency and λ is the wavelength which is equal to 1/f. Theoretically, the physical function g(x) is required to be either periodical or of infinite length (in this case, the function can be said to be of a infinite length of period). In practice, the discrete Fourier transform is deployed to estimate the power spectral density. In this study, the Fast Fourier Transform (FFT) is used. The fractal dimension of a profile or a surface then can be derived from the distribution pattern of the power spectral density.

Because the spectral techniques have been developed primary for the application of stationary data which are sampled at equal-intervals, cautions must be taken when applied to non-stationary profiles or surface data (Fox, 1989; Hough, 1989). Furthermore, the theoretical assumption of periodical or infinite length of a profile can hardly be reached in practice. Therefore, some processes, such as detrending and applying window functions, are needed to be taken before a FFT can be applied on the simulated fractals, and their effects on the fractal dimensions will be discussed. Based on the Nyquist theory, the variations of the power spectral density between the length of the profile and twice the sampling interval will be discussed in this study.

2.5.2. The one-dimensional spectral method

The 1-d spectral method was carried out by the program *SP1D* written in *VISUAL BASIC* codes. It is described as follows.

Firstly, the original profile was linearly resampled at 2^n equal intervals if the profile data were not sampled at equal intervals and/or had not 2^n data points. The simulated profiles have a equal sample interval of 1, and $N = 1024 = 2^{10}$ data points as shown in Fig.

2.6a and c. A best-fit line was fitted to the original profile by a robust line-fitting algorithm (Press *et. al.*, 1986), and the deviation of the profile from the fitted line forms the trend removed profile (Fig. 2.6b and d).

Secondly, the Hanning window was used to weight the simulated 1-d fBm profiles in order to reduce the truncation effect (i.e., the Gibbs phenomena). As mentioned in Section 2.5.1, the calculation of the FFT is based on the theoretical assumption of a infinite length of a profile, whereas the simulated 1-d fBm profiles have the same length of 2^{10}. This truncation of the profile length from the infinite to a limited length (here is 1024) will inevitably cause some error and this error is termed truncation effect or Gibbs phenomena. The Hanning window is given by Press *et. al.* (1992),

$$W_h(i) = \frac{1}{2}\left[1 - \cos\left(\frac{2\pi(i-1)}{N-1}\right)\right] \qquad i = 1,2,\ldots N$$

where N is the number of data points of the profile. Therefore, the variation of the profile $y_i = g(x_i)$ is filtered by multiplying the Hanning window function $W_h(i)$, and a new profile $y_i' = g'(x_i)$ is obtained. That is, the Hanning window weighted profile is given by,

$$y_i' = y_i\, W_h(i) = \frac{y_i}{2}\left[1 - \cos\left(\frac{2\pi(i-1)}{N-1}\right)\right] \qquad i = 1,2,\ldots N$$

Whereas x_i remains unchanged. The further processes will be applied on the four types of profiles: the original, the detrended, without Hanning window applied, and Hanning window applied profiles.

Thirdly, the FFT was applied to the profile data which were processed by the first step, and the power spectral density at different frequency (or wavelength) were calculated. Suppose that the profile data are recorded as [x, y = g(x)], where x = 0,1, 2, ... N-1, then the FFT transform and the power spectral density (time-integral squared amplitude) of a profile, in this study, are estimated by,

$$G(f) = \sum_{x=0}^{N-1} g(x)\, e^{\frac{2\pi i f x}{N}} \qquad i = \sqrt{-1}$$

and

$$P(f) = \frac{L_n}{N} |G(f)|^2$$

where N is the number of the profile data points, f is the frequency, g(x) and G(f) are functions of the profile in the physical and frequency domain respectively. The profile has a nominal length of L_n and L_n / (N - 1) is the sampling interval.

Fourthly, the power spectral density of the profile P(λ) and their corresponding wavelength (λ) were plotted on a log-log scale paper as shown in Fig. 2.8. The power-law dependence of P(λ) on λ follows the form of,

$$P(\lambda) = C_{1f} \lambda^{\beta} \tag{2.3}$$

where λ is the wavelength, f is the frequency (λ = 1/f), and β is the slope of the regression fitted line over a certain wavelength range (fractal limits). Because the wavelength progression is arithmetic (i.e. adjacent wavelengths are L/i, i = 1, 2, 3, ...), many more estimates of the total power were made at the smaller than longer wavelengths on a log-log plot of P(λ) against λ. The longest and shortest wavelengths, which are considered to be useful for determining the value of β, were equal to the nominal length of a profile (L_n) and twice the sampling interval (the reciprocal of the "Nyquist" wavelength) respectively.

Fifthly, the fractal dimension of the profile was determined for β. Some studies [Mandelbrot, 1986; Voss, 1985a, b, 1988; Berry and Lewis, 1980] have shown that the relationship between the fractal dimension D_{1f} of a profile and the slope of the spectral distribution (the power spectra against frequency) β, which is given by,

$$D_{1f} = \frac{(5 - |\beta|)}{2} \tag{2.4}$$

The fractal dimension of a profile is expected to lie in the range of $2 > D_{1f} > 1$; and the corresponding range of β is $1 < \beta < 3$. Based on equation (2.1) the estimate error Δβ is the twice of the estimate error ΔD_{1f}, i.e.,

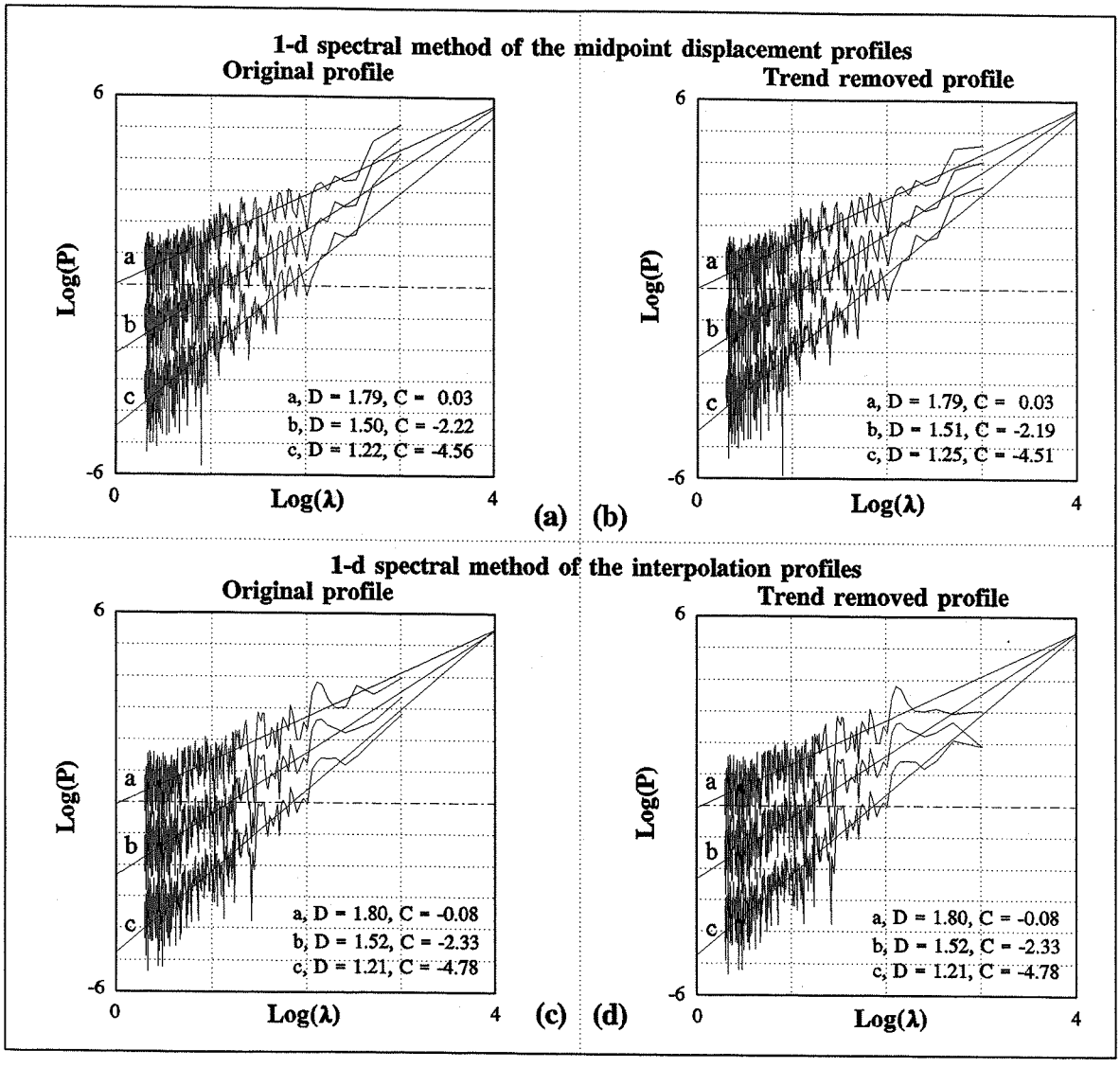

Fig. 2.8. Illustration of the 1-d spectral method. The spectral method is applied on the original and trend removed (Hanning window weighted) 1-d fBm profiles (mp12, mp15, mp18; int12, int15 and int18) generated by the midpoint displacement and interpolation method. **(a)** and **(b)** Log-log plots of the power spectral density P(λ) against the wavelength λ for the 1-d spectral method applied on the original and trend removed profiles generated by the midpoint displacement method. **(c)** and **(d)** Log-log plots of the power spectral density P(λ) against the wavelength λ for the 1-d spectral method applied on the original and trend removed profiles generated by the interpolation method.

$$\Delta D_{1f} = \frac{1}{2}\Delta\beta$$

where the estimate errors of the spectral exponent $\Delta\beta$ and the intercept ΔC_{1f} was determined by equation (2.1).

In order to illustrate the physical meaning of the parameters C_{1f} and D_{1f}, if $P(\lambda)$ is substituted by its amplitude $A(\lambda)$ in equation (2.3), then,

$$A(\lambda) = \sqrt{P(\lambda)} = \sqrt{C_{1f}\ \lambda^{\beta}} = C_{1f}'\ \lambda^{\frac{\beta}{2}}$$

Thus C_{1f}' is a simple scaling factor for roughness. Its value does not necessarily correspond to any particular feature of the profile, but only to the amplitude of the spectral components at wavelength ($\lambda = 1$), i.e., $C_{1f}' = A(1)$.

The interpretation of the exponent β is less intuitive. If the ratio of amplitude to wavelength is termed 'aspect ratio ' as suggested by Fox and Hayes (1985), then for $\beta = 2$ (for which $D_{1f} = 1.5$), the profile is the well-known Brownian noise. The aspect ratio is a constant over all wavelengths, and the magnitude of this ratio depends on the scaling factor C_{1f}' only. In all other cases, the aspect ratio changes as a function of wavelength. For values of $1 < \beta < 2$ (then $1.5 < D_{1f} < 2.0$), the aspect ratio increases with decreasing wavelength. This means that the profile appears to be rougher at finer scales. For values of $2 < \beta < 3$ (then $1.0 < D_{1f} < 1.5$), however, the aspect ratio decreases with decreasing wavelength, causing the profile to be relatively smoother at smaller scales.

2.5.3. The two-dimensional spectral method

The combination of the 1-d Fourier transform approach and fractal analysis for 1-d profiles can be easily extended to 2-d data analysis (Dubuc *et. al.*, 1989b). Suppose that a surface of a size of N by N is presented by the variations [x, y, z = g(x, y)] where x = 0, 1, ..., N-1, and y = 0, 1, ..., N-1 denote the positions of a data point in the x-y coordinates system. The grid data are equally spaced a plane, therefore the grid size is L by L (L = N - 1) and the grid data points are discrete at an interval of 1. The determination of the fractal dimension of a fractal surface by the 2-d spectral method (program *SP2D* was written in *VISUAL BASIC* codes) is illustrated as follows.

Firstly, the simulated 2-d fBm surfaces of equally spaced grid data of (64, 64), which were generated by the midpoint displacement and interpolation techniques, were filtered by the 2-d Hanning window. The Hanning window $W_h(x, y)$ is given by Subba Rao, (1991),

$$W_h(x,y) = W_h(x) \bullet W_h(y) \bullet W_h(xy)$$

where $W_h(x)$, $W_h(y)$, and $W_h(xy)$ are given by,

$$W_h(x) = \frac{1}{2}\left[1 - \cos\left(\frac{(x-1)\pi}{N-1}\right)\right] \qquad x = 1,2,\ldots N$$

$$W_h(y) = \frac{1}{2}\left[1 - \cos\left(\frac{(y-1)\pi}{N-1}\right)\right] \qquad y = 1,2,\ldots N$$

$$W_h(xy) = \frac{1}{2}\left[1 - \cos\left(\frac{(x-y)\pi}{N-1}\right)\right] \qquad x,y = 1,2,\ldots N$$

where N^2 is the number of data points of the surface. Therefore, the variation of the surface $z = g(x, y)$ is filtered by multiplying the Hanning window function $W_h(x, y)$, and the new variation of the surface $z' = g'(x, y)$ is obtained, i.e.,

$$z' = g'(x,y) = g(x,y) \bullet W_h(x,y) \qquad x,y = 1,2,\ldots N$$

Secondly, both the original (Fig. 2.7a and c) and the detrended surfaces (Fig. 2.7b and d) were prepared for FFT in order to observe the spectral effects caused by longer wave lengths (lower frequencies). The linear trend plane was fitted to the original surface by the robust fitting algorithm (Press *et. al.*, 1986), and the detrended surface is the subtraction of the original surface and this trend plane.

Thirdly, the 2-d discrete FFT was carried out on the surface of a N by N data set. Therefore, a N by N array of complex coefficients G(s, t) was obtained by,

$$G(s,t) = \left(\frac{L}{N}\right)^2 \sum_{x=0}^{N-1} \sum_{y=0}^{N-1} g(x,y)\, e^{-\frac{2\pi i}{N}(sx+ty)}$$

where s and t respectively denote the positions along the x and y directions of the complex coefficients G(s, t), s = 0, 1, ..., N - 1, and t = 0, 1, ..., N - 1, and g(x, y) and G(s, t) are

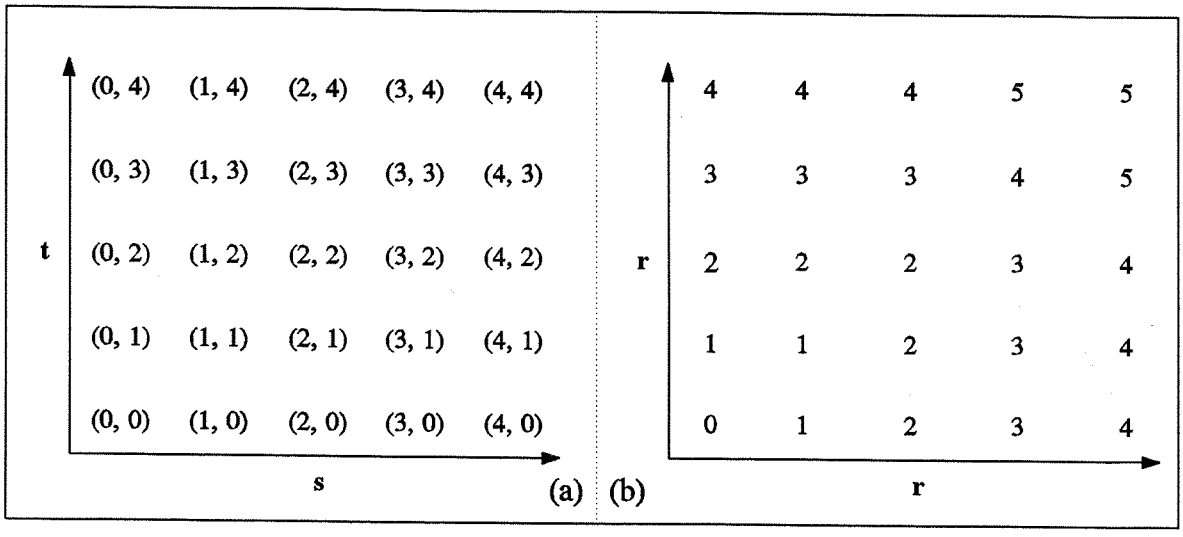

Fig. 2.9. The transformation of the coordinate systems. **(a)** Euclidean x-y coordinate system. The variations of the surface are presented as [x, y, z = g(x, y)] and their Fourier transform complex coefficients are presented as G(s, t). **(b)** radial coordinate system. The Fourier transform coefficients G(s, t) are transformed into G(r) where $r = \sqrt{s^2 + t^2}$ (Huang and Turcotte, 1990b).

functions of the trend-removed surface in physical and frequency domain respectively. L/N is actually the sampling interval. Then the complex coefficients G(s, t) in x-y coordinates (Fig. 2.9a) were assigned to those in a radial system (Fig. 2.9b) by,

$$r = \sqrt{\left(s^2 + t^2\right)}$$

The transformation of the x-y coordinate system to a radial system is shown in Fig. 2.9 (Huang and Turcotte, 1990b).

Fourthly, supposed that N_j is the number of those complex coefficients G(s, t) which satisfy $j \le r < j + 1$ for each radial number j, then the 2-d mean power spectral density P_{2j} for the radial wave number k_j, where $k_j = 2\pi r_j/L$, is given by,

$$P_{2j} = \frac{1}{L^2 N_j} \sum_1^{N_j} |G(s,t)|^2$$

where L is the side length of the grid data. The relationship between the wave number k and

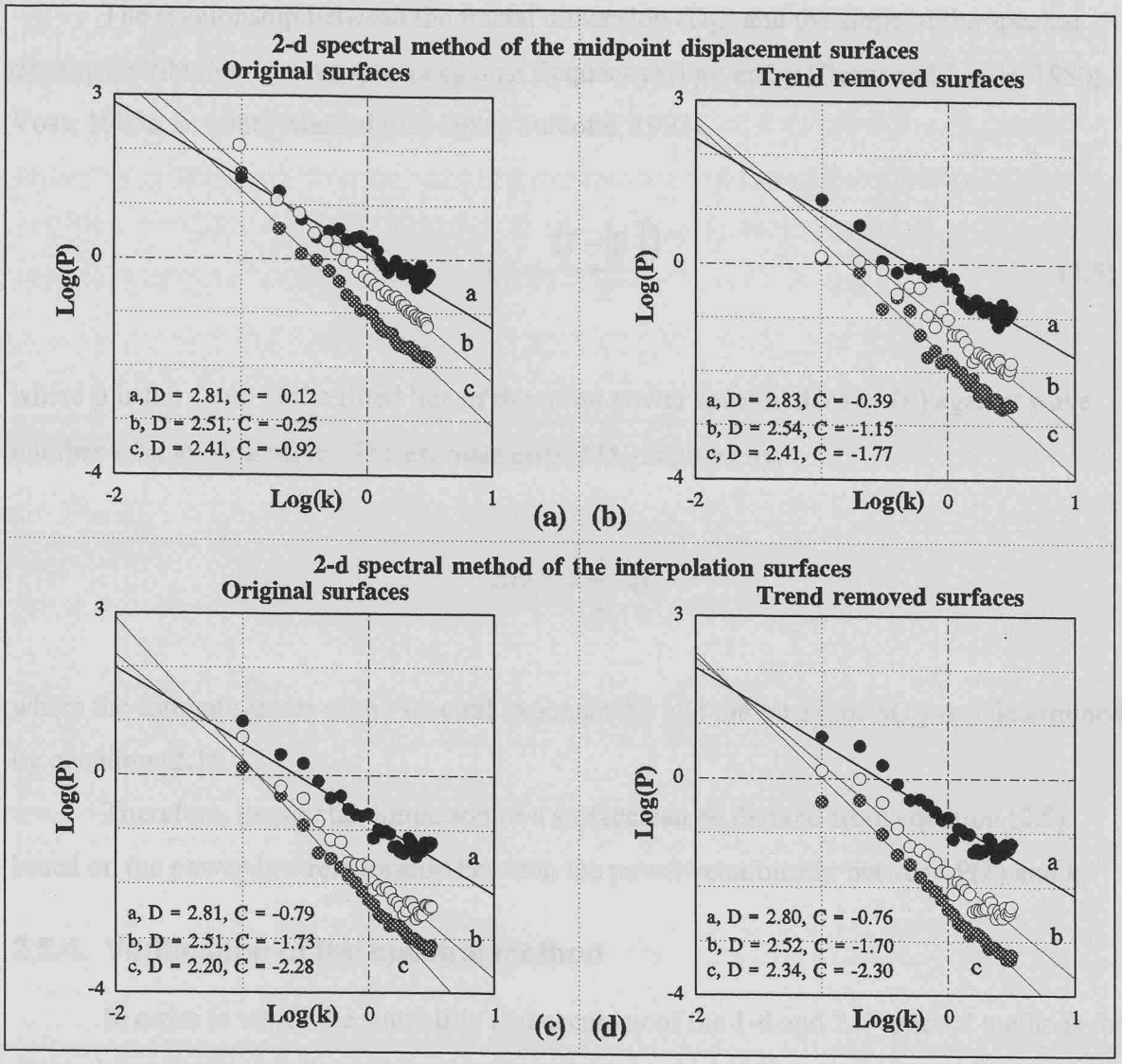

Fig. 2.10. Illustration of the 2-d spectral method. The method is applied on the original and trend removed 2-d fBm surfaces (with Hanning window weighted) simulated by the midpoint displacement and the interpolation techniques using parameter H = 0.2, 0.5, 0.8. Their surfaces are shown in Fig. 2.7. **(a)** and **(b)** are log-log plots of the power spectral density P(k) against the radius wave number k for the original and trend removed surfaces generated by the midpoint displacement method. **(c)** and **(d)** are log-log plots of the power spectral density P(k) against the radius wave number k for the original and trend removed surfaces generated by the interpolation method.

the wavelength λ is $k = 2\pi/\lambda$ (Turcotte, 1992).

Finally, the 2-d mean power spectral density P_{2j} was plotted against the radial wave number k_j on log-log scale paper as shown in Fig. 2.10(c). The slope of the regression line β over a certain range of wave number was obtained.

The relationship between the fractal dimension (D_{2f}) and the slope of the spectral density distribution (power spectra against frequency) β given by (Berry and Lewis, 1980; Voss, 1985a, b, 1988; Mandelbrot, 1986; Turcotte, 1992),

$$D_{2f} = \frac{(7 - |\beta|)}{2} \tag{2.5}$$

where β is the slope of the fitted line of the mean power spectral density (P) against wave number k on log-log scale. The estimate error ΔD_{2f} is given by,

$$\Delta D_{2f} = \frac{1}{2}\Delta\beta$$

where the estimate errors of the spectral exponent Δβ and the intercept ΔC_{2f} was determined by equation (2.1).

Therefore, the fractal dimension of a surface can be derived from equation (2.5) based on the power-law relationship between the power-relationship between P(λ) and k.

2.5.4. Verification of the spectral method

In order to verify the suitability and accuracy of the 1-d and 2-d spectral methods for determining the fractal dimension of random fractals, six 1-d fBm profiles (mp12, mp15, mp18; int12, int15, and int18) and six 2-d fBm surfaces (mp22, mp25, mp28; int22, int25, and int28) generated by the midpoint displacement and the interpolation methods using H = 0.8, 0.5, 0.2 as shown in Fig. 2.6 and Fig. 2.7 are taken as examples. Their log-log plots are shown in Figs. 2.8 and 2.10.

2.5.4.1. Verification of the 1-d spectral method

Table 2.5 summarizes the fractal dimensions of these original (without removing trend), trend removed, without Hanning window weighted, and Hanning window weighted profiles determined by the 1-d spectral method over the wavelengths range between $\lambda = 2^3$ and $\lambda = 2^8$. The estimated errors ΔD_{1f} and ΔC_{1f} were determined by equation (2.1). Fig. 2.8 is the log-log plots of the 1-d spectral method for the generated 1-d fBm weighted by the

Hanning window. The first several points of the right-hand side of the power spectra (longer wave lengths) have not been taken into account during the determination of the fractal dimensions of the trend removed profiles (Fig. 2.8b and c), this flattening spectral behaviour is caused by the trend removing procedure. This explains that D values of the trend removed profiles (int12, int15, and int18) are roughly the same as those of the original profiles, whereas their spectra look so different for the longer wavelengths.

Table 2.5. Fractal dimensions of 1-d fBm determined by the 1-d spectral method

Without Hanning window weighted						
	Theoretical values		Original (not removing trend) profiles		Trend removed profiles	
	H	D	$D_{1f} \pm \Delta D_{1f}$	$C_{1f} \pm \Delta C_{1f}$	$D_{1f} \pm \Delta D_{1f}$	$C_{1f} \pm \Delta C_{1f}$
mp12	0.80	1.20	1.52 ± 0.02	-2.29 ± 0.04	1.50 ± 0.03	-2.72 ± 0.06
mp15	0.50	1.50	1.55 ± 0.04	-1.65 ± 0.10	1.50 ± 0.04	-1.69 ± 0.08
mp18	0.20	1.80	1.80 ± 0.04	0.46 ± 0.09	1.76 ± 0.04	0.41 ± 0.08
int12	0.80	1.20	1.56 ± 0.03	-2.85 ± 0.06	1.40 ± 0.04	-3.63 ± 0.09
int15	0.50	1.50	1.53 ± 0.04	-1.74 ± 0.08	1.56 ± 0.04	-1.72 ± 0.08
int18	0.20	1.80	1.82 ± 0.04	0.47 ± 0.08	1.84 ± 0.04	0.51 ± 0.08
With Hanning window weighted $W_h(i) = 0.5\ \{1 - \cos[2\pi(i-1)/(N-1)]\}$						
	Theoretical values		Original (not removing trend) profiles		Trend removed profiles	
	H	D	$D_{1f} \pm \Delta D_{1f}$	$C_{1f} \pm \Delta C_{1f}$	$D_{1f} \pm \Delta D_{1f}$	$C_{1f} \pm \Delta C_{1f}$
mp12	0.80	1.20	1.22 ± 0.05	-4.56 ± 0.10	1.25 ± 0.05	-4.51 ± 0.10
mp15	0.50	1.50	1.50 ± 0.04	-2.22 ± 0.10	1.51 ± 0.04	-2.19 ± 0.10
mp18	0.20	1.80	1.79 ± 0.05	0.03 ± 0.10	1.79 ± 0.05	0.03 ± 0.10
int12	0.80	1.20	1.21 ± 0.05	-4.78 ± 0.10	1.21 ± 0.05	-4.78 ± 0.10
int15	0.50	1.50	1.52 ± 0.05	-2.33 ± 0.11	1.52 ± 0.05	-2.33 ± 0.11
int18	0.20	1.80	1.80 ± 0.05	-0.08 ± 0.10	1.80 ± 0.05	-0.08 ± 0.10

The verification of the 1-d spectral method covers three factors: the power spectral density distribution patterns; the fractal dimensions; and the effects of applying the Hanning window.

1. **The power spectral density distribution patterns:** The detrending process has little effects on the spectral patterns within observation scales of the short wavelength, however, the power spectra within the several points of longest wavelengths are flattened after detrending (by the comparison between Figs. 2.8a and 2.8b; and between Figs. 2.8c and 2.8d). This is because the relief of the trend line rapidly approaches that of the data at larger scales. Furthermore, within the longer wavelengths the flattening behaviours

are more obvious as H decreases from 0.8 to 0.2 as shown in Fig. 2.8(d), this can be explained by the fact that the trend line (H = 1) has a fractal dimension of D = 1 (i.e., D = 2 - H = 1 for the trend line), and the profile of H = 0.2 (hence the profile has D = 2 - 0.2 = 1.8) is more significant different from the trend line than the profile of H = 0.8 (hence the profile has D = 2 - 0.8 = 1.2). Therefore, the trend removal procedure disproportionately affects the profile relief at larger length scales, and the scaling behaviours of the original profile at the longer wavelength is distorted more than that at the short wavelength. This is consistent with the results obtained by Weissel *et. al.* (1994).

2. **The fractal dimensions:** The coincidence of D values of the original and detrended profiles strongly suggests that the procedure of detrending a profile need not to be necessary for the spectral method (compare the middle and right parts of Table 2.5). At least, this is true for the simulated 1-d fBm profiles discussed. For the determination of the fractal dimension of a detrended profile, some care should be taken into account for the flattening behaviours of its power spectral distribution at longer wavelength scales, i.e., the flattened points at the longer wavelength end should be excluded for fitting the regression line. Brown (1987) suggested that for a profile of a small trend, the detrending process applied on the profile affects little on its D value. The consistence of D values between the original and detrended profiles is not because that the trends of all the simulated 1-d fBm profiles are small, but the detrending process has little effect on their fractal dimensions. As shown in Table 2.3, the values of %RSS (and the correlation coefficient r) of the six profiles show that these profiles have different trends ranging from slight to high trend.
3. **The effects of applying the Hanning window:** The application of the Hanning window to the simulated 2-d fBm surfaces is essential for the determination of their D values especially as $H \rightarrow 1$, but has little effects as $H \rightarrow 0$ (compare between upper and lower parts of Table 2.5). On one hand, the fractal dimensions of the profiles (mp12 and int12) determined by the spectral method without applying Hanning window do not coincide with the theoretical D value of 1.2, but are about D = 1.5. This is because the truncation effect caused by applying the spectral method to the profiles of limited length (refer to Section 2.5.2 for more details), whereas, the estimation of the power spectral density is based on the theoretical assumption of a infinite length of a profile. The correct D values can be derived from applying Hanning window to the profiles before the FFT was carried

out. On the other hand, the effects of applying Hanning window decreases as H → 0. This might be explained that the simulated profiles of H near to 0 show more and more periodical properties than those of H near to 1 as shown in Fig. 2.6, therefore, the estimation of their power spectral density is much less affected by the truncation effect.

2.5.4.2. Verification of the 2-d spectral method

The fractal dimensions of the simulated 2-d fBm original (without removing linear trend), trend removed, without Hanning window weighted, and Hanning window weighted surfaces are determined by the 2-d spectral method and summarized in Table 2.6. The fractal limits are between the wave numbers 2/64 and 16/64. Fig. 2.10 is the log-log plots of the mean power spectral P(k) against the radius wave number k for the generated 2-d fBm surfaces which were weighted by the Hanning window.

Table 2.6. Fractal dimensions of 2-d fBm determined by the 2-d spectral method

Without Hanning window weighted						
	Theoretical values		Original profiles		Trend removed profiles	
	H	D	$D_{2f} \pm \Delta D_{2f}$	$C_{2f} \pm \Delta C_{2f}$	$D_{2f} \pm \Delta D_{2f}$	$C_{2f} \pm \Delta C_{2f}$
mp22	0.80	2.20	2.43 ± 0.02	-0.19 ± 0.01	2.42 ± 0.03	-0.50 ± 0.02
mp25	0.50	2.50	2.51 ± 0.03	-0.13 ± 0.03	2.53 ± 0.03	-0.23 ± 0.02
mp28	0.20	2.80	2.81 ± 0.03	0.58 ± 0.03	2.82 ± 0.03	0.57 ± 0.02
int22	0.80	2.20	2.42 ± 0.02	-0.80 ± 0.01	2.38 ± 0.03	-1.65 ± 0.02
int25	0.50	2.50	2.54 ± 0.04	-0.65 ± 0.03	2.56 ± 0.05	-0.73 ± 0.03
int28	0.20	2.80	2.79 ± 0.04	0.19 ± 0.03	2.80 ± 0.04	0.19 ± 0.03
With Hanning window weighted						
$W_h(i,j) = \frac{1}{2}\left[1-\cos\left(\frac{(i-1)\pi}{N-1}\right)\right] \bullet \frac{1}{2}\left[1-\cos\left(\frac{(j-1)\pi}{N-1}\right)\right] \bullet \frac{1}{2}\left[1-\cos\left(\frac{(i-j)\pi}{N-1}\right)\right]$						
	Theoretical values		Original profiles		Trend removed profiles	
	H	D	$D_{2f} \pm \Delta D_{2f}$	$C_{2f} \pm \Delta C_{2f}$	$D_{2f} \pm \Delta D_{2f}$	$C_{2f} \pm \Delta C_{2f}$
mp22	0.80	2.20	2.41 ± 0.02	-0.92 ± 0.02	2.41 ± 0.04	-1.77 ± 0.02
mp25	0.50	2.50	2.51 ± 0.07	-0.25 ± 0.07	2.54 ± 0.04	-1.15 ± 0.03
mp28	0.20	2.80	2.81 ± 0.11	0.12 ± 0.12	2.83 ± 0.03	-0.39 ± 0.03
int22	0.80	2.20	2.20 ± 0.03	-2.28 ± 0.02	2.34 ± 0.03	-2.30 ± 0.02
int25	0.50	2.50	2.51 ± 0.05	-1.73 ± 0.03	2.52 ± 0.05	-1.70 ± 0.03
int28	0.20	2.80	2.81 ± 0.05	-0.79 ± 0.03	2.80 ± 0.05	-0.76 ± 0.03

Similar to that described in the Section 2.4.5.1, the verification of the 2-d spectral

method can be achieved in three way: the power spectral density distribute patterns; the fractal dimensions; and the effects of applying the Hanning window.

1. **The power spectral density distribution patterns:** The detrending process has little effects on the spectral density distribute patterns within larger wave number (short wavelength), whereas the flattening behaviour of spectra occurs within larger observation scales (small wave number) still exists between the original and planar trend removed surfaces (compare between Figs. 2.10a and 2.10b; and between Figs. 2.10c and 2.10d) although it is not as obvious as that observed in 1-d fBm profiles. This is because the relief of the trend line rapidly approaches that of the data. Weissel *et. al.* (1994) obtained similar results.
2. **The fractal dimensions:** The consistent D values of the original and detrended profiles strongly suggests that the procedure of detrending a profile need not to be necessary for the spectral method (compare the middle and right parts of Table 2.6). The flattened points at the longer wavelength end were excluded for the determination of D values. The consistence of D values between the original and detrended profiles, again, is not because of the small trends of all the simulated 2-d fBm, but the detrending process has little effect on their fractal dimensions. Table 2.4 is the values of %RSS of the six surfaces which have different trends ranging from slight to high trend.
3. **The effects of applying the Hanning window:** Table 2.6 shows that applying Hanning window to the simulated 2-d fBm surfaces is essential for the determination of their D values especially as $H \rightarrow 1$, but has little effects as $H \rightarrow 0$. See the explanation shown in 2.4.5.1.3.

After applying the Hanning window, the comparison of the D values of mp12 profile (D = 1.22 in Table 2.5) and mp22 surface (D = 2.41 in Table 2.6) with their theoretical D values shows that the non-stationary increments in mp22 are more severe than those in mp12.

In summary, the spectral method (1-d and 2-d) is a successful model for determining the fractal dimensions of simulated 1-d fBm profiles and 2-d fBm surfaces weighted by the Hanning window. The D values of the profiles or surfaces are consistent with the theoretical D values which are given by H values as the fBm were generated (refer to Appendix 1 for more details). Applying the Hanning window is essential for the determination of the fractal dimension especially as H is near to 1. The application of

detrending procedure, flattens the power spectral density at longer wavelength (short wave number), but has little effects on the spectra at short wavelength, hence changes little in D values as the flattened points were excluded. This is consistent with the results obtained by Weissel *et. al.* (1994).

Previous studies (Mandelbrot, 1983; Barnsley, 1988; Scholz and Mandelbrot, 1989; Turcotte, 1992) had not mentioned the effects of applying filters (e.g. Hanning window) on the 1-d profiles or 2-d surfaces. A variety of previous studies (Fox and Hayes, 1985; Power, 1987; Fox, 1989; Gilbert, 1989; Huang and Turcotte, 1989; Turcotte, 1992, Malinverno, 1995) have found D values near to 1.5 for the most profiles and D values near to 2.5 for most surfaces they studied. This might indicate some of the fractal dimensions of profiles or surfaces were over estimated by the spectral method without applying a Hanning window. For example, Turcotte (1992) collected and analyzed 24 latitude and longitude profiles from three different parts of Oregon. The three regions cover different geomorphic and tectonic settings: Willamette lowland is dominated by the sedimentary processes; the Wallowa Mountains are associated with a major tectonic uplift; and the Klamath Falls area belongs to the basin and range tectonic regime. The fractal dimensions of eight profiles of each region were averaged and they are 1.47, 1.50, and 1.50.

2.6. THE STRUCTURE FUNCTION METHOD

2.6.1. The structure function

The structure function is a statistical model concerned with the variety of a regionalized variable, g(x), at a certain order q in space (and/or time, Olea, 1991). The q^{th} order structure function (i.e., q^{th} moments) of a profile or a surface is generally defined as (Monin and Yaglom, 1971; Parisi and Frisch, 1985),

$$\Delta g_q(h) = E\left\{ \left| g(x+h) - g(x) \right|^q \right\}$$

where E{} denotes the expect and q is an exponent that is usually taken as positive integers. Furthermore, if a study object possesses simple scaling properties describable by a single scaling exponent, then the equation above could be linked with the parameter H by (Mandelbrot and Wallis, 1969a, Weissel *et. al.*, 1994),

$$\Delta g_q(h) = E\left\{ \left| g(x+h) - g(x) \right|^q \right\} \propto C_q h^{qH}$$

where coefficient C_q and exponent qH are independent on the lag h, but on the order q and the parameter H. The structure function is a well-know method to directly measure the fractal dimensions of profiles and surfaces (Mandelbrot, 1977, 1982; Goodchild, 1980; Mark and Aronson, 1984; Pentland, 1984; Voss, 1985a, b; Roy *et. al.*, 1987; Journel & Huijbregts, 1987; Weissel *et. al.*, 1994).

The 1-d and 2-d structure function methods will be discussed in this study. Obviously, the 1st order structure function method (q = 1) reveals the dependent relationship between the absolute mean relief M(h) and h, whereas, the 2nd order structure function method (q = 2) reveals the dependent relationship between the variance 2γ(h) and h, where γ(h) is usually termed the semivariogram (Journel and Huijbregts, 1978), which is the half of the variance as the name implies. Given h (termed lag) is the spatial distance between any pair data on the study object, then the absolute mean relief M(h) and the semivariance γ(h) are defined respectively by,

$$M(h) = \Delta g_1(h) = E\{|g(x+h) - g(x)|\}$$

$$\gamma(h) = \frac{1}{2}\Delta g_2(h) = \frac{1}{2}Var[g(x+h) - g(x)]$$

In this section, both the 1st order (absolute mean relief) and the 2nd order (the semivariogram) structure functions will be used to analyze those synthetic 1-d fBm profiles and 2-d fBm surfaces of different H values. Because of the sample sizes of the topographic surfaces are finite, the 1-d and 2-d Hanning windows (shown in Sections 2.5.3 and 2.5.4 respectively) were applied on the simulated 1-d fBm profiles and 2-d fBm surfaces before calculating the 1st and 2nd moments. See Section 2.5 for more explanation of the truncation effect (Gibbs phenomena). The 1-d and 2-d Hanning windows are given by Press *et. al.* (1992) and Subba Rao (1991). Therefore, on one hand, these two structure functions could be compared, on the other side, the multi-scaling behaviours of 2-d fBm and TM imagery can be investigated later.

2.6.2. The one-dimensional structure function method

Suppose that the discrete profile data set is presented as $[x_i, g(x_i)]$ (i = 1, 2, ..., N), the first order structure function M(h) can be written as,

$$M(h) = \frac{1}{N_h}\sum_{i=1}^{N_h}|g(x_i + h) - g(x_i)| \quad \propto \quad h^H \quad = \quad h^{2-D}$$

and the 1-d semivariogram can be given by,

$$\gamma(h) = \frac{1}{2N_h}\sum_{i=1}^{N_h}[g(x_i + h) - g(x_i)]^2 \quad \propto \quad h^{2H} \quad = \quad h^{4-2D}$$

where M(h) is the absolute mean relief, $\gamma(h)$ is the semivariance of the profile, ordinal number i = 1, 2, ..., N_h, and N_h is the number of paired data which have spatial distance of h, x_i is the positions along the x-direction, and h is the lag which is the distance between any pairs on the profile data, and D is the fractal dimension. The fractal dimension, D_{1s}, of a

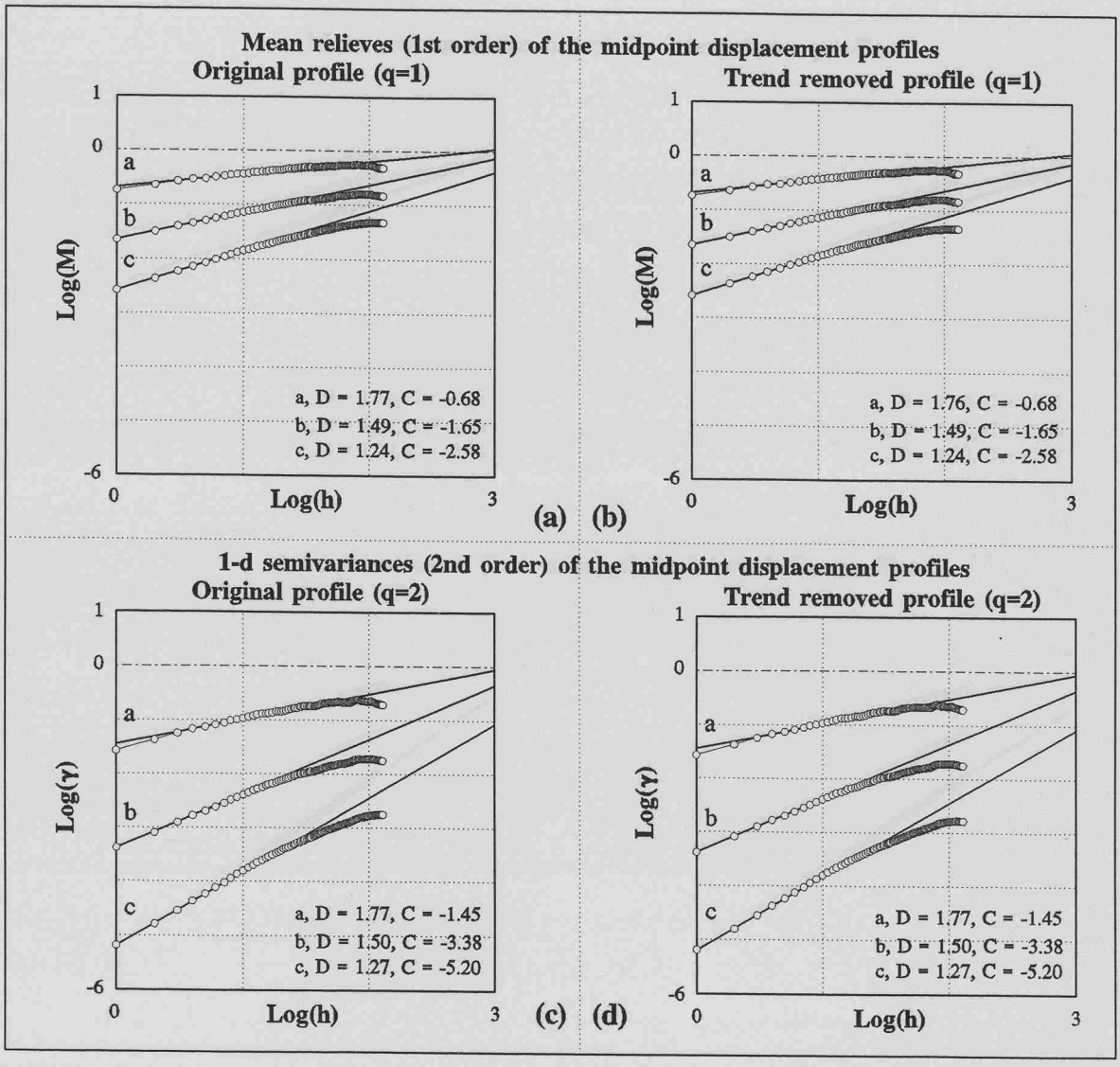

Fig. 2.11. The log-log plots of the 1st and 2nd order function structures of the 1-d fBm profiles weighted by Hanning window, generated by the midpoint displacement method using parameter H = 0.2, 0.5, and 0.8, over $2 < h < 64$. The original and trend removed 1-d fBm profiles are shown in Fig. 2.6(a) and (b). **(a)** and **(b)** are the log-log plots of the absolute mean relief M(h) against the lag h for the original and trend removed profiles. **(c)** and **(d)** are the log-log plots of the semivariance γ(h) against the lag h for the original and trend removed profiles.

profile can be determined by,

$$\begin{aligned} &For\ q = 1, \quad D_{1s} = 2 - \beta_1\ ; \\ &For\ q = 2, \quad D_{1s} = 2 - \frac{\beta_2}{2}. \end{aligned} \tag{2.6}$$

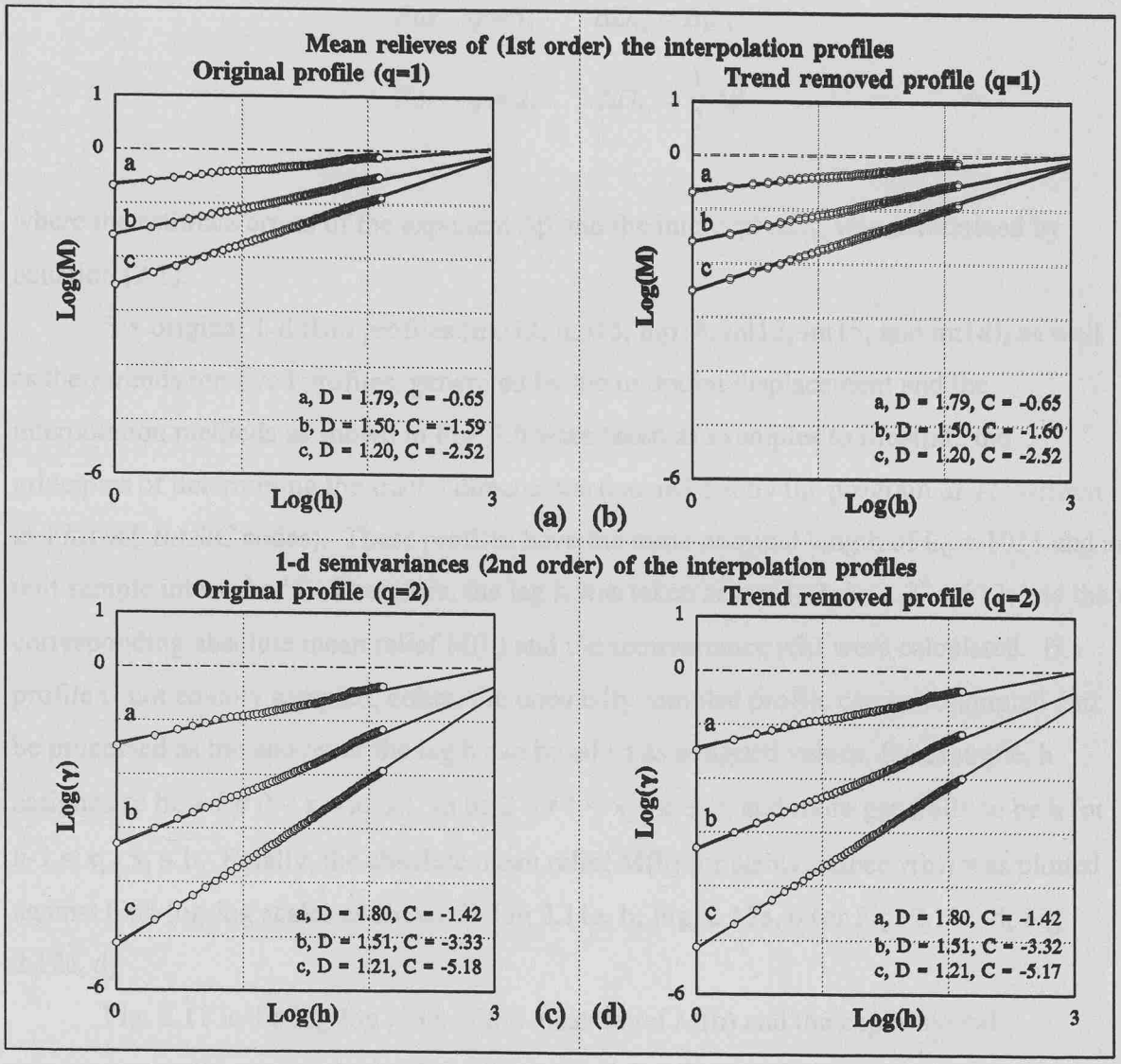

Fig. 2.12. The log-log plots of the first and second order function structures of the 1-d fBm profiles weighted by Hanning window, generated by the interpolation method using parameter H = 0.2, 0.5, and 0.8, over $2 < h < 64$. The original and trend removed 1-d fBm profiles are shown in Fig. 2.6(c) and (d). **(a)** and **(b)** are the log-log plots of the absolute mean relief M(h) against the lag h for the original and trend removed profiles. **(c)** and **(d)** are the log-log plots of the semivariance $\gamma(h)$ against the lag h for the original and trend removed profiles.

where β_1 and β_2 are the slopes of the regression lines of the log-log plot of the mean relief M(h) and the semivariance $\gamma(h)$ against the lag h. The range of lag h is usually taken between the twice sample interval (based on the Nyquist theory) and the half of the nominal profile length. From equation (2.6), the estimate error ΔD_{1s} for the 1st and 2nd order structure functions are respectively given by,

$$For \quad q = 1, \qquad \Delta D_{1s} = \Delta\beta \ ;$$

$$For \quad q = 2, \qquad \Delta D_{1s} = \frac{1}{2}\Delta\beta$$

where the estimate errors of the exponent $\Delta\beta$ and the intercept ΔC_{1s} was determined by equation (2.1).

Six original 1-d fBm profiles (mp12, mp15, mp18; int12, int15, and int18), as well as their trends removed profiles, generated by the midpoint displacement and the interpolation methods as shown in Fig. 2.6 were taken as examples to illustrate the principles of determining the fractal dimensions (carried out by the program *SF1D* written in *VISUAL BASIC* codes). These profiles have the same nominal length of $L_0 = 1023$ and an unit sample interval of 1. Therefore, the lag h was taken as h = 1, 2, 3, ...,$2^9 = 512$, and their corresponding absolute mean relief M(h) and the semivariance $\gamma(h)$ were calculated. If a profile is not equally sampled, either, the unequally sampled profile can be resampled and be processed as the above; or the lag h can be taken as assigned values, for example, h assigned to be 1 for $0 < x_i - x_j \le 1$, to be 2 for $1 < x_i - x_j \le 2$, and more generally to be h for $h-1 < x_i - x_j \le h$. Finally, the absolute mean relief M(h) (or semivariance $\gamma(h)$) was plotted against h on log-log scales as shown in Fig 2.11a, b; Fig. 2.12a, b (or Fig. 2.11c, d; Fig. 2.12c, d).

Fig. 2.11 is the log-log plots of the mean relief M(h) and the experimental semivariance $\gamma(h)$ against the lag h for the original 1-d fBm profiles (a and c) and their trend removed profiles (b and d) generated by the midpoint displacement method using H = 0.8, 0.5, and 0.2. Fig. 2.12 is the same plots for the original 1-d fBm profiles (a and c) and their detrended profiles (b and d) generated by the interpolation method.

2.6.3. The two-dimensional structure function method

The concept of the 1-d structure function can be easily extended to the 2-d space to construct the 2-d structure function except in the way that the lag h in 2-d space is assigned. Suppose that an equally spaced discrete grid of N by N size is recorded as $[x_i, y_j, z_{ij} = g(x_i, y_j)]$, where x_i and y_j (i = 0, 1, ..., N - 1, j = 0, 1, ..., N - 1) denote the positions of a data point in the x-y coordinate system as shown in Fig. 2.9. Then the distance between any one pair of the data points $[g(x_i, y_j)]$ and $[g(x_{i'}, y_{j'}]$ in the grid can be given by,

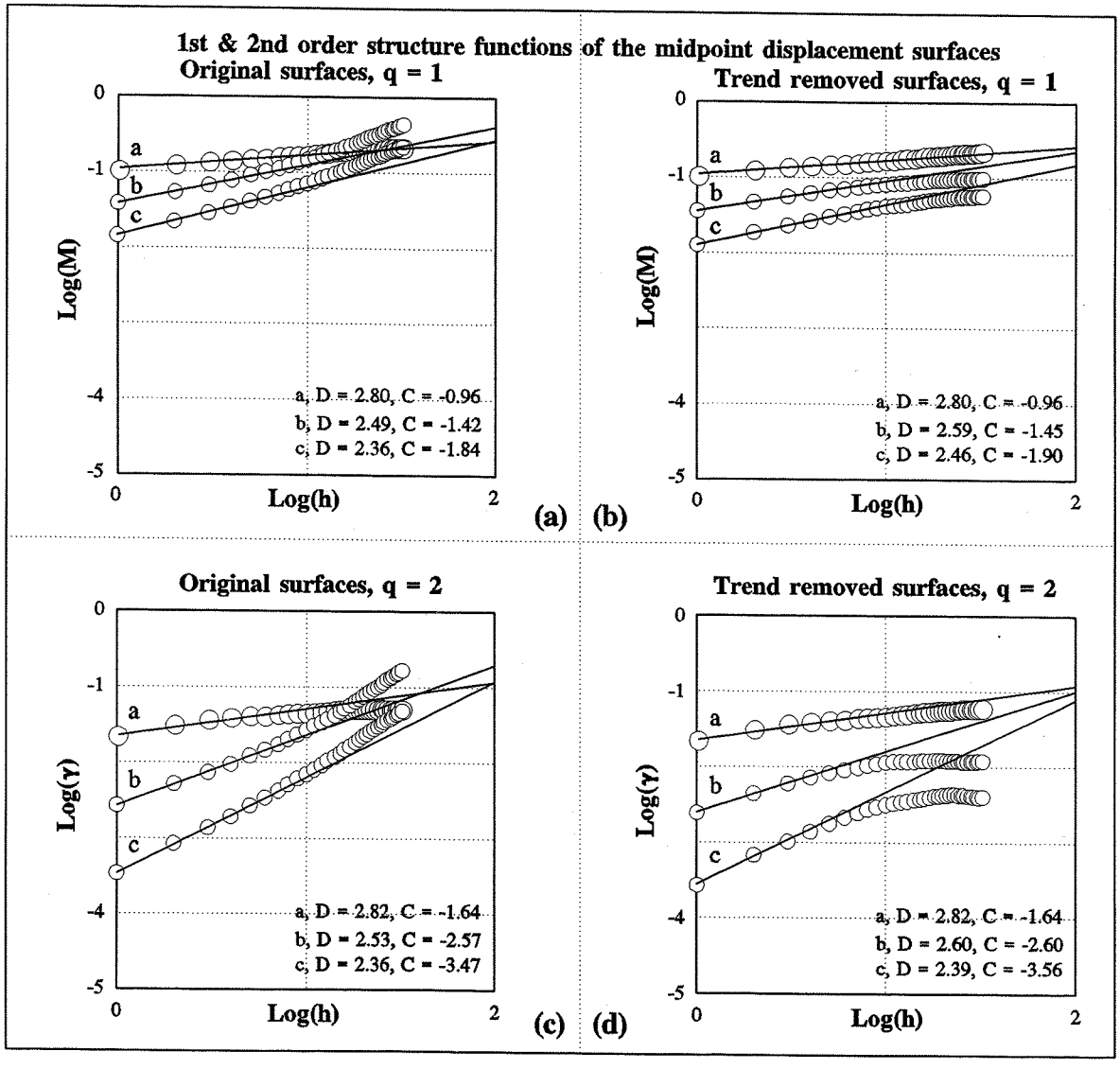

Fig. 2.13. The log-log plots of the first and second order function structures of the 2-d fBm surfaces weighted by Hanning window, generated by the midpoint displacement method using parameter H = 0.2, 0.5, and 0.8, over lag range $2 < h < 16$. The original and trend removed 2-d fBm surfaces are shown in Fig. 2.7(a) and (b). **(a)** and **(b)** are the log-log plots of the absolute mean relief M(h) against the lag h for the original and trend removed surfaces. **(c)** and **(d)** are the log-log plots of the semivariance γ(h) against the lag h for the original and trend removed surfaces.

$$r = \sqrt{\left(x_{i'} - x_i\right)^2 + \left(y_{j'} - y_j\right)^2} = \sqrt{(\Delta x)^2 + (\Delta y)^2}$$

Obviously, the spatial distance r will not be the integer in most cases (the maximum r value could reach $\sqrt{2}(N-1)$), but it can assigned to an integer in this way. The spatial distance

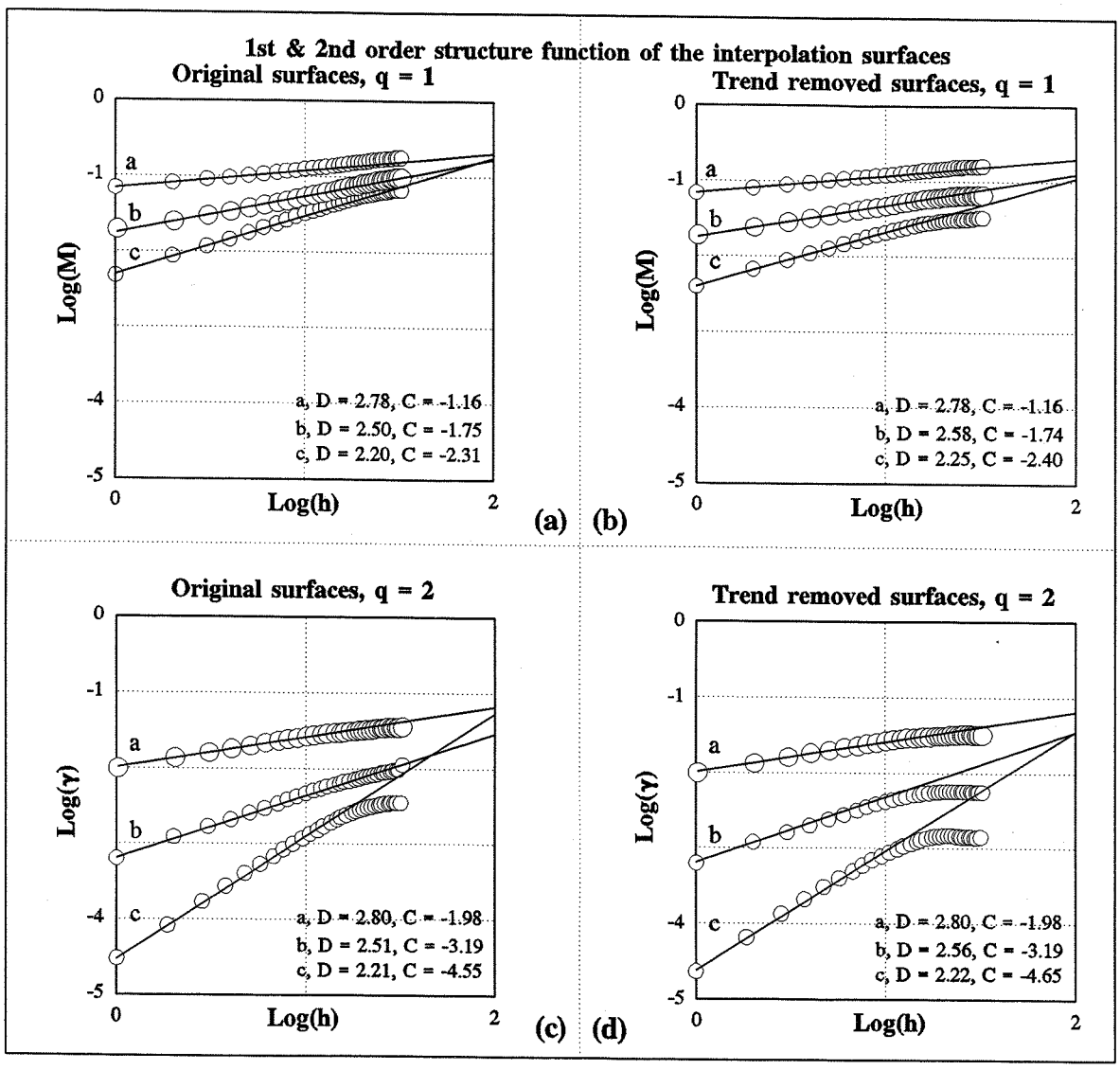

Fig. 2.14. The log-log plots of the first and second order function structures of the 2-d fBm surfaces weighted by Hanning window, generated by the interpolation method using parameter H = 0.2, 0.5, and 0.8, over lag range $2 < h < 16$. The original and trend removed 2-d fBm surfaces are shown in Fig. 2.7(c) and (d). **(a)** and **(b)** are the log-log plots of the absolute mean relief M(h) against the lag h for the original and trend removed surfaces. **(c)** and **(d)** are the log-log plots of the semivariance $\gamma(h)$ against the lag h for the original and trend removed surfaces.

of any pairs of data points, which fall into a range between h and h + 1 (i.e., $h <= r < h + 1$), is assigned to be h, where h = 1, 2, 3, ..., N - 1. In practice, the range of lag h is taken between 1 and N/2. The structure function for lags between N/2 and $\sqrt{2}(N-1)$, tends to be a constant (a sill value), which is beyond the investigating interests. Therefore, the first order structure function of a simulated 2-d fBm surface, [i.e., the absolute mean relief of the

surface M(h)], can be given by (Mandelbrot and Wallis, 1969a, Weissel *et. al.*, 1994),

$$M(h) = \frac{1}{N_j}\sum_{i=1}^{N_j}\left|g(r_i + h) - g(r_i)\right| \quad \propto \quad h^H \quad = \quad h^{3-D}$$

and the second order structure function (the 2-d semivariance), $\gamma(h)$, is given by,

$$\gamma(h) = \frac{1}{2N_j}\sum_{i=1}^{N_j}\left[g(r_i + h) - g(r_i)\right]^2 \quad \propto \quad h^{6-2D}$$

where N_j is the number of the pairs of data points whose separation spatial distances, r, are between the lags h and h + 1, M(h) and $\gamma(h)$ are the absolute mean relief and the semivariance of the surface.

Based on either the Log[M(h)] or Log[$\gamma(h)$] against lag h, the fractal dimension, D_{2s}, of a surface can be determined by,

$$D_{2s} = 3 - \beta_1, \quad as\ q = 1, the\ first\ order\ structure\ function;$$

$$D_{2s} = 3 - \frac{\beta_2}{2}, \quad as\ q = 2, the\ second\ order\ structure\ function. \qquad (2.7)$$

where β_1 and β_2 are the slopes of the regression lines of the log-log plot of the absolute mean relief M(h) and the semivariance $\gamma(h)$ against the lag h. From equation (2.7), the estimate error ΔD_{2s} for the 1st and 2nd order structure functions are respectively given by,

$$For \quad q = 1, \qquad \Delta D_{2s} = \Delta\beta;$$

$$For \quad q = 2, \qquad \Delta D_{2s} = \frac{1}{2}\Delta\beta$$

where the estimate errors of the exponent $\Delta\beta$ and the intercept ΔC_{2s} were determined by equation (2.1). The calculation was made by the program *SF2D* in *VISUAL BASIC* codes.

Fig. 2.13(a) and (b) are the log-log plots of the mean relief M(h) (q = 1) and Fig. 2.13(c) and (d) are the experimental semivariance γ(h) (q = 2) against the lag h for the original 2-d fBm surfaces and their trend removed surfaces generated by the midpoint displacement method using H = 0.8, 0.5, and 0.2 (refer to Fig. 2.7a and b). Fig. 2.14 has the same structure as Fig. 2.13, however, the original 2-d fBm surfaces (Fig. 2.14a and b) and their trends removed surfaces (c and d) are generated by the interpolation method using H = 0.8, 0.5, and 0.2 (refer to Fig. 2.7c and d).

2.6.4. Verification of the structure function method

The verification of the structure function method consists of the verifications of the 1-d and 2-d structure function methods and the comparison of the D values of fBm determined by the spectral and the structure function methods.

2.6.4.1. Verification of the 1-d structure function method

Fig. 2.11 and Fig. 2.12 are the log-log plots of the 1-d fBm profiles derived from the 1st and 2nd order structure function methods, and Table 2.7 summarizes the determined D

Table 2.7. D values of 1-d fBm profiles determined by 1st and 2nd structure functions

	Theoretical values		Original profiles		Trend removed profiles	
	H	D	$D_{1s} \pm \Delta D_{1s}$ (β)	$C_{1s} \pm \Delta C_{1s}$	$D_{1s} \pm \Delta D_{1s}$ (β)	$C_{1s} \pm \Delta C_{1s}$
First order structure function (q = 1)						
mp12	0.80	1.20	1.24 ± 0.01 (0.76)	-2.58 ± 0.01	1.24 ± 0.01 (0.76)	-2.58 ± 0.01
mp15	0.50	1.50	1.49 ± 0.01 (0.51)	-1.65 ± 0.01	1.49 ± 0.01 (0.51)	-1.65 ± 0.01
mp18	0.20	1.80	1.77 ± 0.01 (0.23)	-0.68 ± 0.01	1.76 ± 0.01 (0.24)	-0.68 ± 0.01
Second order structure function (q = 2)						
mp12	0.80	1.20	1.27 ± 0.01 (1.46)	-5.20 ± 0.01	1.27 ± 0.01 (1.46)	-5.20 ± 0.01
mp15	0.50	1.50	1.50 ± 0.01 (1.00)	-3.38 ± 0.01	1.50 ± 0.01 (1.00)	-3.38 ± 0.01
mp18	0.20	1.80	1.77 ± 0.01 (0.46)	-1.45 ± 0.01	1.77 ± 0.01 (0.46)	-1.45 ± 0.01
First order structure function (q = 1)						
int12	0.80	1.20	1.20 ± 0.01 (0.80)	-2.52 ± 0.01	1.20 ± 0.01 (0.80)	-2.52 ± 0.01
int15	0.50	1.50	1.50 ± 0.01 (0.50)	-1.59 ± 0.01	1.50 ± 0.01 (0.50)	-1.60 ± 0.01
int18	0.20	1.80	1.79 ± 0.01 (0.21)	-0.65 ± 0.01	1.79 ± 0.01 (0.21)	-0.65 ± 0.01
Second order structure function (q = 2)						
int12	0.80	1.20	1.21 ± 0.01 (1.58)	-5.18 ± 0.01	1.21 ± 0.01 (1.58)	-5.17 ± 0.01
int15	0.50	1.50	1.51 ± 0.01 (0.98)	-3.33 ± 0.01	1.51 ± 0.01 (0.98)	-3.32 ± 0.01
int18	0.20	1.80	1.80 ± 0.01 (0.40)	-1.42 ± 0.01	1.80 ± 0.01 (0.40)	-1.42 ± 0.01

values of the 1-d fBm original and trend removed profiles (Fig. 2.6) over the range between about h = 2 and h = 64. (β) in Table 2.7 is the slope of the regression line of the log-log plot of Figs. 2.11 and 2.12.

There is very little difference between the 1st (or 2nd) order moment distribution patterns, and very little difference between the calculated D values, of the original and the trend removed fBm profiles. This can be seen from comparing between Fig. 2.11(a) and (b), between Fig. 2.11(c) and (d), between Fig. 2.12(a) and (b), between Fig. 2.12(c) and (d), and between the middle and right columns of Table 2.7. Therefore, the detrending process for a profile need not to be necessary for both the 1st and 2nd order structure function methods.

Suppose that β_1 is the slope of the fitted regression line of the log-log plot of the mean relief M(h) against the lag h and β_2 is the slope of the fitted regression line of the log-log plot of the semivariance γ(h) against the lag h. Then, we have $\beta_2 \approx 2\beta_1$ (Table 2.7).

2.6.4.2. Verification of the 2-d structure function method

Fig. 2.13 and Fig. 2.14 are the log-log plots of the simulated 2-d fBm surfaces (refer

Table 2.8. D values of 2-d fBm surfaces determined by 1st and 2nd structure functions

	Theoretical values		Original profiles		Trend removed profiles	
	H	D	$D_{2s} \pm \Delta D_{2s}$ (β)	$C_{2s} \pm \Delta C_{2s}$	$D_{2s} \pm \Delta D_{2s}$ (β)	$C_{2s} \pm \Delta C_{2s}$
First order structure function (q = 1)						
mp22	0.80	2.20	2.36 ± 0.01 (0.64)	-1.84 ± 0.01	2.46 ± 0.01 (0.54)	-1.90 ± 0.01
mp25	0.50	2.50	2.49 ± 0.01 (0.51)	-1.42 ± 0.01	2.59 ± 0.01 (0.41)	-1.45 ± 0.01
mp28	0.20	2.80	2.80 ± 0.01 (0.20)	-0.96 ± 0.01	2.80 ± 0.01 (0.20)	-0.96 ± 0.01
Second order structure function (q = 2)						
mp22	0.80	2.20	2.36 ± 0.01 (1.28)	-3.47 ± 0.01	2.39 ± 0.03 (1.22)	-3.56 ± 0.02
mp25	0.50	2.50	2.53 ± 0.01 (0.94)	-2.57 ± 0.01	2.60 ± 0.02 (0.80)	-2.60 ± 0.01
mp28	0.20	2.80	2.82 ± 0.02 (0.36)	-1.64 ± 0.02	2.82 ± 0.02 (0.36)	-1.64 ± 0.02
First order structure function (q = 1)						
int22	0.80	2.20	2.20 ± 0.02 (0.80)	-2.31 ± 0.01	2.25 ± 0.02 (0.75)	-2.40 ± 0.01
int25	0.50	2.50	2.50 ± 0.01 (0.50)	-1.75 ± 0.01	2.58 ± 0.01 (0.42)	-1.74 ± 0.01
int28	0.20	2.80	2.78 ± 0.01 (0.22)	-1.16 ± 0.01	2.78 ± 0.01 (0.22)	-1.16 ± 0.01
Second order structure function (q = 2)						
int22	0.80	2.20	2.21 ± 0.03 (1.58)	-4.55 ± 0.03	2.22 ± 0.03 (1.56)	-4.65 ± 0.03
int25	0.50	2.50	2.51 ± 0.02 (0.98)	-3.19 ± 0.01	2.56 ± 0.02 (0.88)	-3.19 ± 0.01
int28	0.20	2.80	2.80 ± 0.01 (0.40)	-1.98 ± 0.01	2.80 ± 0.01 (0.40)	-1.98 ± 0.01

to Fig. 2.7), and their determined D values over the range between about h = 2 and h = 16 were summarized in Table 2.8.

Unlike the 1-d structure function method for which detrending process has very little effects on determined D values (Figs. 4.11 and 4.12), the removal of the planar trend plane from a 2-d fBm surface affects in two ways (Figs. 4.13 and 4.14): 1). The mean relieves or the semivariograms are flattened at larger observation scales (larger lag h); 2) the detrending process results in over estimated D value of the surface except as H is near to 0 (D is near to 3). The influence caused by detrending process of mp data is more severe than that of int data. This can be seen from comparing the middle column with the right column of Table 2.8. For example, the D value of the original surface int25 is 2.50, whereas that of detrended surface is 2.58 for the 1^{st} order structure function method.

The over estimated D values of the surfaces generated by the midpoint displacement technique are due to the non-stationary increments in the data themselves. The non-stationary increments may also be used to explain the crossover phenomena of M(h) and $\gamma(h)$ distribution patterns of mp22 and mp25 with those of mp28 [Fig. 2.13(a) and (c)].

Similar relationship $\beta_2 \approx 2\beta_1$ can be obtained from Table 2.8 (values in brackets are β), where β_1 and β_2 are the slopes of the regression lines from the log-log plots of the mean relief M(h) and the semivariance $\gamma(h)$ against the lag h.

2.6.4.3. Comparison of D values determined by the spectral and structure function methods

The fractal dimensions of the Hanning windows filtered 1-d fBm profiles and 2-d fBm surfaces derived from the structure function method are compared based on the analysis results of Sections 2.5 and 2.6,

The comparison of the lower part of Table 2.5 and Table 2.7 shows that the D values of the 1-d fBm profiles, generated by both the midpoint displacement and interpolation techniques, are reasonably consistent as determined by the spectral and structure function methods. The slightly higher D values of mp12 for both the methods are due to the non-stationary increments of the simulated mp data.

The comparison of the lower part of Table 2.6 and Table 2.8 also shows that the D values of the 2-d fBm surfaces, generated by both the midpoint displacement and interpolation techniques, are reasonably consistent for the both methods. The much higher

D values of mp22 than that of mp12 resulted from applying both the methods may be explained by the reasons that there are more non-stationary increments in the simulated 2-d fBm surfaces data than those in the simulated 1-d fBm profiles.

The removal of the linear and planar trend of fBm for determining the D values by the spectral and structure function methods are shown to be not necessary.

In summary, the fractal dimensions of the Hanning windows filtered synthetic profiles or surfaces derived from the structure function method are reasonable consistent with the theoretical D values which were initially given by H values, and the implementation of the methodologies and the programs developed are verified. The slope of the Log[γ(h)] against Log(h) is about the two times the slope of Log [M(h)] against Log(h). The 1st and 2nd order structure functions patterns are not affected by the detrending process of the synthetic profiles (Figs. 4.11 and 4.12), but affected by the removal of the planar trend plane from the synthetic surface (Figs. 4.13 and 4.14): 1). The detrending process may not to be necessary for the determination of D values of a fractal as the structure function method is deployed. This is consistent with the results obtained by Weissel (1994). Therefore, the 1st and 2nd order structure functions are successful fractal models to describe the synthetic 1-d fBm profiles and 2-d fBm surfaces.

2.7. THE INTERSECTION METHOD – THE ZEROSET THEORY

The intersection method is based on the zeroset theory. Its principle is that the fractal dimension of a surface can be deduced from the fractal dimension of its intersected profile plus 1, and the fractal dimension of a profile can be deduced from the fractal dimension of its intersected points plus 1 (Goodchild, 1982; Burrough, 1981; Barnsley *et. al.*, 1988).

2.7.1. The zeroset theory

The zeroset theory points out that dimensions of shapes are reduced by 1 after they are intersected with a plane. For example, a cube has a dimension of 3, its intersection with a plane gives a 2-d square. The intersection of this square with another plane produces a 1-d straight line segment, and a 0-d point will be created if this segment is intersected with yet another plane. This concept is true when applied to the fractals (Voss, 1988). Therefore, the relationship between the fractal dimension D and parameter H is given by,

$$D = E - H \tag{2.8}$$

where E is the Euclidean dimension in which the fractal takes. For example, E = 2 for a profile, and E = 3 for a surface.

It is obvious that the zeroset of a self-similar fractal yields another self-similar fractal, however, the zeroset of a self-affine fractal could become either a self-similar or a self-affine fractal. For instance, the zeroset of a self-affine 1-d fBm is a set of disconnected points obtained from intersecting 1-d fBm ($V_H(x)$, with a fractal dimension D_1) with a plane parallel to the x-axis. This zeroset is a self-similar fractal and has a topological dimension of zero and a fractal dimension of $D_0 = D_1 - 1$. The zerosets of a self-affine 2-d fBm ($V_H(x, y)$, with a fractal dimension D_2) however, could be either self-similar or self-affine since two types of zerosets can be obtained. One is the intersection of 2-d fBm with a horizontal plane which is parallel to x-y coordinates. This zeroset is a series of contours of the same height, and is a self-similar fractal with a fractal dimension $D_1 = D_2 - 1$. An other type of zeroset is a vertical section as the surface is intersected with a plane that parallels to the x- or y-axis. This zeroset (profile) may show mostly self-affinity and has a fractal dimension again $D_1 = D_2 - 1$. Generally, $0 < D_0 < 1$, $1 < D_1 < 2$, and $2 < D_2 < 3$. Most importantly, we

have,

$$D_0 + 1 = D_1 = D_2 - 1 \tag{2.9}$$

Therefore, from intersecting the trend removed profile (or surface) with a horizontal plane, a set of disconnected points (or contours of same elevation) can be obtained, and from equation (2.9), the fractal dimension of a profile D_{1i} (or a surface D_{2i}) can be estimated by calculating the fractal dimension of its set of intersected points D_{int1} (or intersected contours D_{int2}) by the box counting method, i.e., $D_{1i} = D_{int1} + 1$ or $D_{2i} = D_{int2} + 1$. The ways of calculating the fractal dimension of a profiles is termed as 1-d intersection method, and of a surface as 2-d intersection method. Six 1-d trend removed profiles (mp12, mp15, mp18; int12, int15, int18) and six trend removed surfaces (mp22, mp25, mp28; int22, int25, int28), which are generated by the interpolation method using H = 0.80, 0.50, and 0.20 (Fig. 2.6 and Fig. 2.7), are taken as examples to demonstrate the principles of the intersection method.

2.7.2. The one-dimensional intersection method

The 1-d intersection method is defined as the estimation of the fractal dimension of the set of the intersected points from intersecting a profile with a horizontal plane. From intersecting the profile with a horizontal plane of y = g(x) = avg, a set of disconnected points can be obtained, where avg is termed the average value of the vertical variations of g(x) for the profile data. Suppose that a profile has a very marked trend, there will be just a couple of intersected points obtained from intersecting the original profiles with a horizontal plane, and the intersection method will not be able to be applied on the set of intersected points. To overcome this problem, the horizontal plane could be rotated so that the plane contains the trend line. In other words, the set of the intersected points actually are from intersecting the trend removed profiles with y = g(x) = avg = 0, and generally the maximum number of intersected points are obtained. Then the box counting method is applied to the set of the intersected (disconnected) points to determine its fractal dimension as D_{int1}, and the fractal dimension of the profiles is $D_{1i} = D_{int1} + 1$. The calculation and the log-log plots were made by the programs *IS1D*.

Fig. 2.15(a) and (b) are the log-log plots of the 1-d intersection method, where N is the number of the filled boxes and r is the box size for the sets of the intersected points from intersecting the 1-d fBm trend removed profiles, generated by the midpoint

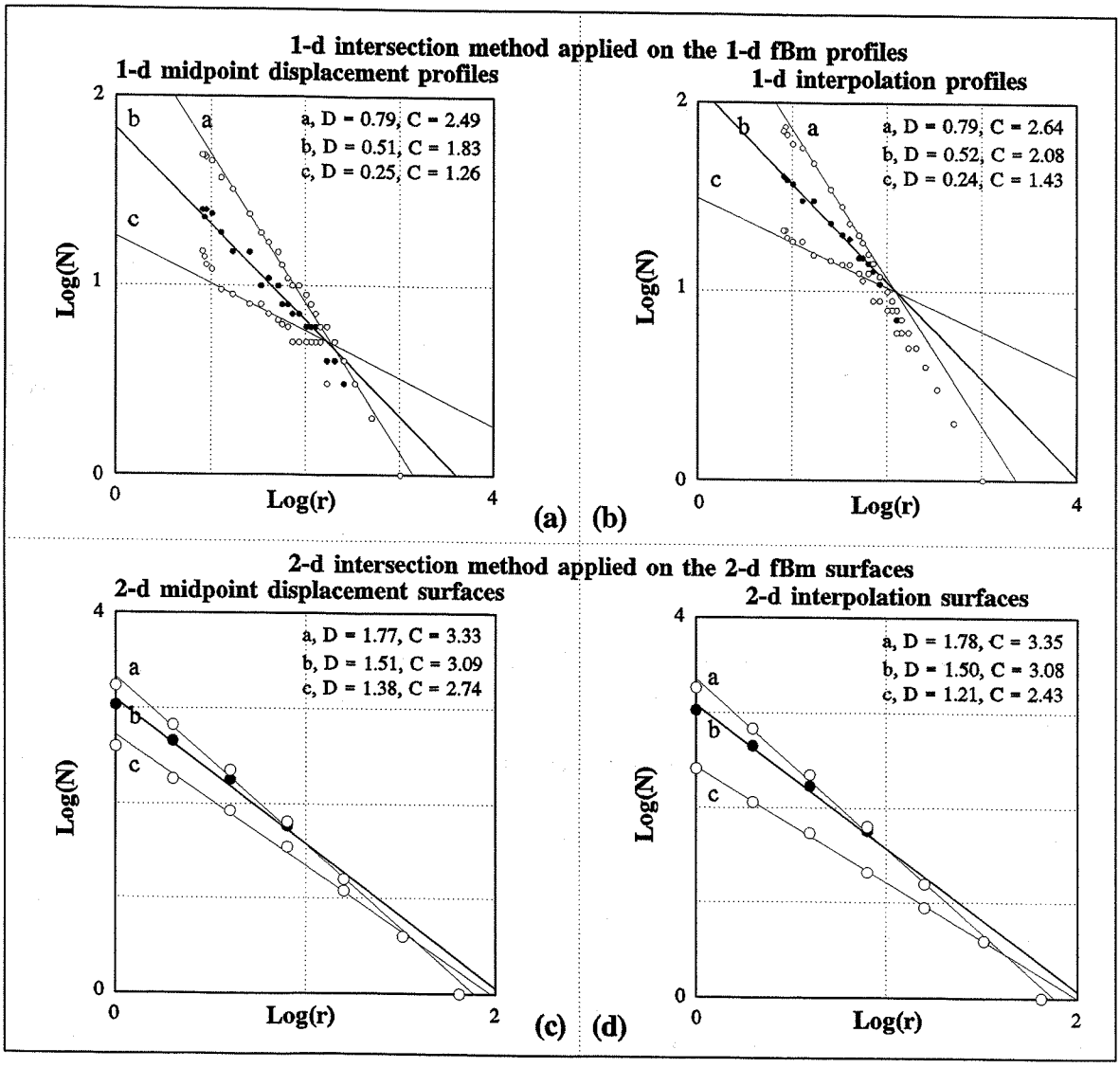

Fig. 2.15. Log-log plots of the box-counting method for determining the fractal dimensions of the sets of the intersected points and contours. The 1-d fBm profiles and 2-d fBm surfaces are generated by the midpoint displacement and interpolation methods using H = 0.2, 0.5, and 0.8. **(a)** and **(b)** are the log-log plots of the number of the filled boxes (N) against the box size (r) as the box-counting method is applied on the sets of the intersected points, which are the results from intersecting the 1-d fBm trend remove profiles (mp12, mp15, mp18) and (int12, int15, int18) with a horizontal plane of g(x) = 0. **(c)** and **(d)** are the log-log plots of the number of the filled boxes (N) against the box size (r) as the box-counting method is applied on the sets of contours, which are the results of intersecting the 2-d fBm trend removed surfaces (mp22, mp25, mp28) and (int22, int25, int28) with a horizontal plane of g(x, y) = 0.

displacement and interpolation methods using H = 0.8, 0.5, and 0.2, with a horizontal plane of y = g(x) = 0. The fractal dimensions of these sets of intersected points D_{intl} are determined by the box-counting method (refer to Section 2.3), and the fractal dimensions of

their corresponding profiles $D_{1i} = 1 + D_{int1}$, and the results are shown in Table 2.9. The estimate error of D value of the intersected points $\Delta D_{int1} = \Delta\beta$ which is determined by equation (2.1), where β is the slope of the regression line for the plot of the box-counting method applied on the set of the disconnected intersecting points (Fig. 2.15a and b).

Table 2.9. Fractal dimensions derived from the 1-d intersection method

	Theoretical values		Number of	D of intersected points	D_{1i} of the profile
	H	D	intersected points	$D_{int1} \pm \Delta D_{int1}$	$D_{1i} = D_{int1} + 1$
mp12	0.80	0.20	21	0.25 ± 0.07	1.25
mp15	0.50	0.50	48	0.51 ± 0.03	1.51
mp18	0.20	0.80	116	0.79 ± 0.04	1.79
int12	0.80	0.20	33	0.24 ± 0.05	1.24
int15	0.50	0.50	67	0.52 ± 0.02	1.52
int18	0.20	0.80	176	0.79 ± 0.03	1.79

2.7.3. The two-dimensional intersection method

Similarly, from intersecting the original surface with a horizontal plane of g(x, y) = avg, a set of contours of the elevation of avg were obtained (Fig. 2.16), where avg is the average value of the vertical variations of g(x, y). These contours are self-similar because of the equivalency of x- and y- coordinates. The box counting method was deployed to estimate the fractal dimensions of the set of contours D_{int2}. Fig. 2.15(c) and (d) are log-log plots of the number of the filled boxes (N) against the box size (r) for the sets of contours from the intersection of the trend removed surfaces, which are generated by the midpoint displacement and interpolation using H = 0.8, 0.5, and 0.2, with a horizontal plane. Therefore, the fractal dimensions of these surfaces $D_{2i} = D_{int2} + 1$. Table 2.10 shows the fractal dimensions obtained from the log-log plots of the box-counting method for those intersected sets of contours and their corresponding surfaces. The estimate error of D value of the intersected points $\Delta D_{int2} = \Delta\beta$ which is determined by equation (2.1), where β is the slope of the regression line for the plot of the box-counting method applied on the set of contours (Fig. 2.15c and d). All the determination of D values and log-log plots were carried out by the *VISUAL BASIC* program *IS2D*.

It is worth pointing out that any a single contour from Fig. 2.16 (of a reasonable

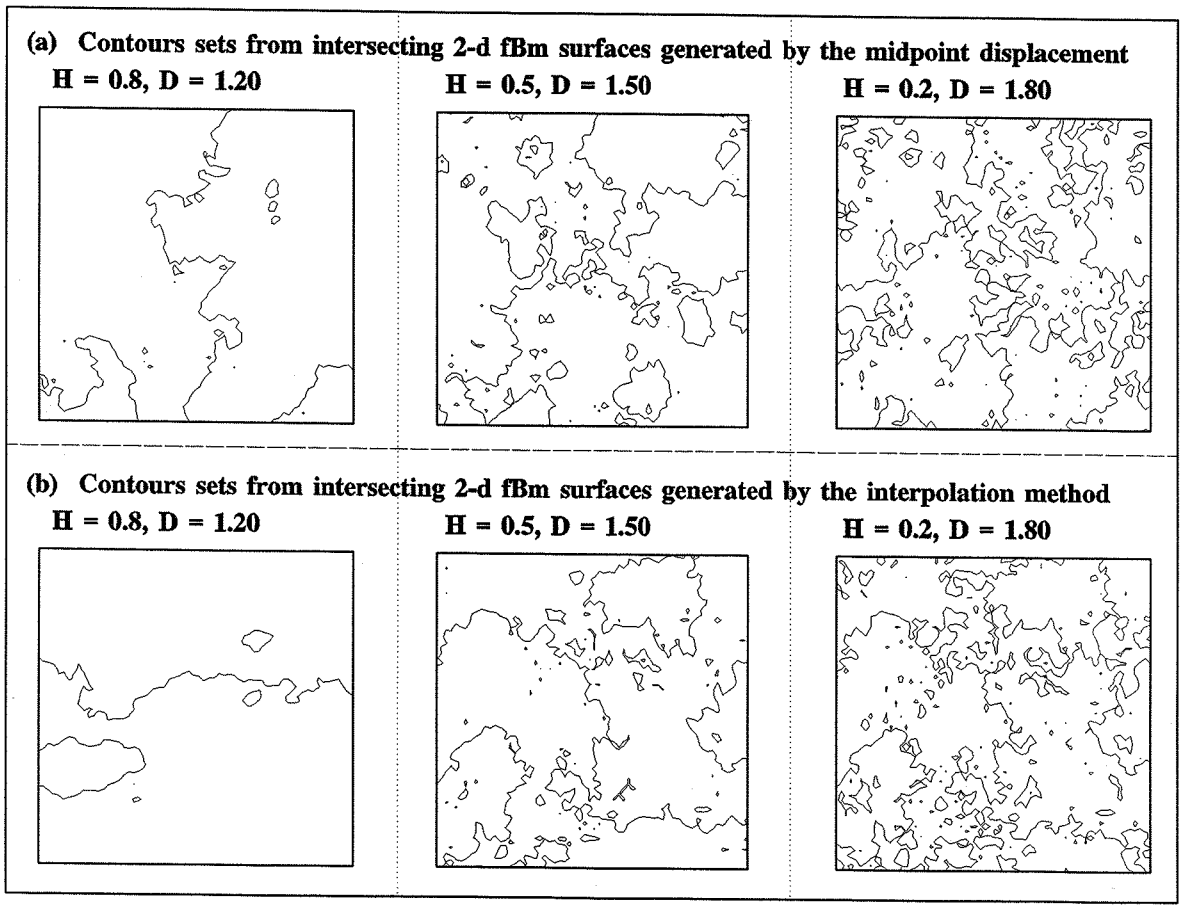

Fig. 5.16. The sets of intersection contours. They are the results of intersecting the original 2-d fBm surfaces generated by the midpoint displacement and interpolation methods using H = 0.8, 0.5, and 0.2 with a horizontal plane of g(x, y) = avg.

Table 2.10. Fractal dimensions derived from the 2-d intersection method

	Theoretical values		Number of intersected contours	D of intersected contours	D_{2i} of the surface
	H	D		$D_{int2} \pm \Delta D_{int2}$	$D_{2i} = D_{int2} + 1$
mp22	0.80	1.20	20	1.38 ± 0.06	2.38
mp25	0.50	1.50	82	1.51 ± 0.07	2.51
mp28	0.20	1.80	139	1.77 ± 0.06	2.77
int22	0.80	1.20	6	1.21 ± 0.02	2.21
int25	0.50	1.50	78	1.50 ± 0.07	2.50
int28	0.20	1.80	156	1.78 ± 0.06	2.78

contour length, of course), yields the roughly same fractal dimension of D =1.24 as it is determined by the box-counting method, i.e., the fractal dimension of a single contour does not depend on H values of a surface. This shows that the relationship between D and H as

shown in equation (2.9) does not exist. This does not contradict the zeroset theory as the intersection of a surface with a plane yields a set of contours, not a single one. Thus, the fractal dimension of a set of contours should be calculated and compared with those of a surface.

2.7.4. Verification of the intersection method

From Table 2.9, the fractal dimensions of the synthetic profiles D_{1i} determined by the 1-d intersection method are close to their theoretical D values. It is also consistent with the D values obtained by the 1-d spectral and structure function methods (Tables 2.5 and 2.7), thus the 1-d intersection method is a successful method to estimate the fractal dimension of a profile.

The fractal dimensions of the 2-d fBm surfaces generated by the interpolation methods are consistent with their theoretical D values as the 2-d intersection method is applied (Table 2.10). However, the application of the same method to the midpoint displacement surface (mp22) leads to a greater fractal dimension (2.38) than the theoretical values of 2.20. This difference also occurred when the surface was analyzed by the spectral and structure function methods(refer to Tables 2.6 and 2.8), and maybe explained by the non-stationary increments in the midpoint displacement technique deployed. In other words, there are more non-stationary increments in 2-d mp series surfaces than those in 1-d mp profiles. The difference also occur as the 2-d spectral and 2-d structure function methods are used.

In summary, the fractal dimensions of 1-d fBm profiles and 2-d fBm surfaces by the intersection method (D_{1i}, and D_{2i}) are reasonably consistent with the theoretical D values. The concepts of a set of disconnected points and a set of contours are introduced and used for determining the fractal dimensions of their profiles and surfaces. Given a certain H value, a set of disconnected points (or contours) has a fractal dimension of its profile's (or surface's) minus 1, it only depends on the value of H. However, a single contour generally has a fractal dimension of about 1.2 even if the single contour is taken from intersecting a 2-d fBm surface of H = 0.2 (D = 2.8) with a horizontal plane.

2.8. THE CUBE-COUNTING METHOD

The cube-counting (or named 3-d box-counting) method for computing D values of self-similar surfaces could be easily extended from the concept of the box-counting method.

Suppose there is an example surface, which is equally sampled raster grid of 65 by 65 (grid size has an unit length) and the height variation ranges from 0 to 64, then the data can be presented as [x, y, z = g(x, y)], where x, y, z = 0, 1, ..., 64. The choice of such an example surface and the number 64 is for the purposes of simplicity and of keeping the cube side length to be a power of 2. Therefore, the largest size of the cube is 64 (initial cube).

Firstly, the initial cube (Fig. 2.17a) can be divided into $(2^1)^3$ (Fig. 2.17b), $(2^2)^3$ (Fig. 2.17c), $(2^3)^3$, $(2^4)^3$, ..., and so on. Those cubes in which any portion of the surface occurs are named *'filled cubes'*, and the number of the filled cubes is recorded as N. For each cube size r, the number of filled cubes is recorded as N_r. Therefore, a series of the filled cubes (N_r) is obtained for different cube sizes (r).

Then the series of data sets are plotted at the log-log scale as shown in Fig. 2.17(d). The several points plotted at larger scales should be excluded since these points are usually have a slope of 3; and the first point as r = 1 can either be omitted or retained. The rest plotted points then are fitted by a straight line using least square technique. The slope of the fitted line is $\beta = -2.34$.

Finally, the fractal dimension of the surface, D_{2b}, is determined by equation (2.2), i.e., $D_{2b} = -\beta = 2.34$ over a range of r values between 1 and 5.

The program *CC3D* was made both in *FORTRAN 77* and *VISUAL BASIC* codes to determine the fractal dimensions of surfaces and plot the log-log distribution patterns.

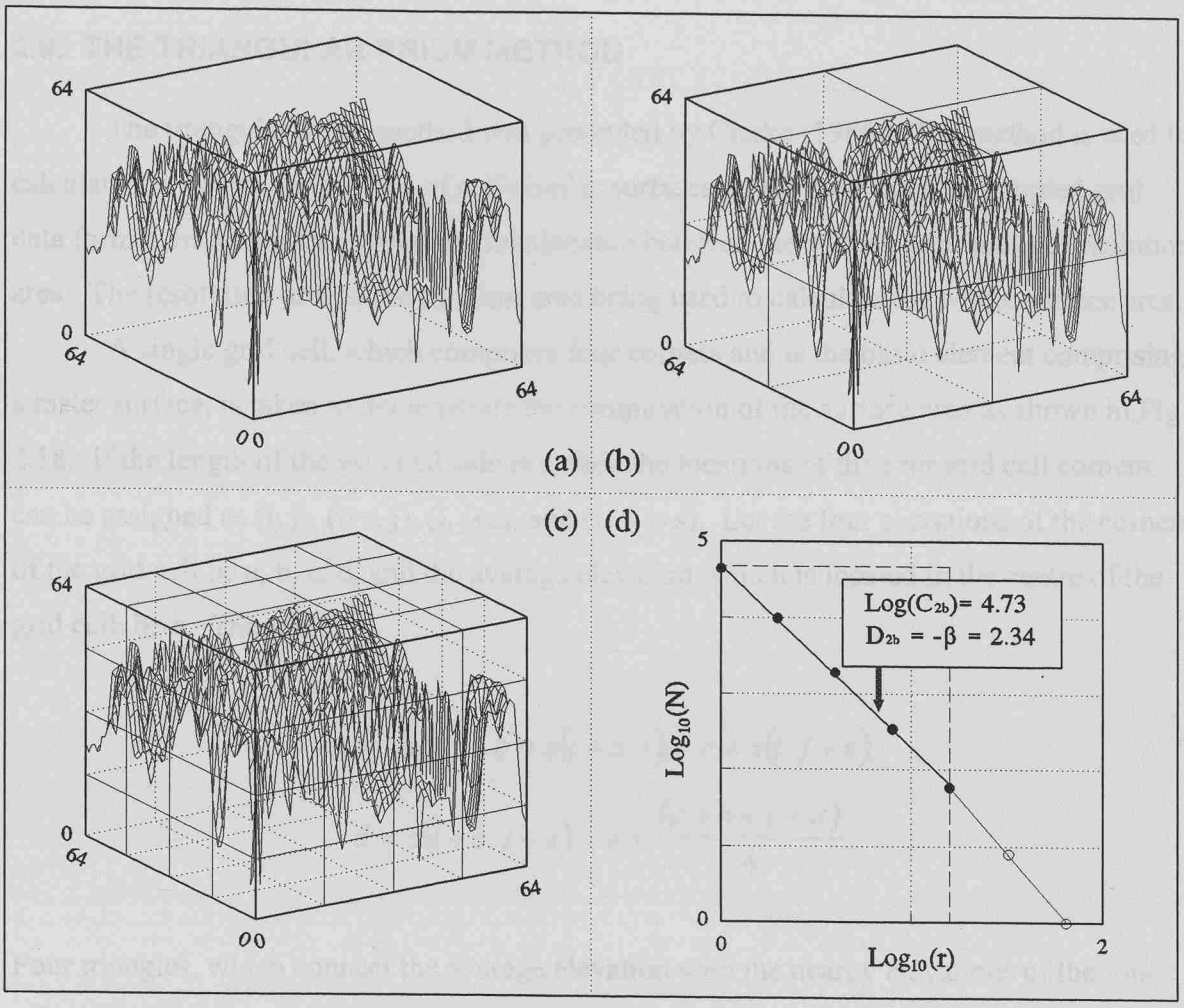

Fig. 2.17. Illustration of the principles of the cube-counting method, which is deployed for calculating the fractal dimensions of self-similar surfaces. The example grid data are 65 by 65, and the variation of height [z = g(x, y)] ranges from 0 to 64. The number of the filled cubes (N) increases as the size of the cube (r) decreases. **(a)** A cube of a size of 64 is used to contain the example surface, thus as r = 64, then N = 1. **(b)** As the initial cube is divided into $(2^1)^3$ small equal cubes, then N = 8, and r = 32. **(c)** As the initial cube is divided into $(2^2)^3$ small equal cubes, then N = 59, and r = 16. **(d)** Log-log plot of the number of the filled cubes against the cube side length shows that the slope of the regression line over a range between 30 m and 150 m is $D_{2b} = \beta = 2.34$.

2.9. THE TRIANGULAR PRISM METHOD

The triangular prism method was presented by Clarke (1986). The method is used to calculate the fractal dimensions of self-similar surfaces which have equally sampled grid data format, based on the power-law relationship between the surface area and the resolution area. The resolution area is the smallest area being used to calculate the whole surface area.

A single grid cell, which comprises four corners and is the basic element comprising a raster surface, is taken to demonstrate the computation of the surface area as shown in Fig. 2.18. If the length of the grid cell side is s, then the locations of the four grid cell corners can be assigned as (i, j), (i+s, j), (i, j+s), and (i+s, j+s). Let the four elevations of the corners of the grid cell be a, b, c, d, and the average elevation, which is located in the centre of the grid cell, be e. Therefore,

$$a = z(i, j), \quad b = z(i+s, j), \quad c = z(i, j+s),$$

$$d = z(i+s, j+s), \quad e = \frac{(a+b+c+d)}{4}.$$

Four triangles, which connect the average elevation with the nearby elevations of the four grid corners, represent the new surface of the grid. The side lengths of these triangles are given by,

$$w = \sqrt{(a-b)^2 + s^2}; \quad x = \sqrt{(b-c)^2 + s^2};$$

$$y = \sqrt{(c-d)^2 + s^2}; \quad z = \sqrt{(d-a)^2 + s^2};$$

$$o = \sqrt{(a-e)^2 + \left(\frac{\sqrt{2}}{2}s\right)^2}; \quad p = \sqrt{(b-e)^2 + \left(\frac{\sqrt{2}}{2}s\right)^2};$$

$$q = \sqrt{(c-e)^2 + \left(\frac{\sqrt{2}}{2}s\right)^2}; \quad r = \sqrt{(d-e)^2 + \left(\frac{\sqrt{2}}{2}s\right)^2}.$$

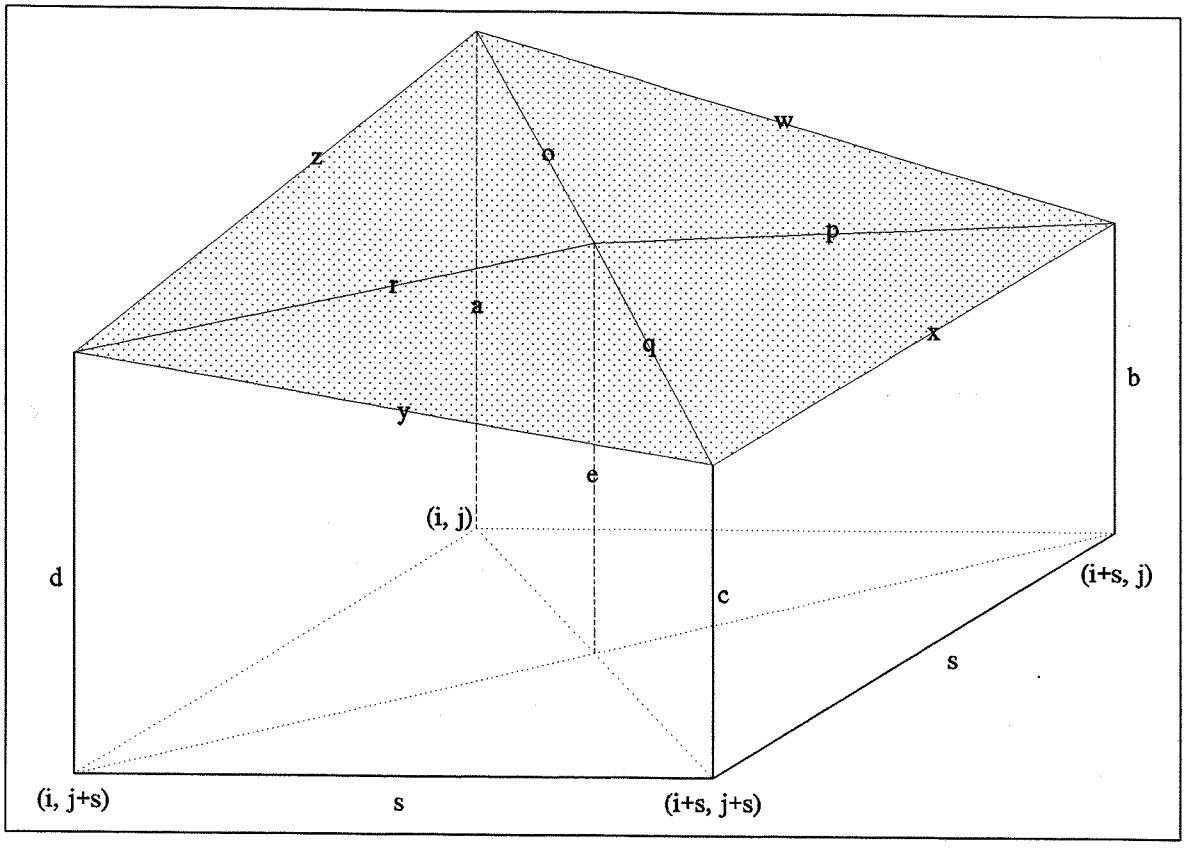

Fig. 2.18. Illustration of the principles of the triangular prism method. It demonstrates the way to calculate the surface area of the single cell (i, j) with the resolution area of s^2. Refer to text for more details.

Using Heron's formula,

$$sa = \frac{1}{2}(o + w + p); \quad sb = \frac{1}{2}(p + x + q);$$
$$sc = \frac{1}{2}(q + y + r); \quad sd = \frac{1}{2}(r + z + o).$$

Therefore the areas of the four triangles are give by,

$$A = \sqrt{sa(sa - o)(sa - p)(sa - w)}; \qquad B = \sqrt{sb(sb - p)(sb - x)(sb - q)};$$

$$C = \sqrt{sc(sc - q)(sc - y)(sc - r)}; \qquad D = \sqrt{sd(sd - r)(sd - z)(sd - o)}.$$

Finally, the area of the single cell grid surface is equal to the sum of the areas of these four

triangles, i.e.,

$$S_{(i,j)} = A + B + C + D$$

Aggregated over all grid cells in the study area, total area of the surface, S, can be computed by,

$$S = \sum_{i=1}^{N_s} \sum_{j=1}^{N_s} S_{(i,j)}$$

where N_s is the number of grid cells along one direction of the x-y coordinate system for the resolution square which has a side length of s and a resolution area of s × s.

The areas of the surface can be computed repeatedly whilst incrementally increasing the size of the resolution square. As the size of the square increases, the total area of the surface decreases. The side length of the resolution square increases in the form of power of 2, thus the a series of surfaces areas (S) can be obtained by measuring the surface using a resolution areas of s^2. Then the series of data are plotted at log-log scale, and the slope β of the regression line can be determined.

The fractal dimension, D, of the surface is calculated as (Clarke, 1986),

$$D_t = 2 - \beta$$

where β is the slope of the regression line of the log-log plot of the surface area (S) against the resolution area (s × s).

Fig. 2.19(a) shows a 3-d display of an example surface. Fig. 2.19(b) shows its log-log plot of the surface area (S) against the resolution area (s × s). The power-law relationship between S and s × s gives that the fractal dimension $D_t = 2 - \beta = 2.26$, where β is the slope of fitted line over the range between 1 × 1 and 5 × 5. The triangular prism method was carried out by *TP2D* program written in *FORTRAN* and *VISUAL BASIC* codes.

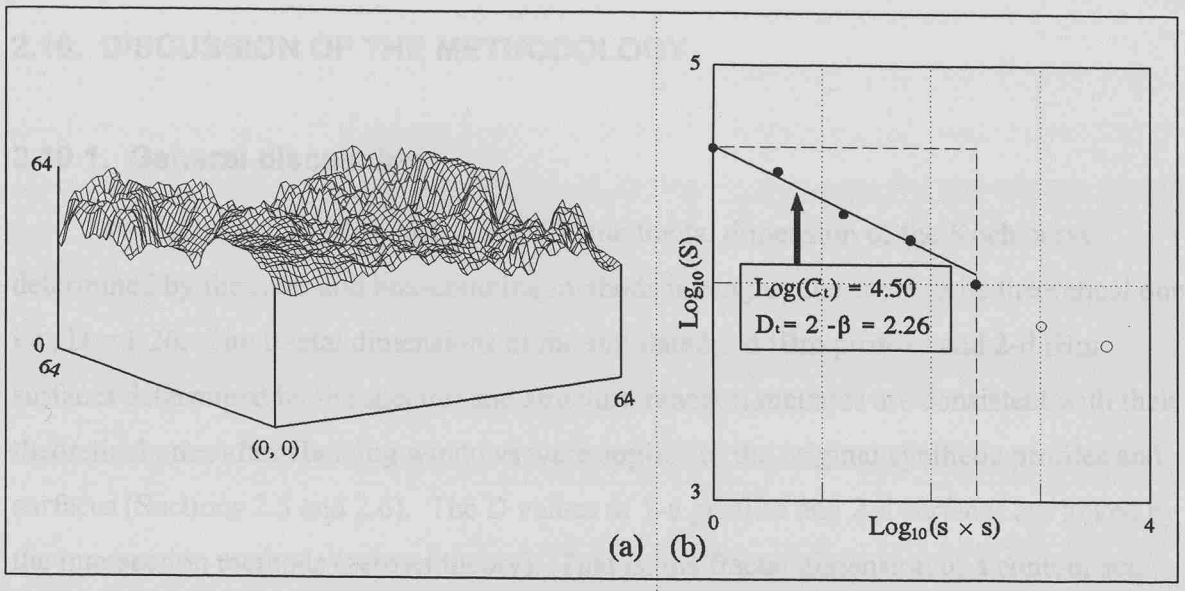

Fig. 2.19. The application of the triangular prism method on an example surface. The surface is unit-length equally sampled grid data of 65 by 65, and the height [z = (x, y)] varies from 0 to 64. **(a)** 3-d perspective view of the surface. **(b)** Log-log plot the surface area (S) against the resolution area s^2. The slope of the regression fitted line $\beta = -0.26$, and therefore the fractal dimension of the surface $D_t = 2 - \beta = 2.26$.

2.10. DISCUSSION OF THE METHODOLOGY

2.10.1. General discussion

As discussed in Sections 2.2 and 2.3, the fractal dimension of the Koch curve determined by the ruler and box-counting methods is roughly the same as its theoretical one, i.e., D = 1.26. The fractal dimensions of the simulated 1-d fBm profiles and 2-d fBm surfaces determined by the spectral and structure function methods are consistent with their theoretical ones after Hanning windows were applied to the original synthetic profiles and surfaces (Sections 2.5 and 2.6). The D values of 1-d profiles and 2-d surfaces are linked by the intersection methods (zeroset theory). That is, the fractal dimension of a contour set, resulted from intersected the surface with a horizontal plane, is equal to that of the surface plus 1.

The fractal dimension of a fractal line and surface can be determined by a variety of methods. Based on the self-similarity and self-affinity of a line or a surface, the methods discussed above can be categorized into two groups. One is for determining the fractal dimensions of self-similar fractals, such as the ruler, box-counting, cube-counting, and triangular prism methods. The other is for determining the fractal dimensions of self-affine fractals, such as the spectral and structure function methods.

These two groups of methods are measuring two different types of power-law relationship. For example, the fractal dimensions derived from the ruler method represent the changing degree of the power-law relationship between the curve length and the ruler length used to measure the curve, which is a function of the variance of the profile (Mandelbrot, 1985; Brown, 1987; Wong, 1987). For a topographic contour, its fractal dimension characterizes the roughness of the contour, whereas the intercept is very much dependent on the length of the contour observed. It, together with the box-counting method, 3-d box-counting and the triangular prism methods, measures the "*area filling*" capacity of a line or a surface. It is a roughness descriptor. However the fractal dimensions derived from the 1-d spectral (and 1-d structure function) method reveal the changing degree of the power-law relationship between the spatial energy [$P(\lambda)$, $\gamma(h)$] and the wavelength (λ) or the spatial lag (h). In other words, its fractal dimension D characterizes the property how the roughness varies with length scales, whereas, the intercept is the amplitude parameter C which describes the amplitude of the profile or surface roughness. By magnifying the

vertical scale of a surface at any scale will not change the fractal dimension D for the spectral and structure function methods, but change the amplitude parameter C. For example, a contour set that results from intersecting the vertically magnified surface with a horizontal plane is the same as the contour set resulted from intersecting the original surface with the horizontal plane. Generally, both the two parameters, the fractal dimension D and the intercept parameter C, are needed to describe the scaling behaviours of a self-affine fractal. The determination of fractal dimensions of a surface (or a line) can be linked with a set of lines (or a set of points) through the intersection method.

Some care should be taken when applying the ruler or box-counting method to self-affine fractals (Mandelbrot, 1985; Brown, 1987; Wong, 1987; Brown, 1987; Fox, 1989; Hough, 1989). Table 2.11 shows the fractal dimensions of 1-d fBm profiles generated by the midpoint displacement and the interpolation methods using H = 0.8, 0.5, and 0.2 as the ruler and box-counting methods are deployed. All D values are very close to 1 no matter how much H value varies. This is expectable because of the self-affinity of these generated profiles whose horizontal and vertical coordinates are not equivalent. Their fractal dimension should be determined by the spectral or the structure function methods. On the other hand, as the spectral method is applied on a self-similar profile, the exponent of the log-log plot will be -3 (Brown, 1987; Power and Tullis, 1991; Malinverno, 1995).

Table 2.11. Fractal dimensions of 1-d fBm determined by the ruler and box-counting methods

	Theoretical H		Ruler method	Box-counting method
	H	D	$D_r \pm \Delta D_r$	$D_{1b} \pm \Delta D_{1b}$
mp12	0.80	1.20	1.001 ± 0.001	1.001 ± 0.002
mp15	0.50	1.50	1.003 ± 0.003	1.008 ± 0.014
mp18	0.20	1.80	1.010 ± 0.007	1.011 ± 0.070
int12	0.80	1.20	1.001 ± 0.001	1.001 ± 0.002
int15	0.50	1.50	1.002 ± 0.001	1.006 ± 0.004
int18	0.20	1.80	1.007 ± 0.005	1.009 ± 0.050

Similarly, the fractal dimensions of 2-d self-affine fBm surfaces are very close to 2 as the cube-counting and triangular prism methods are deployed as shown Table 2.12. The fractal dimensions obtained are independent on the parameter H values.

For the spectral method, the detrending procedure disproportionately affects relief at

larger observation length scale, and therefore distorts the scaling behaviours of the original profiles or surfaces (Weissel, 1994). The power spectral density within larger wavelengths becomes flattened (Fig. 2.8). This distortion for a profile is more significant than that for a surface. Therefore, some care is needed when determining the fractal dimension of a trend removed profile (i.e., those several spectra of longest wavelengths should be excluded as determining the spectral exponent β). However, both the first M(h) and second γ(h) order structure functions are affected little by the trend removing procedure Figs. 2.11, 12, 13, and 14).

Table 2.12. Fractal dimensions of 2-d fBm determined by the cube-counting and triangular prism methods

	Theoretical H		Cube-counting method	Triangular prism method
	H	D	$D_{2b} \pm \Delta D_{2b}$	$D_t \pm \Delta D_t$
mp12	0.80	2.20	2.001 ± 0.001	2.001 ± 0.001
mp15	0.50	2.50	2.003 ± 0.004	2.003 ± 0.005
mp18	0.20	2.80	2.007 ± 0.008	2.046 ± 0.020
int12	0.80	2.20	2.001 ± 0.001	2.001 ± 0.001
int15	0.50	2.50	2.002 ± 0.001	2.003 ± 0.001
int18	0.20	2.80	2.005 ± 0.004	2.036 ± 0.010

2.10.2. Conclusions

1. The consistence between the calculated and theoretical fractal dimensions of the Koch curve, simulated 1-d, and 2-d fBm fractals verified the implementation of the methodologies and developed programs of the ruler, box, spectral, and structure function methods.
2. The ruler and box-counting methods are successful fractal models to describe the self-similar fractals, while the spectral and q^{th} order structure function (i.e., q^{th} moments) methods are suitable to deal with self-affine fractals. Generally, the methods for determining the fractal dimension of a self-similar fractal should not be used for determining the fractal dimension of a self-affine fractal. Otherwise, meaningful results would be hardly obtained. The ruler dimension (determined by the ruler or box counting method) is different from the spectral dimension (determined by the spectral or structure function method). The former is a roughness descriptor and focuses on the "*area filling*

capacity" of a curve in the space at certain range of observation scales; whereas the latter is to describe how roughness varies within observation scales and the intercept characterizes the amplitude of roughness.

3. The application of Hanning window to the synthetic fBm is essential in order to obtain correct fractal dimensions for the spectral method and structure function methods. This is because the principles of the methods were deduced from the theoretical assumption of the infinite sample size, and the truncation phenomena (Gibbs effects) resulted from applying the theory to the data of finite sample size in practice. Table 2.5 and 2.6 show that the D values of 1-d and 2-d fBm can be correctly determined as the fBm were Hanning window weighted for the spectral method. Comparisons between the lower part of Table 2.5 and Table 2.7, and between the lower part of Table 2.6 and Table 2.8 show the D values of the synthetic fBm are roughly the same as determined by the spectral and structure function methods. They are consistent with the D values determined by the intersection methods, as well as consistent with the theoretical D values which are given by H.
4. Detrending procedure needs not to be necessary for determining the D values of synthetic fBm for the spectral and structure function methods although trends of some samples are reasonably high (refer to RSS% of Tables 2.3 and 2.4). In some cases, trend removal process could over estimate the D value. For example, the D value of the original surface int25 is 2.50, whereas that of detrended surface is 2.58 (Table 2.8) for the 1^{st} order structure function method.
5. The fractal dimensions of 1-d fBm are less influenced by the non-stationary increments caused by the midpoint displacement method than those of 2-d fBm for the spectral, structure function, and intersection methods. The D values of 2-d mp fBm surfaces biased more form the theoretical D values than those of 1-d mp fBm profiles. This might be due to that there are more non-stationary increments in 2-d surfaces than those in 1-d profile caused by the midpoint displacement technique. For example, mp22 surface has a D value of (= 2.35 ~ 2.5, $D_{theoretical} = 2.20$), but mp12 profile has a D = 1.25 derived from the spectral, structure function, and intersection methods.
6. The intersection method is a powerful tool to link the D values of 1-d and 2-d fractals. For example, the D value of a fBm surface (D_2) could be obtained by calculating the D value of its intersected contour set (D_1) based on zeroset theory, i.e., $D_2 = D_1 + 1$.

2.11. PROGRAMS USED

Programs used for calculating fractal dimension and plotting profiles and surfaces are written in *VISUAL BASIC* code, some of them are also written in *FORTRAN* code. The programs have been developed to carry out almost every calculation and analysis needed in the thesis as shown in Table 2.13.

Table 2.13. A list of programs used in the thesis

N	Name	Functions	Code
		Digitizing map data	
01	*DIGICON*	Digitize map data (such as contours, profiles, chips)	VB
		Fractal analysis for the 1-dimensional data	
02	*RULERM*	Ruler method, determine the fractal dimensions of curves.	VB
03	*BOXCM*	Box-counting method, determine the fractal dimensions of curves.	VB
04	*SP1D*	1-dimensional spectral method, determine the fractal dimensions of profiles.	VB, F
05	*SF1D*	1-dimensional structure function method, determine the fractal dimensions of the curves.	VB, F
06	*IS1D*	1-dimensional intersection method, determine the fractal dimensions of the set of intersected points.	VB, F
		Fractal analysis for the 2-dimensional data	
07	*CC3D*	The cube (3-dimensional box) counting method, determine the fractal dimensions of self-similar fractal grid data.	VB, F
08	*TR3D*	Triangular prism method, determine the fractal dimensions of self-similar fractals of grid data.	VB, F
09	*SP2D*	2-dimensional spectral method, determine the fractal dimensions of grid data.	VB, F
10	*SF2D*	2-dimensional structure function method, determine the fractal dimensions of grid data.	VB, F
11	*IS2D*	2-dimensional intersection method, determine the fractal dimensions of the set of intersected contours.	VB, F
		Simulating 1-dimensional and 2-dimensional fractal data	
12	*MP1D*	Mid-point displacement method to simulate 1-dimensional fractals.	VB, F
13	*MPAD1D*	Mid-point addition method to simulate 1-dimensional fractals.	VB, F
14	*INT1D*	Interpolating method to simulate 1-dimensional fractals.	VB, F
15	*MP2D*	Mid-point displacement method to simulate 2-dimensional fractals.	VB, F
16	*MPAD2D*	Mid-point addition method to simulate 2-dimensional fractals.	VB, F
17	*INT2D*	Interpolating method to simulate 2-dimensional fractals.	VB, F
		Plot and save plot for the data and results	
18	*LOGP*	Log-log plot of x-y data sets.	VB
19	*PROFP*	Profile plot of x-y data sets.	VB
20	*SURFP*	Surface plot of grid data sets.	VB
21	*CONTP*	Contouring grid data sets and plot the set of the contours.	VB

VB: *VISUAL BASIC* code; **F:** *FORTRAN 77* code.

CHAPTER 3.

APPLICATION OF THE FRACTAL CONCEPT TO CONTOURS

CHAPTER 3

APPLICATION OF THE FRACTAL CONCEPT TO CONTOURS

3. APPLICATION OF THE FRACTAL CONCEPT TO CONTOURS

3.1. INTRODUCTION

Followed the work done by Richardson (1961), the coast of Britain was the first topographic contour (has a elevation level of 0 m) to be analyzed using the fractal concept by Mandelbrot (1967), and the study has shown it is a self-similar fractal with a fractal dimension of about D = 1.25 (Mandelbrot, 1967). Especially, the west coast has a higher fractal dimension (D = 1.30) than the east coast (D = 1.20) (Kaye, 1989). Indeed, a topographic contour is self-similar. As shown in Fig. 1.5(b), when the portion of the topographic contour is magnified isotropically by a factor r =3, the enlargement is statistically similar to the original one. A topographic contour is defined by a series of x- and y- coordinates at a certain elevation level, and the two coordinates are equivalent. Thus, rescaling a topographic contour isotropically does not change the scaling properties if they have the same overall roughness. Notice that a topographic contour resembles the Koch curve, and there might be more than one y-value(s) corresponding to a single x-value for a contour. This excludes the applicability of some fractal analysis method, e.g. the spectral method. Therefore, the ruler and box-counting methods are used to determine the fractal dimensions and fractal limits of contours.

In this chapter, 132 contours were digitized from maps of regions near the border between Spain and Portugal at different scales (1:200,000, 1:50,000, and 1:20,000) and

analyzed by the ruler and box-counting methods. Based on the analysis results of the 132 topographic contours, the general fractal features (fractal dimensions and fractal limits) of topographic contours will be investigated and comparison made of:

- the ruler and box-counting methods;
- water shore lines and their nearby topographic contours;
- contours determined at different map scales;
- the upper fractal limits and the contour lengths;
- contours of different elevations (i.e., adjacent contours); and
- contours from different rock types.

3.2. DATA SOURCE

Topographic contours of maps were digitized as a series of coordinates (x, y) using a TDS digitizing table and corresponding digitizing programs (see Section 3.2.1). 132 contours, including topographical contours and shore lines to lakes, were taken from geological maps of regions near the border between Spain and Portugal as shown in Fig. 3.1 (around areas of N39°18′, W7°01′). These contours were digitized from maps of different scales (1:200,000, 1:50,000, and 1:20,000), and the contours from the 1:50,000 map cover two rock groups of granite and metamorphic rocks. Table 3.1 shows more details about the contours from the different map scales and lithological units.

Table 3.1. Digitized contours from maps of different scales and rock types

Files	Map scales	N	Lithological units	Type of contours
D2	1:200,000	13	Quartzite, Phyllite	Topographic contours
G-M2	1:50,000	3	Muscovite granite	Topographic contours
G22B	1:50,000	17	Mica granite	Topographic contours
GP	1:50,000	28	Porphyritic mica granite	Topographic contours
K1	1:50,000	18	Schist, slate	Topographic contours
K2	1:50,000	16	Quartzite, Schist, Phyllite, Hornfels	Topographic contours
PC2	1:50,000	15	Biotite schist, Phyllite (Pre. C.)	Topographic contours
D1	1:50,000	13	Quartzite, Phyllite	Topographic contours
L2	1:50,000	4		Shore line and nearby
L1	1:20,000	5		topographic contours
Total		132		

All these contours were processed by the ruler and box-counting methods. The contour details, together with their processed results in terms of fractal dimensions D and fractal limits, are listed in Appendix 2.

3.2.1. Programs used

For the purposes of accuracy and efficiency, a digitizer and a PC have been used to collect and analyze the contours and shore lines. Programs utilized were developed by Professor David J Sanderson in *QUICK BASIC* for use with an IBM PC and TDS digitizing table.

DIGICON program allows the digitizing of contours from maps as a series of

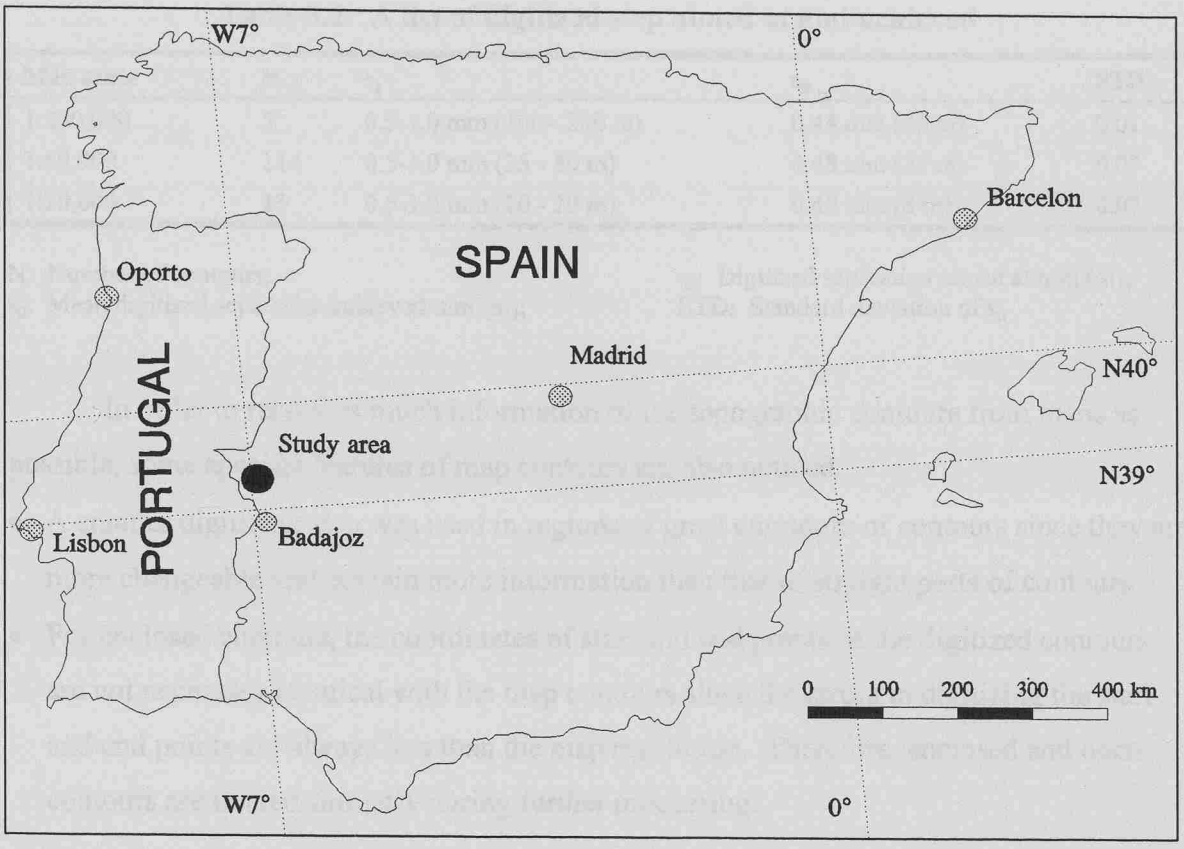

Fig. 3.1. Location of the sampling region.

(x, y, z) coordinates, where the z-value is the elevation value of the contour or other identifier. Such data sets are stored in ASCII files with the extension of **.CON*. *RULERM* and *BOXCM* programs accept and analyze digitized **.CON* files. These two programs count and store the contour lengths (L) for specific ruler lengths (r), and the number (N) and the proportion (P) of *'filled'* boxes for the specific box sizes (r) respectively. *'Filled'* boxes are those which contain part of a contour or curve.

3.2.2. Digitizing of contours

Since the resolution is usually 0.5 mm to 1.0 mm on map, the aim, during the digitizing procedure, was to digitize one to two points per millimetre, i.e., digitizing step is < 1.00 mm. This allows most of the information of a map contour to be retained in the digitized file.

Table 3.2 compares the digitizing steps aimed at and those achieved (refer to Appendix for more detail) and indicates that digitized contours retain most of the information contained in the map contours.

Table 3.2. A list of digitized step aimed at and achieved

Map scale	N	s_a	s_0	STD
1:200,000	5	0.5-1.0 mm (100 - 200 m)	0.44 mm (88 m)	0.01
1:50,000	114	0.5-1.0 mm (25 - 50 m)	0.48 mm (24 m)	0.07
1:20,000	13	0.5-1.0 mm (10 - 20 m)	0.40 mm (8 m)	0.07

N: Number of contours; s_a: Digitized separation aimed at mm (m);
s_0: Mean digitized separation achieved mm (m); STD: Standard deviation of s_0

In order to record as much information of the topographic contours from maps as possible, some specific features of map contours are also noticed.

- A smaller digitizing step was used in regions of great curvature of contours since they are more changeable and contain more information than that of straight parts of contours
- For enclosed contours, the coordinates of start and end points of the digitized contours are not necessary identical with the map contours since the errors in digitizing the start and end points are always less than the map resolution. Therefore, enclosed and open contours are treated similarly during further processing.

3.2.3. Some fractal characteristics of contours using the ruler and box-counting methods

From the example contour PC2031 employed to introduce the ruler and box-counting methods in Chapter 2, some common fractal characteristics of contours can be outlined.

Firstly, a contour is a fractal only over certain range bounded by the lower fractal limit and the upper fractal limit. In the study, r_{RL} and r_{BL} stand for the lower fractal limit derived from the ruler and box-counting methods, whereas r_{RU} and r_{BU} stand for the upper fractal limit derived from the ruler and box-counting method in later discussions.

Secondly, the plotted points of $Log(N_r)$ (or $Log(N_b)$, or Log(L), or Log(P)) against Log(r) of a contour, within the fractal limits, do not fit a perfect line but are scattered such that a topographic contour is a statistical fractal, where N_r and N_b are numbers of rulers and filled boxes of the ruler and box-counting methods, L is the length of a contour as measured by different rulers r and P is the percentage of the numbers of the filled boxes (N_b) and the total boxes (N), i.e., $P = N_b / N * 100\%$. The regression line of these scattered points characterizes the fractal properties of a contour, the regression correlation coefficient R^2,

therefore, is required to be sufficient high in determining the fractal dimensions, as well as the fractal limits. For this study, R^2 is ≥ 0.85 in most cases.

Thirdly, a contour digitized from a map has a finite contour length, L_0, which is determined by the separation of the digitized points, and the accuracy and resolution of the map. If a digitized topographic contour is recorded as N pairs of coordinates (x_i , y_i) where i = 1, 2, …, N, then the contour length L_0 is given by,

$$L_0 = \sum_{i=1}^{N-1} \sqrt{(x_{i+1} - x_i)^2 + (y_{i+1} - y_i)^2}$$

Fourthly, the general features of the log-log plots of N (or L) against r, as shown in Fig. 2.2(a), and those of N (or P) against r, as shown in Fig. 2.4(a), can be categorized into three regions.

- The situation of either $r < r_{RL}$ (or r_{BL}), or $r > r_{RL}$ (or r_{BL}) is beyond the statistical validity of the fractal technique.
- For r_{RL} (or r_{BL}) $< r < r_{RU}$ (or r_{BU}), $1 < D < 2$ represents the fractal nature of a contour, and appears to correlate closely with the variations in the contours caused by the topography since a map contour neither represents a straight line (D = 1) nor completely fills the map area (D = 2).

3.3. COMPARISON OF THE RULER AND BOX-COUNTING METHODS

In order to compare the ruler and box-counting methods, the D values (D_r, D_{1b}), lower (r_{RL}, r_{BL}), and upper (r_{RU}, r_{BU}) fractal limits of all these 132 contours derived from the ruler and box-counting methods are plotted in Fig. 3.2. The x-axis represents the fractal dimension of topographic contours derived from the ruler method, while on the y-axis are those from the box-counting method.

The average fractal dimensions derived from the ruler and box-counting methods are $D_r = 1.23 \pm 0.06$ and $D_{1b} = 1.23 \pm 0.08$ (refer to Appendix 2 for more details). Therefore, the topographic contours have an average fractal dimension of about D = 1.23 over a fractal range between 50 m and 14 km, i.e. about 2 orders of magnitude for both the ruler and box-counting methods (Table 3.3).

The plot of D_{1b} against D_r on linear paper (Fig. 3.2a), shows that D_{1b} has a clear linear trend with a gradient of about 1.0 with D_r, although the points are quite scattered. The analysis of regression shows that the correlation (correlation coefficient $R^2 = 0.50$) between D_{1b} and D_r can be mathematically presented as,

$$D_{1b} = D_r \pm 0.15$$

with about 95% of the plotted points falling between these two lines.

The fractal limits (r_{BL} and r_{BU}) derived from the box-counting method are plotted against those (r_{RL} and r_{RU}) derived from the ruler method in Fig. 3.2(b) and (c) respectively. These two plots show a correlation with a gradient of about 1 between the two methods, i.e., $r_{BL} \approx r_{RL}$ and $r_{BU} \approx r_{RU}$.

Two types of statistical analysis methods have been deployed to test if any difference exists between the fractal dimensions derived from the ruler (D_r) and box counting (D_{1b}) methods.

One is the "paired comparison t-test". Obviously, each contour has a pair of fractal dimensions determined by the ruler method (D_r) and the box counting method (D_{1b}). Since determined D values are independent on the map scales, the 132 pairs of D values from different map scales were analyzed by the t-test. The lower (r_L) and upper (r_U) fractal limits were analyzed by the t-test based on same map scales. The t-test was carried out at a

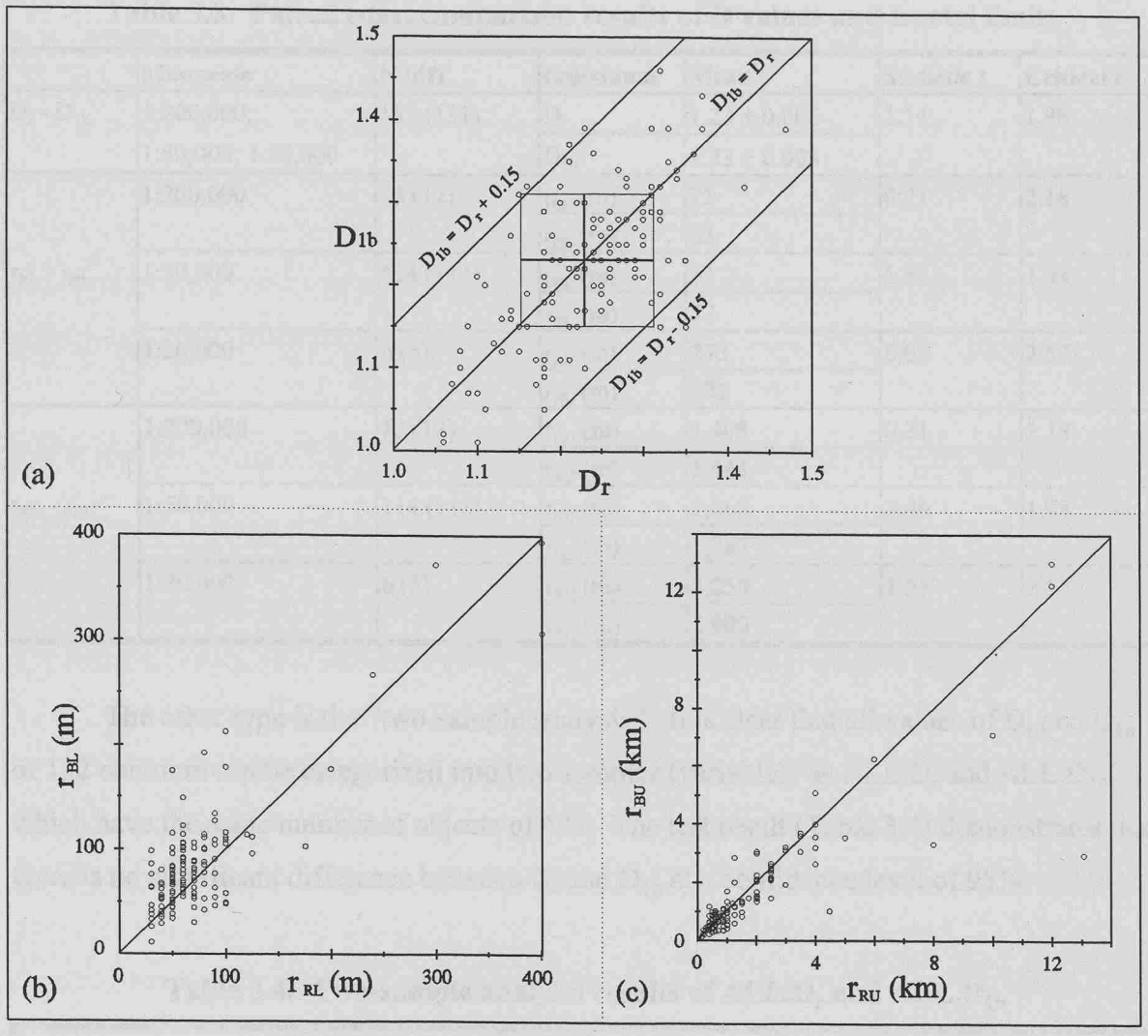

Fig. 3.2. Comparison of the ruler and box-counting methods, in terms of the fractal dimension (D_r and D_b); the lower (r_{RL} and r_{BL}) and upper (r_{RU} and r_{BU}) fractal limits. **(a)** linear relationship between D_{1b} and D_r in the range of (1.0, 1.5). Although D_r and D_{1b} are quite scattered, a clear linear trend with gradient of 1.0 shows that about 95% of the plotted points, statistically, fall between the two trend lines of $D_{1b} = D_r \pm 0.15$. **(b) and (c)** are linear plots of r_{BL} against r_{RL} and r_{BU} against r_{RU}. Both plots show a correlation of a gradient of about 1. That is, $r_{BL} = r_{RL}$ and $r_{BU} = r_{RU}$. Therefore, there is no significant difference between these two methods in terms of fractal dimensions and fractal limits.

confidence level of 95% (i.e., $\alpha = 0.05$) for the hypothesized mean difference $H_0 = 0$. The statistic t were taken as the absolute values, whereas the critical t were theoretical values at a confidence level of 95% and the responding df (degree of freedom).

The paired comparison t-test results show that there is no significant difference between the ruler and box-counting methods in terms of fractal properties (including the D value, lower and upper fractal limits) as shown in Table 3.3 (statistical t < critical t).

Table 3.3. Paired t-test comparison results of D values and fractal limits

	Map scale	N (df)	Individual	Mean	Statistic t	Critical t
D_r - D_{1b}	1:200,000; 1:50,000; 1:20,000	132 (131)	D_r	1.23 ± 0.006	1.14	1.98
			D_{1b}	1.23 ± 0.008		
r_{RL} - r_{BL}	1:200,000	13 (12)	r_{RL} (m)	75	0.71	2.18
			r_{BL} (m)	83		
	1:50,000	114 (113)	r_{RL} (m)	63	1.82	1.98
			r_{BL} (m)	77		
	1:20,000	6 (5)	r_{RL} (m)	273	0.09	2.57
			r_{BL} (m)	271		
r_{RU} - r_{BU}	1:200,000	13 (12)	r_{RU} (m)	1,408	0.31	2.18
			r_{BU} (m)	1,443		
	1:50,000	114 (113)	r_{RU} (m)	1,368	1.46	1.98
			r_{BU} (m)	1,287		
	1:20,000	6 (5)	r_{RU} (m)	8,250	1.55	2.57
			r_{BU} (m)	6,900		

The other type is the "two-sample analysis". It is clear that all values of D_r and D_{1b} of 132 contours can be categorized into two samples (variables) as ALL.D_r and ALL.D_{1b}, which have the same number of objects of 132. The test result (Table 3.4) demonstrates that there is no significant difference between D_r and D_{1b} at a confidence level of 95%.

Table 3.4. Two-sample analysis results of ALL.D_r and ALL.D_{1b}

		ALL.D_r	ALL.D_{1b}	Pooled
Sample statistics: Number of objects.		132	132	264
	Average	1.232	1.225	1.228
	Variance	6.146E-3	8.318E-3	7.23E-3
	Std. deviation	0.078	0.091	0.085
	Median	1.24	1.23	1.23
Difference between means = 6.818E-3		Conf. interval for diff. in means: 95%		
(Equal vars.) Sample 1 - Sample 2		-0.0138	0.0274	262 df
(Unequal vars.) Sample 1 - Sample 2		-0.0138	0.0274	262 df
Ratio of variances = 0.739		Conf. interval for ratio of variances: 95%		
Sample 1 , Sample 2	0.524	1.042	131 df	131 df
Hypothesis test for	**H0:** Diff = 0;	Computed t statistic = 0.651 vs Alt: NE		
Sig. Level = 0.515	at α = 0.05	**SO DO NOT REJECT H0.**		

In summary, there is no significant difference, in terms of fractal dimension and fractal limit, between the ruler and box-counting methods as they are applied to topographic contours.

3.4. COMPARISON OF SHORE LINES AND NEARBY CONTOURS

Generally, shore lines (such as lake or sea edges) may be more accurately mapped than topographic contours because the latter are determined from interpolation of spot heights, and subject to greater smoothing. This might lead the loss of some finer details of the nearby topographic contours. Have shore lines the same fractal characteristics as their nearby topographic contours?

To investigate this, the Caia lake area, at ground N39°01′, W07°10′, (Fig. 3.3), was studied by analysing two lake shore lines (L1001 and L2001) and two nearby topographic contours (L1002 and L2004). The shore lines and topographic contours have elevations of 240 m and 300 m. The shore lines L1001 and L2001 are of the same feature - the same lake shore margin digitized from different map scales(1:200,000 and 1:50,000). Both the shore line and the topographic contour on Fig. 3.3(b) are distinctively 'rougher' than those on Fig. 3.3(a), representing the increased detail present on the 1:50,000 map.

The ruler and box-counting methods were implemented to calculate the fractal dimensions and the fractal limits of the shore lines and their nearby topographic contours. For the ruler method, the lengths of the contours (L) are plotted against the ruler lengths (r) on a logarithm scale (Fig. 3.4a) over a range between r = 200 m and 10 km. For the box-counting method, the proportions of filled boxes (P) are plotted against the side length of the boxes (r) on a logarithm scale (Fig. 3.4b), which range between r = 100 m and 4 km.

The fractal dimensions and fractal limits are determined from the log-log plots of Fig. 3.4, and their results are summarized in Table 3.5.

Table 3.5. Comparison of lake shore lines and nearby topographic contours

Map scale	Contours	D_r	r_{RL} - r_{RU} (m)	D_{1b}	r_{BL} - r_{BU} (m)	avg. D
1:200,000	L1001, water, L_0 = 71,043	1.33	200- 5,000	1.39	177-3,548	1.36
	L1002, topo.(300m) , L_0 = 86,488	1.31	240-10,000	1.29	267-7,112	1.30
1:50,000	L2001, water, L_0 = 104,951	1.33	100- 4,000	1.39	109-4,003	1.36
	L2004, topo.(300m) , L_0 = 62,064	1.36	100- 8,000	1.36	111- 3,318	1.36

r_{RL} - r_{RU} (m): The lower and upper fractal limits in the ruler method in metres;
r_{BL} - r_{BU} (m): The lower and upper fractal limits in the box-counting method in metres.

Table 3.5 indicates that the fractal dimension of the shore line and its nearby

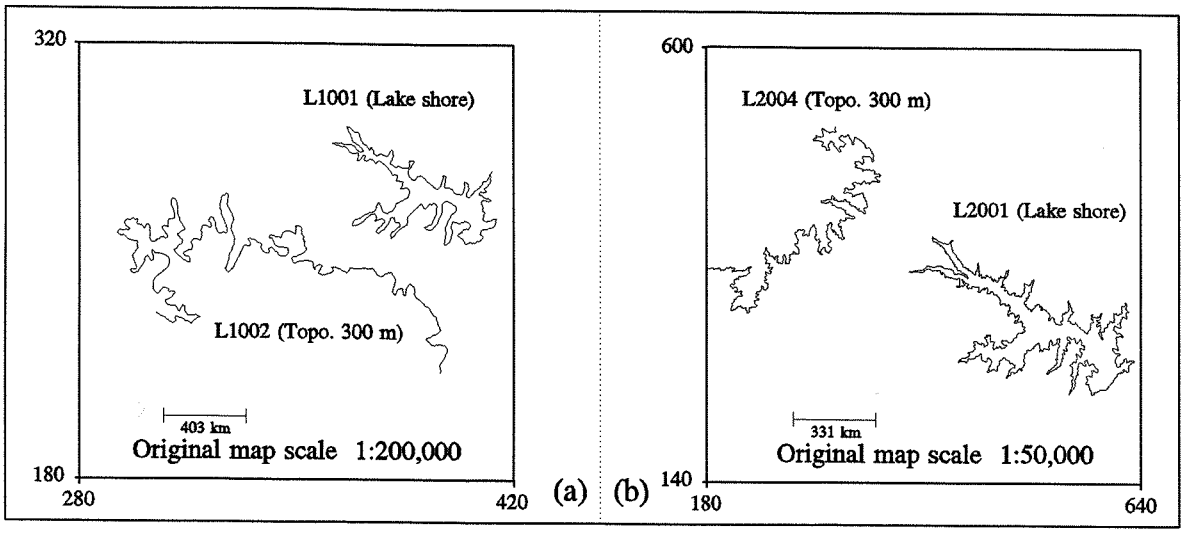

Fig. 3.3. Display of the digitized shore lines and their nearby topographic contours from maps of different scales. **(a)** compressed *Caia* lake shore (L1001, enclosed) of 240 m elevation and its nearby topographic contour (L1002) of 300 metres elevation from the 1:200,000 map. **(b)** compressed *Caia* lake shore (L2001, enclosed) of 240 m elevation and its nearby topographic contour (L2004) of 300 metres elevation from the 1:50,000 map. Intuitively, both the water shore line and topographic contour on (b) contain smaller scale details and rougher than those on (a).

contour varies little as the ruler and box-counting methods are deployed, D_r being in the range of 1.31 to 1.36 and D_{1b} in the range of 1.29 to 1.39. The average value of D = 1.35 applies over fractal limits from 100 m up to 10 km. Compared with the average D-values (D = 1.23) of topographic contours, as discussed in Section 3.3, the D-values of the water shore lines and their nearby contours (D = 1.35) are higher. Thus, there is no significant difference between the shore lines and their nearby topographic contours in terms of D-values.

Table 3.5 also shows that there is no significant difference between the shore lines and their nearby topographic contours in terms of the lower fractal limit. However, the lower fractal limits of the contours from the 1:50,000 map are the half of those from the 1:200,000 map. This is because that the larger scales of maps preserve more information of contours than smaller ones.

In summary, there is no significant difference between the shore lines and their nearby topographic contours in terms of D-values and fractal limits.

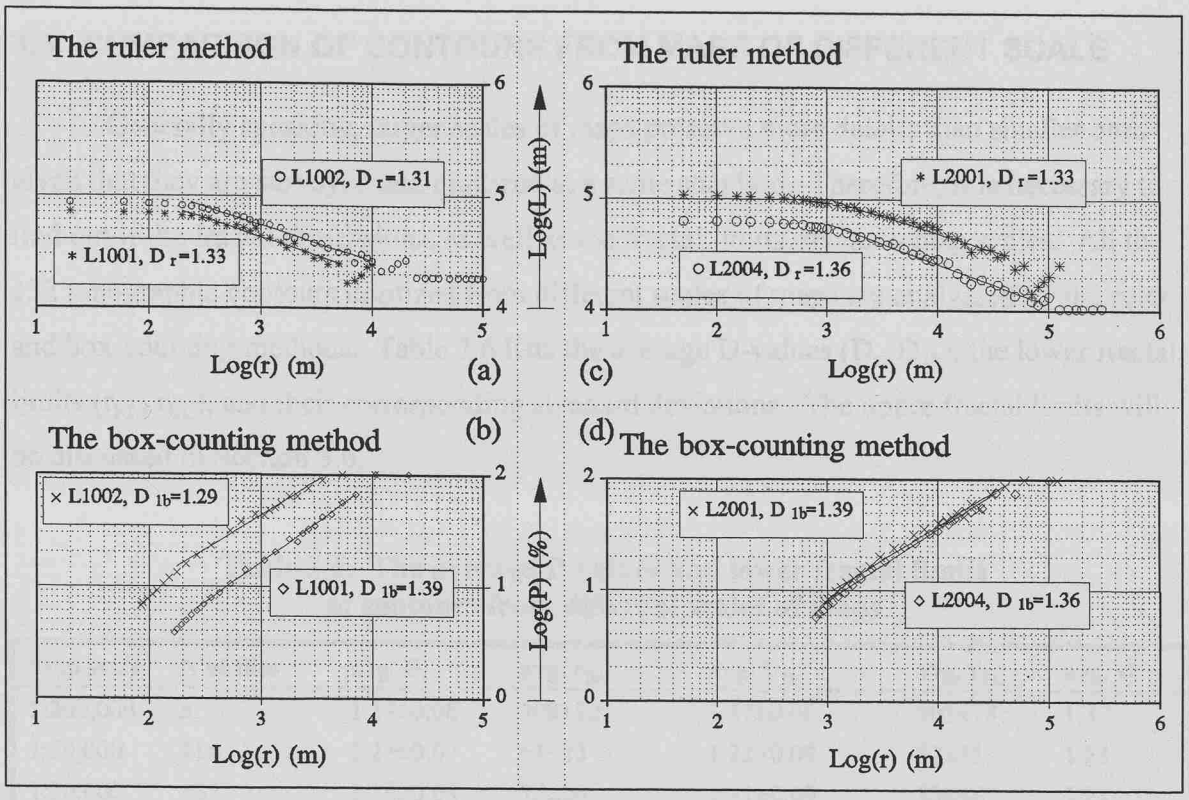

Fig. 3.4. Log-log plots for shore lines and nearby topographic contours of 300 m elevation when analyzed by the ruler and box-counting methods. **(a) and (b)** are log-log plots, for the shore line L1001 and its nearby topographic contour L1002 (of 300 m of elevation) from the 1:200,000 map, using the ruler and box-counting methods respectively. L1001 has a slightly higher D-value (D_r=1.33, D_{1b}=1.39) than L1002 (D_r=1.31, D_{1b}=1.29). The shore line L1001 has an average value D = 1.36 over fractal limits 200 m to 5 km, topographic contour has an average value D = 1.30 over 200 m to 10 km. **(c) and (d)** are log-log plots, for the shore line L2001 and its nearby 300 m topographic contour L2004 from the 1:50,000 map, using the ruler and box-counting methods. The shore line L2001 and its nearby contour have roughly the same D value (D = 1.36) over fractal limit ranges between 100 m and 4 km.

3.5. COMPARISON OF CONTOURS FROM MAPS OF DIFFERENT SCALE

Generally speaking, larger scales of maps preserve more details than smaller ones given that they are surveyed and digitized at a same standard. Therefore, it is necessary to find out if the fractal dimensions, as well as the fractal limits, relate to map scales. All the 132 topographic contours digitized from different scales of maps are analyzed by the ruler and box-counting methods. Table 3.6 lists the average D-values (D_r, D_{1b}), the lower fractal limits (r_{RL}, r_{BL}), and their corresponding standard deviations. The upper fractal limits will be discussed in Section 3.6.

Table 3.6. The average D values and lower fractal limits of contours from different scales of maps

Map scale	N of files	avg. D_r	avg. r_{RL}	avg. D_{1b}	avg. r_{BL}	avg. D
1:200,000	5	1.37±0.06	308±82	1.37±0.06	303±78	1.37
1:50,000	114	1.23±0.07	63±23	1.22±0.09	77±31	1.23
1:20,000	13	1.20±0.08	75±26	1.21±0.09	83±48	1.21

Fig. 3.5 is a plot of D values (D_r, D_{1b}) of 132 contours of different map scales, and shows the variation of fractal dimensions among the map scales.

Both Table 3.6 and Fig. 3.5 show that there is no systematic relationship between map scales and D values, i.e., they are independent. The average D value of contours from 1:20,000 map (D = 1.21) is roughly the same as that of contours from 1:50,000 map (D = 1.23). However, the contours from 1:200,000 map (D = 1.37) seem to have higher D value than those from 1:20,000 and 1:50,000 maps. This is because the paired contours themselves (linked solid line) between 1:50,000 and 1:20,000 maps have higher D-value, and thus the higher D-value of these contours are not the results of difference map scales.

In terms of the lower fractal limits, the variation among different map scales was investigated. The lower fractal limits were determined and are plotted against map scales on double logarithm paper as shown in Fig. 3.6. For 1:50,000 map, note that more data points appeared in Fig. 3.6(b) for the box-counting method than those appeared in Fig. 3.6(a) for the ruler method. This is because, firstly, there are 114 contours; and secondly a consistent series of ruler lengths is used for the ruler method, whereas the box sizes are determined by the sizes of contours for the box-counting method.

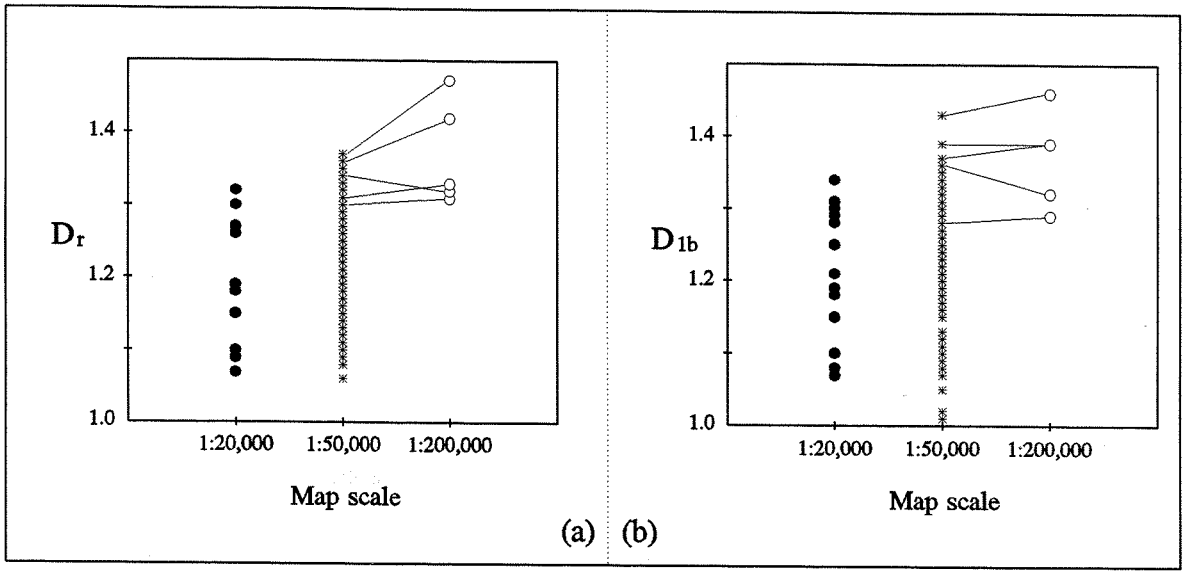

Fig. 3.5. Linear plot of the fractal dimension D against map scales, where D_r and D_{1b} are D-values derived from the ruler and box-counting methods. The two plots indicate that the fractal dimension and map scales are independent. Solid lines tie the paired contours of equal height from different scale maps.

From Fig. 3.6, the lower fractal limit is observed to decrease as the map scales increase from 1:200,000 to 1:50,000. This decreasing trend is also expected from map scales from 1:50,000 to 1:20,000 theoretically. In other words, the lower fractal limit of contours from the 1:200,000 map is expected to be higher than that from the 1:50,000 map, and higher than that from 1:20,000 map. This is because the topographic contours from well surveyed maps preserve more finer details of topographic variance than those from poor surveyed ones. However, the lower fractal limits from the maps of 1:20,000 and 1:50,000 are roughly the same. This is because the map of 1:20,000 used here was not as well surveyed as the map of 1:50,000, and leads the finer details of the topographic contours from the 1:20,000 map were lost. Comparison of the lower fractal limits derived from the topographic contours at different map scales reflects the quality (resolution) of topographic maps. In other word, for the same map scale and standard of digitizing procedures, the lower the lower fractal limit of the contour is, the better the topographic maps produced.

If the 1:20,000 map had the same quality as the 1:50,000 or 1:200,000 maps, the lower fractal limit should be lower than it is, and it might be true that the lower fractal limits have a power-law dependence on the map scales.

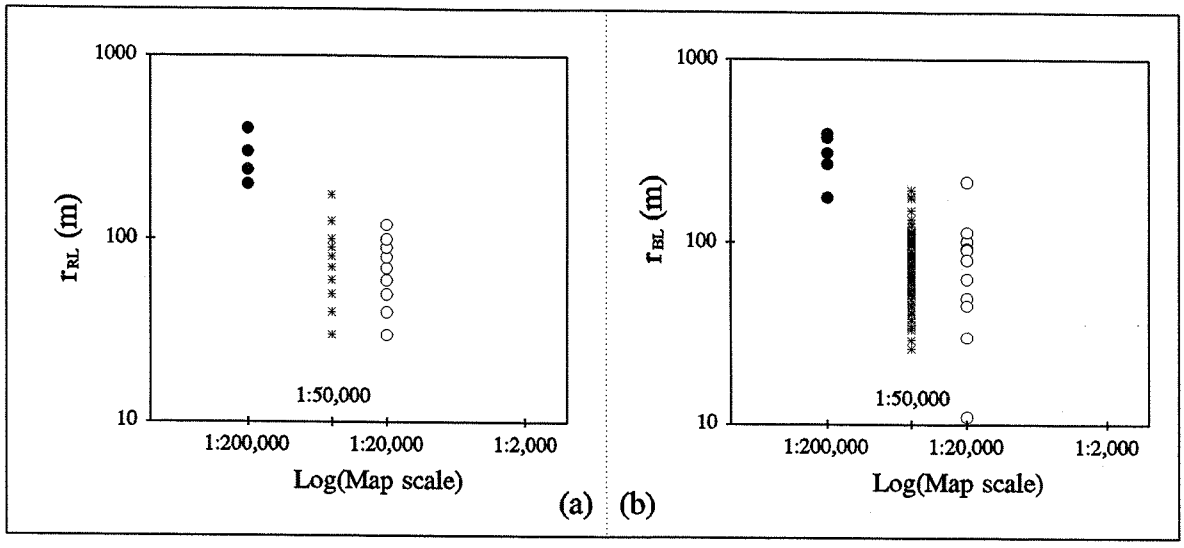

Fig. 3.6. Log-Log plot of the lower fractal limit against the map scale. **(a)** The lower fractal limits are derived from the ruler method. **(b)** The lower fractal limits are derived from using the box-counting method. These plots both indicate that the lower fractal limit depends on the map scale.

3.6. COMPARISON OF THE UPPER FRACTAL LIMITS AND THE CONTOUR LENGTHS

The lower fractal limits of contours are controlled by the map scales and map quality, but what controls the upper fractal limits? The plots of upper fractal limits (r_{RU}, r_{BU}) derived from the ruler and box-counting methods against lengths of contours (L_C) are shown in Fig. 3.7. To clarify the correlation between the upper fractal limits and the lengths of contours, the small portions marked by solid rectangles in Fig. 3.7(a) and (b) which contain the bulk of the data are magnified in Fig. 3.7(c) and (d).

Fig. 3.7 indicates that the upper fractal limit is positively correlated with lengths of contours which are defined in Section 3.2.3 for both the ruler ($R^2 = 0.58$) and box-counting ($R^2 = 0.57$) methods. Since more widely separated fractal limits will allow more accurate determination of fractal dimensions, this result indicates that longer contours provide more accurate fractal dimension.

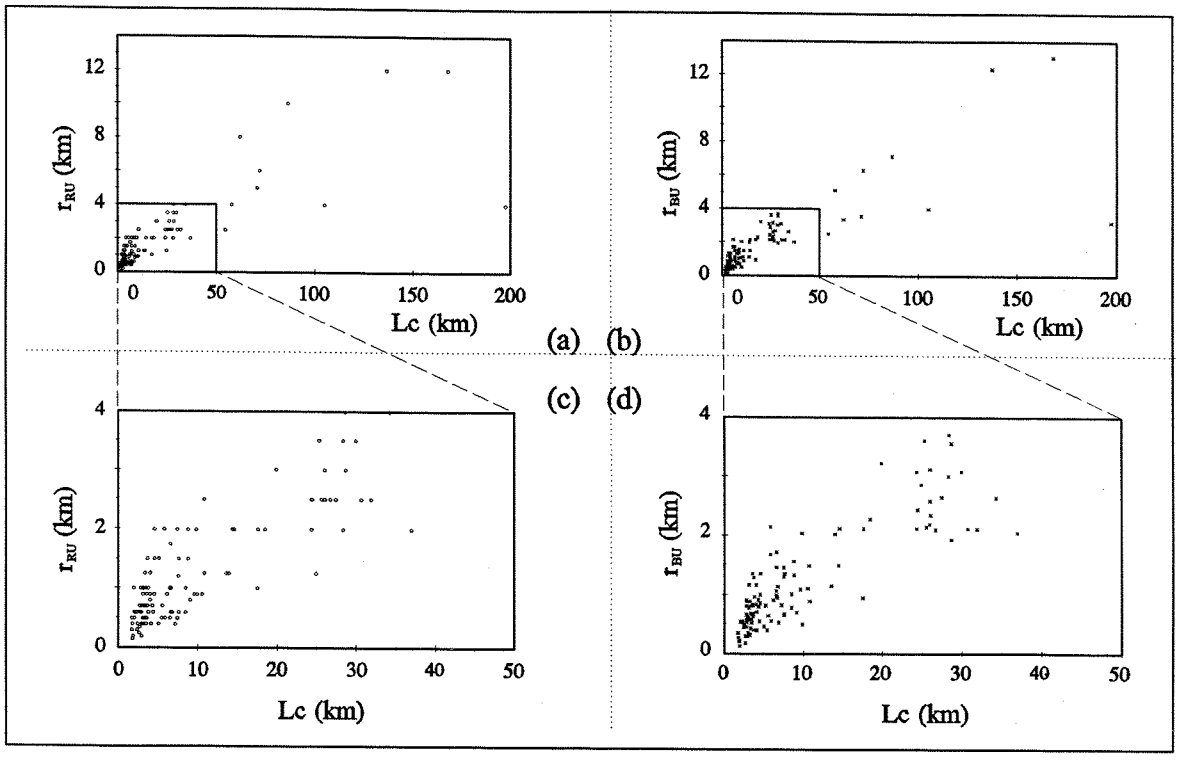

Fig. 3.7. Relationship between the upper fractal limits derived from the ruler and box-counting methods and the contour lengths. **(a)** Upper fractal limits from the ruler method (r_{RU}) against contour length (L_C). As contour length increases, (r_{RU}) increases. They are positively correlated. **(b)** Upper fractal limits of the box-counting method (r_{BU}) against contour length (L_C). The increasing linear trend with increasing contour lengths shows their positive correlation. **(c)** and **(d)** are respectively expanded diagrams of those two small portions delineated on (a), and (b).

3.7. COMPARISON OF CONTOURS OF DIFFERENT ELEVATION

To investigate the relationship and variation between contours of different elevation in terms of fractal dimension, the fractal dimensions of 123 contours digitized from 1:50,000 and 1:20,000 maps are plotted against the contour elevations (CE) as shown in Fig. 3.8. Refer to Appendix 2 for more details. As listed in Table 3.1, there are 75 contours from metamorphic rocks areas, whereas 48 contours from granites areas for all the 123 topographic contours (except 9 shore lines).

Fig. 3.8(a) and (b) are linear plots of fractal dimensions derived from the ruler (D_r) and box-counting (D_{1b}) methods against the CE for the topographic contours of metamorphic rock areas, and Fig. 3.8(c) and (d) are linear plots of D_r and D_{1b} of the granite contours against CE.

The fractal dimensions of these contours derived from the ruler (D_r) and box-counting (D_{1b}) methods are averaged based on different CE as shown in Table 3.7, and Fig. 3.8(e) and (f) are the error bars plots of D_r and D_{1b}) at a confidence level 95%.

Table 3.7. The list of the average contour level, D_r, and D_{1b} of 132 contours

CE	N	Dr	std	D1b	std	CE	N	Dr	std	D1b	std
280	2	1.11	/	1.19	/	440	6	1.22	0.08	1.22	0.08
290	1	1.21	/	1.37	/	460	8	1.24	0.07	1.26	0.06
300	6	1.25	0.07	1.27	0.07	480	8	1.20	0.07	1.20	0.12
320	13	1.21	0.08	1.21	0.09	500	7	1.12	0.06	1.11	0.07
340	16	1.24	0.09	1.20	0.10	520	3	1.23	0.04	1.23	0.03
350	1	1.24	/	1.23	/	540	2	1.19	/	1.15	/
360	11	1.25	0.06	1.22	0.08	560	2	1.19	/	1.08	/
370	1	1.3	/	1.29	/	580	1	1.2	/	1.11	/
380	13	1.26	0.04	1.24	0.06						
400	13	1.23	0.05	1.25	0.05	total N = 123		avg D_r = 1.22		avg D_{1b} = 1.21	
420	9	1.21	0.06	1.19	0.07			std = 0.05		std = 0.07	

N: Number of contours being averaged; **CE:** Contour Elevation (m);
Total number of contours: 123; **D_r:** Fractal dimension derived from the ruler method;
D_{1b}: Fractal dimension derived from the box-counting method.

For metamorphic and granite rock unit, the fractal dimensions (D_r and D_{1b}) of contours of the same elevation are averaged and listed in Table 3.8 in order to eliminate the effects caused by different rock units.

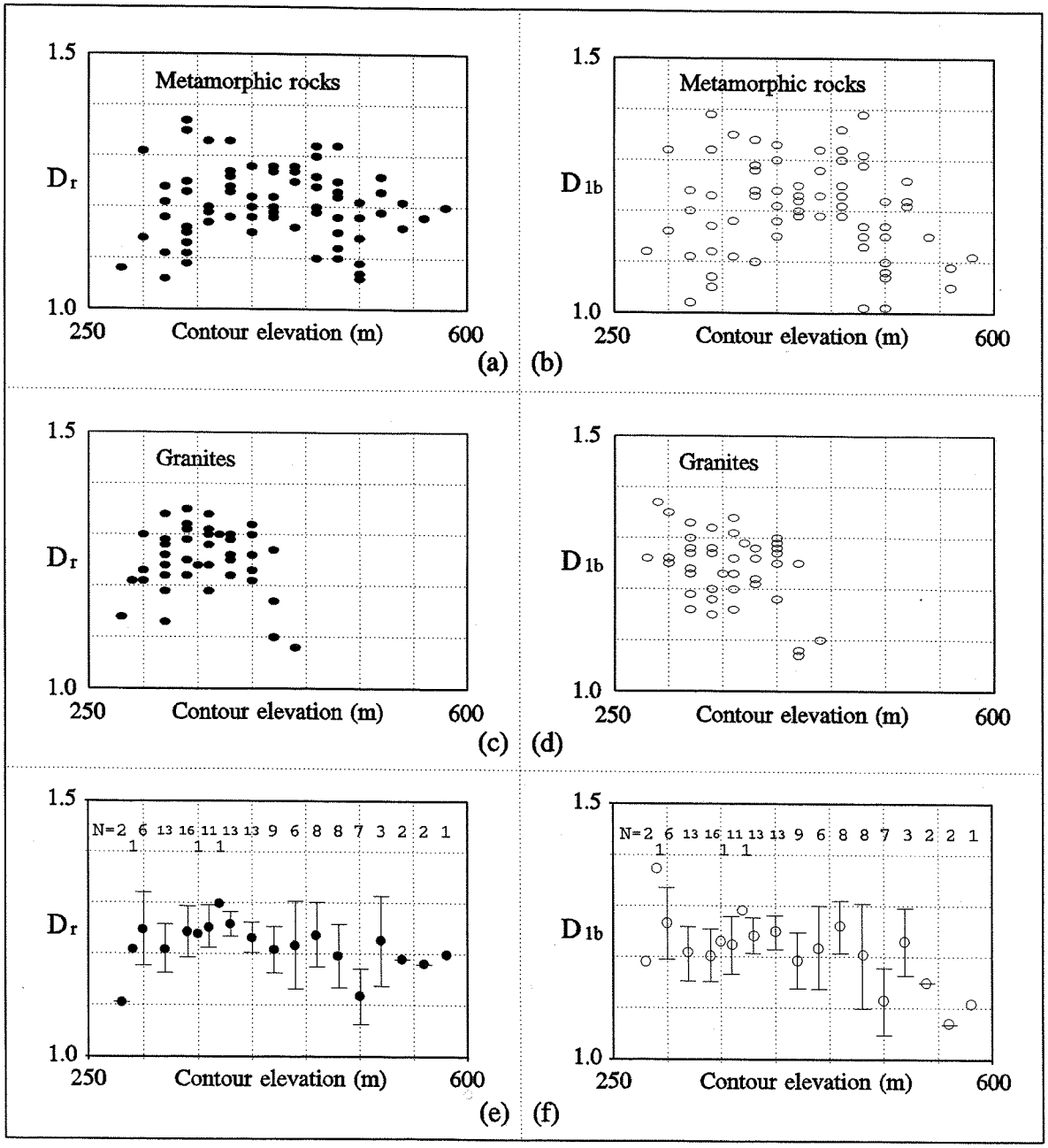

Fig. 3.8. Comparison of contours of different elevation in terms of fractal dimensions D. Linear scatter diagram of fractal dimensions derived from the ruler (D_r) and box-counting (D_{1b}) methods against the contour elevation (CE). N denotes the number of contours at a certain elevation. **(a)** and **(b)** are the linear plots of D_r and D_{1b} of 75 metamorphic contours derived from the ruler and box-counting methods against the contour elevation (CE). **(c)** and **(d)** are the linear plots of D_r and D_{1b} of 48 granite contours against the contour elevation (CE). **(e)** and **(f)** are the error bars plots of D_r and D_{1b} of all 123 topographic contours at a confidence level of 95%.

As shown in Fig. 3.8(a), (b), (c), and (d), there is a gentle discernible trend in each plot with the fractal dimensions of topographic contours tending to decrease as the contour

elevations increase. The trend is not statistically significant since this vague trend is caused by the small numbers of contours encountered among higher contour elevations. For example, at CE = 420 m (Fig. 3.8c), D_r varies from 1.10 to 1.27 and yields a standard deviation of 0.09. Suppose that the plot points of small numbers of contours (say N = 1, 2 and 3) are removed from the plot, it would be much clear that both the D values derived from the ruler and box-counting methods are independent of contours elevations. This can be confirmed by the error bars shown in Fig. 3.8(e) and (f).

Table 3.8. Average D values (D_r, & D_{1b}) of different contour elevations

Metamorphic rocks						**Granites**					
CE	N	Dr(M)	std	D1b(M)	std	CE	N	Dr(G)	std	D1b(G)	std
280	1	1.08	/	1.12	/	280	1	1.14	/	1.26	/
300	2	1.23	/	1.24	/	290	1	1.21	/	1.37	/
320	5	1.16	0.07	1.14	0.09	300	4	1.26	0.05	1.28	0.05
340	9	1.20	0.10	1.19	0.11	320	8	1.24	0.06	1.25	0.06
360	4	1.22	0.07	1.19	0.11	340	7	1.29	0.05	1.22	0.07
380	6	1.25	0.05	1.25	0.08	350	1	1.24	/	1.23	/
400	6	1.20	0.04	1.24	0.07	360	7	1.27	0.05	1.24	0.06
420	6	1.22	0.04	1.22	0.03	370	1	1.3		1.29	
440	5	1.25	0.05	1.24	0.06	380	7	1.27	0.03	1.24	0.03
460	8	1.24	0.07	1.26	0.06	400	7	1.26	0.04	1.26	0.04
480	8	1.20	0.07	1.20	0.12	420	3	1.18	0.09	1.13	0.10
500	7	1.12	0.06	1.11	0.07	440	1	1.08	/	1.10	/
520	3	1.23	0.04	1.23	0.03						
540	2	1.19	/	1.15	/						
560	2	1.18	/	1.07	/						
580	1	1.20	/	1.11	/						
	75	avg: 1.20		avg: 1.20			48	avg: 1.25		avg: 1.24	
		std: 0.07		std: 0.09				std: 0.06		std: 0.07	

CE: Contour elevation (m); **N:** Number of contours being averaged;
Total number of contours: 123; **D_r:** Fractal dimension derived from the ruler method;
D_{1b}: Fractal dimension derived from the box-counting method.

In summary, the fractal dimensions (D_r and D_{1b}) of topographic contours have no significant correlation with the contour elevations in statistical terms. After analysing the topographic contours from Sawtooth Mountains of Idaho, USA (the regions are underlain by granite plutons), Norton and Sorenson (1989) concluded that the contours have D values ranging from 1.11 to 1.26 as contour elevations vary from 7,400 to 9,800 feet. Turcotte (1989) also shown that four topographic contours of different contour elevations (1,000;

3,000; 5,400; and 10,000) from several mountain belts (the Cobblestone Mountain Transverse ranges, California) have fractal dimensions D = 1.19, 1.21, 1.21, and 1.15. Therefore, the previous studies also confirmed that the variation of D values is independent upon the contour elevations

3.8. LITHOLOGICAL COMPARISON

In order to find out more details of the influences of different rock groups on the fractal dimension, the 123 contours are categorized into two major rock groups - Igneous (48 contours) and Metamorphic (75 contours), and further seven minor lithological units as mapped on the ITGE geological maps of the border area of Spain and Portugal as shown in Table 3.9.

Table 3.9. Comparison of D-value and rock types

Rock group	Files	Lithological units	D_r	D_{1b}	N of contours
Granites	G-M2	Muscovite granite	1.24	1.17	3
	G22B	Mica granite	1.26	1.23	17
	GP	Porphyritic mica granite	1.25	1.25	28
Metamorphic rocks	K1	Schist, Slate	1.21	1.19	18
	K2	Quartzite, schist, Phyllite, hornfels	1.18	1.17	16
	PC2	Biotite schist, Phyllite (Pre. C.)	1.23	1.22	15
	D1 & D2	Quartzite, Phyllite	1.19	1.21	26

Table 3.10 shows the results of the t-test at 95% confidence level. It indicates that D_r (or D_{1b}) values of contours from granite area are significantly different from those of contours from the metamorphic country rock area at $\alpha = 0.05$. The contours from within granite (and metamorphic) groups share the same D-value at $\alpha = 0.05$ although the rock type may vary. The exception of the G-M2.D_{1b} vs G22B.D_{1b} pair may be caused by the

Table 3.10. Results of t-test ($\alpha = 0.05$)

Sample 1 vs Sample 2	H_0: $\mu_1 = \mu_2$	Sample 1 vs Sample 2	H_0: $\mu_1 = \mu_2$
G-M2.D_r vs G22B.D_r	✓	G-M2.D_{1b} vs G22B.D_{1b}	×
G-M2.D_r vs GP.D_r	✓	G-M2.D_{1b} vs GP.D_{1b}	✓
G22B.D_r vs GP.D_r	✓	G22B.D_{1b} vs GP.D_{1b}	✓
K1.D_r vs K2.D_r	✓	K1.D_{1b} vs K2.D_{1b}	✓
K1.D_r vs PC2.D_r	✓	K1.D_{1b} vs PC2.D_{1b}	✓
K1.D_r vs D1D2.D_r	✓	K1.D_{1b} vs D1D2.D_{1b}	✓
K2.D_r vs PC2.D_r	✓	K2.D_{1b} vs PC2.D_{1b}	✓
K2.D_r vs D1D2.D_r	✓	K2.D_{1b} vs D1D2.D_{1b}	✓
PC2.D_r vs D1D2.D_r	✓	PC2.D_{1b} vs D1D2.D_{1b}	✓
Igneous (D_r) vs Meta. rocks (D_r)	×	Igneous (D_{1b}) vs Meta. rocks (D_{1b})	×

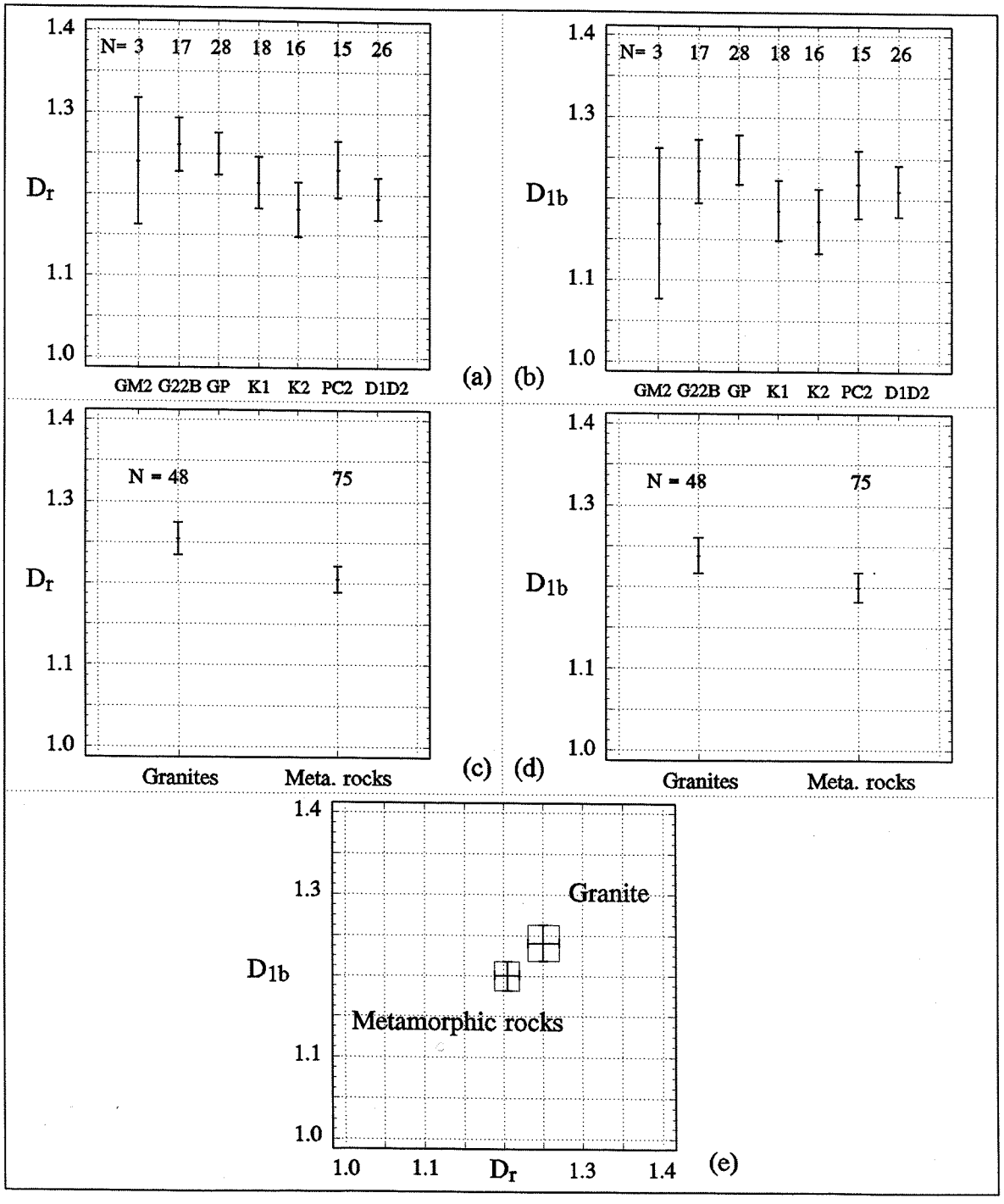

Fig. 3.9. The mean plots of D-value against different rock types for the analysis of variance at the confidence level of 95% ($\alpha = 0.05$). All the contours are from the 1:50,000 map, and categorized into six rock units and two major rock groups respectively. **(a)** and **(b)** plot the mean D_r and D_{1b} values derived from contours grouped on the basis of six rock types. **(c)** and **(d)** plot mean of D_r and D_{1b} values derived from contours categorized into two rock groups, granite and metamorphic country rocks. **(e)** is the sum of (c) and (d) This shows a distinctive difference between the two different rock groups in D_r and D_{1b}.

UNIVERSITY OF SOUTHAMPTON LIBRARY

small number of samples from G-M2.

Fig. 3.9 illustrates the error bar plots of the D-value (D_r and D_{1b}) for the two major different rock groups and seven rock units at a confidence level of 95% ($\alpha = 0.05$).

From Tables 3.8, 3.9 and Fig. 3.9, it can be seen that the fractal dimensions of the contours from the granite area are slightly higher than those from the metamorphic rock area, and it shows that the topographic contours from granite areas are more rugged than those from the metamorphic rock areas. This difference is small, but it is statistically significant. It is not caused by the methods employed, but by the difference of rock groups.

This difference is resulted from the different fracture joint control patterns, which inevitably leads to different weathering procedures, in granite and metamorphic rock areas. In granite areas, the larger scale fracture joints (1 m to 10 m) could form fracture zones of 100 m to 1 km scales and control drainage system of the areas. Thus, different weathering produces rugged topographic contours and rougher surfaces of the areas. However, the metamorphic rock in the study areas is dominated by fracture joints of < 1 m scale, and the rock mass (soil) weathering procedure contributes the formation of smoother topographic contours and surfaces, like the river meandery system. Norton and Sorenson (1989) also have shown that small D values derived from contours where accumulation of screen erosion has smoothed the surfaces, whereas larger D values derived from contours along aretes terrain.

In summary, the major rock groups have different D values, but the lithological changes within each major group can not be demonstrated to be significant. Topographic contours from granite areas are rougher than those from metamorphic rock areas due to different fracture control patterns and different weathering procedure, and this property is characterized by D (granite) > D (metamorphic rocks) in the studied areas.

3.9. CONCLUSIONS

The purpose of this Chapter was to examine how different data sources and fractal analysis methods influence the fractal dimensions of map contours. Based on the fractal analysis of the 132 topographic contours digitized from maps of the border areas between Spain and Portugal at different scales (1:200,000; 1:50,000; and 1:20,000) by the ruler and box-counting methods, the following conclusions can be reached.

1. The topographic contours are self-similar fractals in a statistical sense. In the study areas, the contours have an average fractal dimension of D = 1.23 (ranges from 1.01 to 1.47, standard deviation = 0.07 over 132 contours) over length scales ranging from 30 m to 13 km.
2. The lake shore lines and nearby topographic contours from the same scale of maps share roughly the same D-value over fractal limits ranging from about 100 m to 10 km.
3. D values derived from the ruler and the box-counting methods are the same at the 95% confidential level ($\alpha = 0.05$), i.e. $D_r \approx D_{1b}$ or $D_{1b} = D_r \pm 0.15$.
4. The D values are not significantly different when measured at different map scales.
5. The lower fractal limit is controlled by the map scale (or map resolution) as well as the map accuracy. The lower fractal limit of contours from small scales of maps is higher than those from large scales of maps, and indicates that they might be used to quantify the quality of surveyed map. In other words, the lower the lower fractal limit is, the more detail the maps preserves of the topographic variance, i.e., the more accurate the map is.
6. The upper fractal limit depends largely upon the length of the contour. This is because the longer contour, under the same conditions of map, digitizing, etc., shows fractal properties in a wider range than the shorter one.
7. The D-value does not significant correlate with the contour elevation over a range scale about from 300 m to 600 m.
8. The D values of topographic contours of granites are higher than those of nearby metamorphic country rocks. This difference is small, but is statistically significant. D for the granite is 1.25 ± 0.02, and D for the metamorphic rock is 1.20 ± 0.02. The difference is caused by the different fracture joint control patterns and different weathering procedures in granite (larger scale fracture joints, down cutting weathering) and metamorphic rock (smaller scale fracture joints, rock mass weathering) areas.

However, the contours of minor rock units in a major rock group cannot be demonstrated to have significant variance in fractal dimension.

An overall conclusion from this study is that a consistent, reproducible fractal dimension can be estimated from a contour of any elevations on any maps providing care is taken to define fractal limits. Better estimation of fractal dimension arise when analyzed contour lengths are large. Similar fractal dimensions are obtained from the ruler and box-counting methods. There is some evidence that contours from different rock types have different fractal dimensions, therefore the method may have some geological applications.

CHAPTER 4.

FRACTAL ANALYSIS OF COASTAL AND CLIFF PROFILES

CHAPTER 4

FRACTAL ANALYSIS OF COASTAL AND CLIFF PROFILES

4. FRACTAL ANALYSIS OF COASTAL AND CLIFF PROFILES

4.1. INTRODUCTION

Natural profiles can be obtained by intersecting a surface with a horizontal or vertical plane, they are irregular and contain a variety of shapes on a wide ranges of scales. They can be compared using the concepts of self-similar and self-affine fractals (refer to Chapter 1.4). As described in Chapter 3, there is little doubt that the horizontal profiles of topographic surfaces, topographic contours, are self-similar fractals, because in general the two coordinates characterized topographic contours are equivalent. The topographic contours have a fractal dimension D = 1.24 over fractal limits ranging from 30 m to 13 km (3 orders of magnitude). The D value is roughly the same as that of the coast of Britain D = 1.25 (Mandelbrot, 1967), and the same as the Earth's topography (Mandelbrot, 1975; 1983). In the natural world, vertical profiles also possess characteristics which appear to be independent of length scales of observation.

There are a number of studies of applying the fractal concept to profiles, either to describe the earth's topography (Goodchild, 1980; Shelberg, 1983; Mark and Aronson, 1984; Fox and Hayes, 1985; Goff *et. al.*, 1988; Brown, 1985; 1987; Roy *et. al.*, 1987; Turcotte, 1987; Dubuc *et. al.*, 1989a, b; Gilbert, 1989) or to study the mechanism of crack or fracture propagation (such as Nolte *et. al.*, 1989; Pickering and Sanderson, 1994; Xie, 1993; Xie and Sanderson, 1994,1995).

To investigate the fractal behaviour of topography of southern England, thirteen cliff profiles were analyzed by three methods (the ruler, the 1-d spectral, and the 1-d structure function), and their fractal features were determined. These methods have been discussed in Chapter 2, and each method provides two parameters; one is the fractal dimension D which describes how the roughness changes with the scale of observation, and the other is the intercept C which describes the steepness of the topography, or the total profile variance (Power and Tullis, 1991). The average roughness measurement which is characterized by the root mean square roughness (RMS or R_q) and the centre-line average roughness (CLA or R_a) [Myers, 1962; Thomas, 1982] are also determined from these profiles.

The aims of the Chapter are

- to examine the scaling properties of horizontal cliff profiles from the scales of kilometres (digitized map profiles) down to centimetres (field measured profiles);
- to compare the analytical results between the ruler and the 1-d spectral (and 1-d structure function) methods;
- to discuss the characteristics and scaling properties of rock surfaces produced by the different erosion processes;
- to discuss the spectral distribution patterns as the 1-d spectral and structure function methods applied to the coastal and cliff profiles; and
- to compare the different fractal behaviours of lithology, using the profiles of dolostone and shale units at the same locality.

4.2. DATA SOURCES

Two types of data sources, map and field profiles of cliffs, from Dorset area (the southern coast of England) were acquired for the fractal description of profiles. The study area covers Kimmeridge Bay and Studland Bay and its location is shown in Fig. 4.1. These areas were chosen because they represent parts of the coastal lines which are bounded by cliffs with fairy restricted rock units and little incision by river networks.

There are three map profiles which were digitized from 1:10,000 maps, and ten field profiles which were measured at intervals of 1 m, 0.5 m, 0.1 m and 0.01 m in the field of Kimmeridge Bay and Studland Bay. The digitizing steps used for the map profiles and the measuring intervals used in the field are termed the sample interval (s) in the later discussion. Different sample intervals deployed for these profiles are needed in order to investigate the variations of the fractal features, including the fractal dimension and the fractal limits, with changing the measuring scales.

Table 4.1. Statistical criteria of map and field profiles

	location	profile	L_n (m)	L_0 (m)	s (m)	avg	std	max	min	lithology
Field	Kimmeridge	kmgl	155.1	169.8	0.50 (0.48*)	28.77	0.981	54.72	1.21	clay, shale
	Bay	kmgm	11.5	14.3	0.10 (0.10)	1.40	0.078	3.22	0.00	clay, shale
		kmgs	2.0	2.9	0.01	0.13	0.008	0.40	0.00	clay, shale
		ksh1	10.0	10.8	0.10	0.71	0.025	1.20	0.22	Clay, shale
		ksh2	11.8	14.4	0.10	0.75	0.026	1.32	0.04	Clay, shale
		kdo1	10.0	12.0	0.10	0.58	0.027	1.24	0.13	Dolostone
		kdo2	11.8	15.1	0.10	0.63	0.029	1.24	0.04	Dolostone
	Studland	stdl	155.6	165.4	1.00 (0.97)	19.02	0.959	46.30	1.25	chalk
	Bay	stdm	11.2	11.7	0.10 (0.10)	-0.33	0.010	0.01	-0.56	chalk
		stds	1.0	1.1	0.01	0.04	0.002	0.07	0.00	chalk
	Studland	mlw	2130	3315	2.74	3886	12.69	4892	3545	??
	Kiimmeridge	mhw	2755	4288	3.59	5091	15.57	5716	4165	??
Map	Studland	c001	1078	1187	5.47	3082	2.34	3138	3021	??

0.50 (0.48) m: A profile was measured at 0.5 m intervals in the field for every trend, the value in the brackets 0.48 m is the overall sample interval after the coordinates transformation procedure as discussed later.

In order to quantify the outlines of these cliff profiles, Table 4.1 shows some of the statistical criteria, such as the curve length (L_0), nominal length (L_n), sampling intervals (s), maximum (max) and minimum (min) variations of profiles etc. Suppose a profile is

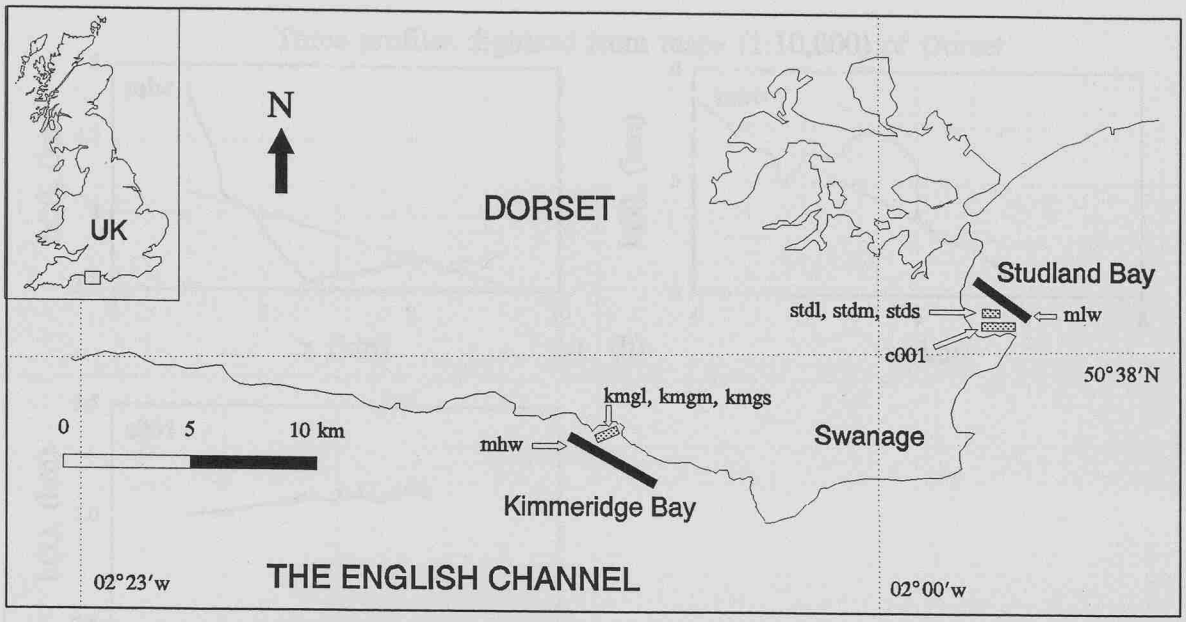

Fig. 4.1. Location of the study area of south coast of England, where the field and map profiles were obtained.

recorded as a series of N numbers of paired coordinates $[x_i, y_i]$, where i =1, 2, …, N, then the nominal length (L_n) and the curve length (L_0) of a profile are defined as,

$$L_n = x_N - x_1$$

$$L_0 = \sum_{i=1}^{N-1} \sqrt{(x_{i+1} - x_i)^2 + (y_{i+1} - y_i)^2}$$

4.2.1. Map profiles

Two coast lines and one topographic contour along the cliff from the 1:10,000 maps of Kimmeridge Bay and Studland Bay were digitized. The digitizing procedure is the same as that described in Chapter 2.2. These digitized profiles are mean low water (mlw), mean high water (mhw) shore lines, and a contour (c001) profile of an elevation of 25 m. These map profiles were chosen in such a way that they possess no overhangs along their trends, therefore, they can be regarded as sub-horizontal profiles (special contours). Fig. 4.2 shows these three digitized map profiles.

4.2.2. Field profiles

Ten sub-horizontal profiles of cliffs at Studland Bay and Kimmeridge Bay were

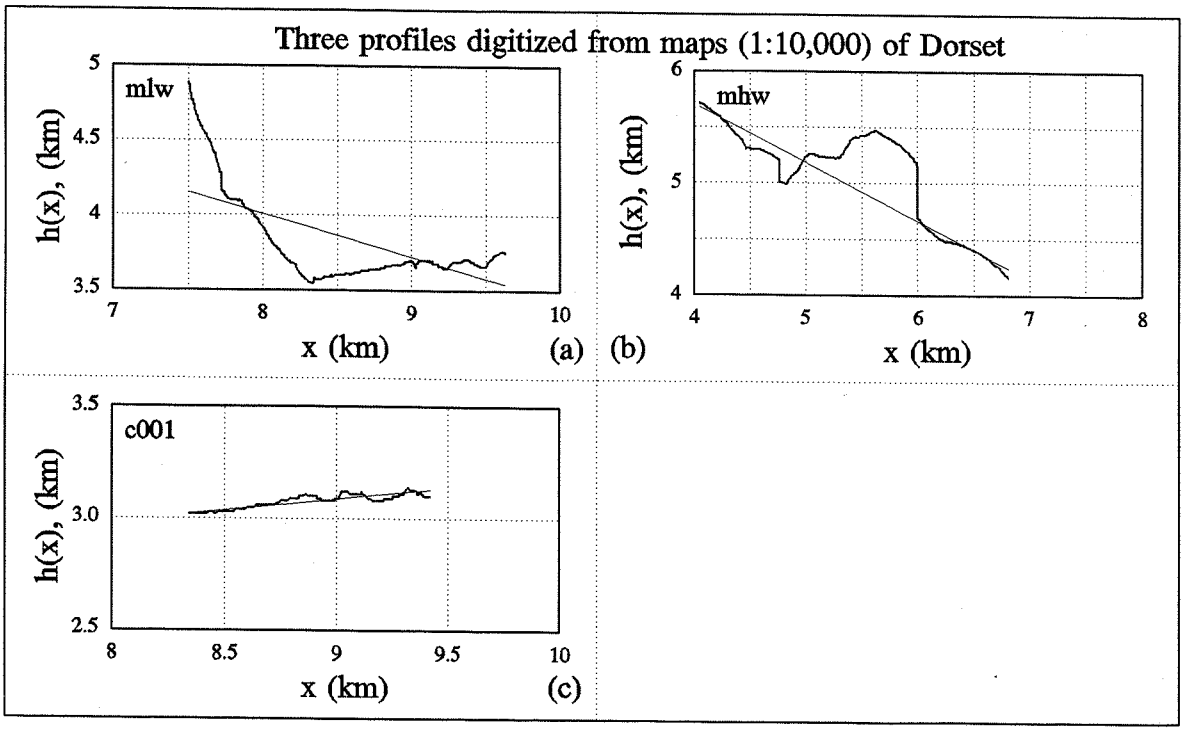

Fig. 4.2. Three map profiles digitized from 1:10,000 maps of Dorset (south coast of England). Refer to Fig. 4.1 for their precise locations. File names of mlw and mhw stand for the mean low and mean high water shore lines; and c001 the topographic contour of an elevation of 25 m along the cliff. The trend of the curve is marked by the solid line crossing over the curve.

acquired by measuring the cliff variations (y = g(x)) from the general trend (x) of the cliff at different sample intervals as shown in Table 4.1. Three of the profiles are from the Studland Bay, and recorded as stdl, stdm, and stds. Seven of them are from the Kimmeridge Bay, and first three letters of the profile names were recorded as **kmg**. Among these seven profiles, two pairs were measured at an intervals of 0.1 m in both dolostone and shale. For each pair, the Kimmeridge dolostone layer lies on top of the shale layer, and has the same nominal length (L_n), i.e., kdo1 and kdo2 lie on the top of ksh1 and ksh2 respectively. This allows comparison of fractal features with changing the lithological units at the same locality observational scale.

The principle of the measurement procedure made in the field is illustrated in Fig. 4.3. A stretched tape of a length 30 m was laid on ground as the base line for reference. Suppose the selected curve line as shown in Fig. 4.3(a) was longer than the stretched tape (30 m), then the curve needs to be measured by using two baselines (***AB*** and ***BC***) to record the cliff variations. The measurement made on the baseline ***BC*** is the repetition of that

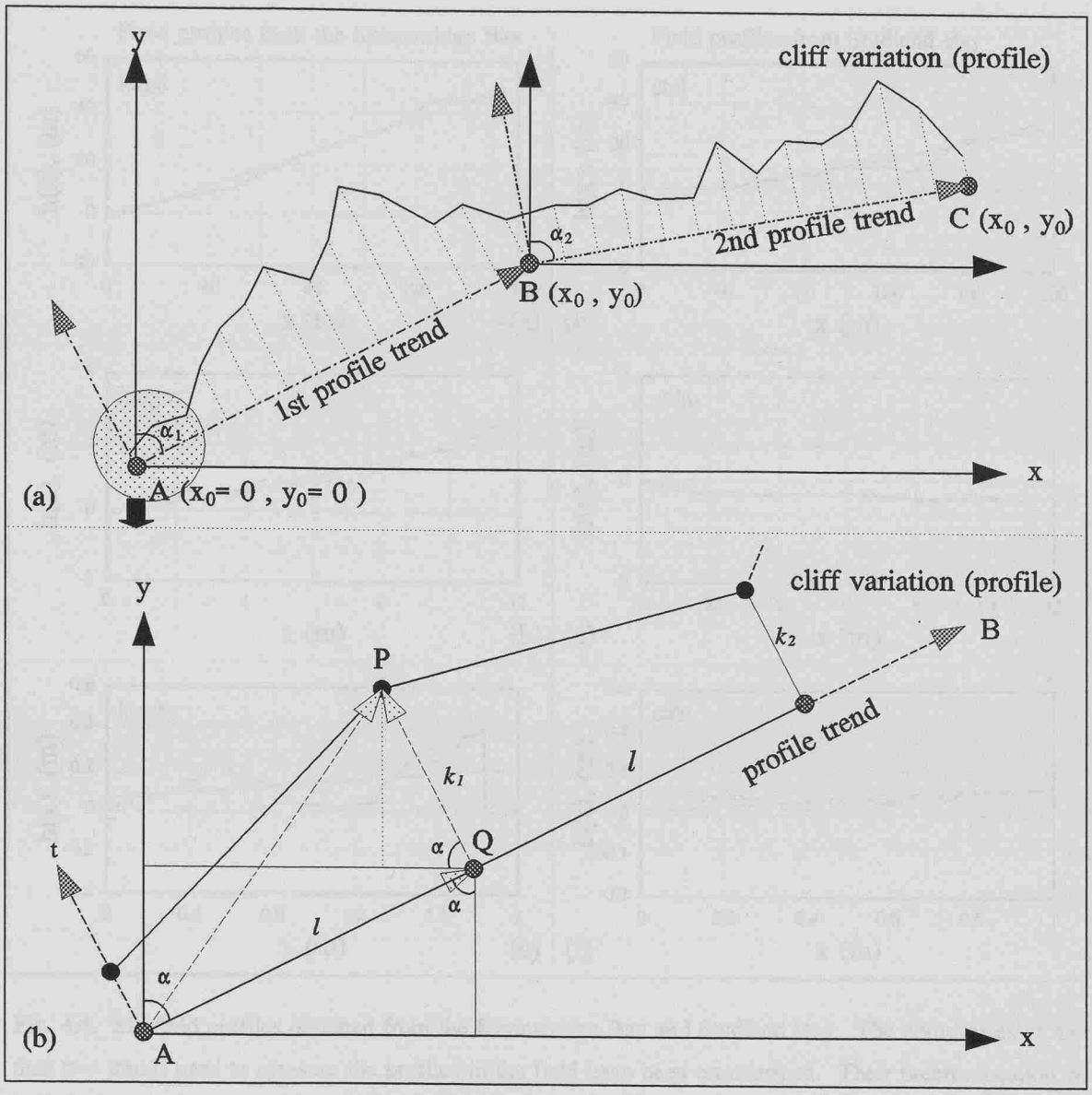

Fig. 4.3. Illustrations of the procedure for measuring a profile in the field. The figure also shows principles of the coordinates transformation (refer to the text for more details). **(a)** shows a measured cliff profile is longer than 30 m. **(b)** illustrates the principles of the measurement made in the field and the principles of the coordinate transformation.

made on the baseline ***AB***, thus the circled part of the bottom-left of Fig. 4.3(a) is magnified to demonstrate the principles of the measurement made on the base line ***AB*** as shown in Fig. 4.3(b). Firstly, the stretched tape (30 m long) was laid on the ground as a reference line (***AB***), which parallels to the general trend of the cliff portion, and the orientation of the baseline α was recorded. Then the orthogonal distances (***k***) between the stretched tape and

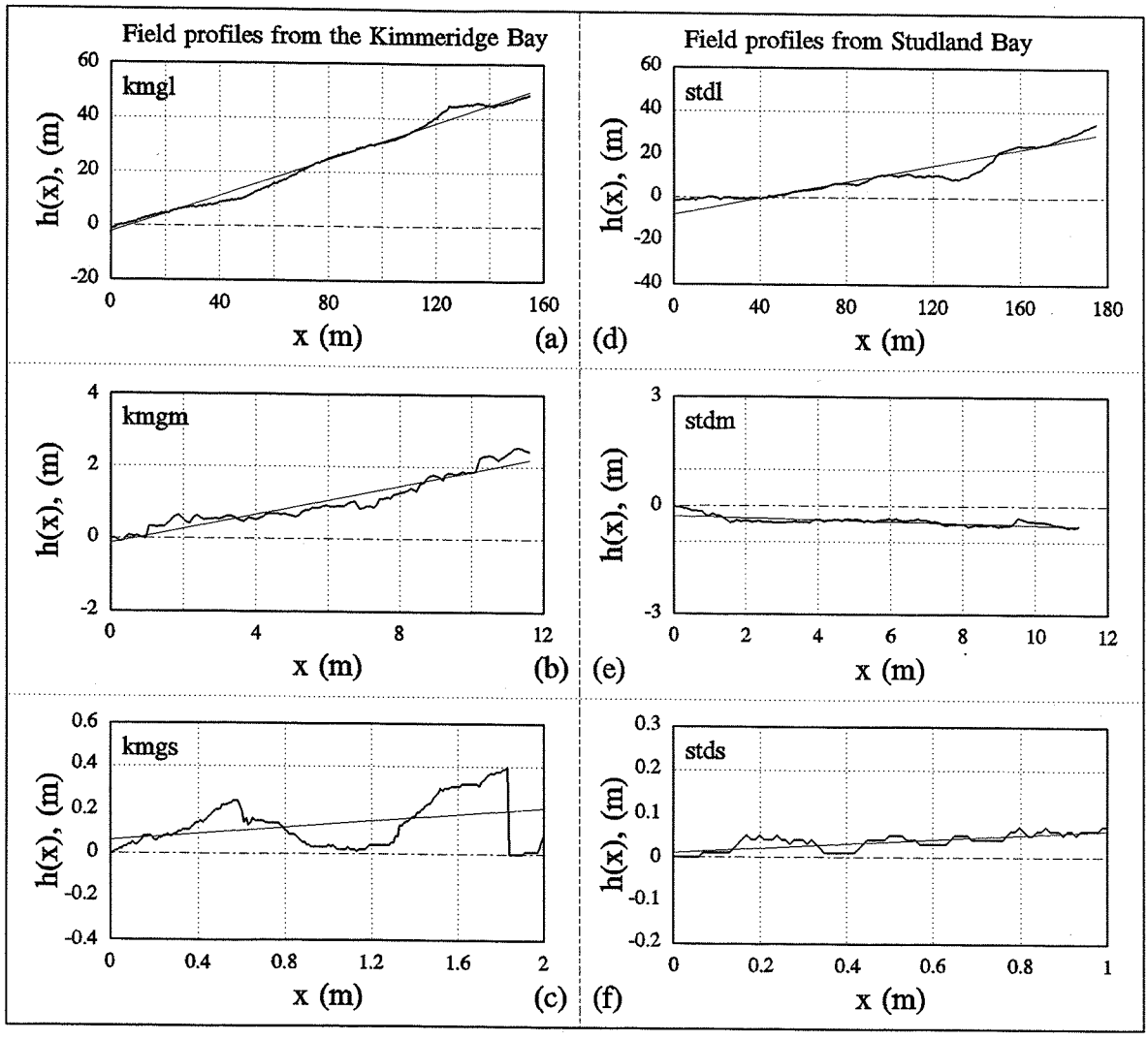

Fig. 4.4. Six field profiles obtained from the Kimmeridge Bay and Studland Bay. The coordinates of more than two trends used to measure the profiles in the field have been transformed. Their precise location was shown in Fig. 4.1, and their statistical criteria were listed in Table 4.1. The trend of the curve is marked by the solid line crossing over the curve. **(a)**, **(b)**, and **(c)** are three field profiles measured at intervals of 0.5 m, 0.1 m, and 0.01 m in Kimmeridge bay. **(d)**, **(e)**, and **(f)** are three field profiles measured at intervals of 1.0 m, 0.1 m, and 0.01 m in Studland bay.

the cliff were measured for a given sampling interval (l). Thus, the cliff variations were recorded as a series of records $(i \times l, k_i)$ made along the base line AB, where i = 1, 2, …, n. The same measurement procedure could be carried out in the same way for the second base line BC, and so on, until a satisfactory observation scale of the cliff was reached.

If a cliff length is shorter than the length of a single baseline (i.e., < 30 m), then the series of recorded data $(i \times l, k_i)$ could be directly used to present the variation of the cliff,

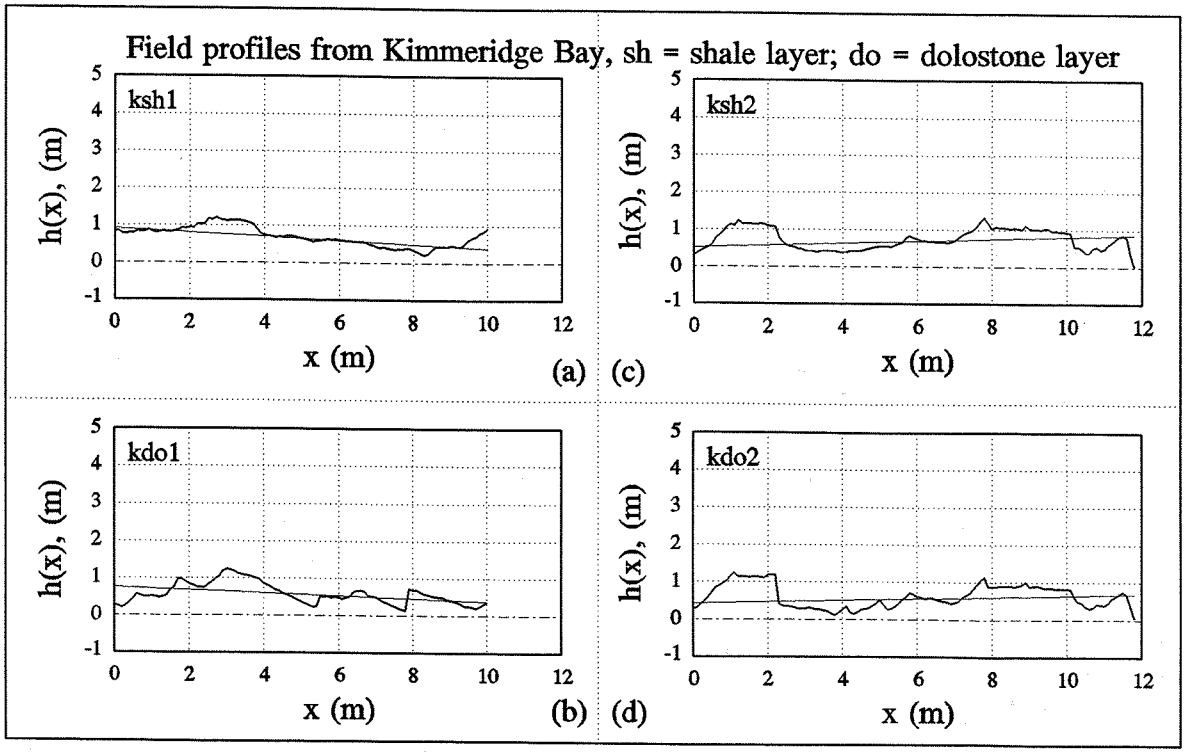

Fig. 4.5. Four field profiles of different lithology measured in Kimmeridge Bay. The trend of the curve is marked by the solid line crossing over the curve. **(a)** and **(c)** were measured field profiles of shale (ksh1 and ksh2), and **(b)** and **(d)** were measured field profiles of dolostone (kdo1, and kdo2) at a measuring interval of 0.1 m. The shapes of dolostone profiles are more irregular than the shale profiles. This is because they possess different weathering procedures, i.e., the dolostone profiles are the results of fracture controlled weathering, whereas the shale profiles are more related with the wave weathering procedure.

and renamed as (x, y). However, in order to obtain a longer profile (>30 m), the cliff curve was measured using two or more baselines (Fig. 4.3a). This also avoids the difficulties of measuring long distance between the tape and cliff. It is obvious that the data sets collected in this way would have different orientations for different baselines, and the data sets are required to be transformed to a common orientation (i.e., they should have a single coordinate system, say (x, y) in Fig. 4.3a. Supposed that the coordinates of the start point of each baseline are assigned to be (x_0, y_0), then (x_0, y_0) is assigned to be (0, 0) for the first baseline ***AB***. For the second and subsequent trends, the coordinates of the last point (x_{Tp}, y_{Tp}) of the previous baseline are added to new transformed position (Fig. 4.3a). This procedure is called the coordinate transform which can be, generally, given by,

$$x_i = x_{Tp} + il\sin(\alpha) - k_i\cos(\alpha)$$

$$y_i = y_{Tp} + il\cos(\alpha) + k_i\sin(\alpha)$$

where (x_i, y_i) is the transformed coordinates, $i \times l$ and k_i are the original measurements of the cliff variation, α is the orientation of the baseline.

The procedure of the coordinate transformation inevitably led a sample of the profile at unequally subdivided value of x. Therefore, the profiles were resampled at equal intervals to meet the theoretical backgrounds of some fractal analysis methods, such as the spectral method (see Section 4.3.2).

Various intervals of l = 1 m, 0.5 m, 0.1 m, and 0.01 m were deployed for the measurements carried out in the areas of Studland Bay and Kimmeridge Bay. Fig. 4.4 shows six of the field profiles obtained from the Kimmeridge Bay and Studland Bay, the coordinates of the profiles measured by two or more trends were transformed. In Fig. 4.4 the profiles at Kimmeridge Bay (kmgl, kmgm, and kmgs) were measured at intervals of 0.5 m, 0.1 m, and 0.01 m respectively, whereas the field profiles at Studland Bay (stdl, stdm, and stds) were measured at intervals of 1.0 m, 0.1 m, and 0.01 m, respectively.

Fig. 4.5 shows two pairs of field profiles, which were measured by a single baseline, of different lithology (shale and dolostone) measured in Kimmeridge Bay at a measuring interval of 0.1 m. One pair of profiles are ksh1 and kdo1, which have the same nominal length of 10 m. The other pair is ksh2 and kdo2 which have a nominal length of 11.80 m. The shapes of the dolostone profiles are more irregular than the shale profiles (see Section 4.6).

4.3. METHODOLOGY

The ruler, 1-d spectral, 1-d structure function, and the average measurement for the roughness of profiles, were used for the description and comparison of the scaling behaviours of the profiles mentioned in Section 4.2. The principles of the first three methods have already been discussed in Chapter 2, and only a brief outline is given here, whereas the average measures of roughness of profiles [the root mean square (RMS or R_q) and the centre-line average deviation (CLA or R_a)] are more fully discussed in this section.

4.3.1. The ruler method

The ruler method, as described in Chapter 1.3, reveals the power-law relationship between either the number of rulers (N_r) or the length of the curve (L_r) as a ruler length r is used measure the curve. The variation of N_r (or L_r) with r is characterized by the fractal dimension D_r;

$$N_r = C r^{-D_{1b}}$$

$$L_r = C r^{1-D_{1b}} \tag{4.1}$$

where C is the intercept which is a constant of proportionality. It has been commonly accepted that the higher the D-value, the rougher the curve is.

Fig. 4.6 shows the log-log plots of the profile length L_r against ruler length r as the ruler method was applied on the 13 profiles. The determination of the fractal dimensions of the profiles depends very much on the fractal limits chosen. Therefore, some care needs to be taken during fitting the regression line. The upper fractal limit (r_{rU}) was chosen to be half of the nominal length of the profile i.e., $r_{rU} = L_n/2$. The lower fractal limit (r_{rL}) was taken as twice the sampling interval, i.e., $r_{rL} = 2s$. The sampling interval, s was the average sampling interval value of a profile. Table 4.2 summarizes the results for the ruler method applied to the 13 cliff profiles. The estimate errors in the fractal dimension D and the intercept C were derived based on equation 2.1 as described in Chapter 2.2. Here, $\Delta D_r = \Delta\beta$ and $\Delta C_r = \Delta C$.

From Table 4.2, as well as Fig. 4.6, the fractal dimensions derived by the ruler

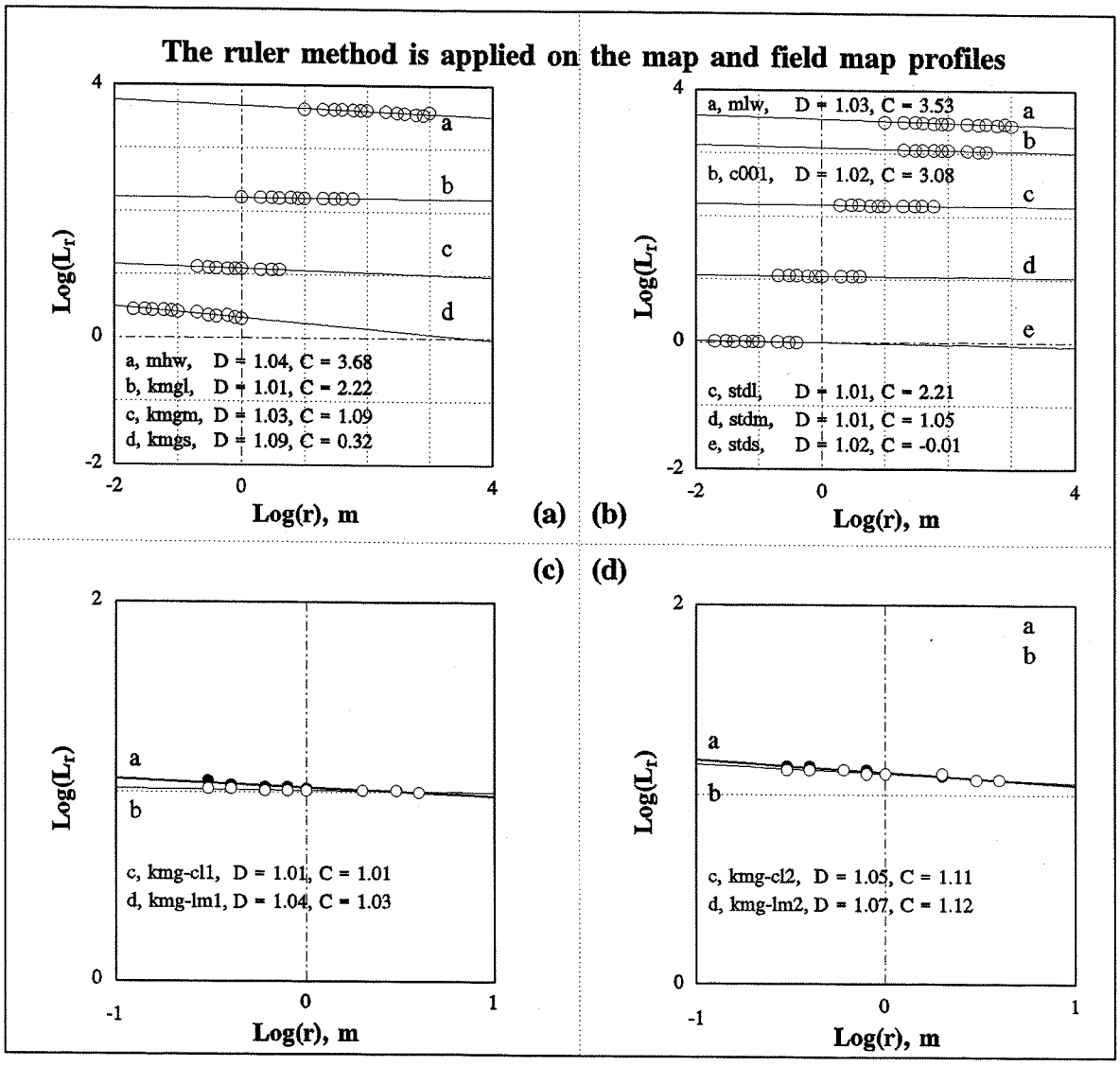

Fig. 4.6. Log-log plots of the ruler method applied on the 13 cliff profiles from the Kimmeridge and Studland Bays, where L_r is the length of the profile as it was measured by a ruler r. Therefore $D_r = 1 + \beta$, where β is the slope of the regression line. They are plots **(a)** of one map mean high water shore line (mhw) and three field profiles (kmgl, kmgm, kmgs) sampled at 0.5 m, 0.1 m, and 0.01 m from Kimmeridge Bay; **(b)** of two map profiles (mlw and c001) and three field profiles (stdl, stdm, stds) sampled at 1.0 m, 0.1 m, and 0.01 m from Studland Bay; **(c)** & **(d)** of two paired profiles of different lithology from Kimmeridge Bay (ksh1 vs kdo1, ksh2 vs kdo2) at a sample interval of 0.10 m.

method range from 1.01 to 1.09 (the average $D_r = 1.03$, and the standard deviation = 0.02), and are independent of the length (L_0) or the nominal length (L_n) of the profile, whereas the intercept C_r is dependent on L_0 or L_n (the longer L_0 or L_n is, the greater C_r is). The right-most column of Table 4.2 shows the values of 10^{Cr}, which lie between the nominal length L_n and the curve length L_0.

Table 4.2. The fractal features of the cliff profiles derived from the ruler method.

	Profiles	L_n (m)	L_0 (m)	s (m)	$D_r \pm \Delta D_r$	$C_r \pm \Delta C_r$	10^{Cr}
Field	kmgl	155.1	169.8	0.48	1.01 ± 0.01	2.22 ± 0.01	166.0
	kmgm	11.5	14.3	0.10	1.03 ± 0.01	1.09 ± 0.01	12.3
	kmgs	2.0	2.9	0.01	1.09 ± 0.02	0.32 ± 0.02	2.1
	ksh1	10.0	10.8	0.10	1.01 ± 0.01	1.01 ± 0.01	10.2
	ksh2	11.8	14.4	0.10	1.05 ± 0.02	1.11 ± 0.01	12.9
	kdo1	10.0	12.0	0.10	1.04 ± 0.02	1.03 ± 0.01	10.7
	kdo2	11.8	15.1	0.10	1.07 ± 0.02	1.12 ± 0.01	13.2
	stdl	155.6	165.4	0.97	1.01 ± 0.01	2.21 ± 0.01	162.2
	stdm	11.2	11.7	0.10	1.01 ± 0.01	1.05 ± 0.01	11.2
	stds	1.0	1.1	0.01	1.02 ± 0.01	-0.01 ± 0.01	1.0
Map	mlw	2130	3315	2.74	1.03 ± 0.01	3.53 ± 0.02	3388
	mhw	2755	4288	3.59	1.04 ± 0.02	3.68 ± 0.02	4786
	c001	1078	1187	5.47	1.02 ± 0.01	3.08 ± 0.01	1202
	Total				1.03 ± 0.02		

L_n: Nominal length of a profile (m); L_0: profile length (m); **1.03 ± 0.02**: stands for the average value and its standard deviation; **s**: Sampling intervals; D_r & C_r: Fractal dimension and intercept derived from the ruler method.

4.3.2. 1-d spectral method

As mentioned in Section 4.2.1, three map cliff profiles have been carefully selected, and they have no overhangs. To satisfy the underlying theory of the 1-d fast Fourier transform (FFT), the unequal-interval profile was resampled linearly at 2^{10} equal-intervals in the study. Thus the resampled profile has a sampling interval of $L_n / (2^{10} - 1)$, and $L_n = x_N - x_1$. Based on the results drawn in Chapter 2.5.4, a profile recorded as $[x_i, y_i = g(x_i)]$, where i = 1, 2, …, N, needs to be weighted by Hanning window which is given by,

$$W_h(i) = \frac{1}{2}\left\{1 - \cos\left[2\pi\left(\frac{i-1}{N-1}\right)\right]\right\}, \qquad i = 1,2,\ldots,N$$

Therefore, the Hanning window weighted profile becomes $[x_i, y_i\, W_h(i) = g(x_i)\, W_h(i)]$. As discussed in Chapter 2.4.1, the power spectral density $P(\lambda)$ of a profile has a power law

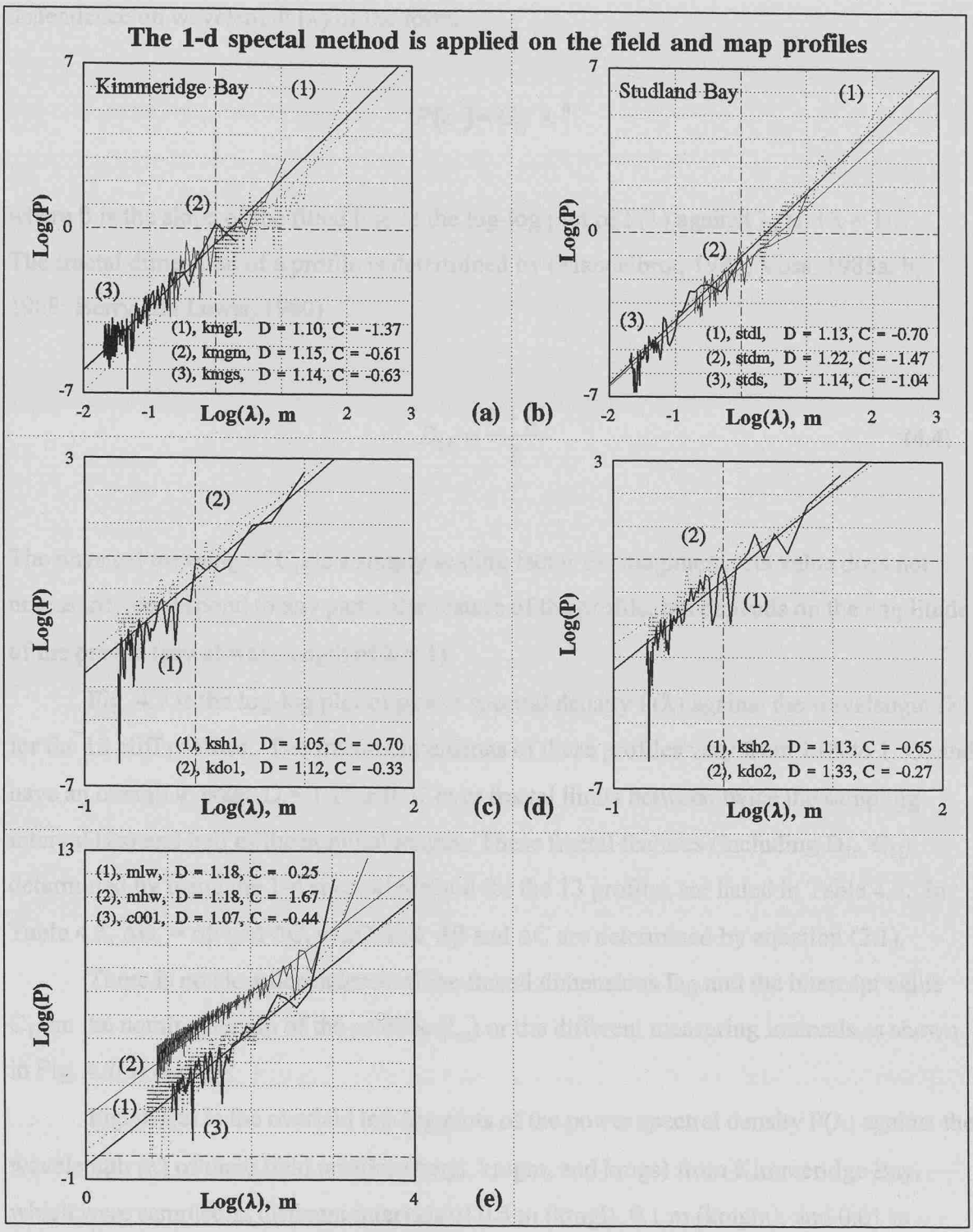

Fig. 4.7. Log-log plots of the 1-d spectral method applied on the 10 field and 3 map profiles. These are the power spectral density P(λ) against wavelength λ **(a)** of three field profiles from Kimmeridge Bay (kmgl, kmgm, and kmgs) sampled at 0.5 m, 0.1 m, and 0.01 m; **(b)** for three field profiles from Studland Bay (stdl, stdm, and stds) sampled at 1.0 m, 0.1 m, and 0.01 m); **(c)** and **(d)** for two paired field profiles of different lithology from Kimmeridge Bay (ksh1 vs kdo1 and ksh2 vs kdo2) at a sample interval of 0.10 m; **(e)** is of three map profiles digitized from 1:10,000 maps of southern coast of England.

dependence on wavelength (λ) of the form,

$$P(\lambda) = C_{1f}\ \lambda^{\beta}$$

where β is the slope of the fitted line of the log-log plot of $P(\lambda)$ against λ, and $\lambda = 1/f$. The fractal dimension of a profile is determined by (Mandelbrot, 1986; Voss, 1985a, b, 1988; Berry and Lewis, 1980),

$$D_{1f} = \frac{5-\beta}{2} \qquad \textbf{(4.4)}$$

The physical meaning of C_{1f} is a simply scaling factor for roughness. Its value does not necessarily correspond to any particular feature of the profile, but depends on the amplitude of the profile (say at wavelength of $\lambda = 1$).

Fig. 4.7 is the log-log plot of power spectral density $P(\lambda)$ against the wavelength (λ) for the 13 cliff profiles. The fractal dimensions of these profiles vary from 1.05 to 1.33, and have an overall average $D = 1.15 \pm 0.07$ over fractal limits between twice the sampling interval (2s) and half of the nominal length. These fractal features (including D_{1f}, C_{1f}) determined by using the 1-d spectral method for the 13 profiles are listed in Table 4.3. In Table 4.3, $\Delta D_r = \Delta\beta$ and $\Delta C_r = \Delta C$, and $\Delta\beta$ and ΔC are determined by equation (2.1).

There is no clear dependence of the fractal dimensions D_{1f} and the intercept value C_{1f} on the nominal length of the profiles (L_n) or the different measuring intervals as shown in Fig. 4.7(a) and (b).

Fig. 4.7(a) is the overlaid log-log plots of the power spectral density $P(\lambda)$ against the wavelength (λ) of three field profiles (kmgl, kmgm, and kmgs) from Kimmeridge Bay, which were sampled at different intervals of 0.5 m (kmgl), 0.1 m (kmgm), and 0.01 m (kmgs). Their spectral distribution shows a distinguished pattern of constant fit over a wavelength of $\lambda = 2$ cm to $\lambda = 100$ m. The overall average slope of the spectra over this range is roughly $\beta = 2.8$, hence $D_{1f} = 1.1$ and $\text{Log}(C_{1f}) = -1.2$.

For the series of profiles obtained in Studland Bay (stdl, stdm, and stds) which were sampled at 1.0 m, 0.1 m; and 0.01 m, similar spectral distribution pattern could also be

found as shown in Fig. 4.7(b). There is a general agreement in their power spectral density, which has an average slope of $\beta = 2.7$, and therefore an overall $D_{1f} = 1.15$ and $\text{Log}(C_{1f}) = -1.1$ with an overlap ranges between 2 cm and 100 m.

Table 4.3. The fractal features of the cliff profiles derived from the spectral method.

	Profiles	L_n (m)	L_0 (m)	s (m)	s_r (m)	$D_{1f} \pm \Delta D_{1f}$	$C_{1f} \pm \Delta C_{1f}$
Field	kmgl	155.1	169.8	0.48	0.151	1.10 ± 0.15	-1.37 ± 0.30
	kmgm	11.5	14.3	0.10	0.011	1.15 ± 0.19	-0.61 ± 0.15
	kmgs	2.0	2.9	0.01	0.002	1.14 ± 0.08	-0.63 ± 0.21
	ksh1	10.0	10.8	0.10	0.010	1.05 ± 0.18	-0.70 ± 0.17
	ksh2	11.8	14.4	0.10	0.012	1.13 ± 0.10	-0.65 ± 0.08
	kdo1	10.0	12.0	0.10	0.010	1.12 ± 0.08	-0.33 ± 0.08
	kdo2	11.8	15.1	0.10	0.012	1.33 ± 0.12	-0.27 ± 0.09
	stdl	155.6	165.4	0.97	0.152	1.13 ± 0.34	-0.88 ± 0.94
	stdm	11.2	11.7	0.10	0.011	1.22 ± 0.21	-1.47 ± 0.18
	stds	1.0	1.1	0.01	0.001	1.14 ± 0.21	-1.04 ± 0.37
Map	mlw	2130	3315	2.74	2.080	1.18 ± 0.07	0.25 ± 0.23
	mhw	2755	4288	3.59	2.690	1.18 ± 0.07	1.67 ± 0.30
	c001	1078	1187	5.47	1.053	1.07 ± 0.11	-0.44 ± 0.36
	Total					1.15 ± 0.07	

L_n: Nominal length of a profile (m); L_0: profile length (m); **1.15 ± 0.07**: stands for the average value and its standard deviation; **s**: Sampling intervals; s_r: resampling intervals for FFT; D_{1f} & C_{1f}: Fractal dimension and intercept derived from the spectral method.

This fitness of power spectral density of profiles, of different sample intervals, against wavelength in the log-log plot (Fig. 4.7a and b) with an exponent β near to 3. Some studies (Brown, 1987; Power and Tullis, 1991; Weissel *et. al.*, 1994; Malinverno, 1995) have concluded that the power spectra from self-similar fractals have slopes of $\beta = 3$ on log-log plots of power spectral density against spatial frequency, while spectra from self-affine fractals have slopes of β other than 3. This is because for exponent of $\beta = 3$, we have the parameter $H = 1$, and hence $D = 1.0$. It shows that a rescaled part by a constant factor r ($r^H = r^1 = r$) in both horizontal and vertical coordinates is similar to the original. It is self-similarity. In this study, the field and map profiles have an average fractal dimension of $D = 1.15$ as determined by the spectral method. Their exponent β is reasonably close to 3.0, thus they can be concluded as self-similar profiles although self-affinity may exist.

4.3.3. 1-d structure function method

As described in Chapter 2.6, the first and second orders structure functions lead to the very same results for the simulated 1-d fBm profiles of different H values. Therefore, the fractal dimensions of the profiles will be determined by constructing their 1st order structure functions, i.e., their absolute mean relief M(h) against the lag h. The original profile is also weighted by Hanning window described in Section 4.3.2. The absolute mean relief of a profile [M(h)] of the lag h is given by,

$$M(h) = \frac{1}{N_h}\sum_{i=1}^{N_h}\left|g(x_i + h) - g(x_i)\right| \quad \propto \quad h^H \quad = \quad h^{2-D}$$

where N_h is the number of the paired data points which have a spatial distance of h. The power-law relationship between M(h) and the lag [h] leads to the determination of the fractal dimension (D_{1s}) of a profile, which is given by,

$$D_{1s} = 2 - \beta \tag{4.5}$$

where β is the slope of the fitted line on the log-log plot of the mean relief M(h) against h over the fractal limits. The estimating errors ΔD_{1s} and ΔC_{1s} are equal to Δβ and ΔC which are determined by equation (2.1).

Unlike the simulated 1-d fBm profiles, those field profiles measured by using two or more trends in the field after the coordinates transformation (kmgl, kmgm, stdl, and stdm) and three map profiles (mlw, mhw, and c001) are not equally sampled. Therefore, the lag h for these profiles are assigned values. The assignation of the lag h is give by,

$$h = \left[h - \frac{s}{2}, h + \frac{s}{2}\right)$$

where s is the average sampling intervals of the profile, $[x_1, x_2)$ means $x_1 \le X < x_2$. If the

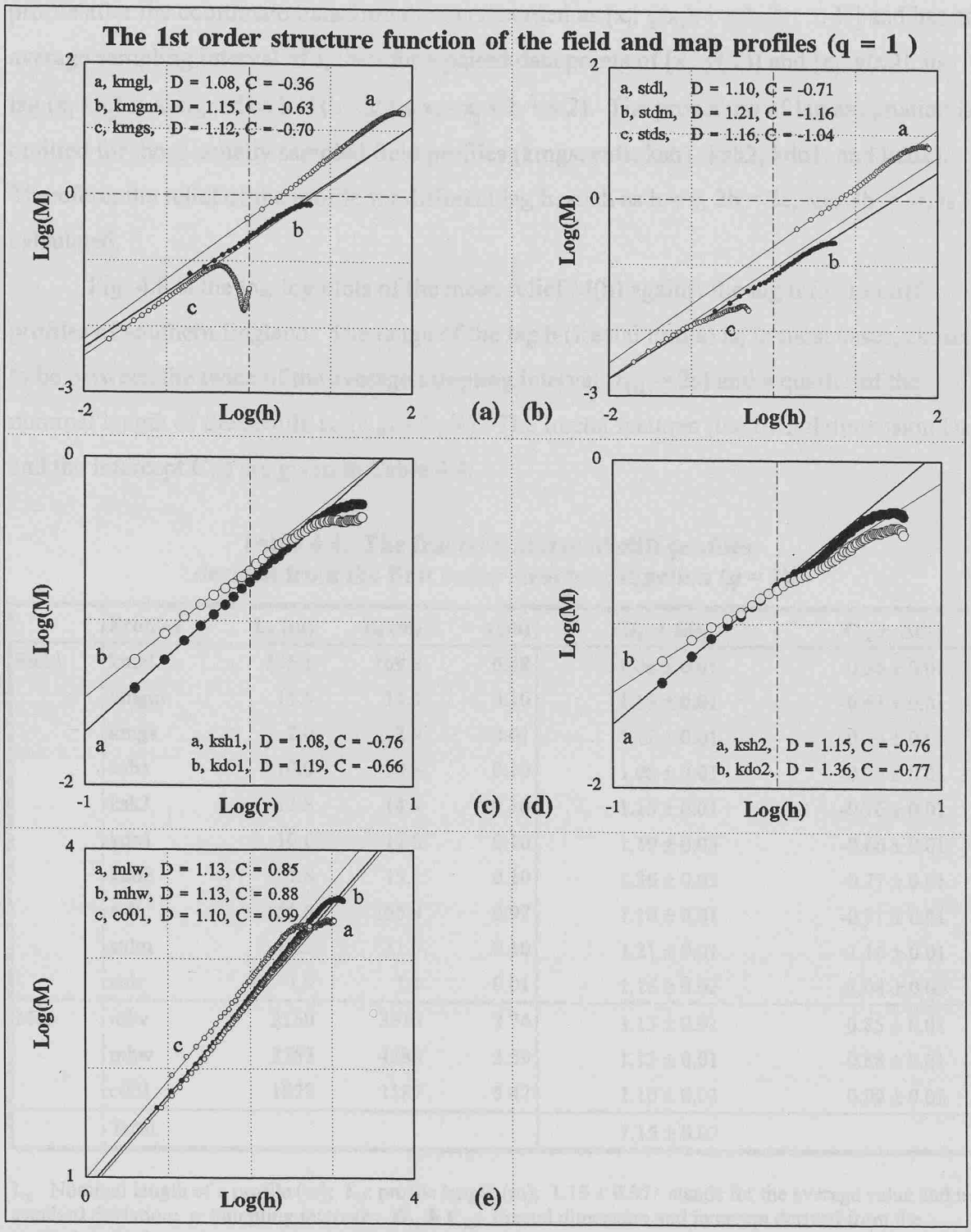

Fig. 4.8. Log-log plots of the first order structure function method applied on the 10 field and 3 map profiles. These plots the mean relief log[M(h)] against the lag log[h] of **(a)** three field profiles from Kimmeridge Bay (kmgl, kmgm, and kmgs) sampled at 0.5 m, 0.1 m, and 0.01 m; **(b)** three field profiles from Studland Bay (stdl, stdm, and stds) sampled at 1.0 m, 0.1 m, and 0.01 m; **(c)** and **(d)** two paired field profiles of different lithology from Kimmeridge Bay (ksh1 vs kdo1 and ksh2 vs kdo2) at a sample interval of 0.10 m; **(e)** is of three map profiles digitized from 1:10,000 maps of Dorset.

profile after the coordinate transformation is recorded as $[x_i, g(x_i), i = 1, 2, \ldots, N]$ and has an average sampling interval of s, then for a paired data points of $[x_i, g(x_i)]$ and $[x_j, g(x_j)]$, its lag $(x_i - x_j)$ is assigned as h if $(h - s/2 \leq x_i - x_j < h + s/2)$. The procedure of lag assignation is omitted for those equally sampled field profiles (kmgs, stds, ksh1, ksh2, kdo1, and kdo2). Therefore, the relief of the profile for different lag h, such as h = s, 2h = 2s, and 3h = 3s, is calculated.

Fig. 4.8 is the log-log plots of the mean relief M(h) against the lag h for 13 cliff profiles of southern England. The range of the lag h (fractal limits) is, in most cases, chosen to be between the twice of the average sampling interval ($r_{1sL} = 2s$) and a quarter of the nominal length of the profile L_n ($r_{1sU} = L_n/4$). The fractal features (the fractal dimension D_{1s} and the intercept C_{1s}) are given in Table 4.4.

Table 4.4. The fractal features of cliff profiles derived from the first order structure function ($q = 1$).

	Profiles	L_n (m)	L_0 (m)	s (m)	$D_{1s} \pm \Delta D_{1s}$	$C_{1s} \pm \Delta C_{1s}$
Field	kmgl	155.1	169.8	0.48	1.08 ± 0.01	-0.36 ± 0.01
	kmgm	11.5	14.3	0.10	1.15 ± 0.01	-0.63 ± 0.01
	kmgs	2.0	2.9	0.01	1.12 ± 0.01	-0.70 ± 0.01
	ksh1	10.0	10.8	0.10	1.08 ± 0.01	-0.76 ± 0.01
	ksh2	11.8	14.4	0.10	1.15 ± 0.01	-0.76 ± 0.01
	kdo1	10.0	12.0	0.10	1.19 ± 0.03	-0.66 ± 0.01
	kdo2	11.8	15.1	0.10	1.36 ± 0.03	-0.77 ± 0.01
	stdl	155.6	165.4	0.97	1.10 ± 0.01	-0.71 ± 0.01
	stdm	11.2	11.7	0.10	1.21 ± 0.01	-1.16 ± 0.01
	stds	1.0	1.1	0.01	1.16 ± 0.02	-1.04 ± 0.03
Map	mlw	2130	3315	2.74	1.13 ± 0.01	0.85 ± 0.01
	mhw	2755	4288	3.59	1.13 ± 0.01	0.88 ± 0.01
	c001	1078	1187	5.47	1.10 ± 0.01	0.99 ± 0.02
	Total				1.15 ± 0.07	

L_n: Nominal length of a profile (m); **L_0**: profile length (m); **1.15 ± 0.07**: stands for the average value and its standard deviation; **s**: Sampling intervals; **D_{1s} & C_{1s}**: Fractal dimension and intercept derived from the spectral method.

Table 4.4 reveals that the D-value of the 13 cliff profiles is between the range of 1.08 and 1.36 with an overall average of $D_{1s} = 1.15 \pm 0.07$. The fractal dimension and the intercept have no systematic relationships with the nominal lengths (L_n).

Fig. 4.8(a) is the log-log plot of the 1st order structure function M(h) against the lag h

of the three field profiles kmgl, kmgm, kmgs, which have different sample intervals of approximately 0.5 m, 0.1 m, and 0.01 m respectively. Three field profile (stdl, stdm, and stds) obtained in Studland Bay, which were sampled at 1.0 m, 0.1 m, and 0.01m respectively, have similar distribution pattern of their mean relief M(h) against the lag h in the log-log plot (Fig. 4.8b).

4.3.4. The average measurement method

If the surface roughness is considered to be the variability of heights (or depths), the variation in height may be used to describe the roughness of a surface. Perhaps the most widely used average roughness parameters are the root mean square deviation RMS (or R_q) and the centre-line average deviation CLA (or R_a). They may be mathematically defined (Ward, 1982) as,

$$RMS\left(R_q\right)=\sqrt{\frac{1}{L}\int_0^L z^2\,dx} \tag{4.6}$$

and

$$CLA\left(R_a\right)=\frac{1}{L}\int_0^L |z|\,dx \tag{4.7}$$

where L is the nominal length of a profile (i.e., the profile span along the horizontal or x-coordinate). For a practical (or discrete) profile, equations (4.6) and (4.7) could be given by,

$$RMS\left(R_q\right)=\sqrt{\frac{1}{N}\sum_1^N |z_i|^2}\ ,\quad i=1,\ \ldots,\ N$$

and

$$CLA\left(R_a\right)=\frac{1}{N}\sum_1^N |z_i|\ ,\quad i=1,\ldots,\ N$$

where N is the number of measures made of the profile, and z is the orthogonal distance measured between the mean line and the profile. The mean line is defined as the line such that the area above the line is equal to the area below the line for a profile.

Table 4.5. The root mean square (R_q) and centre-line average (R_a) values of map and field profiles derived from the average measures of roughness.

	Profiles	L_n (m)	L_0 (m)	s (m)	R_q	R_a	R_q/R_a	$Rq' = R_q/L_n$	D_r
Field	kmgl	155.1	169.8	0.477	1.686	1.422	1.185	0.011	1.01
	kmgm	11.5	14.3	0.095	0.331	0.283	1.171	0.029	1.03
	kmgs	2.0	2.9	0.010	0.105	0.086	1.213	0.053	1.09
	ksh1	10.0	10.8	0.100	0.178	0.123	1.116	0.018	1.01
	ksh2	11.8	14.4	0.100	0.287	0.232	1.178	0.024	1.05
	kdo1	10.0	12.0	0.100	0.247	0.195	1.251	0.025	1.04
	kdo2	11.8	15.1	0.100	0.324	0.262	1.167	0.027	1.07
	stdl	155.6	165.4	0.968	1.564	1.168	1.340	0.010	1.01
	stdm	11.2	11.7	0.098	0.174	0.16	1.088	0.016	1.01
	stds	1.0	1.1	0.010	0.213	0.213	1.001	0.213	1.02
Map	c001	2130	3315	5.470	236.91	162.47	1.458	0.111	1.03
	mlw	2755	4288	2.740	281.76	187.89	1.500	0.102	1.04
	mhw	1078	1187	3.590	15.32	12.123	1.264	0.014	1.02
	Total						1.23 ± 0.14		

L_n: Nominal length of a profile(m); **s**: sample interval (m); **1.23 ± 0.14**: stands for the average value and its standard deviation; R_q **(RMS)**: Root mean square; R_a **(CLA)**: Centre-line average.

For a symmetrical Gaussian distribution, relationship of R_q and R_a is given by (Sayles, 1982),

$$\frac{RMS(R_q)}{CLA(R_a)} = \sqrt{\frac{\pi}{2}} = 1.253 \qquad (4.8)$$

The ratios of R_q/R_a from the map and field profiles vary between 1.17 and 1.45, with an average value close to 1.25 expected from a symmetrical Gaussian surface (Table 4.5).

Based on Table 4.5, the root mean square R_q and the centre line average R_a values of the 13 profiles being considered are plotted versus the nominal length (L_n) in a log-log scale as shown in Fig. 4.9. The regression lines of a slope of about 1 indicate that R_q and R_a are

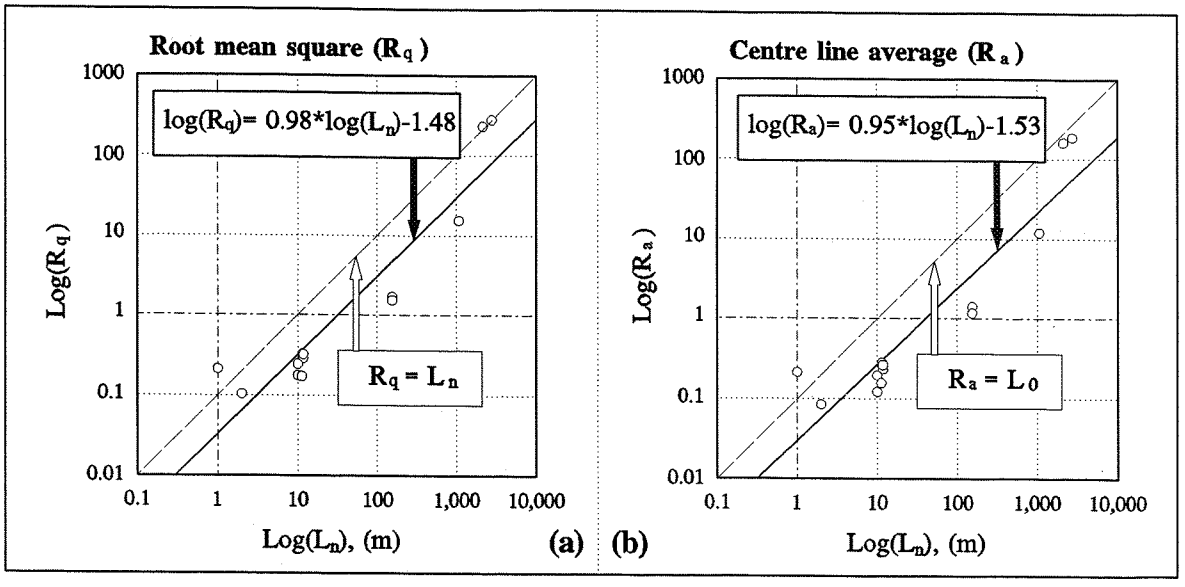

Fig. 4.9. Log-log plots of the root mean square (R_q) and centre line average R_a against the nominal length (L_n) of field and map profiles. They show that both R_q and R_a increases as L_n increases, they are totally positively correlated, hence failed to describe the profiles roughness..

very much positively correlated with the nominal length of the profile (L_n). In other words, both R_q and R_a failed to describe the roughness of the profiles.

The dependence of R_q or (R_a) on L_n (or L_0) is very similar, therefore the pair of R_q and L_n is taken as an example. To remove the effects of L_n on R_q, we provide a new parameter $R_q' = R_q/L_n$, which is more effective, to describe the profile roughness based on the study of these 13 profiles. The coincidence between the new roughness descriptor R_q' and the fractal dimension D_r determined by the ruler method, as shown in the most right column of Table 4.5, indicates that R_q' is a successful parameter to describe the roughness of the 13 cliff profiles.

4.4. COMPARISON OF THE METHODOLOGY

In this section, the fractal features (including the fractal dimensions and the intercept C) derived from the ruler, 1-d spectral, and first order structure function methods are compared, and the discussion of the fractal behaviours of the field and map profiles is followed.

4.4.1. Fractal behaviours from different methods

4.4.1.1. Fractal dimensions derived from different methods

The fractal dimension D is scale-invariant and describes how the roughness of a profile varies with length scale. Fig. 4.10(a) and (b) are the linear-log plots of the fractal dimensions D, which are determined by the ruler (D_r), 1-d spectral (D_{1f}), and 1st order structure function (D_{1s}) methods, against the nominal length (L_n) and the sample intervals (s) of the 13 cliff profiles described in this Chapter. The log scale for L_n (or s) deployed here is not only for the purpose of revealing any kind of possible power-law relationship, but also to allow the comparison of the D values over a wider range scales. The two liner-log plots clearly indicate the determined D values are independent on observation scales.

To compare the D values derived from the ruler, spectral, and structure function methods, their error bars have been plotted in Fig. 4.10(c) at a confidence level of 95%. Fig. 4.10(d) is the error bar plots of three types of D values (D_r, D_{1f}, and D_{1s}) at a confidence level of 95% as the field and map profiles were separated.

Table 4.6. Paired comparison t-test of D values (D_r, D_{1f}, D_{1s}) of the 13 cliff profiles.

	D_r	D_{1f}	D_r	D_{1s}	D_{1f}	D_{1s}
Mean	1.03	1.15	1.03	1.15	1.15	1.15
Variance	0.001	0.005	0.001	0.005	0.005	0.005
df (degree of freedom)	12		12		12	
$\|t\|$ (statistical value)	6.55		6.34		0.16	
t_c (critical two-tail value)	2.18		2.18		2.18	

df: The degree of freedom (the number of the profiles is 13) in the analysis; $|t|$: calculated statistical t value; t Critical two-tail: the theoretical t value at a confidential level of 95% ($\alpha = 0.05$).

Table 4.6 is the results of the paired comparison t-test (2-tails) at a 95% confidence

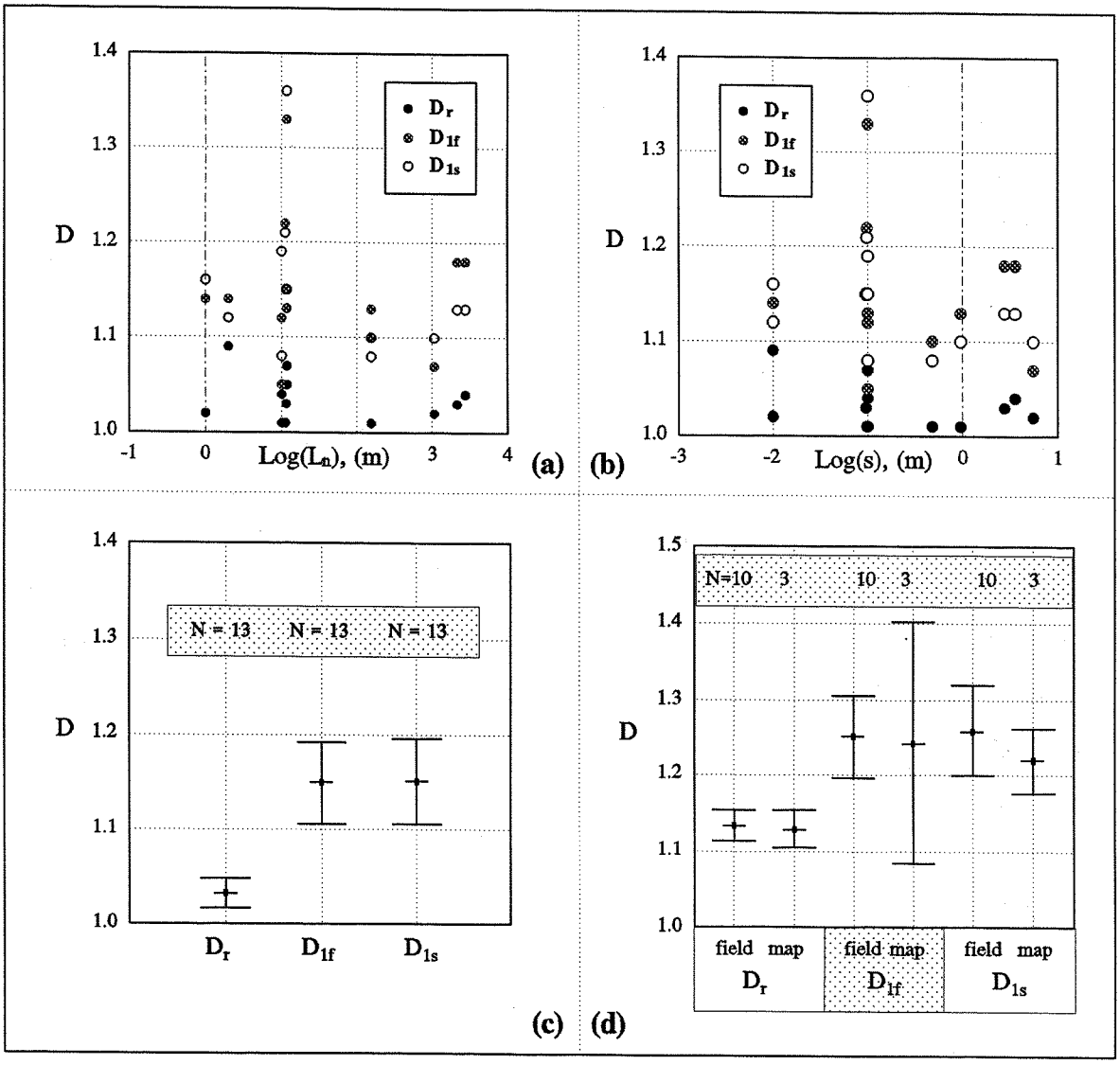

Fig. 4.10. Comparison of the fractal dimensions determined by different methods. The ruler, 1-d spectral, and 1st order structure function methods, which are represented by the subscripts $_r$, $_{1f}$, and $_{1s}$. **(a) and (b)** are linear-log plots of the fractal dimensions (D_r, D_{1f}, and D_{1s}), which are presented by the solid, shaded, and empty circles respectively, against the nominal length of profiles (L_n) and the sample intervals (s) for the 13 field and map profiles. They indicate that the fractal dimensions determined by the three methods have no systematic relationships with the observation scales. **(c)** error bars plot of the three types of D values at a confidence level of 95% (i.e., $\alpha = 0.05$) for the field and map profiles. It shows that D values determined by the ruler method is statistically significant difference from the spectral (and structure function) methods. **(d)** error bars plot of the fractal dimensions for the 10 field profiles, as well as for the 3 map profiles, for the application of the three different methods. There seems to be no statistically significant difference in D-values between the field and map profiles.

level (i.e. $\alpha = 0.05$). $|t|$ is the calculated value, and t is the critical t value of the inverse of

the student's t-distribution (2-tails) for a degree of freedom of 12 at a confidential level of 95%, here $t_c = 2.18$ as df = 12 (degree of freedom) at $\alpha = 0.05$. As $|t| > t_c$, the paired t-test comparison indicates there is significant difference between two samples at a confidential level of 95%. Therefore, it is clear that there is a significant difference between D_r and D_{1f}, and between D_r and D_{1s}, whereas no significant difference between D_{1f} and D_{1s}.

As shown in Fig. 4.10 and Table 4.6, the fractal dimension of the cliff profiles determined by the ruler method (D_r) are significantly different from the fractal dimensions of the cliff profiles determined by the spectral and structure function methods (D_{1f} and D_{1s}), whereas, the spectral and structure function methods yield no significant difference between the determined D values (D_{1f} and D_{1s}) at a confidential level of 95%.

Fundamentally, there is no reason why the fractal dimensions determined by the different methods should be the same (Turcotte, 1991). Indeed, as a profile is analyzed by the same types of methods, such as the ruler and box-counting methods, it should yield the same D values. It must be made clear that the ruler method dimension is different from the spectral dimension. They characterize different scaling properties of a profile. The ruler dimension is a roughness descriptor, which characterizes the "filling capacity" of a profile, however, the spectral dimension is measuring the variation of the power spectra at different wavelength (or frequency), i.e., the variance of the profile.

4.4.1.2. Intercepts derived from different methods

To reveal the relationship between the intercept C and the profile length, the intercepts of the ten field and three map profiles determined by the ruler (C_r), 1-d spectral (C_{1f}), and 1-d 1st order structure function (C_{1s}) methods are plotted against the profile length (L_0) and against the nominal length of the profiles (L_n) at log-log scale as shown in Fig. 4.11. The plotting results of these three methods are symbolised by the solid, shaded, and empty circles, and their regression lines (least squared method) by the straight, dashed, and dotted lines. β is the slope of the regression line, and the subscripts $_r$, $_{1f}$, and $_{1s}$ are used to distinguish the results derived from the three methods.

It is obvious that the dependence of the intercept C on the profile length (L_0) is roughly the same as that on the nominal length of the profiles (L_n). Therefore, Fig. 4.11(b) is taken as an example for further discussion. As shown in Fig. 4.11(b), the intercepts C_r has a power-law relationship with the nominal length of a profile (L_n). The power-law

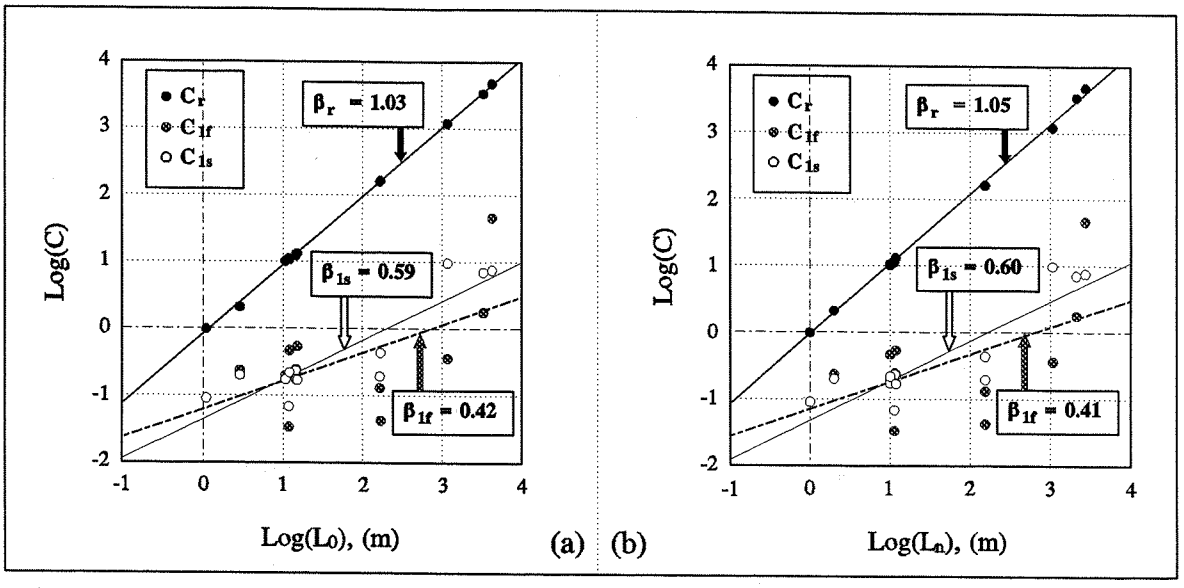

Fig. 4.11. The power-law dependence of the intercepts C derived from the ruler, 1-d spectral, and 1st order structure function methods on the profile length (L_0) and the nominal length of the profile (L_n). The subscripts $_r$, $_{1f}$, and $_{1s}$ are used to characterized the intercepts derived from the ruler, 1-d spectral, and 1st order structure function methods, and are symbolised by solid, shaded, and empty circles respectively. β is the slope of the linear regression line for the plotted points. **(a)** log-log plot of the intercept (C_r C_{1f}, and C_{1s}) against L_0 for all 13 profiles. **(b)** log-log plot of the intercept (C_r C_{1f}, and C_{1s}) against L_n of the 13 profiles.

relationship can be given $C_r = 1.05\ \text{Log}(L_n) - 0.03$ ($R^2 = 0.998$). However, C_{1f} derived from the 1-d spectral method is less dependent on L_n, in the form of $C_{1f} = 0.41\ \text{Log}(L_n) - 1.15$ ($R^2 = 0.34$). It shows a poor correlation between C_{1f} and L_n, i.e., it maybe said C_{1f} has no systematic relationship with L_n. The dependence of C_{1s} on L_n lies between them, i.e., $C_{1s} = 0.60\ \text{Log}(L_n) - 1.32$ ($R^2 = 0.79$).

In summary, the intercept determined by the ruler method depends very much on the length of the profile. Physically, it shows the length of a profile as the profile is measured by a unit length. The intercept determined by the spectral method is independent on the length of the profile, it characterizes amplitude of the profile at a wavelength $\lambda = 1$. The intercept determined by the structure function method lies between two cases, it is the mean relief (or semivariance for the 2nd or structure function method) at a unit lag of the profile.

4.4.2. Discussions

There are two types of methods to determine the fractal dimension of a profile, one is the ruler and box-counting methods, and the other is the spectral and the q^{th} order

structure function methods. These two methods deal with different types of power-law relationships. The former reveals the changing degree of the power-law dependence of the curve length (L_r) on the ruler length (r) used to measure the curve, and the later reveals the changing degree of the power-law relationship among the spatial energy $P(\lambda)$ for a certain wavelength λ. Both types of methods produce two parameters to describe the scaling behaviours of a profile, an amplitude (intercept) C and a fractal dimension D which is determined by the scaling exponent β. Generally speaking, the amplitude parameter C characterizes the amplitude of the profile roughness (usually at a unit length scale) and the fractal dimension (determined by the scaling exponent β) describes how the roughness varies with scales. This is true for the second type of method, but might be not the case for the first type of method. For example, the vertical scale variation of a profile (or surface) produces no change in D values for the spectral and structure function methods since the zeroset of the profile (or surface) do not change (refer to Chapter 2.7 for more details). However, for the ruler and ruler method, it is clear that the amplitude parameter C greatly depends on the profile length (L_0) or the nominal length (L_n) of the profile.

It has been accepted that some special cares should be taken when applying the ruler method to self-affine fractals; or applying the spectral method to self-similar fractals (Mandelbrot, 1985; Wong, 1987; Brown, 1987; Fox, 1989; Hough, 1989; Power and Tullis, 1991; Malinverno, 1995). For example, the ruler method has been widely applied to self-affine fractals (Aviels *et. al.*, 1987; Okubo and Aki, 1987; Carr and Warriner, 1987; Turk *et. al.*, 1987). Some of their reported fractal dimensions are very low (close to 1). This can be explained by either the concept of the crossover length or the profiles from the study areas do possess a low fractal dimension.

Wong (1987) pointed out that the ruler method always gives a fractal dimension close to 1 for resolutions greater than the crossover length of profiles, and suggested that the crossover length (b) can be given by (Brown, 1987),

$$\sigma = b\left(\frac{\lambda_0}{b}\right)^{2-D}$$

where σ is the standard deviation of heights of a profile, r is the sampling interval, and D is the fractal dimension.

Suppose that a self-affine fractal profile of a nominal length (i.e., the length of the profile along the horizontal coordinate) λ_0 has a sampling intervals of length r, a standard deviation of heights σ, then the total length of the profile λ is determined by,

$$\lambda = \frac{\lambda_0}{r}\sqrt{(r^2+\sigma^2)}$$

This is because the σ can be regarded as the average value of the vertical fluctuation over sampling intervals r. Combining this equation with the definition of crossover length, we have,

$$\lambda = \lambda_0\sqrt{1+\left(\frac{b}{r}\right)^{2(D-1)}}$$

Since the fractal dimension $D > 1.0$, for $r << b$, the equation is equivalent to,

$$\lambda = \lambda_0\sqrt{\left(\frac{b}{r}\right)^{2(D-1)}} = \lambda_0\left(\frac{r}{b}\right)^{1-D}$$

then the slope of log-log plot of λ against r is 1-D; for $r >> b$, we have $\lambda = \lambda_0$, then the fractal dimension is always $D \approx 1.0$.

The fractal dimension derived from the ruler method in this study area is relatively close to 1.0, and has an average of $D = 1.03$.

As the spectral method is applied on the profiles, the spectral exponent β may vary between 3 and 1, and have an average value of $\beta = -2$ (Berry and Hannay, 1978). Some previous studies (Fox and Hayes, 1985; Power *et. al.*, 1987; Turcotte, 1987; Huang and Turcotte, 1989; Fox, 1989) have suggested or implied that a profile of spectral exponent $\beta = -2$ is self-similar. They argued that the units of power spectral density to be length squared, i.e.,

$$P(\lambda) \propto \lambda^2$$

This is not the case. For profiles with $\beta = -2$, and $D = 1.5$, we have the parameter H used for rescaling $H = 0.5$; i.e., if a profile is rescaled in the horizontal coordinate by a factor r, then its vertical coordinate must be rescaled by a factor of $r^{0.5}$ in order to keep the rescaled part to be similar to the original. As later studies (Brown, 1987; Power and Tullis, 1991; Malinverno, 1995) have shown that power spectra from self-similar surfaces have slopes of $\beta = 3$ on log-log plots of power spectral density against spatial frequency, while spectra from self-affine surfaces have slopes of β other than 3. For profiles with $\beta = 3$, and $D = 1.0$, we have the parameter $H = 1$. It shows that a rescaled part by a constant factor r in both horizontal and vertical coordinates is similar to the original. It is self-similarity. Power and Tullis (1991) have collected some natural surface profiles data from the studies of Brown and Scholz (1985) and Power *et. al.* (1987, 1988), and shown that these profiles are approximately self-similar within the 6.5 order of magnitude wide wavelength band of 10 μm to 40 m (the general trend of the profiles has a slope of $\beta = 3$) although the spectral exponent of some profiles were biased from 3.

The spectral slopes of the 10 field and 3 map profiles is $\beta = 2.7$ (rather than $\beta = 3$) in the study area, and yield an average spectral dimension of $D = 1.15$ over a range of scales between 2 cm and 1.4 km. They are self-similar fractals. Firstly, three map profiles digitized from the 1:10,000 maps of Dorset are topographical contours of different elevations and have self-similar scaling properties. Secondly, the field profiles possess similar scaling behaviours as the map profiles. Their spectral exponent of $\beta = 2.7$ located in the biased areas of the results presented by Power and Tullis (1991)

The question arisen here is why the profiles from southern England have a such low fractal dimension by comparing the topographic contours discussed in Chapter 3 (which have an average fractal dimension of $D = 1.23$)?

Kaye (1989) analyzed the west and east coast shore lines of Great Britain, and summarized that the fractal dimensions, as determined by the ruler method, of west coast is $D = 1.30$; of east coast is $D = 1.20$; and the entire coast of Great Britain is $D = 1.25$. After study the fractal dimensions of the north ($D = 1.29$) and south (D 1.09) shorelines of Manitoulin Island (which is the world's largest island in the fresh water), as determined by the ruler method, Kaye concluded that "the erosive forces forming the two sides of the island have produced shorelines of very different ruggedness".

From the empirical data of Richardson quoted by Mandelbrot (1977), the fractal

dimensions of some coast lines and land frontiers vary a lot as shown in Table 4.7. This shows the variations in D values are caused by the different types of curves studied, not by the different methodologies deployed.

Table 4.7. The D values of different types of curves

	Austrian coast	South Africa coast	German land frontier	West coast of Great Britain	Land frontier of Portugal
D	1.172	1.024	1.172	1.26	1.122

4.5. COMPARISON OF DIFFERENT DATA TYPES

It might be worthy while investigating whether there is a significant difference among the different profile types in terms of D-value derived from a single method, this could exclude any effects may be caused by different methods.

Fig. 4.10(d) is the error bars plot of D values derived from the three methods (the ruler, 1-d spectral, and 1st order structure function methods) of 10 field and 3 map profiles at a confidence level of 95%. From the mean plot, it is clear that when the 10 field profiles and 3 map profiles are grouped separately, the mean plots of each type of D values (D_r, D_{1f}, and D_{1s}) show there is no statistically significant different between the field and map profiles.

Table 4.8 lists the average and the standard deviation of the fractal dimensions of the 10 field and 3 map profiles determined by the ruler (D_r), 1-d spectral (D_{1f}), and 1st order structure function (D_{1s}) methods.

Table 4.8. The average and standard deviation of D value for different data sources and methods.

	D_r	D_{1f}	D_{1s}
Field profiles	1.03 ± 0.03 (10)	1.15 ± 0.08 (10)	1.16 ± 0.08 (10)
Map profiles	1.03 ± 0.01 (3)	1.14 ± 0.06 (3)	1.12 ± 0.02 (3)
Total	1.03 ± 0.02 (13)	1.15 ± 0.07 (13)	1.15 ± 0.07 (13)

1.03 ± 0.03 (10): stands for the average value is 1.03; the standard deviation is 0.03; and the number of data values used is 10.

Fig. 4.12 is the plot of D-values of 10 field and 3 map profiles determined by the ruler, spectral, 1st order structure function methods. Both Table 4.8 and Fig. 4.12 indicate that there is no statistically significant difference between the D values determined from different type of data sources.

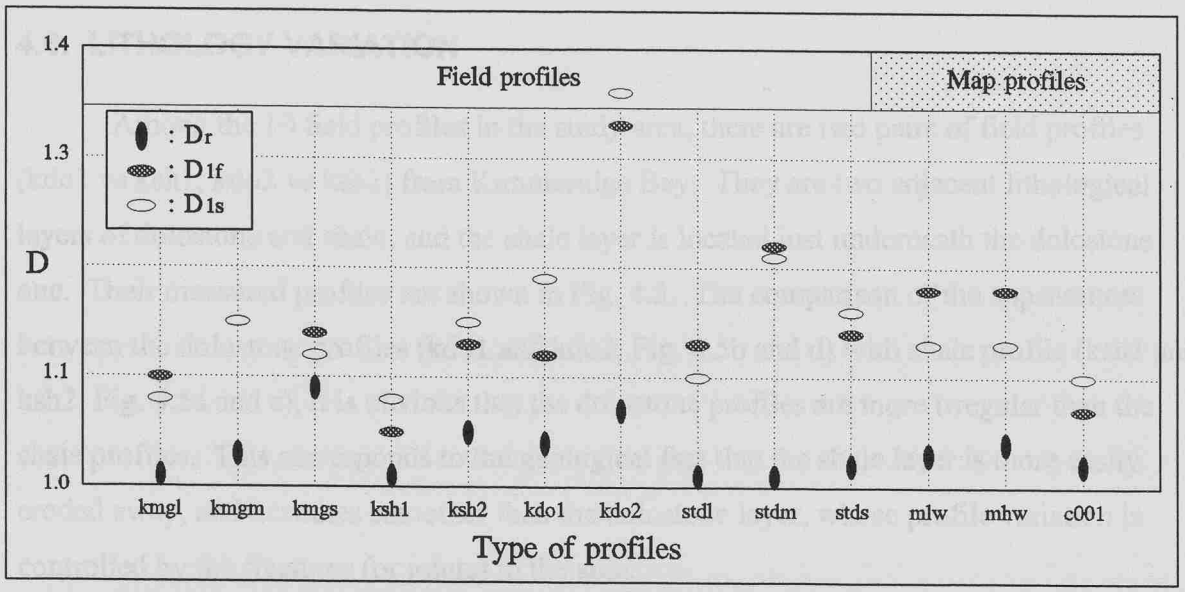

Fig. 4.12. A distribution of the fractal dimensions (D_r, D_{1f}, and D_{1s}) derived from the ruler, 1-d spectral, and 1-d first order structure function methods for the 13 field and map profiles. The plot shows that the fractal dimensions D have no systematic relationships with data types.

4.6. LITHOLOGY VARIATION

Among the 10 field profiles in the study area, there are two pairs of field profiles (kdo1 vs ksh1; kdo2 vs ksh2) from Kimmeridge Bay. They are two adjacent lithological layers of dolostone and shale, and the shale layer is located just underneath the dolostone one. Their measured profiles are shown in Fig. 4.5. The comparison of the appearances between the dolostone profiles (kdo1 and kdo2, Fig. 4.5b and d) with shale profile (ksh1 and ksh2, Fig. 4.5a and c), it is obvious that the dolostone profiles are more irregular than the shale profiles. This corresponds to the geological fact that the shale layer is more easily eroded away, and becomes smoother than the dolostone layer, whose profile variation is controlled by the fractures (or joints) in the area.

Table 4.9. Comparison of the two pairs of field profiles from Kimmeridge Bay.

Profiles	L_n (m)	s (m)	D_r	C_r	D_{1f}	C_{1f}	D_{1s}	C_{1s}	R_q	R_a	R_q/L_n
ksh1	10.0	0.1	1.01	1.01	1.05	-0.70	1.08	-0.76	0.178	0.123	0.018
kdo1	10.0	0.1	1.04	1.03	1.12	-0.33	1.19	-0.66	0.247	0.195	0.025
ksh2	11.8	0.1	1.05	1.11	1.13	-0.65	1.15	-0.76	0.287	0.232	0.024
kdo2	11.8	0.1	1.07	1.12	1.33	-0.27	1.36	-0.77	0.324	0.262	0.027

The two pairs of profiles were analyzed by the above four techniques discussed in Section 4.3, which includes the ruler (Fig. 4.6c and d), 1-d spectral (Fig. 4.7c and d), and 1st order structure function (Fig. 4.8c and d), and the average roughness description (R_q, R_a) methods, and their analyzed results are shown in Table 4.9. As shown in Table 4.9, all the values of the fractal features (including fractal dimensions, intercepts C) and R_q/L_n derived from different methods of dolostone profiles are (slightly) higher than those of shale profiles except C_{1s} from the pair of kdo2 versus ksh2 which are reasonable close. These analysis results coincide with the fact that the dolostone profiles are move variable than the shale profiles (refer to the standard deviation of the two paired profiles in Table 4.1,). This can be explained by the geological fact that the dolostone profile is rougher than the shale profile, and the former is much more controlled by the fracture joints.

For the ruler method (Fig. 4.6c and d), both the D values and intercept of dolostone profiles are higher than those of shale profiles.

The 1-d spectral (Fig. 4.7c and d) and the 1st order structure function (Fig. 4.8c and d) methods show that the dolostone profiles have overall more power (energy) than shale

profiles between the range of scales observed. Both the D values (D_{1f}, D_{1s}) and the intercepts (C_{1f}), derived from the two methods, of dolostone profiles are greater than those of shale profiles. In other words, the dolostone profiles have greater amplitude of roughness, and the roughness varies with length scale at a faster rate, than the shale profiles over a range between 0.2m and 5 m.

The values of R_q (root mean square), R_a (centre line average), and R_q/L_n resulted from the average measurement method (the very right column of Table 4.9) of dolostone profiles are slightly higher than those of shale profiles. This indicates that the dolostone profiles have more variation, hence rougher, than the shale profiles. Furthermore, this also show that although the R_q and R_a values are dependent on the nominal length of a profile, the profile roughness does contribute to the values of R_q and R_a. In order to remove the effects of nominal length of a profile for describing the roughness of the profile, the new parameter R_q/L_n as described in Section 4.3.4 should be used to characterize the roughness of a profile.

As mentioned in the introduction of this chapter, the fractal dimension D describes how the roughness changes with the scale of observation (horizontally), while the intercept C describes the amplitude of a profile roughness (vertically). The analysis result strongly suggests that the dolostone profiles are rougher than the shale ones, which corresponds to the geological fact. Therefore, the fractal models presented in Section 4.3 are successful roughness descriptors of the natural profiles.

4.7. CONCLUSIONS

Based on the analysis of the ten field and three map profiles from the Dorset area of southern England using the ruler, 1-d spectral, 1st order structure function, and the average measurement methods, the following tentative conclusions may be drawn.

1. The field and map profiles are self-similar fractals with an average D = 1.03 by the ruler method over a range between 2 cm and 1.4 km, i.e., about 2 magnitudes. The fractal limits (r_L and r_U) are roughly between the range of the twice average sample intervals and a quarter the nominal length of profiles (L_n). Two pairs of profiles, which were sampled at different intervals (1st pair: kmgl, 0.5 m, kmgm, 0.1 m, kmgs, 0.01 m; 2nd pair: stdl, 1 m, stdm, 0.1 m, stds, 0.01 m), generate a very good linear fit in terms of the spectral distribution patterns versus wavelength on a log-log scale (Fig. 4.7a and b). The 1st order structure functions of these profiles produce similar distribution patterns between the mean relief and lag (Fig 4.8a and b). The spectral and 1st structure function yield an average fractal dimension of D =1.15.
2. Field and map profiles have no significant difference in terms of D values.
3. Comparison of the two pairs of field profiles of shale and dolostone layers from Kimmeridge Bay, ksh1 vs kdo1 and ksh2 vs kdo2, reveals that the dolostone profiles have higher fractal dimensions than the shale profiles. This corresponds to the geological fact that the shale layer is more easily eroded away, and becomes smoother than the dolostone layer, where fracture joints control its formation.
4. Different erosion process could lead to the variation of the fractal dimension of topographic contours. The down cutting erosion process, which involved river network or faults, usually results in higher fractal dimension of about D = 1.25 (as discussed in Chapter 3) than the wave erosion process, which leads in lower fractal dimension of about D 1.08 for the 10 field and 3 map profiles from southern England.
5. The symmetrical Gaussian distribution is a good approximation for deviation of field and map profiles, the ratio of the root mean square and the centre line average $R_q/R_a = 1.23$. The traditional roughness descriptors R_q(or R_a) is dependent on the nominal length (L_n) of a profile, and failed to describe the roughness of profiles of different lengths. The ratios $R_q' = R_q/L_n$ corresponds well with the fractal dimension determined by the ruler method, and are successful to describe the roughness of profiles.

6. The power-law dependence of the intercept C_r derived from the ruler method is dependent on the profile length L_0 or the nominal length of the profile (L_n). The intercept C_{1f} derived from the 1-d spectral method, however, has no systematic relationship with L_0 or L_n. The dependence of intercept C_{1s} derived from the 1st order structure function method on L_n lies between the two cases.

CHAPTER 5.

DISCUSSION ON FRACTAL DIMENSIONS OF COASTLINES AND CONTOURS

CHAPTER 5

DISCUSSION ON FRACTAL DIMENSIONS OF COASTLINES AND CONTOURS

5. DISCUSSION ON FRACTAL DIMENSIONS OF COASTLINES AND CONTOURS

5.1. INTRODUCTION

The fractal concept is a successful model to describe coastlines, land frontiers, and contours (e.g. Richardson, 1961; Mandelbrot, 1977; Goodchild, 1980; Feder, 1988; Kaye, 1989; Turcotte, 1992; Chapters 3 and 4). Table 5.1 lists some published fractal dimensions of coastlines and land frontiers and shows that different fractal dimensions occur even when the same method is used.

A typical example was quoted by Mandelbrot (1977) based on the empirical data of Richardson (1961), the fractal dimension of the South African coastline is D = 1.02 which is very close to 1, whereas the fractal dimension of the coast of Great Britain is D = 1.25, both determined by the ruler method. The coastline of Great Britain is much irregular than that of the South Africa. The former is controlled by different erosive processes such as glacier, river down-cutting, and wave erosions, whereas the latter is a fairly straight coastline, and dominated by the wave erosive (cliff / retreat) process. This suggests that the difference in fractal dimensions of coastlines and contours may reflect their formation mechanism, including the controls of erosive processes, lithology, fractures, etc.

Table 5.1. D values of some coastline and contours determined by the ruler method

location	D_r	literature sources
South Africa coast	1.02	
land frontier of Portugal	1.12	Richardson (1961),
German land frontier	1.17	quoted by Mandelbrot (1977)
Australian coast	1.17	
coast of Great Britain	1.25	Mandelbrot (1977)
east coast of Great Britain	1.20	
west coast of Great Britain	1.30	Kaye (1989)
south shore line, Manitoulin, Canada	1.09	
north shore line, Manitoulin, Canada	1.29	
Norway coast	1.35	Feder (1988)
topographic contours covering granite plutons	1.11 - 1.26	Norton and Sorenson (1989)
Vulcano, Italy	1.05 - 1.34	
Stromboli Italy	1.02 - 1.04	Leonardi *et. al.* (1994)
Alicudi, Italy	1.02	

Other fractal curves arising in rocks may also be diagnostic of processes. For example, Xie (1993) and Xie and Sanderson (1995) suggested that the transgranular cracking produces higher fractal dimension (D = 1.36) than the intergranular cracking (D = 1.25). The study may reveal the control of the fracture patterns over the coastlines in terms of coastline shape and the fractal measurements of coastline.

The objectives of the Chapter are:

- to compare different fractal dimensions of coastlines and contours determined by the ruler method from
  1), worldwide literature;
  2), a re-analysis of parts of the coastlines of Great Britain and Ireland;
  3), the results of previous chapters.
- to examine the role of different erosive process on the fractal dimension;
- to examine the roles of lithology and structure on the fractal dimension.

5.2. DATA SOURCES

5.2.1. Locations of the coastline sections

Fig. 5.1 is a diagram of Great Britain and Ireland, where the Great Britain part was digitized from 1:625,000 geological maps and the Ireland from the 1:1,000,000 map of mineral deposits of Ireland. The digitizing procedure was carried out on the TDS digitizing table using the ***DIGICON*** program developed by Professor David J Sanderson in Quick Basic. Fig. 5.1 shows the locations of eleven coastline sections sampled around the islands. The coastlines gb, gbe, gbw, and ire are shown in Fig. 5.2. In addition, the western and eastern boundaries of the Dixie valley of Nevada, USA, presented by Zhang *et. al.* (1991), were also digitized to evaluate the role of fault scarps in terms of the fractal dimension.

Table 5.2. List of coastline portions and contours

file	map scale	s (km)	L_0 (km)	locations
gb	1:625,000	3.935	7016	entire coast of Great Britain (GB)
gbw	1:625,000	4.272	3894	west coast of GB
gbe	1:625,000	3.591	3164	east and south coast of GB
ire	1:1,000,000	3.220	3713	entire coast of Ireland
e1	1:625,000	0.864	201	south-east coast of England
e2	1:625,000	0.646	159	Dorset coast of England
e3	1:625,000	0.714	463	south coast of Cornwall, England
s1	1:625,000	0.406	397	north-west coast of Scotland
s2	1:625,000	0.504	511	north-west coast of Scotland
s3	1:625,000	0.538	160	Caithness coast of Scotland
s4	1:625,000	0.488	127	north-east coast of Scotland
s5	1:625,000	0.461	218	east coast of Scotland
i1	1:1,000,000	0.592	745	south coast of Ireland
i2	1:1,000,000	0.519	742	south-west coast of Ireland
i3	1:1,000,000	0.695	229	north-east coast of Northern Ireland
dxw	1:1,613,000	1.094	138	west profile of the Dixie valley, Nevada, USA
dxe	1:1,613,000	0.844	254	east profile of the Dixie valley, Nevada, USA

Table 5.2 summarized some basic features of the coastline from Great Britain and Ireland, and of contours from the Dixie valley. L_0 is the digitized length of the curve, which is given by,

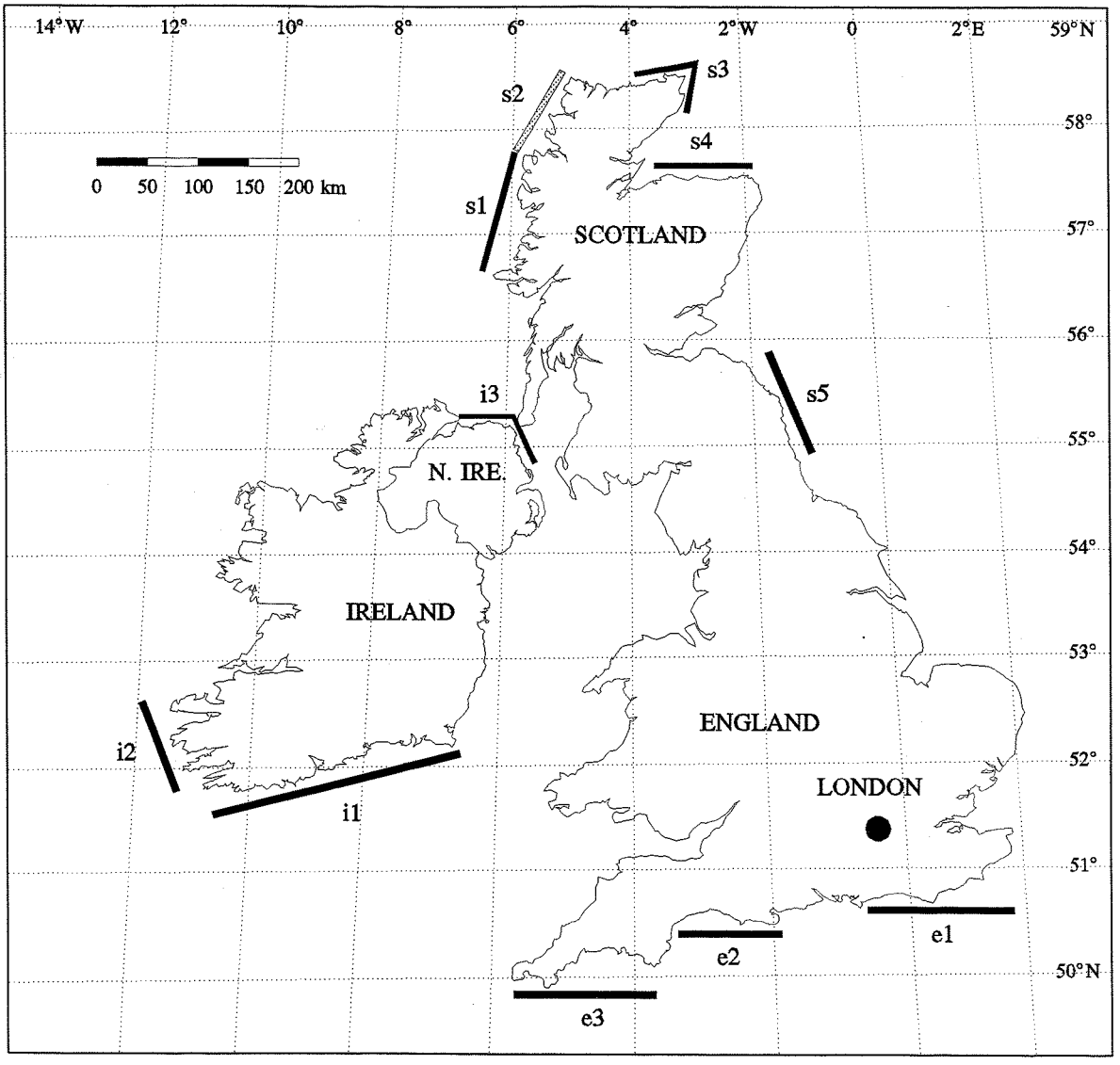

Fig. 5.1. Digitized coastlines of Great Britain and Ireland and the locations of coastline portions used in the study. The coastline sections gbe and gbw are shown in 5.2(a).

$$L_0 = \sum_{i=1}^{N-1} \sqrt{(x_{i+1} - x_i)^2 + (y_{i+1} - y_i)^2}$$

where (x_i, y_i) is the recorded coordinates of a digitized curve, and N is the number of the points used to digitize the curve. s is the average sampling interval of the coastline, which is given by $s = L_0 / N$.

5.2.2. Brief description of the geology of the coastline sections

In this section, a brief description of the geology of the coastline sections samples in

the study area is presented, and appropriate controls over these coastline sections are emphasised as shown in Table 5.3.

Table 5.3. Brief description of the geology of the sampled coastline sections

section	geology
gb	closed coastline; wide variety of geological settings and geomorphologic processes.
gbw	variety of old metamorphic rocks, traversed by a series of ancient geological movements which led to NE-SW orientated structures, dominated by both the drowned river (rias) and glacier (fjord) valleys.
gbe	variety of Devonian to Quaternary sediments mainly flat-lying. Relatively fewer large rivers except Solent, Thames, Humber, and Firth of Forth lay with intervening coast dominated by wave action / cliff retreat erosion.
ire	variety of rock types from Dalradian metamorphics, Devonian sediments, to Tertiary lavas, mainly involved the E-W or NE-SW strike structures (faults and folds). South-west part is dominated by river down-cutting erosion, whereas north-east part by the cliff retreat erosive process.
e1 & e2	E-W oriented coastline of Mesozoic sediments, generally flat-lying. The E-W oriented Mesozoic and Tertiary structures (folds, faults, and inverted faults) control the general trend of the coastline of the English Channel. The main structures roughly parallel to the coastline, and the strata dipping gently to north and south. Few major river networks and drowned valleys in the area allow the coast to assume a more mature aspect: long sweeping and flatter curves are characteristics and the headlands in the area have generally been cut back (Steers, 1948). Wave erosion / cliff retreat processes control the share of the coastline sections.
e3	The E-W oriented coastline section is mainly composed of Devonian sediments, Variscan intrusive granite, and the Lizard complex (Evans, 1990). The sedimentary rocks around the coastline are generally resistant, and the outcrop strata is typified by rugged cliffs with relatively little coastal erosion taking place. The general orientation of the coastline section parallels and is controlled by Variscan thrusts with flat-lying Mesozoic sediments located in off-shore areas. The river down-cutting erosive process controls the coastline section producing classical rias, where the sea penetrates along drowned river valleys.
s1 & s2	The two sections are NE-SW oriented and composed of Lewisian gneiss, Torridonian

	sandstones and Moine meta-sediments. The general trend of the coastline is parallel to the Moine thrust. NW-SE orientated Tertiary basic dikes are perpendicular to the general trend of the coastline. The area was greatly modified by Quaternary ice sheets which strongly eroded much below the present sea level, producing drowned glacier valleys or fjords, and the most rugged coastline in the UK. The most significant difference between the geology of the Scottish landmass and the submarine geology off its west coast is that a larger area offshore is underlain by Permian and Mesozoic rocks.
s3	Devonian old red sandstone (ORS), and flat-lying. The fault strike is mostly NE-SW oriented. Few major river / glacial drainage valleys involved in the area. The coastline is controlled by the cliff retreat process.
s4	Dalradian metamorphic rocks overlain by the non-marine Devonian-Cretaceous sediments. The E-W oriented coastline parallel to the bedding of the off-shore Mesozoic rocks, locally parallel to the fault strike (faults along the River Firth). Few major river / glacial valleys. The coastline is dominated by the cliff line retreat / wave action process.
s5	Carboniferous and Silurian sediments with flat-lying. The bedding of the off-shore sediments rocks (Carboniferous and Permian) parallels to the coastline section sampled, but small faults are locally perpendicular to the coastline. The area is involved few major river drainage valleys, and the coastline is controlled by the cliff retreat / wave action erosion.
i1 & i2	Devonian, Carboniferous sediments, folded into major E-W trendy. The coast is controlled by resistant Devonian rocks in cores of major anticline, with long inlets of less resistant Carboniferous rocks in cores of syncline and along faults. River erosion produced long E-W valleys at sea level and typical ria coastline. i2 is a N-S oriented section which is perpendicular to the main structure lines and valleys, whereas i1 parallels to the main structures but involved some river valleys. The coastlines are dominated by the fluvial erosion (large drainage valleys).
i3	Coastline is dominated by Tertiary basalt with Dalradian metamorphic rocks and flat-lying carboniferous-Cretaceous sediments. Few major river drainage valleys involved in the area, and the coastline controlled by the cliff retreat / wave action erosion.

In summary, the coastline of the N-W of Scotland (s1 and s2) is by far the most rugged part of any area of UK, this diversity is due mainly to the glacial erosion acting on

rocks of great variable strengths. The fabric drainage networks in the area also contribute the formation of the ruggedness of the coastline. The river down-cutting erosive process plays an important role for the formation of coastline sections of e3, i1, and i2, with post-glacial sea level rise producing drowned valleys or rias. The straighter coastline sections sampled in the British Isles (e1, e2, s3, s4, and s5) have a common characteristic: the bedding of the off-shore sediment rocks mostly parallels to the orientation of the coastline and few major drainage river networks are involved. These coastlines are mainly controlled by the wave action / cliff line retreat.

5.2.3. Brief description of the erosive processes

Glacial erosion: During the Quaternary (glacier ages), immense supplies of ice drained from the mountainous areas of North and West of Britain, and produced deep glacier valleys. Glaciers often cut into the bedrock much deeper than the sea level. These glacier valleys generally cut across geological fractures and structures, although some major faults could control valleys.

Fjords have resulted from the well developed valley systems (especially in the greatly over-deepened glacial troughs in the North and West of Scotland, which extends below the present-day sea level. Therefore, even with the uplift of the crust (due to the removal of glaciers) and the rise of the sea level (due to the melt water), the coastline in NW of Scotland is still dominated by the glacier valleys, and formed the most rugged coastline in the UK.

River down-cutting erosion: The development of a river valley depends on the original surface, the climate (rainfall), and the underlying geological structure (faults, folds, and varied resistance to erosion of rocks). The river down-cutting involves the incision of stream channels into bedrocks, the downstream transportation and the deposition of the eroded sediments.

River system usually form a tree (or branching) structure, where deeper valleys in mountainous areas and plateaus that have raised high above sea-level. Such river network systems are typically fractals (Gan *et. al.*, 1992). River networks, and to some extent glacier valley system, represent a system of lines of erosion which lead to area filling ($D \rightarrow 2$) fractal geometry (Norton and Sorenson, 1989).

Simple down-cutting of river channels produces gorge valleys. Down-cutting may proceed a long way before the valley walls are worn back to any great extent, and their

eventual removal by the river. Down-slope transportation of materials produces V-shaped valleys, where the rate of deepening slows down and widening begins to catch up, with production of a cross-profile approximating to a V-shape. Typically, while the valley is being widened by the wasting back of its sides, the river itself begins to widen its valley floor by under-cutting its banks, where both down-cutting and lateral cutting are taking place simultaneously or alternately from time to time.

After the later glaciation, the rise of the sea level produced coastlines dominated by the rias in the SW England and SE Ireland where the absence of ice sheets produced a little uplift. The coastline sections (e.g., e3, i1 and i2) are dominated by the river down-cutting erosion.

Most rivers drain directly into the sea. Except in mountainous terrains most river channels are flanked by an area of subdued relief termed a floodplain formed by deposits laid down when the river floods. Along the east coastline of England, deposition processes, which produced floodplains and estuary (e.g., Humber, Thames, and Firth of Forth) filled the river and coupled with cliff retreat and resulted in straight coastline.

Wave action / cliff retreat erosion: Major processes of cliff retreat are the basal erosion and removal of collapsed materials by waves. Where wave action undercuts the base of cliffs and is capable of removing all debris accumulating at the base of the cliff, lithological and structural controls become significant in influencing cliff form. The wave action / cliff retreat is actually eating the landward of the coastal area back, and generate a straight coastline, especially when the bedding and main structure strikes of the area parallel to the general trend of coastline.

The coastline sections (s3, s4, s5, e1, e2, and i3) located in the areas where few major rivers involved are straight, controlled by wave action / cliff retreat erosion, locally by the estuary deposition process.

Lithology also plays an important role in the formation of the coastline. Generally homogeneous rock types have equivalent resistance to erosion, and produces straighter coastline, such as coastlines in Caithness, Antrim, Dorset. Heterogeneous rock types together with some structures often lead to differential erosive process, and generate more rugged coastline (Cornwall).

In summary, the coastline of NW of Scotland (s1 and s2) is dominated by the glacier valleys (fjords) even with the post-glacial uplift in the area due to the deep cut into the bedrocks during the galication. The subside sea level rise in SE England produced large

catchment rivers with widely spaced main rivers enter into sea (usually produce estuaries, e.g., Thames), separated by long stretch of coast with no major rivers (dominated by cliff retreat).

5.3. ANALYSIS RESULTS

The ruler method was applied to the data sets listed in Table 5.2, and the determined fractal features, including the fractal dimensions D_r, intercepts C_r, the lower (r_{RL}) and upper (r_{RU}) fractal limits, shown in Table 5.4. The estimated errors ΔD_r and ΔC_r are determined by equation (2.1) of Chapter 2.

Table 5.4. The analysis results of coastline portions and contours by the rule method

file	r_{RL} (km)	r_{RU} (km)	D_r	ΔD_r	C_r	ΔC_r
gb	3	150	1.25	0.01	3.95	0.01
gbw	4	200	1.30	0.01	3.74	0.02
gbe	4	150	1.20	0.01	3.59	0.02
ire	3	200	1.30	0.01	3.66	0.01
e1	2	60	1.04	0.01	2.30	0.01
e2	0.8	20	1.12	0.01	2.16	0.01
e3	1	20	1.30	0.02	2.64	0.02
s1	2	20	1.37	0.05	2.64	0.04
s2	2	40	1.37	0.02	2.78	0.02
s3	0.4	20	1.09	0.01	2.17	0.01
s4	1	10	1.08	0.01	2.09	0.01
s5	1	10	1.10	0.01	2.28	0.01
i1	1	40	1.25	0.01	2.82	0.01
i2	1	40	1.35	0.04	2.88	0.04
i3	0.6	20	1.15	0.01	2.33	0.01
dxw	2	20	1.03	0.01	2.14	0.01
dxe	2	20	1.22	0.02	2.44	0.02

Examples of individual coastlines and log-log plots derived by the ruler method are shown in Figs. 5.2, 5.3, and Fig. 5.4. The log-log plots were shifted (offset) vertically in order to avoid overlaps; The intercept values C_r shown on the figures, as well as in Table 5.4, can be used to recover their correct positions.

As shown in Fig. 5.2 the fractal dimensions of the coastlines of Great Britain coincides with the results determined by Mandelbrot, (1977) and Kaye (1989), i.e., the fractal dimensions, as determined by the ruler method, of west coast is D = 1.30; of east coast is D = 1.20; and the entire coast of Great Britain is D =1.25. The coastline of Ireland has a fractal dimension of 1.30, which is as same as that of west coast of Great Britain.

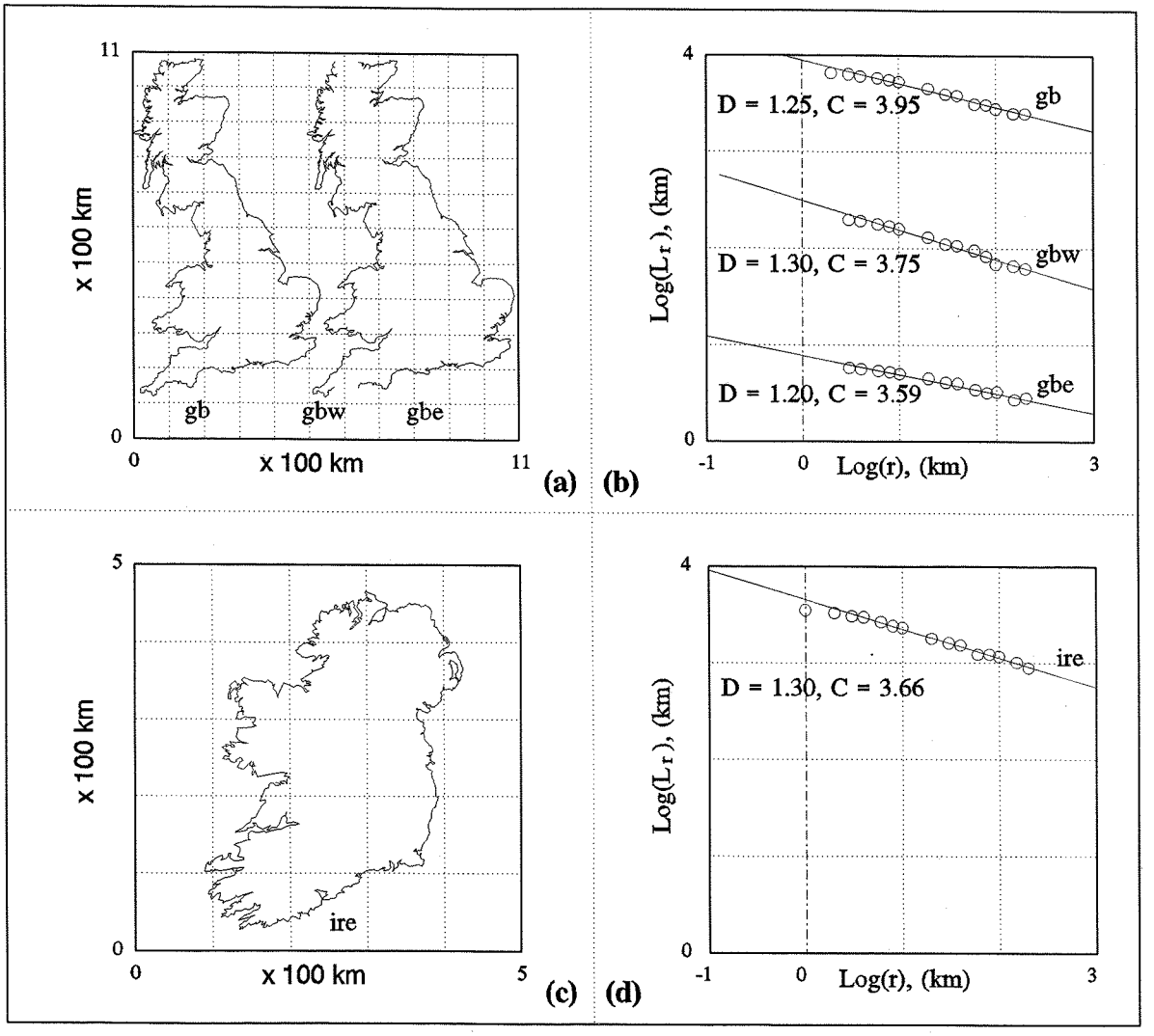

Fig. 5.2. The coastlines of Great Britain and Ireland and their log-log plots as determined by the ruler method. **(a)** The entire (gb), west (gbw), and east (gbe) coastlines of Great Britain. **(b)** The log-log plots coastlines shown in (a) as the ruler method is deployed The log-log plots of the coastlines gbe and gbw were vertically shifted down to avoid the overlaps. Their intercepts C values can be used to restore their original position of the log-log plots. **(c)** and **(d)** are the entire coastline of Ireland (ire) and its log-log plot derived from the ruler method.,

Fig. 5.3 shows the fractal dimensions of coastline sections of British Isles. It demonstrates that 1) D values vary from 1.04 to 1.37; 2) higher D values occur in west areas, whereas lower D values in south and east areas; 3) there is no systematic correlation within rock types, e.g., for Devonian and Carboniferous sediments, i1, i2, and e3 have higher D values ($\approx$ 1.3) than s3; 4) to some extent, D values are controlled by structure, generally, higher D values occur in the folded rock areas (e.g., i1, i2, e3, s1, and s2),

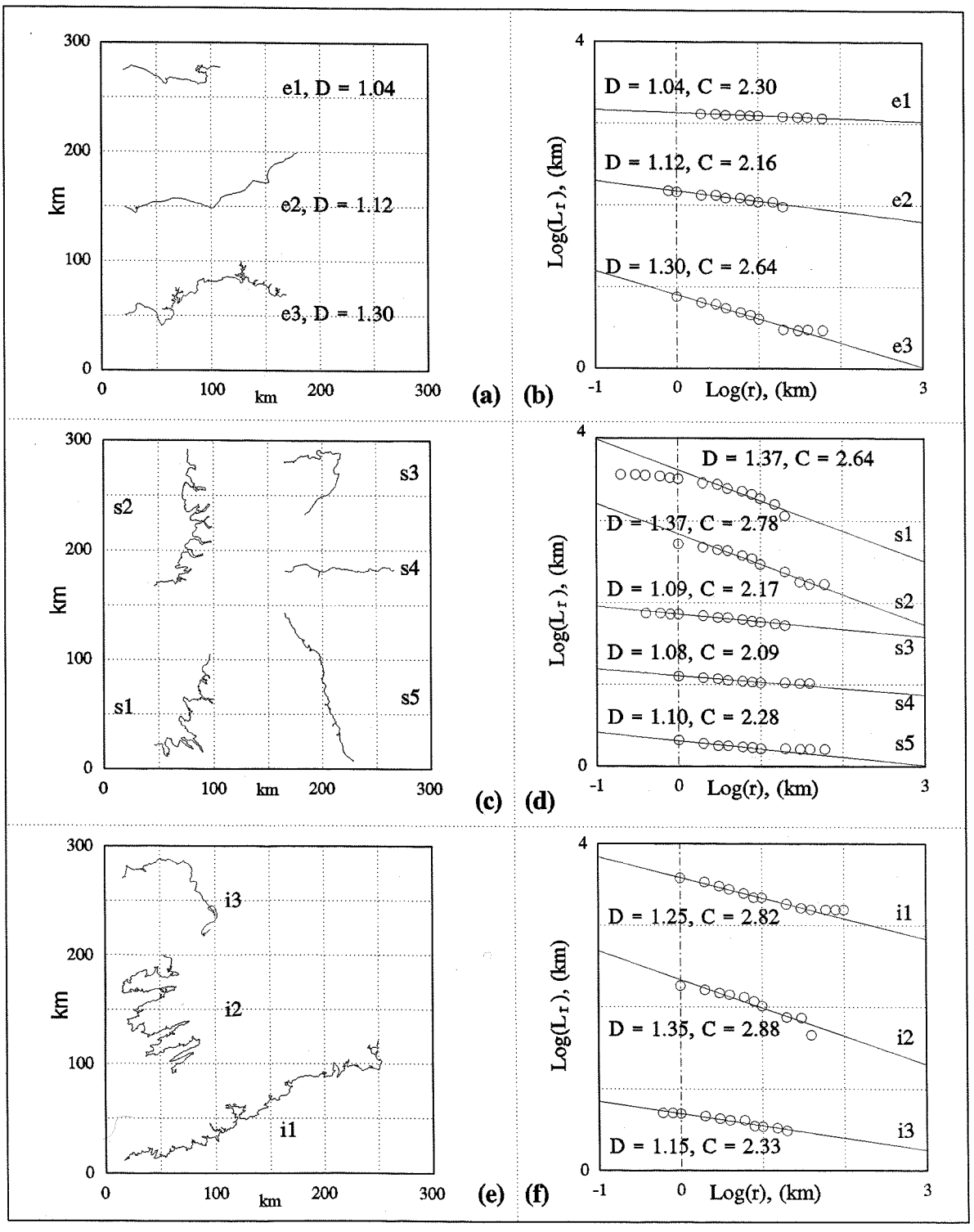

Fig. 5.3. The coastlines portions of Great Britain and Ireland and their log-log plots as determined by the ruler method. **(a) and (b)** are three coastlines of south England (e1, e2, and e3) and their log-log plots of the ruler method. **(c) and (d)** are five portions of the coastline of Scotland (s1, s2, s3, s4, and s5) and their log-log plots. **(e) and (f)** are three sections of coastline of Ireland (i1, i2, and i3) and their log-log plots. In (b), (d), and (f), the log-log plots were vertically shifted (offset) either down or up (e2 and i2 remain unchanged) in order to avoid overlap. The log-log plots can be restored based on the intercept C values.

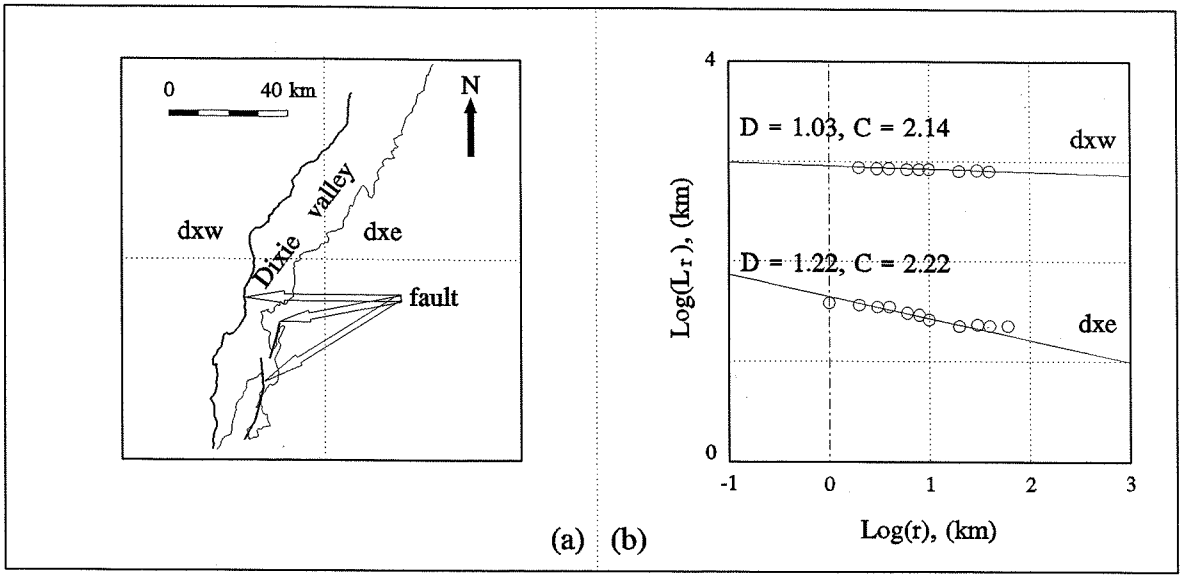

Fig. 5.4. Two topographic contours from the Dixie valley, Nevada, USA and their log-log plots of the ruler method. **(a)** dxw is the valley floor along the Dixie valley active normal fault system (fault deformed / controlled contour), whereas dxe is less controlled by the fault system. **(b)** are the log-log plots of the two contours. The log-log plots were shifted vertically up or down in order to avoid overlap, they can be restored based the intercept C values.

whereas lower D values occur in the areas where few folds involved rock areas (e.g., e1, e2, s3, s4, s5, and i3).

Fig. 5.4(a) shows a typical example of fault controlled valley floor on one side (dxw), and the other side (dxe) is less controlled by the fault system. Their fractal dimensions are significant different. The former has a much lower fractal dimension of D = 1.03 than the later, which has a fractal dimension of D = 1.22.

The next three Sections will discuss and explain why the fractal dimensions of the coastlines and topographic contours are so significantly different from each other. The variations in D values are caused by several geological factors, which control the formation of coastlines and topographic contours. Three geological aspects, the erosive process, lithology, and fracture will be discussed.

5.4. DISCUSSIONS

5.4.1. Erosive process

Different erosive processes, such as glacier action, river down-cutting, and wave action / cliff retreat erosion, could form different coastlines. Their fractal behaviours are to be investigated.

Table 5.5 summarized the fractal dimensions of the coastlines and topographic contours discussed in the previous studies, Chapter 3, and this Chapter. The ruler method is deployed.

Table 5.5. The D values of the coastline and contours formed by different erosive processes

Erosive processes	location	D_r	D_r ranges	sources
glacier	Norway	1.35		Feder, 1988
	s1, s2, Scotland	1.36	1.35-1.37	Chapter 5
river down-cutting	e3, England; i1, i2, Ireland	1.24	1.20-1.30	Chapter 5
	topographic contours of border areas between Spain and Portugal	1.23	1.10-1.47	Chapter 3
	north shore line, Manitoulin, Canada	1.29		Kaye,1989
wave action	South Africa	1.02		Mandelbrot, 1977
	i3, Ireland; e1, e2, England; s3, s4, s5, Scotland	1.11	1.04-1.15	Chapter 5
	cliff profiles of Kimmeridge and Studland Bay	1.03	1.01-1.09	Chapter 4
	south shore line, Manitoulin, Canada	1.09		Kaye,1989

The low D values (D = 1.01 - 1.15) of the coastlines of Dorset (e1 and e2), of the East Scotland (s3, s4, and s5), and of the north-east Ireland (i3) occur where the coastline is controlled by the cliff retreat / wave action. If coastal erosion by wave action and cliff retreat operates on an initially smooth coastline, the waves will cut back the coastline. If there are not any local differences in weathering, the resulting coastlines would be expected to be "straighter" or "smoother", and will have a lower D value, say $D \approx 1.1$ ($1 < D < 1.5$). The D values of field profiles of Dorset also have low D values (D = 1.03), and this suggests that low D values for cliff retreat process occur over a wide ranges of scales (from 10 cm to 60 km). Marked lithology variations may produce some what higher D values.

The moderate D values (D = 1.20 - 1.35) obtained for the coastline sections of the British Isles which are dominated by river down-cutting processes (e3, i1 and i2) are similar

to those of the topographic contours of the border areas between Spain and Portugal as discussed in Chapter 3. Down-cutting erosive processes by river action is associated with large amounts of mass-wasting, feeding sediments into the low reaches of river or sea, and produces rougher and more rugged coastlines. A coastline with a fractal dimension , say D = 1.3, is subject to the locally concentrated river down-cutting erosion process, and is a result of sea-level rises.

The highest D values (1.35 - 1.50) of coastlines around the British isles occur in the north-west of Scotland, where the formation of the coastline dominated by the abundant glacier valleys. This group of D values could be compared with those obtained from the coastlines of Norway (D = 1.35, Feder, 1988).

In summary, the fractal dimensions of the coastlines and contours are dominantly controlled by different erosive processes. The coastlines formed by down-cutting erosion, such as river networks and glaciers, have higher D values ($1.20 < D < 1.37$) than those formed by wave action erosion ($1.03 < D < 1.20$). Coastlines produced by drowned river valley or glacier valley system will have similar fractal dimension. The moderate D values of the coastline sections of British Isles where river down-cutting erosion is dominant are similar to the D values of topographic contours in the border area between Portugal and Spain. In more general terms, the land surface formed by the variation of erosive power on the river network would have a fractal dimension between 2 and 3, and the contours would be expected to have $1 < D < 2$.

5.4.2. Lithology

The 123 contours from the border area between Spain and Portugal as discussed in Chapters 3 were from two major rock groups - Igneous (48 contours) and Metamorphic (75 contours). Erosion in the area is largely controlled by the river down-cutting and associated with mass-wasting processes. For the ruler method, the fractal dimensions of the contours from the granite areas (D = 1.25) are slightly higher than those from the metamorphic rock areas (D = 1.20) as determined by the ruler method (Table 5.6). Although the difference is small, it is statistically significant. Furthermore, the difference is not caused by the methods employed, but by the difference of rock groups. This indicates that the topographic contours from granite areas are more rugged than those from the metamorphic rock areas. The metamorphic rocks in the area tend to be rich in soil, and are controlled by mass-wasting process, hence have smoother contours. The granites in the area, however, are more

resistant to the weathering process and produce more irregular contours.

As discussed in Chapter 4, there are two pairs of field profiles from Kimmeridge Bay, Dorset, England: kdo1 vs ksh1 (nominal length L_n = 10 m) and kdo2 vs ksh2 (L_n = 11.8 m). The shale layer is located just underneath the dolomite one (Fig. 4.5). Their fractal dimensions determined by the ruler method (Table 5.6) show that the dolomite profiles have slightly higher D values (more irregular) than the shale profiles. The small difference in D is effective. Firstly, the observation scale is the same, between the lower and upper fractal limits (r_{RL} = 0.02; r_{RU} = 5 m). Secondly, the difference coincides with the analysis results of the spectral, structure function, and average measurement methods (Table 4.9). Thirdly, the comparison of the appearances between the dolomite profiles (kdo1 and kdo2, Fig. 4.5b and d) with shale profile (ksh1 and ksh2, Fig. 4.5a and c) shows that the dolomite profiles are more irregular than the shale profiles. This corresponds to the geological fact that the shale layer is more easily eroded away, and becomes smoother than the dolomite layer, whose profile variation is mainly controlled by the fractures (or joints) in the area.

Table 5.6. The summary of D values of different contours from Chapters 3 and 4

location	D_r	D_r range	lithology	sources
Spain/Portugal	1.19	1.19 - 1.23	metamorphic rocks, sediments	Chapter 3
	1.25	1.24 - 1.25	igneous rocks	Chapter 3
Dorset (kdo1), England	1.04		Kimmeridge dolomite	Chapter 4
Dorset (kdo2), England	1.07		Kimmeridge dolomite	Chapter 4
Dorset (ksh1), England	1.01		Kimmeridge shale	Chapter 4
Dorset (ksh2), England	1.05		Kimmeridge shale	Chapter 4

Leonardi *et. al.* (1994) conducted fractal analyses of the coastline segments of volcanic islands of Vulcano, Stromboli and Alicudi in southern Tyrrhenian sea, and concluded that high D values (1.34) characterize acid rocks derived effusive activity; intermediate D values (D = 1.07) for pyroclastic deposits from explosive activity; and low D values (D = 1.01) for those deposits strongly reworked and considered as alluvium.

These examples suggest that in some coastal situations rock type may have an effect on D values, but the coastlines of the British Isles show that the lithological control is more subtle than that of river erosion.

Table 5.7 shows the fractal dimensions of the coastlines of England, Scotland, and

Ireland organized at the order of the resistance of rock types to erosion. From Table 5.7, it can be seen that fractal dimensions of the coastline sections of the British Isles have not any systematic relationship with the resistance of the rock types. Although it would appear that erosion processes (as discussed in the previous section) rather than lithologies are dominant in the control of the fractal dimensions of the coastlines of British Isles.

Table 5.7. The D values of the coastline and contours from different lithologies

location	lithology	D_r
resistant	s1 and s2 (Lewisian gneiss, Torridonian sandstone, Moine metamorphic rocks)	1.37
	i3 (Tertiary basal, Dalradian metamorphic rocks, and Carboniferous-Cretaceous sediments);	1.15
	e3 (Devonian sediments, intrusive rocks); s3 (Devonian old red sandstone); s4 (metamorphic rocks and Devonian sediments); i1 and i2 (Devonian, Carboniferous sediments)	1.08 - 1.35
less resistant	e1 and e2 (Mesozoic sediments); s5 (Carboniferous sediments) .	1.04 - 1.12

In summary, different lithologies contribute to the variation of D values. The studies carried out in Chapter 3 shows that the fractal dimensions of igneous rocks are significant higher than those of meta-sediments, and dolostone have higher D value than the shales. In these two cases, the effects on D of erosive processes were excluded, whereas the variations in D values of coastlines of England, Scotland and Ireland are compound controlled by the erosive process and lithologies. Therefore, the erosive process might be the primary control, and lithology tends to produce more subtle variations in D values of coastlines and topographic contours.

5.4.3. Fractures

Different fracture patterns also contribute to the variation in the fractal dimensions although this is not clearly demonstrated in the study of the British Isles. Xie (1993) and Xie and Sanderson (1995) studied the intergranular and transgranular cracking systems, and concluded that the transgranular fractures possess higher fractal dimension (D = 1.37) than the intergranular fractures (D = 1.26) (Table 5.8). After study the topographic contours of Sawtooth Range, Idaho, Norton & Sorenson (1989) shown that the fractal dimensions of the topographic contours vary from 1.11 to 1.26, and that the larger D values occur locally where fractures are most frequent and/or continuous. Xie and Pariseau (1994) provided an empirical relationship between the fractal dimension and the joint roughness coefficient

(JRC) based on the study of the triadic Koch curve, i.e., JRC = 85/2671 $(D-1)^{0.5679}$. In other words, JRC is positively correlated with the fractal dimension.

The fault deformed profile (fault trace) produces a low fractal dimension. For example, the west boundary of the Dixie valley (fault segment) has a low D = 1.03, while the east boundary has a higher D (= 1.22). The fractal dimension of the Dixie fault segment D = 1.03 is similar to that of the San Andreas main fault D = 1.02 (Aviles *et. al.*, 1987).

Table 5.8. D values of the coastline, contours, and profiles oriented with different fractures

fracture features, and/or file	D_r	sources
intergranular fracture	1.26	
transgranular fracture	1.365	Xie and Sanderson (1995)
combined intergranular and transgranular fracture	1.255	
San Andreas main fault line	1.02	Aviels *et. al.* 1987
along fault strike, dxw	1.03	(Zhang, 1991), Chapter 5
unconformity, dxe	1.22	
crossing fault strike, i2	1.35	Chapter 5

The curve perpendicular to the structure strike is more irregular, thus has higher D value, than that parallels to the structure strike. The coastline i2 (SW of Ireland) is perpendicular to the general structure strike (note main effect here is folding), and have high D values of 1.25 and 1.35. This may also be explained as lithological control since folding produces changes in rock types along the coast. Power *et. al.* (1987) concluded that the fault profiles parallel to the slip direction are much smoother than those perpendicular to the slip direction. Fault roughness perpendicular to the slip direction is similar to the roughness of natural joints. This is because the fractures control the locally weathering and erosive processes, hence dominate the formation of coastlines traces and have higher fractal dimension.

In summary, higher D values of coastlines, contours, or profiles are derived from the regions where fractures are abundant. High D values also occur as the orientation of the curve cross-over with the structural strike, whereas fault deformed profile usually leads to low D values.

5.5. CONCLUSIONS

Based on the study carried out in this chapter and the summarized analysis results of Chapter 3 and 4, the following conclusions may be drawn.

1. Significant variations in fractal dimensions exist and are controlled by several geological factors (such as erosive process, lithology, and fractures) which contribute the formation of coastlines, topographic contours, and profiles.
2. The dominant control on the fractal dimension, D, is the erosive processes. Contours and coastlines formed by the down-cutting erosion by rivers and ice have higher D values than those formed by the wave action and cliff retreat processes. The former has a fractal dimension D ranges from 1.1 to 1.5, whereas the latter generally give low D values of D < 1.10. The D values of field profiles of Dorset also have low D values (D = 1.03), and this suggests that low D values caused by the cliff retreat process occur over a wide ranges of scales (from 10 cm to 60 km).
3. Different lithologies generally produce more subtle variation in the fractal dimensions of coastlines and contours. For example, the igneous rocks tend to have higher D (= 1.25) than the metamorphic rocks (D = 1.20) (Chapter 3); dolomite layers produce higher D values (= 1.13) than shale layers (D = 1.02) in Kimmeridge Bay (Chapter 4). However, the coastline of Great Britain, which cover different types of lithologies, generally shows little variation in D values (Table 5.7) with lithology, being dominated by different types of erosive processes.
4. High D values also occur as the orientation of the curve cross-over with the structural strike, whereas a fault deformed profile usually leads to low D values. For example, the fractal dimension of the Dixie fault segment D = 1.03 is similar to that of the San Andreas main fault D = 1.02 (Aviles *et. al.*, 1987).

CHAPTER 6

FRACTAL ANALYSIS OF DEM AND LANDSAT TM DATA

CHAPTER 6

FRACTAL ANALYSIS OF DEM AND LANDSAT TM DATA

6. FRACTAL ANALYSIS OF DEM AND LANDSAT TM DATA

6.1. INTRODUCTION

The fractal concept has, in the last decade, become the most successful mathematical model for characterizing the spatial variation of the Earth's surface. This success is due to the fractal model being able to capture the essence and complexity of the Earth's surface systematically and quantitatively, while other traditional parameters do not (Lam, 1990; Power and Tullis, 1991; Weissel, 1994). There are numerous references, which are listed by Xu *et. al.* (1993), Malinverno (1995), concerning the fractal analysis of the Earth's surface, as well as the methods for calculating fractal dimensions. These studies cover a wide spectrum including landforms, seafloor, river networks, faults, earthquakes etc.

Two popular and convenient representations of the Earth's surface variation involve use of digital elevation models (DEM) and satellite Thermal Mapper (TM) imagery. They are both 2-d, equally intervalled, raster data sets. DEM data are the elevation variations of the Earth's surface, and include only the topographic information. However, TM data reveal the electromagnetic radiation (EMR) variations of different spectral wavelengths of the Earth's surface. In other words, TM data are the representations of the local scale spectral variability, such as roads, buildings, vegetation, shadows etc. Although TM data do not represent the real topographic refection, the local spectral features can indirectly reflect topography. Therefore, DEM and Landsat TM images are useful in characterizing the

spatial variation of the Earth's surface, thus the complexity of these spatial surfaces could be described and measured by the fractal concept. Previous studies have shown that the question of whether or not the fractal model can be applied to DEM and Landsat TM data seems to have a positive answer (Shelberg *et. al.*, 1983; Mark and Aronson, 1984; Roy *et. al.*, 1987; Lam, 1990; Lavallee, 1993; Weissel *et. al.*, 1994). DEM data have fractal dimensions of 2.10 to 2.50 (Shelberg *et. al.*, 1983; Mark & Aronson, 1984; Roy *et. al.*, 1987) by using USGS 30-metre DEM grid data. Lam (1990) demonstrated that TM images of the coastal Louisiana areas have fractal dimensions of 2.54 to 2.87 over the observation scale between 25 m and 150 m.

The methodologies for determining the fractal dimension of DEM data are the 2-d intersection, cube (3-d box) counting, triangular prism, 2-d spectral, first and second order structure function methods; for determining the fractal dimensions of TM data are the 2-d spectral, first and second order structure function methods. The fractal analysis of extracted coastline from TM data is carried out by the ruler and box-counting methods.

The objectives of the fractal analysis of DEM data are to:

- determine the fractal dimension of DEM of the border area between Spain and Portugal and to compare the determined D value with the previous studies;
- relate the determined D value of DEM with the previous work done on contours (Chapter 3) since DEM is the 3-d model of the topographic surface in same area.

The objectives of the fractal analysis of TM data are to:

- investigate whether TM data are fractals;
- study what can be learnt from the fractal properties of TM data, including:
    - ◊ comparison between the D values of TM imagery of Qatar with those derived by Lam (1990), as well as with those of the DEM surfaces;
    - ◊ examination of the effects of different TM bands on D values for same land type;
    - ◊ investigation of the possible variations in D values related to different land types covered. Five study areas are involved;
    - ◊ discussion of the variations of the fractal dimensions determined by different methods that reveal the scaling properties of DEM and TM surfaces;
- relate the fractal properties between 1-d and 2-d TM features by comparing the D value of the extracted coastline of Qatar with those of the 2-d TM surfaces of the coast area.

6.2. FRACTAL ANALYSIS OF DEM DATA

6.2.1. DEM data

The DEM data set was digitized from the 1:20,000 contour map (C.G.S, S.A., July 1987), which was mapped using a 10 metre interval, of the border area between Spain and Portugal. The centre of the data set is located in Spain at about N39°20′, W7°08′ as show in Fig. 6.1. The DEM data set covers a grid of 65 by 65, and an area of 640 m by 640 m.

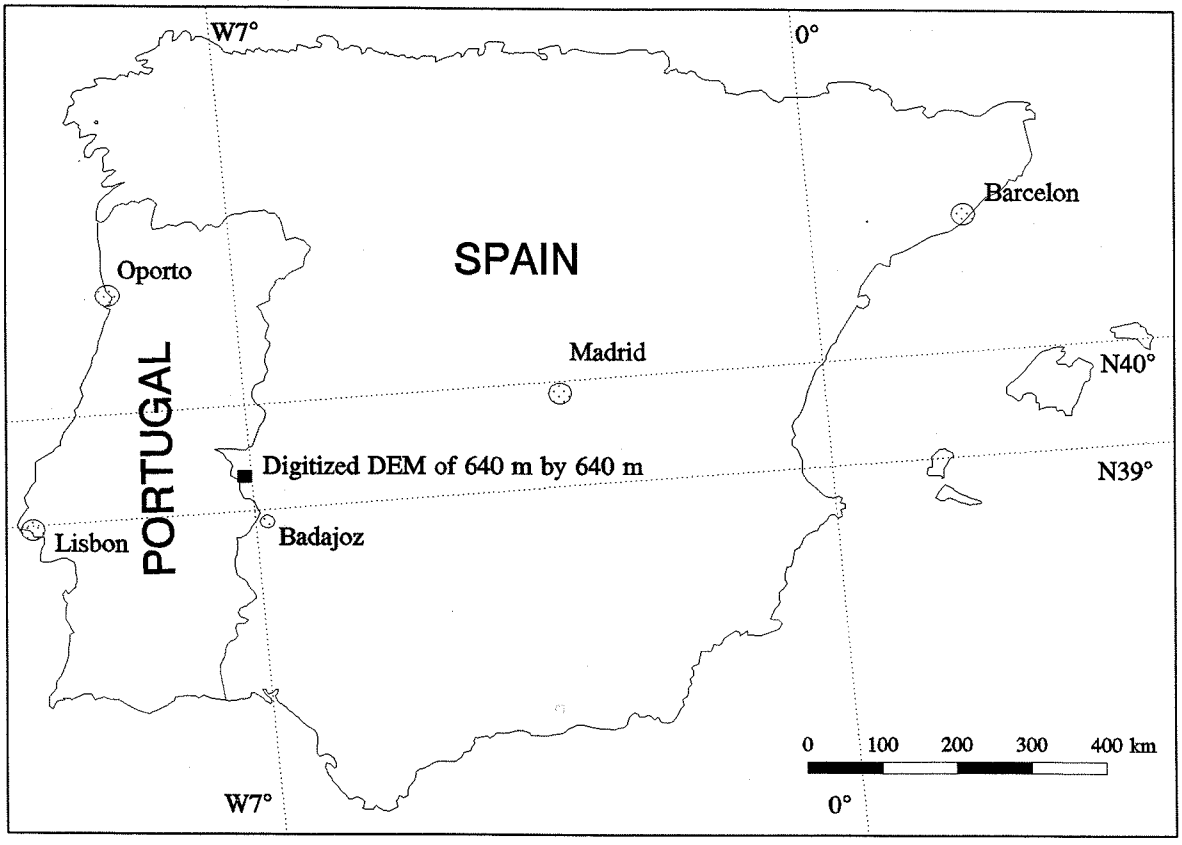

Fig. 6.1. Location of the digitized DEM.

The digitized procedure is described as follows. Firstly, a 65 by 65 square grid (each cell has a side length of 0.5 cm, thus the gridding interval is 10 m) was drawn, covering the study area. Therefore, the data grid size is 65 by 65, and has a side length of 640 m. Then the elevation on each crossing point of the grid was estimated from contours and recorded as a series of (x, y, z), where x and y are the coordinates ranging 0, 1, …, 64, and z is the contour elevation at (x, y). Since the map has a 10 m interval of contours, the estimating

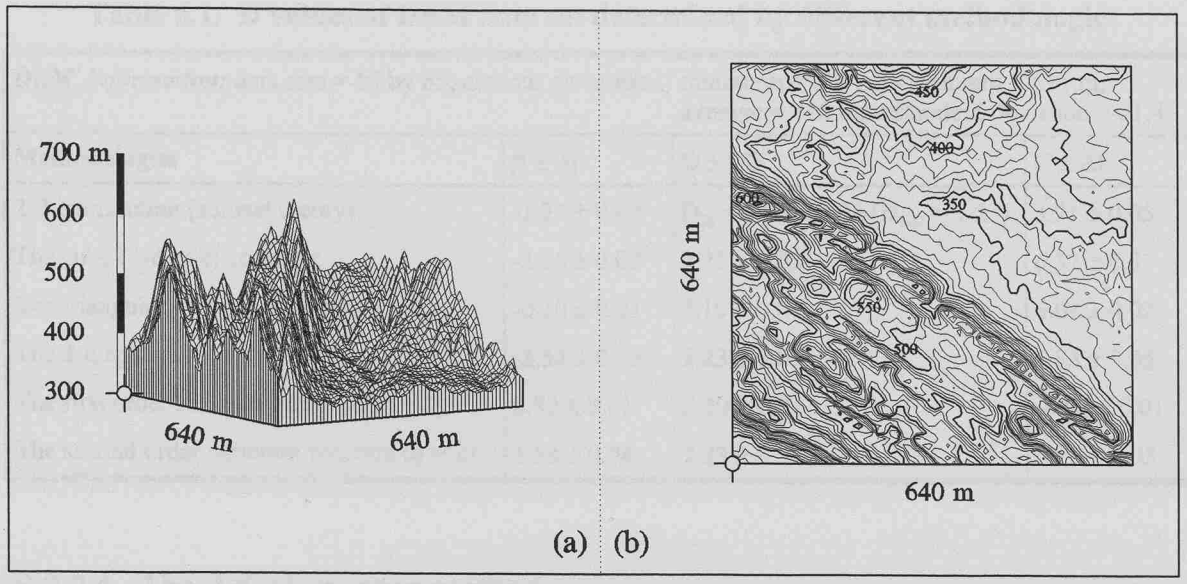

Fig. 6.2. The digitized DEM of an area of 650 m by 650 m. The board crosses in (a) and (b) show their match orientation. **(a)** 3-d perspective view of the DEM. **(b)** The digitized contour map of 10 m interval.

error of the contour elevation is expected to be about 1 m. Fig. 6.2(a) shows the digitized DEM in 3-d perspective view, Fig. 6.2(b) is the digitized contour map at a 10 m contour interval. Any possible errors could occurr during the digitizing procedure; the resulting DEM was deduced by comparing the original 1:20,000 contour map with Fig. 6.2(b).

Therefore, the DEM data set is represented by a 2-dimensional array (65 by 65) of contour elevations equally spaced with 10 m gridding interval, and the side length is 640 m. The DEM has minimum and maximum contour elevation of 309 m and 611 m, and the average and the standard deviation of contour elevation are 418.8 m and 61.4 as shown in the upper part of Table 6.1.

6.2.2. Fractal analysis of DEM data

The 2-d intersection, cube-counting (3-d box-counting), triangular prism, spectral, and structure function methods were deployed to determine the fractal dimensions of the DEM data set digitized from the 1:20,000 contour map. Brief descriptions of the different methodologies are given here, and refer to Chapter 2 for the principles and details of the methodologies.

Table 6.1 lists the fractal dimensions of the DEM data set determined by the 2-d intersection, cube-counting (3-d box-counting), triangular prism, spectral, and structure function methods. The estimation errors $\Delta\beta$, ΔD, and ΔC are given by equation (2.1).

Table 6.1. D values of DEM data set determined by different methodologies

DEM information: data size = 65 by 65; contour elevation: minimum = 309 m; maximum = 611 m; average = 418.8 m; standard deviation = 61.4.			
Methodologies	$\beta \pm \Delta\beta$	**D** $\pm \Delta$**D**	**C** $\pm \Delta$**C**
2-d intersection (zeroset theory)	-1.23 ± 0.04	D_{2i} = 2.23 ± 0.04 (D_{int2} = 1.23)	3.91 ± 0.05
The cube (3-d box) counting	-2.25 ± 0.03	2.25 ± 0.03	6.37 ± 0.07
The triangular prism	-0.10 ± 0.01	2.10 ± 0.01	6.07 ± 0.02
The 2-d spectral	-2.54 ± 0.05	2.23 ± 0.03	1.83 ± 0.05
The first order structure function (q = 1)	0.80 ± 0.01	2.20 ± 0.01	-0.02 ± 0.01
The second order structure function (q = 2)	1.53 ± 0.04	2.23 ± 0.02	0.15 ± 0.05

6.2.2.1. The 2-d intersection method

Fig. 6.3(a) is the contour set, which comprises 17 contour segments, of an elevation 418.8 m (the average elevation for the area). The contour set was resulted from intersecting the DEM surface with a horizontal plane of a vertical height, which is the average of the contour elevation values of the DEM data set. Fig. 6.3(b) is the log-log plot of the box-counting method applied on the contour set shown in Fig. 6.3(a), where N_r is the number of boxes of a side length of r needed to cover the contour set. The fractal dimension of the DEM data set D_{2i} = 2.23, which is the D value of the contour set D_{int2} plus 1 based on the zero set theory (Table 6.1). The estimate errors in D_{2i} and C_{2i} are determined by equation (2.1) as described in Chapter 2.2.1.

6.2.2.2. The cube (3-d box) counting method

The cube-counting method was applied on the digitized DEM data set, which is a 65 by 65 2-dimensional raster array of a equally spaced grdding interval (10 m). Fig. 6.4(a) shows the log-log plot of the number of filled cubes (N_r) against the side length of the cube (r). The "*filled cube*" is defined as such either the cube is located underneath the DEM surface or the cube contains any portions of the DEM surface. In the study, the side lengths of the cube(s) used to contain the DEM data are 640, 320, 160, 80, 40, 20 and 10 m.

As shown in Fig. 6.4(a), the fractal dimension of the DEM data set D_{2b} = 2.25 as determined by the cub-counting method. The estimated errors ΔD_{2b} and ΔC_{2b} were determined by equation (2.1) in Chapter 2, and are shown in Table 6.1.

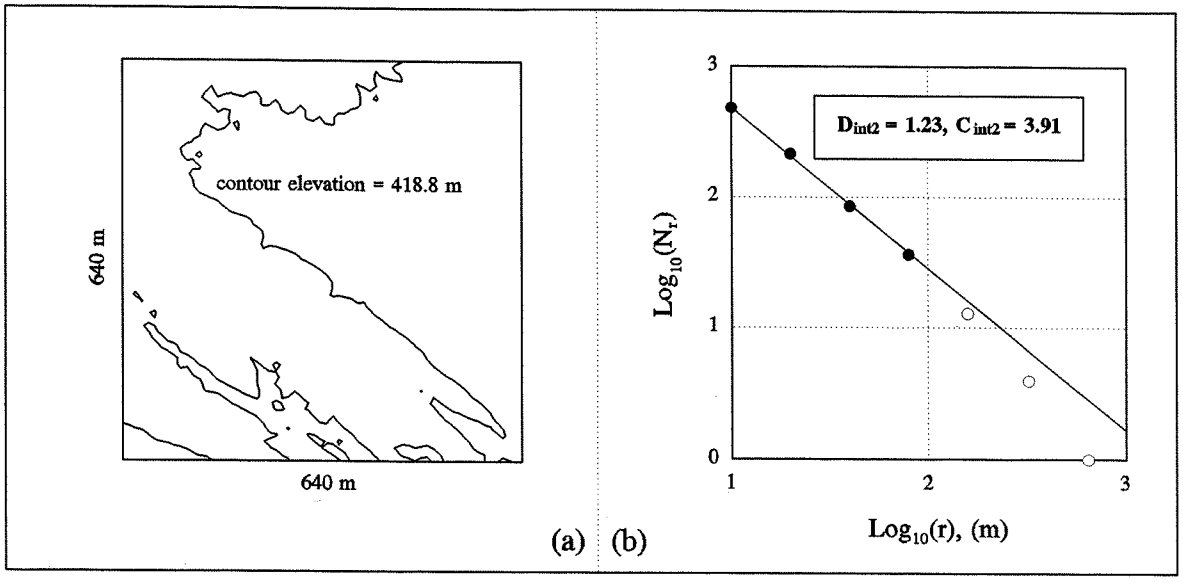

Fig. 6.3. Application of the 2-d intersection method applied on DEM data set. **(a)** perspective view of the intersected contour set (17 contours) of contour elevation of 418.8 m. **(b)** log-log plot of the box-counting method applied on the contour set shown in (a).

6.2.2.3. The triangular prism method

The triangular prism method was used to determine the fractal dimension of the DEM data set. Fig. 6.4(b) shows the log-log plot of the surface area S against the resolution area s, where $s = r^2$ and r ranges from 10 m to 640 m The slope of the regression line is β = -0.10, hence the fractal dimension $D_t = 2.10$. The estimated errors ΔD_{2b} and ΔC_{2b} were determined by equation (2.1) in Chapter 2, and are shown in Table 6.1.

6.2.2.4. The 2-d spectral method

The original DEM surface (without trend removed) were filtered by the 2-d Hanning window presented by Subba Rao (1991), then the mean power spectral density P(k) at radius wave number k was estimated used the method presented by Turcotte (1992). The slope of the fitted line of the plot of Log[P(k)] against Log(k) is β, and the fractal dimensions derived from the 2-d spectral method D_{2f} is given by equation (2.5). The definition of P(k) and k, together with the principles of the method, are given in Chapter 2.5.3.

Fig. 6.4(c) shows the plot of Log[P(k)] against Log(k), where P(k) is the mean power spectral density at the radius wave number k. The slope of the regression line is β = -2.54, thus the fractal dimension of the DEM data $D_{2f} = 2.23$ as determined by the

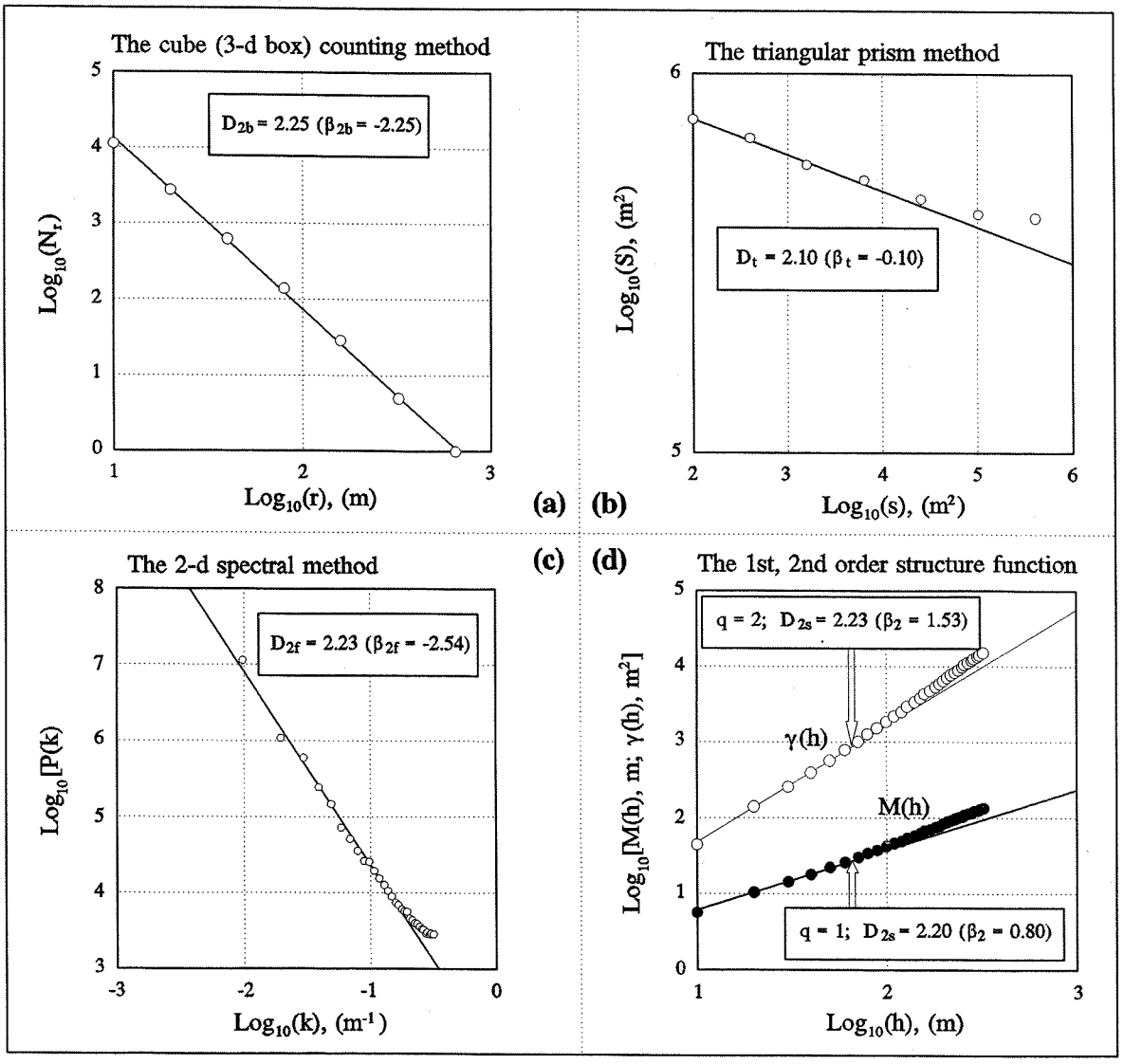

Fig. 6.4. The log-log plots for determining the fractal dimensions of the DEM data using the cube counting **(a)**, triangular prism **(b)**, 2-d spectral **(c)**, 1st and 2nd order structure function **(d)** methods. Refer to text for more details.

2-d spectral method over the range of the radius wave number between 0.01 and 0.11. The estimated errors ΔD_{2f} and ΔC_{2f} were determined by equation (2.1) in Chapter 2, and are shown in Table 6.1.

6.2.2.5. The structure function method

The first (q = 1) and second (q = 2) order structure function methods are constructed to determine the fractal dimension of the DEM data set. The pre-process of the DEM data is similar to that of the 2-d spectral method. The original DEM surface (without trend

removed) were filtered by the 2-d Hanning window, then the mean absolute DEM surface relief M(h) and the mean semivariance $\gamma(h)$ for the lag h ($10 < h < 320$ m) were estimated. Given that the slopes of the fitted line of the plots of Log[M(h)] and Log[$\gamma(h)$]against the lag h are β_1 and β_2, then the fractal dimensions D_{2s} determined are given by equation (2.7).

Fig. 6.4(d) shows the plots of Log[M(h)] and Log[$\gamma(h)$] against Log(h), where M(h) and $\gamma(h)$ are the mean absolute relief and the mean semivariance of the DEM data set, and h is the lag. The slopes of the regression lines are $\beta_1 = 0.80$ and $\beta_2 = 1.53$, thus the fractal dimension of the DEM data $D_{2s} = 2.20$ and 2.23 derived from the 1st and 2nd orders structure function method. The estimated errors ΔD_{2f} and ΔC_{2f} were determined by equation (2.1) in Chapter 2, and are shown in Table 6.1.

6.2.3. Discussions

The fractal dimension of the DEM data set is $D_2 = 2.23$ (Table 6.1) derived from different methodologies except the triangular prism method which leads $D_2 = 2.10$. The difference in D is caused by the methodology (triangular prism method) itself. As discussed in Chapter 2.9, the triangular prism method produces a power-law relationship between the surface area S and a resolution area of s^2. The concept of fractal reveals the power-law relationship between the number of the objects (N_r) and the characteristic size r of the objects (Chapter 1.3), i.e., $N_r = C\, r^{-D}$. Obviously, the triangular prism method does not meet the requirements of the definition of a fractal set. We revealed a power-law relationship between S/s^2 and s, and the slope of the regression line is $\beta = -2.20$ which is closer to the D values derived from the intersection, spectral and structure function methods. But this may require further investigation in the future.

The D values of DEM data and the topographic contours satisfy the zeroset theory. The border area between Spain and Portugal has a fractal dimension of 1.23 for the topographic contours, of 2.23 for the surface elevation variation. As discussed in Chapter 3, the 132 topographic contours have an average fractal dimension of $D_1 = 1.23$ derived from both the ruler and box-counting method. The fractal dimension of the DEM data set as shown in this section is $D_2 = 2.23$ derived from different methodologies (except the triangular prism method).

In summary, the DEM data of the border area of Spain and Portugal of a gridding interval of 10 m (elevation contours are every 10 m) has a fractal dimension of $D_{2s}(q = 2) =$

1.23 and $D_{2s}(q = 1) = 1.20$, i.e., $2\beta_1 - \beta_2 = 0.07 > 0$. Lavalle *et. al.* (1993) and Weissel *et. al.* (1994) revealed that the positive value of $2\beta_1 - \beta_2$ shows the surface is multi-scaling, therefore, the DEM data in the study area behaviours multi-scaling property.

6.3. FRACTAL ANALYSIS OF TM DATA

6.3.1. Brief introduction to Landsat TM data

Since 1972 there have been six Landsat satellites launched by NASA (the National Aeronautics and Space Administration). Landsat 6 failed to be put into orbit, while Landsat 5 an earlier MSS (multi spectral scanners) are still in orbit gathering TM (Thematic Mapper) data. The most important features which characterize TM data are of four types: ***spectral***, ***spatial***, ***radiometric***, and ***temporal resolutions***.

The spectral resolution: The spectral resolution defines a specific wavelength interval, which is often in μm (1μm = 10^{-6} metre) (Simonett, 1983). Records for each spectral wavelength interval form a 'band'. The TM scanner is a multi-spectral scanning system which records the electromagnetic radiation (EMR) in seven intervals of spectral wavelengths (Table 6.2) (Star and Estes, 1990). TM data have a swath width of approximately 185 km (i.e., a single TM image covers an area of about 185^2 km^2) taken from a flight height of approximately 705 km.

Table 6.2 Six spectral bands of Thematic Mapper (TM) (Star and Estes, 1990)

Band	Wavelength (μm)	Characteristics
B1	0.45 - 0.52	Blue-green, maximum penetration of water, useful for mapping coastal water areas, differentiating between soil and vegetation, forest type mapping and detecting cultural features.
B2	0.52 - 0.60	Green, matches green reflectance of peak of vegetation, useful for identifying cultural features.
B3	0.63 - 0.69	Red, matches a chlorophyll absorption band, useful for discriminating vegetation types, determining soil boundary and geological boundary delineations as well as cultural features.
B4	0.76 - 0.90	Reflected-Infrared, useful for determining biomass content and for mapping shorelines.
B5	1.55 - 1.75	Mid-Infrared, sensitive to the amount of water in plants, penetrates thin clouds, good contrast between vegetation types, discriminating clouds, snow and ice.
B6†	10.40 - 12.50	Thermal Infrared, useful for vegetation and crop stress detection, heat intensity, insecticide applications and for locating thermal pollution, and geothermal activity.
B7	2.08 - 2.35	Mid-Infrared, useful for discriminating geologic rock formations and soil boundaries, as well as soil moisture content.

† : This is the thermal band. The Landsat TM data in the study area lack thermal band cover because of the unsuitability of this band in a desert area

The spatial resolution: TM data are organized as raster data of seven layers if a band is regarded as a layer. They are laid out in a grid similar to the square on a checker board in which a grid cell is represented by a pixel. A pixel is the smallest unit of a TM image and is abbreviated from 'picture element'. The spatial resolution is the area of a pixel, which can be recognized by the scanner sensor (Simonett, 1983), and is 30 m by 30 m for all bands except the thermal band (band 6), which has a spatial resolution of 120 m by 120 m. For each band, there are about 6167 (=185,000/30) pixels for a single TM image of a swath width of 185 km.

The pixel value is termed a digital number (DN), which represents the amount of EMR energy for the pixel in a band. The higher the DN is, the more EMR energy the TM scanner received. TM data are thus, digital representations of the earth, stored as an image file on a magnetic tape or computer disk. These representations form images when they are displayed on a screen or output as a hard copy.

The information of a single pixel for each band can be expressed by (x, y, z_i), where x (column) and y (row) are the location of the pixel in a 2-dimensional coordinate system, and z_i is the value of DN of the i^{th} band (layer).

The radiometric resolution: This is also termed the pixel depth, which defines the range of DN values. For a 8-bit system, each pixel has a possible range of DN from 0 to 255 ($= 2^8-1$).

The temporal resolution: It refers how often a sensor obtains imagery of a particular area. For Landsat TM, this is every 16 days. It is not used in the study.

6.3.2. Landsat TM data

The Landsat TM quadrant of the northern part of Qatar, as shown in Fig. 6.5, was selected due to its light cover of vegetation. From the TM quadrant, five study areas which present five distinct ground classes were extracted based on their different land types (from the 1:50,000 geological map of Qatar) as shown in Fig. 6.6. Table 6.3 summarizes the TM quadrant information and image features, including the land features and the upper-left coordinates, of each subset area.

Each of the five study areas is a small subset of the image, which has 64 by 64 = 4096 pixels, and covers an area of approximately 4 km^2. The TM image of the study area lacks thermal band 6 shown in Table 6.2, therefore there is 6 bands and the band 7 replaces

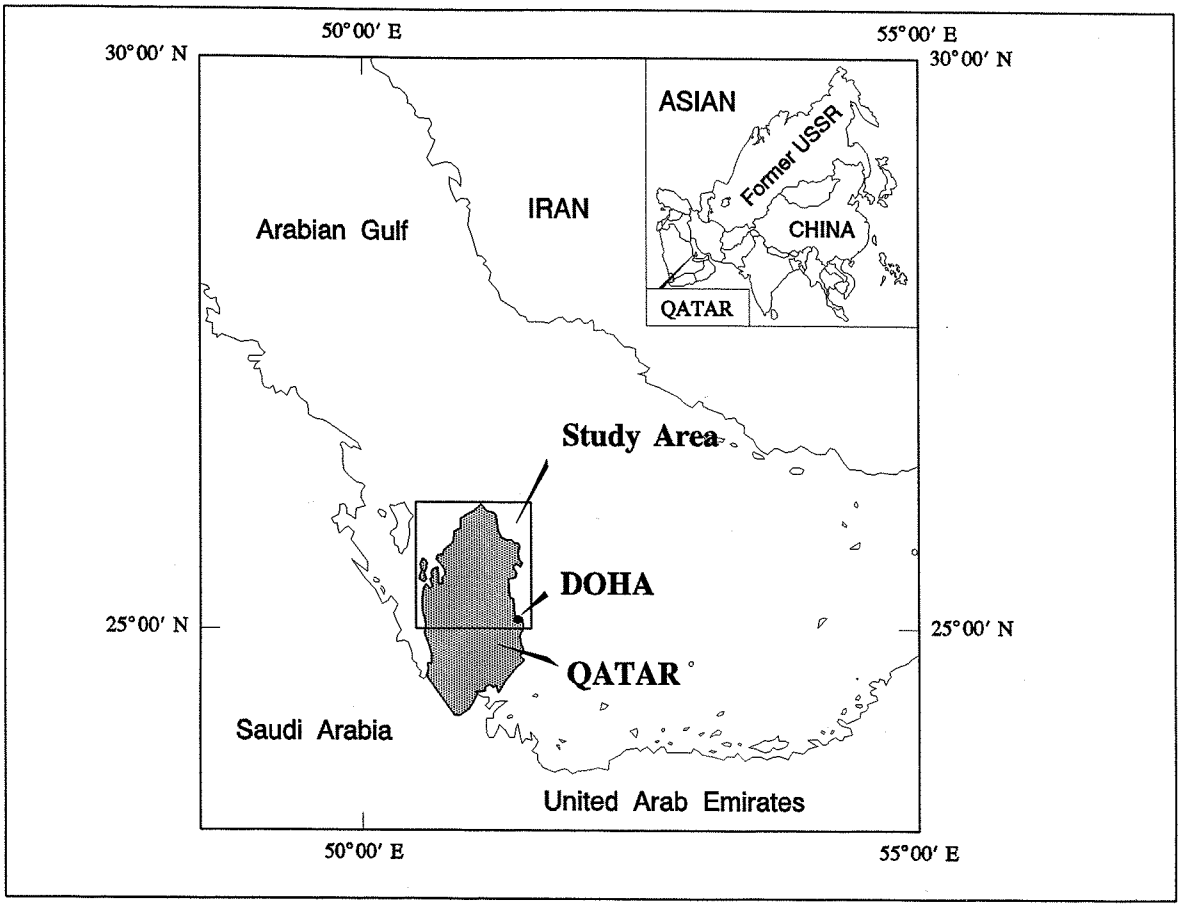

Fig. 6.5. Geographical locations of Qatar and the study area.

Table 6.3 Different land types of five study areas from Qatar

TM information:	Areas	Land features	Upperleft position
Format: **RAE** Spatial resolution: **30 m**	**A**, Edm2	dolomite and limestone	1369, 1144
Block factor: **1** Date: **06-06-1990**	**B**, Qmcs	calcareous sand of marine origin including coastal dunes, locally cemented	2215, 1141
Upper-left: **(1, 1)**	**C**, Qsb	saline, gypsiferous and silt flats	2545, 1639
Lower-right: **(6967, 5965)**	**D**, Coast	coastal area	2524, 2113
Pixel depth: **8-bit**	**E**, Urban	urban area (Doho, the capital of Qatar)	2258, 2445

band 6 in later discussion.

Fig. 6.7 shows composite images of the five study areas A, B, C, D, and E using bands 4 (Red), 3 (Green) and 2 (Blue). The DNs for all the five study areas range between 0 and 127.

Table 6.4 lists statistical summaries of the six bands of TM data from the five study

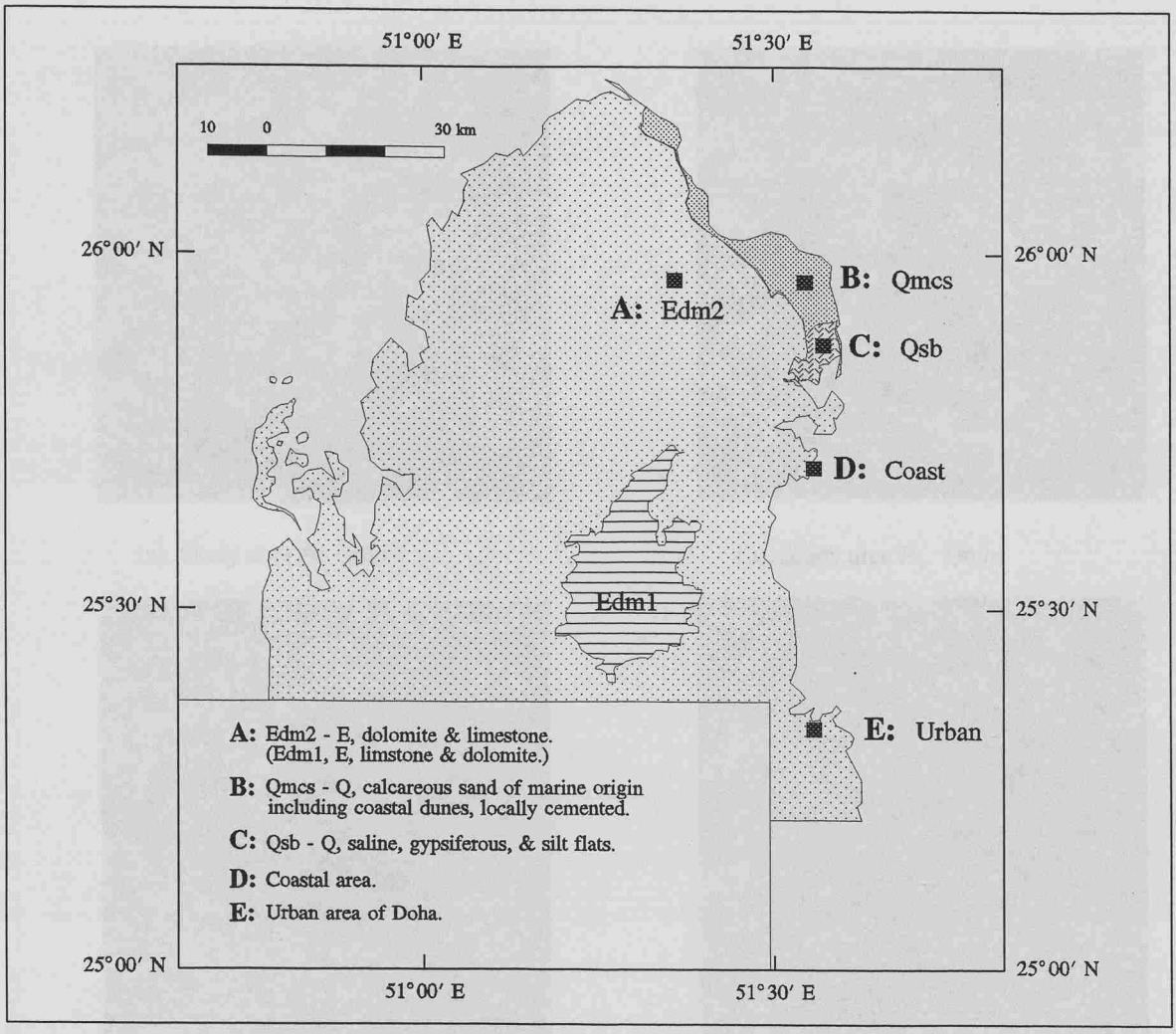

Fig. 6.6. Geographical locations of five Study areas from Qatar.

areas. It is expected that standard deviations in DN of the six bands from the coastal area will be greater than those from the other areas since the coastal area is covered by part land and part sea. The RSS%, which was described in Chapter 2.4.2, is used to characterize the trend of the TM surfaces

6.3.3. Fractal analysis of TM data

All six bands of the five study areas were used for the analysis. Each study area has different land type features (Table 6.3) and, for the same study area, each band reflects different spectral characteristics (different wavelength bands). The purpose of choosing and analyzing the TM image data of different land types and different bands is to investigate the effects of the different land types and different bands on the fractal dimensions.

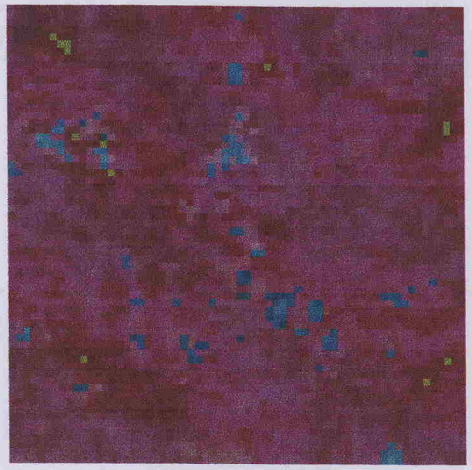

(a). Study area A: Edm2

(b). Study area B: Qmcs

(c). Study area C: Qsb

(d). Study area D: Coast

(e). Study area E: Urban (Doho)

IMAGE =
Bands 4 (Red) + 3 (Green) + 2 (Blue).

Fig. 6.7. Composite images of study areas A, B, C, D, and E using bands 4 (Red), 3 (Green) and 2 (Blue).

Table 6.4 Summary statistics of TM data for all six bands and five study areas

Band	Area, Symbols	Max	Min	Avg	Std	RRS (%)
B1	A, Edm2	45	23	36	2.8	6.8
	B, Qmcs	73	43	60	6.2	69.6
	C, Qsb	127	0	44	20.0	13.1
	D, Coast	127	0	86	35.0	59.1
	E, Urban	127	0	28	14.0	3.0
B2	A, Edm2	105	90	97	1.8	0.0
	B, Qmcs	120	99	111	4.1	71.3
	C, Qsb	121	63	93	11.5	16.9
	D, Coast	123	43	78	27.0	75.0
	E, Urban	121	12	80	8.4	3.5
B3	A, Edm2	127	0	6	7.2	0.1
	B, Qmcs	38	10	26	5.6	69.1
	C, Qsb	127	0	92	36.1	1.9
	D, Coast	127	0	36	24.3	6.2
	E, Urban	127	0	97	16.6	0.2
B4	A, Edm2	127	0	119	20.9	0.1
	B, Qmcs	28	5	18	4.7	71.4
	C, Qsb	127	0	101	18.9	10.4
	D, Coast	127	0	32	34.5	6.8
	E, Urban	127	1	88	11.2	9.2
B5	A, Edm2	105	84	96	3.4	23.3
	B, Qmcs	122	94	109	4.6	56.2
	C, Qsb	127	0	73	34.3	6.6
	D, Coast	125	2	51	28.1	57.8
	E, Urban	127	0	48	48.6	0.9
B6	A, Edm2	127	0	118	22.7	0.3
	B, Qmcs	120	104	110	2.7	19.6
	C, Qsb	89	9	32	14.7	5.2
	D, Coast	126	11	51	41.8	67.8
	E, Urban	127	0	78	10.0	3.0

The spectral, the 1st, and 2nd order structure function methods are deployed to determine the fractal dimensions of all the six bands of five subsets of TM data from Qatar. Different land types of the five TM data subsets were shown in Table 6.3. The pre-processing of the TM data sets are the same as those of simulated surfaces and DEM data

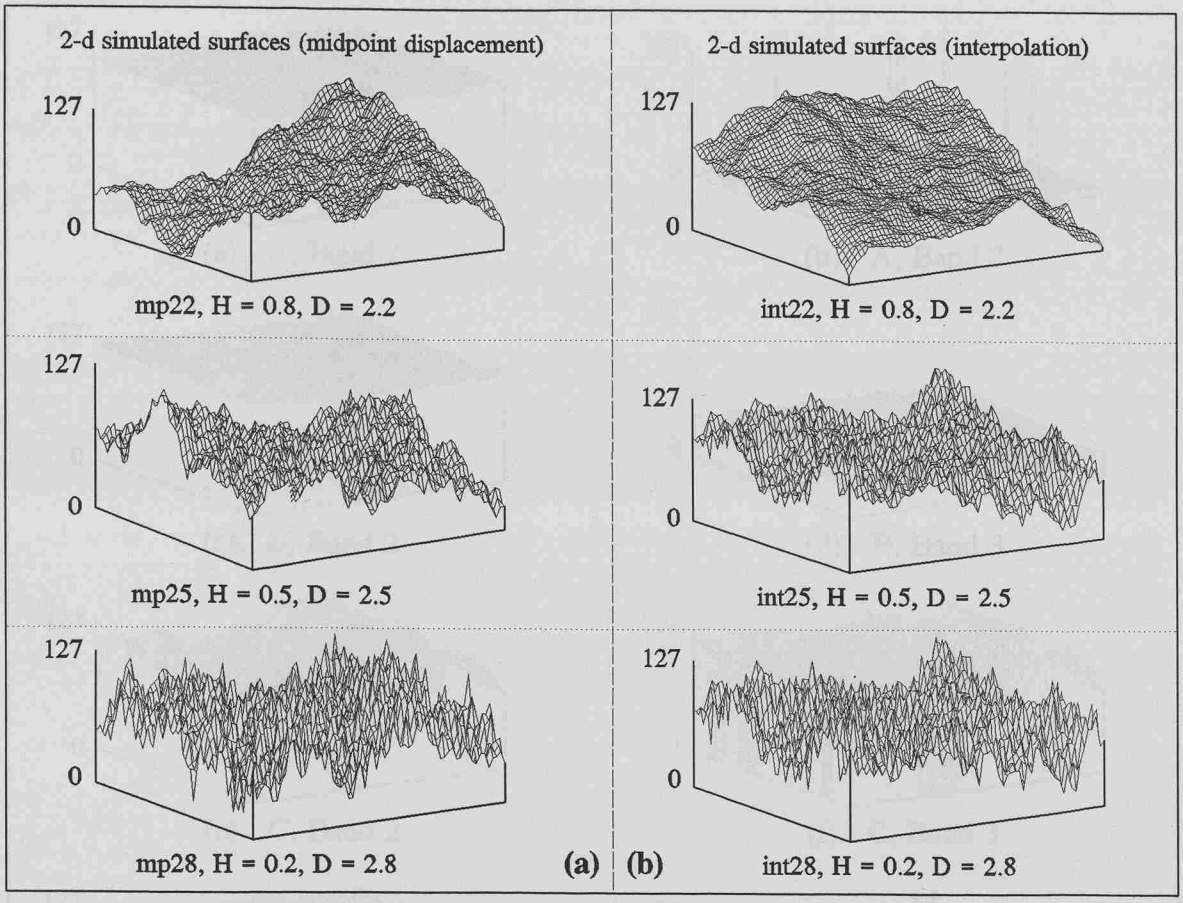

Fig. 6.8. Perspective views of the simulated 2-d fBm surfaces by the midpoint displacement and interpolation techniques using H = 0.8, 0.5, and 0.2. The vertical values of the surfaces have been linearly stretched from the range of (z_{min}, z_{max}) to the range of (0, 127). The fractal dimensions of the new surfaces remain unchanged, as 2.2, 2.5, and 2.8 respectively.

set (Chapter 2.5 and 2.6). For the spectral method, the original TM surface (without trend removed) were filtered by 2-d Hanning window (Subba Rao, 1991), then the power spectral density P(k) at the radius wave number k were estimated (Turcotte, 1992), and the fractal dimension D_{2f} of the TM data was estimated from equation (2.5). For the 1st, and 2nd order structure function methods, the original TM surface (without trend removed) were filtered by 2-d Hanning window, then the mean absolute DEM surface relief M(h) and the mean semivariance $\gamma(h)$ for the lag h ($30 < h < 150$ m) were estimated, and from their log-log plots, the fractal dimensions D_{2s} were determined by equation (2.7).

Table 6.5 summarizes the fractal dimensions (D_{2f}, and D_{2s}) and their fractal limits derived from the spectral, the 1st, and the 2nd order structure function methods for the six bands of the five study areas (A-Edm2, B-Qmcs, C-Qsb, D-Coast, and E-Urban). The

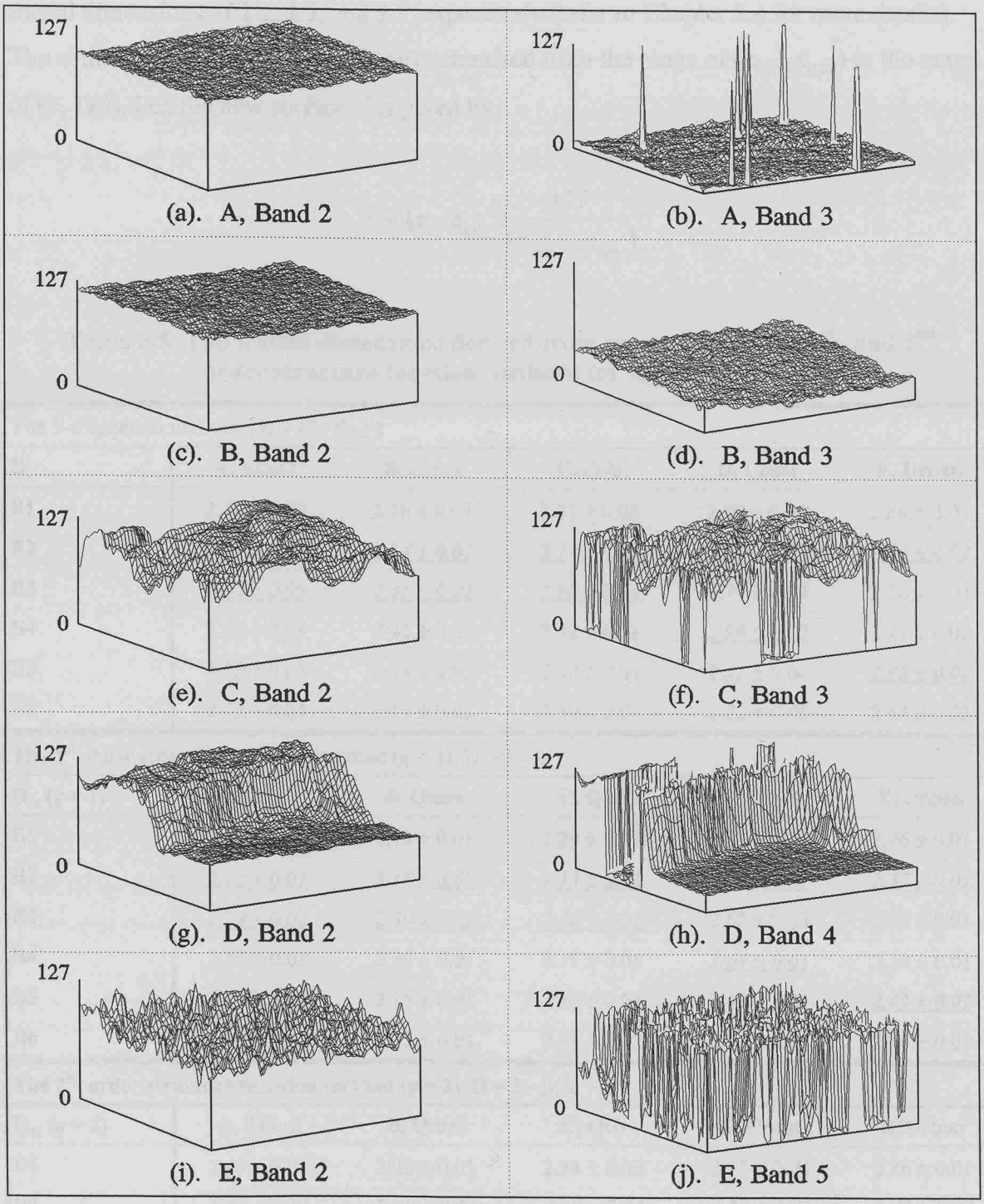

Fig. 6.9. 3-dimensional displays of some TM surface from the five study areas. The vertical values are digital numbers (DN) of the TM imagery, which ranges (0, 127).

features of different bands and different land types are shown in Table 6.2 and Table 6.3.

In order to visually compare the DN of the TM imagery, Fig. 6.8 shows the 3-d perspective view of the simulated 2-d fBm surfaces of H = 0.8, 0.5, and 0.2, they have

fractal dimensions of 2.2, 2.5, and 2.8 respectively (refer to Chapter 2.4 for more details). The simulated surfaces (z) were linearly stretched from the range of (z_{min}, z_{max}) to the range of (0, 127), i.e., the new surface z′ is given by,

$$z' = (z - z_{min}) \frac{127}{(z_{max} - z_{min})}$$

Table 6.5 The fractal dimensions derived from the spectral (D_{2f}), 1st , and 2nd order structure function methods for the study areas

The 2-d spectral method), D = (7 - β_{2f})/2					
D_{2f}	**A, Edm2**	**B, Qmcs**	**C, Qsb**	**D, Coast**	**E, Urban**
B1	2.47 ± 0.02	2.26 ± 0.03	2.31 ± 0.03	2.50 ± 0.03	2.84 ± 0.03
B2	*2.17 ± 0.05*	***2.14 ± 0.07***	*2.17 ± 0.05*	2.25 ± 0.03	*2.42 ± 0.02*
B3	*2.89 ± 0.05*	*2.46 ± 0.02*	*2.80 ± 0.04*	2.77 ± 0.03	2.56 ± 0.02
B4	2.64 ± 0.04	2.41 ± 0.02	2.32 ± 0.01	*2.90 ± 0.03*	2.41 ± 0.01
B5	2.28 ± 0.03	2.18 ± 0.05	2.58 ± 0.04	2.52 ± 0.04	***2.96 ± 0.04***
B6	2.72 ± 0.04	2.17 ± 0.05	2.39 ± 0.03	*2.22 ± 0.05*	2.44 ± 0.02
The 1st order structure function method (q = 1), D = 3 - β_1					
D_{2s} (q = 1)	**A, Edm2**	**B, Qmcs**	**C, Qsb**	**D, Coast**	**E, Urban**
B1	2.35 ± 0.01	2.19 ± 0.01	2.29 ± 0.02	2.37 ± 0.02	2.76 ± 0.01
B2	*2.12 ± 0.01*	***2.10 ± 0.02***	*2.13 ± 0.02*	*2.18 ± 0.01*	*2.37 ± 0.01*
B3	*2.79 ± 0.02*	*2.30 ± 0.01*	*2.46 ± 0.01*	2.52 ± 0.03	2.48 ± 0.01
B4	2.37 ± 0.01	*2.30 ± 0.01*	2.17 ± 0.01	*2.64 ± 0.01*	2.39 ± 0.01
B5	2.17 ± 0.01	2.15 ± 0.01	2.36 ± 0.02	2.43 ± 0.01	***2.81 ± 0.01***
B6	2.40 ± 0.02	2.12 ± 0.01	2.31 ± 0.02	*2.18 ± 0.01*	2.40 ± 0.01
The 2nd order structure function method (q = 2), D = 3 - β_2/2					
D_{2s} (q = 2)	**A, Edm2**	**B, Qmcs**	**C, Qsb**	**D, Coast**	**E, Urban**
B1	2.49 ± 0.01	2.26 ± 0.01	2.34 ± 0.02	2.68 ± 0.01	2.86 ± 0.01
B2	*2.16 ± 0.01*	***2.12 ± 0.01***	*2.18 ± 0.01*	*2.24 ± 0.01*	*2.48 ± 0.01*
B3	*2.90 ± 0.01*	*2.43 ± 0.01*	*2.79 ± 0.01*	2.81 ± 0.01	2.74 ± 0.01
B4	2.79 ± 0.01	2.42 ± 0.01	2.36 ± 0.02	*2.88 ± 0.01*	2.49 ± 0.01
B5	2.23 ± 0.01	2.20 ± 0.01	2.63 ± 0.01	2.63 ± 0.02	***2.95 ± 0.01***
B6	2.81 ± 0.01	2.15 ± 0.01	2.39 ± 0.02	2.26 ± 0.02	2.50 ± 0.02

Bold D-value is the lowest or highest D-value for the same method; *Italic D-value* is the lowest or highest D-value for the same study area; Underline D-value shows those TM surfaces are displayed in Fig. 6.9; Fractal limits for the 2-d spectral, 1st and 2nd order structure function methods are (0.01, 0.11) m^{-1}; (30, 150) m.

where z_{min}, and z_{max} are the minimum and maximum values of the original surfaces. The linear stretch process does not affect the fractal dimensions of the simulated surfaces. This is because the linear stretch consists of two steps and does not affect the scaling property of the original surfaces: the first step is that the original surface is vertically upper shifted by an amount of z_{min}; the second step is that the original surface values are multiplied with a constant of $127/(z_{max} - z_{min})$ given a specific surface.

Fig. 6.9 shows similar perspective views of some TM bands from the five study areas, and provides some visual comparison of the TM surfaces with different study areas and different bands. The displayed TM surfaces in Fig. 6.9 have either the lowest or highest D values(Table 6.5).

Compared Table 6.5 with Table 6.1, TM images have higher fractal dimensions and have more variations in D values than most terrain surfaces, such as digital elevation model (DEM), on the Earth. TM images of the study areas have $D_{2f} = 2.14$ to 2.96 with an average of 2.47 (std = 0.25) at the scale range between the wave number 0.01 and 0.11 m^{-1}; $D_{2s} =$ 2.10 to 2.81 with an average of 2.35 (std = 0.20) for the 1st order structure function method; and $D_{2s} = 2.12$ to 2.95 with an average of 2.51 (std = 0.26) for the 2nd order structure function method at ranges from 30 m to 150 m. The terrain surfaces, however, have fractal dimensions of 2.10 to 2.50 (Shelberg *et. al.*, 1983; Mark & Aronson, 1984; Roy *et. al.*, 1987) by using USGS 30-metre DEM grid data. The digitized DEM data gridded at 10 m interval of the border are between Spain and Portugal has a fractal dimension about D = 2.23 as discussed in Section 6.2.2. This is expected because TM data are more complex than DEM data. The DEM data include only topographic information, whereas, the TM data are the representations of the different spectral characteristics such as roads, vegetation, houses, and land types.

Lam (1990) used the isarithmic line algorithm, which was described by Shelberg *et. al.* (1983), to calculate the fractal dimensions of three different Landsat TM quadrants of coastal areas of Louisiana. Lam demonstrated that most TM images of the areas have fractal dimensions of 2.54 to 2.87 at the scale range between 25 m and 150 m, and concluded that TM images have higher fractal dimensions than most terrain surfaces.

The lowest fractal dimension is found in band 2 of the study area B, where $D_{2f} =$ 2.14, $D_{2s} = 2.10$ ($q = 1$), and $D_{2s} = 2.12$ ($q = 2$). A perspective view of DN is shown in Fig. 6.9(c). This is because study area B is covered by a single rock unit (calcareous sand of marine origin including coastal dunes, locally cemented), and band 2 (wavelength 0.52 -

0.60 μm) produced relatively less complexity of the TM surface in spectral characteristics.

The highest fractal dimensions are found in band 5 of the urban area of Doho (E), where $D_{2f} = 2.96$, $D_{2s} = 2.81$, and $D_{2b} = 2.95$. Fig. 6.9(j) shows its perspective view (band 5), which is so erratic that it nearly fills in the whole cube. This may be explained by the sensitivity of band 5 to the existence of different spectral characteristics and linear structures such as roads, vegetation, houses, and land types in urban area.

As can be seen from Table 6.5 and the comparison with the previous studies (e.g. Lam, 1990), fractal dimensions of TM images vary considerably with changing the methodology, study area, and band. A very important question that may be raised here is "*What dominates the fractal dimensions of TM images?*" A detailed discussion of the roles of the three factors (different land types, bands, and methodologies) on the variations of fractal dimensions is followed. The spectral and 2nd order structure function methods resulted in roughly the same fractal dimensions of the TM imagery, both of them are significant higher than the D values determined by the 1st order structure function method. The difference will be discussed in Section 6.3.3.3.

6.3.3.1. Different land types

The five selected study areas cover different land types (Table 6.3), thus their different spectral characteristics are expected to affect their fractal dimensions. Fig. 6.11 is the linear plot of the fractal dimensions against different bands (each band has five study areas) derived from the 2-d spectral, 1st and 2nd order structure function methods, where the D values are represented by the empty circles, solid circles, empty rectangles, solid rectangles, and empty triangles for the study areas of A, B, C, D, and E.

Table 6.6 shows 1), the mean and standard deviation of D values of the six bands for each study areas; and 2), the paired t-test comparison results (at a confidential level of 95%, i.e., $\alpha = 0.05$) of different study areas in the fractal dimensions determined by the spectral, 1st and 2nd order structure function methods. The paired t-test comparison of areas is compared based on paired variables for each band, and for each method. For example, six D values of six bands of the area A were paired with six D values of six bands of the area B for the spectral method.

The paired t-test comparison results (Table 6.6) indicates that the study area B (Qmcs, covers the calcareous sand of marine origin) produces the lowest D value (D is

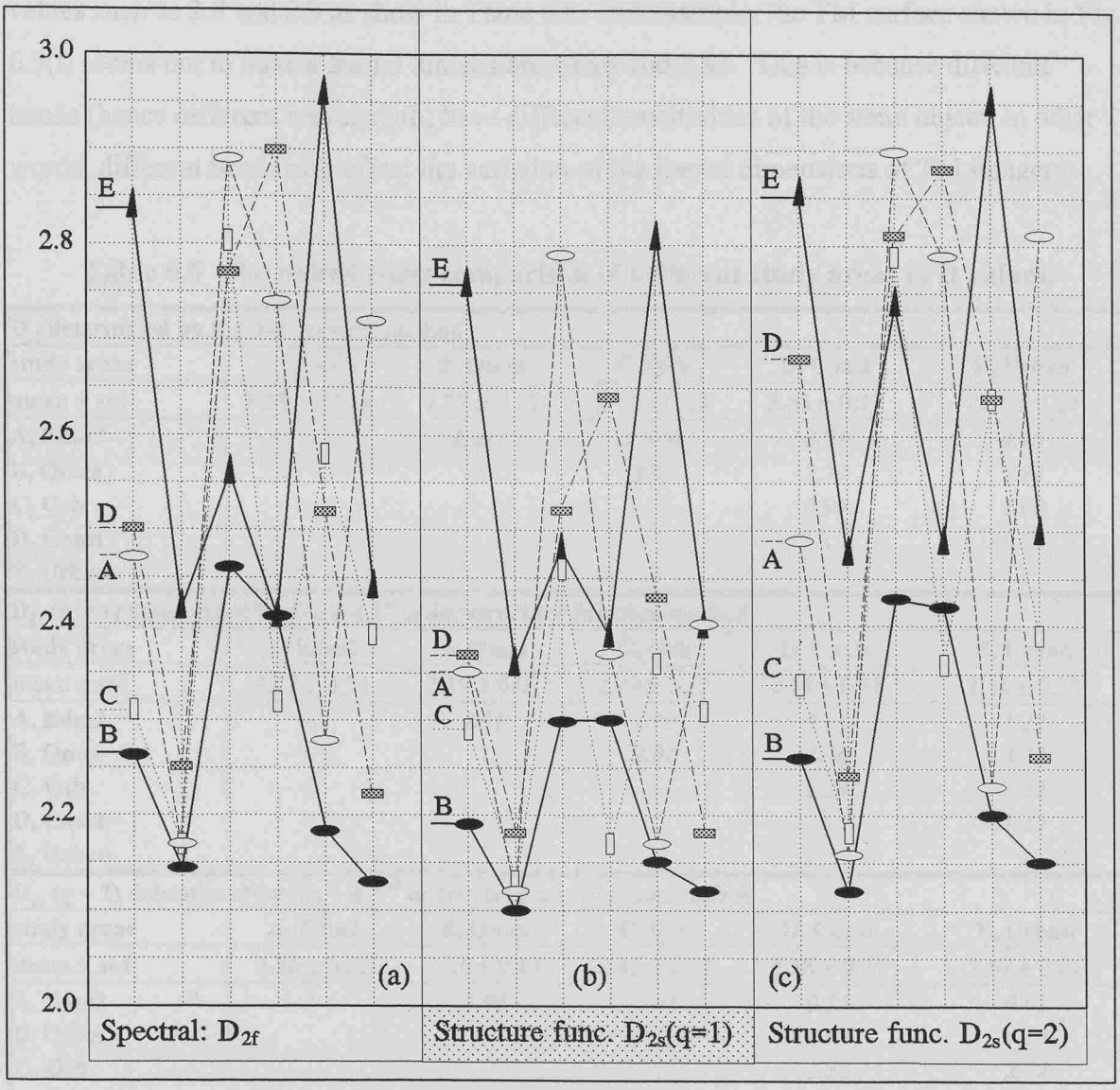

Fig. 6.10. Comparison of the fractal dimensions of TM imagery of the six bands. Each band has five study areas. Different land type features of the different study areas are shown in Table 6.3. **(a)** D values determined by the 2-d spectral method (D_{2f}); **(b) and (c)** D values determined by the 2-d 1st and 2nd order structure function methods.

about 2.25) while the urban area E yields the highest fractal dimension followed by areas D, A, and C (Table 6.6). The study area B is significant different from all other four areas; there is no significantly difference between study areas A, C, and D; The urban area E is significant different from areas B and C, but not A and D. These results are independent of the methodologies used in calculating D values.

Although the existence of the linear structures such as roads, vegetation, houses, and land types occursin urban area E, the area does not always produce the expected high D

values such as 2.8 and 2.9 as show in Table 6.5. For example, the TM surface shown in Fig. 6.9(i) seems not to have a fractal dimensions of around 2.85. This is because different bands (hence different wavelength) have different sensitivities of the same object, in other words, different bands also affect the variation of the fractal dimensions of TM imagery.

Table 6.6 The paired t-test comparison of different study areas in D values.

D_{2f} determined by the 2-d spectral method					
study areas	**A, Edm2**	**B, Qmcs**	**C, Qsb**	**D, Coast**	**E, Urban**
mean ± std	2.53 ± 0.27♣	2.27 ± 0.13	2.43 ± 0.23	2.53 ± 0.27	2.61 ± 0.24
A, Edm2	\	***3.21***♦	*1.04*♥	*0.01*	*0.45*
B, Qmcs		\	***2.03***	***2.79***	***4.18***
C, Qsb			\	*0.90*	***2.02***
D, Coast				\	*0.54*
E, Urban					\
D_{2s} (q = 1) determined by the 2-d 1st order structure function method					
study areas	**A, Edm2**	**B, Qmcs**	**C, Qsb**	**D, Coast**	**E, Urban**
mean ± std	2.37 ± 0.24	2.19 ± 0.09	2.29 ± 0.12	2.39 ± 0.18	2.54 ± 0.20
A, Edm2	\	***2.31***	*1.10*	*0.21*	*1.22*
B, Qmcs		\	***2.02***	***4.30***	***3.73***
C, Qsb			\	*1.24*	***3.32***
D, Coast				\	*1.45*
E, Urban					\
D_{2s} (q = 2) determined by the 2-d 2nd order structure function method					
study areas	**A, Edm2**	**B, Qmcs**	**C, Qsb**	**D, Coast**	**E, Urban**
mean ± std	2.56 ± 0.32	2.26 ± 0.13	2.45 ± 0.22	2.58 ± 0.27	2.67 ± 0.21
A, Edm2	\	***2.96***	*0.91*	*0.15*	*0.62*
B, Qmcs		\	***2.39***	***4.87***	***4.18***
C, Qsb			\	*1.36*	***2.72***
D, Coast				\	*0.79*
E, Urban					\

t Critical one-tail value t_C = 2.02 at a confidential level = 95%, i.e., α = 0.05 (degree of freedom df = 5);

2.53 ± 0.27♣ (normal): is the mean value and standard deviation for study area A of the six bands;

3.21♦ (bold + italic): is the absolute statistical t value of the paired t-test comparison, which is > t_C (2.02) and shows significant difference between the two samples;

1.04♥ (italic): is the absolute statistical t value of the paired t-test comparison, which is < t_C (2.02) and shows no significant difference between the two samples.

6.3.3.2. Different bands

The DN of TM data in each band are the amount of EMR energy transmitted in space for *a specific wave interval*, and received by the multi-scanner installed in satellites (Table 6.2). Therefore different bands reveal different spectral characteristics, and have

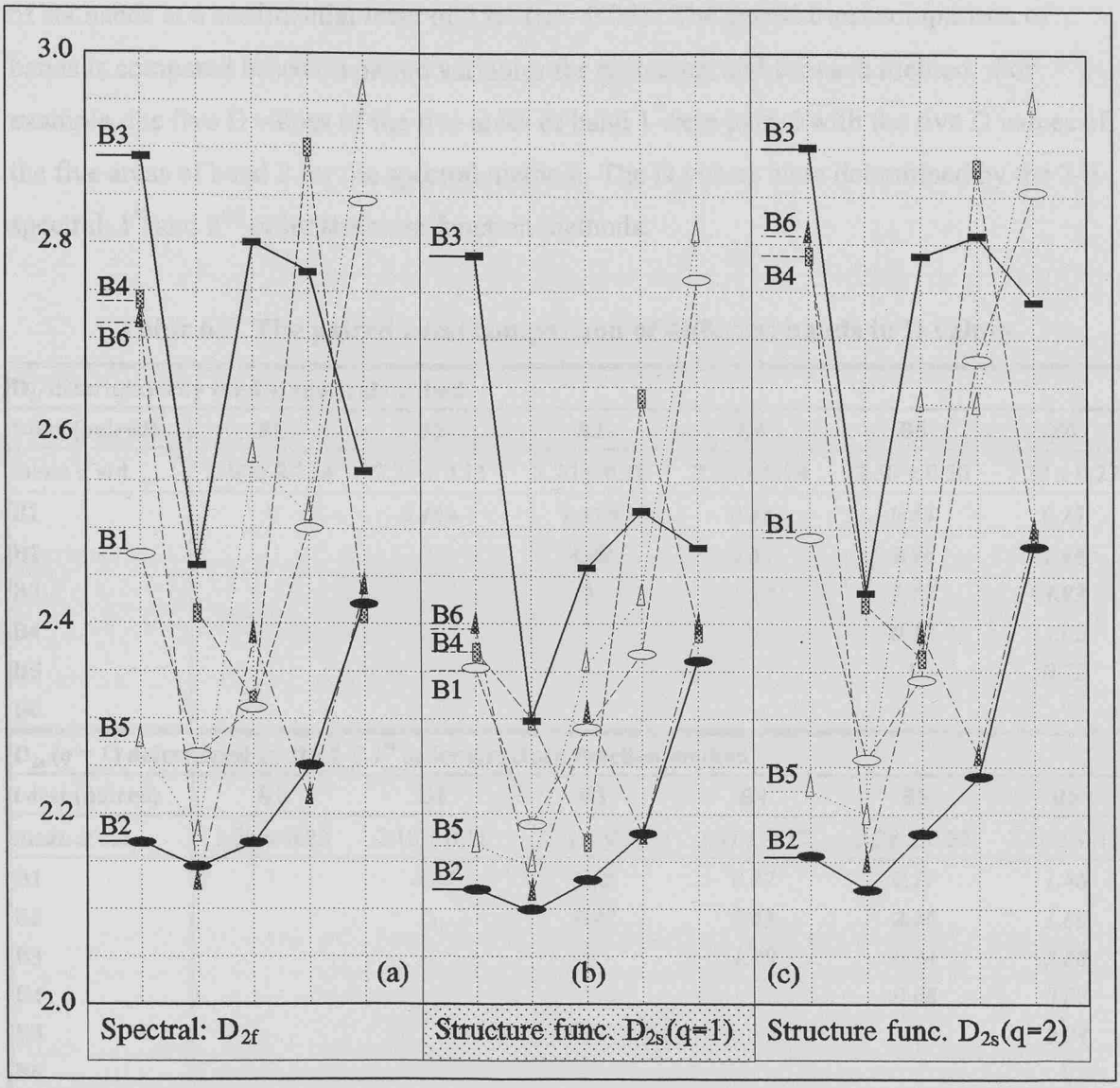

Fig. 6.11. Comparison of the fractal dimensions of TM imagery from five study areas. Different land type features of the different study areas are shown in Table 6.3. **(a)** D values determined by the 2-d spectral method (D_{2f}); **(b) and (c)** D values determined by the 2-d 1st and 2nd order structure function methods.

different sets of DN values for a single study area. This difference is expected to affect the variation in fractal dimensions of different bands. Fig. 6.11 is the linear plot of the fractal dimensions, derived from the spectral, 1st and 2nd order structure function methods, against the land types, where the D values are represented by the empty and solid circles for band 1 and 2; the empty and solid rectangles for band 3 and 4; and the empty and solid triangles for band 5 and 6.

Table 6.7 summarizes 1) the mean and standard deviation of D values of the five study areas for a single band; 2) the results of the paired t-test comparison for the D values

of six bands at a confidential level of 95% ($\alpha = 0.05$). The paired t-test comparison of bands is compared based on paired variables for each area, and for each method. For example, the five D values of the five areas of band 1 were paired with the five D values of the five areas of band 2 for the spectral method. The D values were determined by the 2-d spectral, 1st and 2nd order structure function methods.

Table 6.7 The paired t-test comparison of different bands in D values.

D_{2f} determined by the 2-d spectral method						
t-test (paired)	**B1**	**B2**	**B3**	**B4**	**B5**	**B6**
mean ± std	2.48 ± 0.23♣	2.23 ± 0.11	2.70 ± 0.18	2.54 ± 0.24	2.50 ± 0.30	2.39 ± 0.22
B1	\	***4.48***♦	*1.63*♥	*0.44*	*0.35*	*0.75*
B2		\	***4.42***	***2.63***	***2.96***	*1.48*
B3			\	*1.57*	*1.17*	***3.92***
B4				\	*0.17*	*1.02*
B5					\	*0.72*
B6						\
D_{2s} ($q = 1$) determined by the 2-d 1st order structure function method						
t-test (paired)	**B1**	**B2**	**B3**	**B4**	**B5**	**B6**
mean ± std	2.39 ± 0.22	2.18 ± 0.11	2.51 ± 0.18	2.37 ± 0.17	2.38 ± 0.27	2.28 ± 0.13
B1	\	***4.24***	*1.02*	*0.17*	*0.17*	*1.46*
B2		\	***3.47***	***2.43***	***2.80***	*1.86*
B3			\	*1.39*	*0.84*	***3.88***
B4				\	*0.08*	*0.87*
B5					\	*0.94*
B6						\
D_{2s} ($q = 2$) determined by the 2-d 2nd order structure function method						
t-test (paired)	**B1**	**B2**	**B3**	**B4**	**B5**	**B6**
mean ± std	2.53 ± 0.25	2.24 ± 0.14	2.73 ± 0.18	2.59 ± 0.23	2.53 ± 0.31	2.42 ± 0.25
B1	\	***4.85***	*2.01*	*0.53*	*0.02*	*0.77*
B2		\	***5.43***	***2.83***	***3.26***	*1.53*
B3			\	*1.64*	*1.47*	***4.03***
B4				\	*0.32*	*1.31*
B5					\	*0.57*
B6						\

t Critical one-tail value $t_C = 2.13$ at a confidential level = 95%, i.e., $\alpha = 0.05$ (degree of freedom df = 4);

2.48 ± 0.23♣ (normal): is the mean value and standard deviation for area A of the six bands;

4.48♦ (bold + italic): is the absolute statistical t value of the paired t-test comparison, which is > t_C (2.13) and shows significant difference between the two pairs;

1.63♥ (italic): is the absolute statistical t value of the paired t-test comparison, which is < t_C (2.13) and shows no significant difference between the two pairs.

An examination of the mean D values in Table 6.7 (refer to Table 6.5 for more details), as well as shown in Fig. 6.11, indicates that band 3 usually yields the highest fractal dimensions, whereas band 2 has the lowest D value. The D values of bands 4, 5, 1, and 6 are in between them. Band 5 has highest standard deviation in D values (Table 6.7), i.e., band 5 is more variable than the other bands in D value.

As shown in Table 6.7, the fractal dimension of band 2 is significantly different from those of bands 1, 3, 4, and 5 at a confidential level of 95%; the significant difference also exists between band 3 and band 6. For the other pairs of bands, the paired t-test does not show any significant difference. These results are independent of the methodologies used to calculate the D values.

6.3.3.3. Different methodologies

The spectral, 1st, and 2nd order structure function methods were used to determine the fractal dimensions for all the six bands of the five study areas. The results of these dimensions are shown in Table 6.5.

Fig. 6.12(a), (b), and (c) are the linear plots of D_{2s} ($q = 1$) against D_{2f}, of D_{2s} ($q = 2$) against D_{2f}, and of D_{2s} ($q = 2$) against D_{2s} ($q = 1$) respectively. Their trend lines can be

Table 6.8 The paired t-test comparison of different methodologies in D values.

	Spectral method	**Structure function method**	
	D_{2f}	**D_{2s} (q =1)**	**D_{2s} (q =2)**
D range (min - max) $^{\Theta}$	2.14 - 2.96	2.10 - 2.81	2.12 - 2.95
avg ± std $^{\Psi}$	2.47 ± 0.25	2.35 ± 0.20	2.51 ± 0.26
t-test (paired) $^{\Xi}$	**D_{2f}**	**D_{2s} (q =1)**	**D_{2s} (q =2)**
D_{2f}	\	***7.10*** $^{\xi}$	*-3.15* $^{\zeta}$
D_{2s} (q =1)		\	***-7.32*** $^{\xi}$
D_{2s} (q =2)			\

$^{\Theta}$ The minimum and maximum D values occur in band 2 of the study are B and band 5 of study area E (urban) respectively;

$^{\Psi}$ 2.47 ± 0.25 the average and the standard deviation for a single method;

$^{\Xi}$ the paired t-test comparison among the methodologies at $\alpha = 0.001$ (degree of freedom df = 29); and the t critical one-tail value $t_C = 3.40$;

7.10 $^{\xi}$ (bold + italic): is the absolute statistical t value of the paired t-test comparison, which is > t_C (3.40) and shows significant difference between the two pairs;

3.15 $^{\zeta}$ (italic): is the absolute statistical t value of the paired t-test comparison, which is < t_C (3.40) and shows no significant difference between the two pairs.

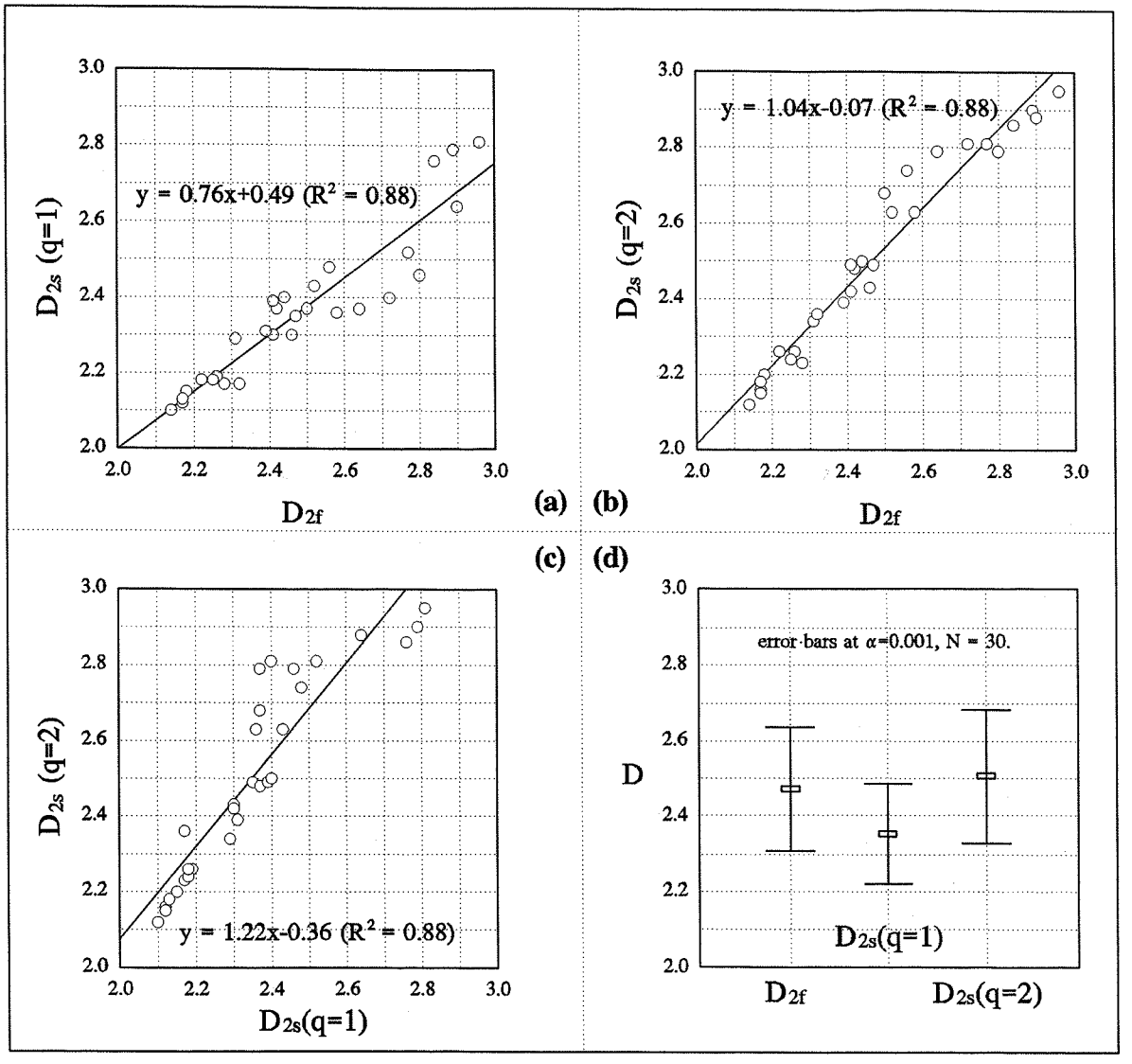

Fig. 6.12. Comparison of different methodologies in D values. The linear plots of **(a)** $D_{2s}(q=1)$ against D_{2f}; of **(b)** $D_{2s}(q=2)$ against D_{2f}; and of **(c)** $D_{2s}(q=2)$ against $D_{2s}(q=1)$. **(d)** is the error bars plot of the D values of all the six bands and five study areas derived from the spectral, 1st and 2nd order structure function methods at a confidential level of $\alpha = 0.001$.

described as D_{2s} ($q = 1$) = 0.76 D_{2f}, +0.49 ($R^2 = 0.88$), D_{2s} ($q = 2$) = 1.04 D_{2f} -0.07 ($R^2 = 0.95$), and D_{2s} ($q = 2$) = 1.22 D_{2s} ($q = 1$) -0.36 ($R^2 = 0.84$) respectively. In other words, D_{2s} ($q = 2$) > D_{2f} > D_{2s} ($q = 1$).

Fig. 6.12(d) is the error bars plot of the fractal dimensions derived from different methods at the confidential level of $\alpha = 0.001$. The error bar plot here does not take account of the facts that the fractal dimensions of TM imagery affected either the different land types or bands.

Table 6.8 summarized the results of the paired t-test comparison at a confidential level of $\alpha = 0.001$ (degree of freedom df = 30 - 1 = 29) for the three types of D values.

From the t-test results and Fig. 6.12, the spectral and 2nd order structure function methods resulted in roughly the same fractal dimensions of the TM imagery, both of them are significant higher than the D values determined by the 1st order structure function method.

The higher fractal dimension derived from the 2nd order structure function method than that derived from the 1st order structure function method could be used to verify the surface behaviours multi-scaling properties (Lavallee *et. al.*, 1993, Weissel *et. al.*, 1994).

Lavallee *et. al.* (1993) suggested that simple and multi-scaling behaviour could be distinguished by examining properties of $\Delta g_q(h)$ (Chapter 2.6.1), which is the q^{th} order structure function of topography g(x). Generally, the scaling exponent β_q of the structure functions depends nonlinearly on the order q. *Lavalee et. al.* (1993) determined the length scaling properties of the 1st and 2nd order ($q = 1$ and $q = 2$; and the scaling exponents are β_1 and β_2 respectively) structure functions from a DEM gridded at 50 m intervals for Deadman's Butte, Wyoming. They found that $2\beta_1 - \beta_2 > 0$, consistent with multi-scaling behaviours. Although the found value ($2\beta_1 - \beta_2$) was small (0.06 ± 0.01), they pointed out that it agreed with the results obtained from using a more accurate technique called the "double trace moment."

Weissel *et. al.* (1994) determined the scaling properties of the 1st and 2nd order structure functions for the DEMs from Ethiopia, Saudi Arabia, and Somalia (DEMs spans 3° (or 1°) of latitude and 1° (or 3°) of longitude for 3600 by 1200 points, elevation contours are every 1000 m). They found that the scaling exponent for the 1st and the 2nd order moments are different, $2\beta_1 - \beta_2 = 0.11 \pm 0.04 > 0$ (where the uncertainty given as two times the standard deviation).

Converting the differences between the scaling exponents of the 1st and 2nd order moments into fractal dimensions, the relationship between D_{2s} ($q = 2$) and D_{2s} ($q = 1$) can be deduced from equation (2.7) in Chapter 2.6.3 as $D_{2s}(q = 2) = D_{2s}(q = 1) + 0.03$ for the results obtained by Lavallee (1993), and $D_{2s}(q = 2) = D_{2s}(q = 1) + 0.06$ for the results obtained by Weissel (1994).

For the TM imagery of northern Qatar, all the six bands of the five study areas of TM data sets were analyzed by the 1st and 2nd order structure function methods. The

average difference between the scaling exponents for the 30 samples are given $2\beta_1 - \beta_2 = 0.33 \pm 0.27$ (the uncertainty is the standard deviation). This difference is higher than those derived from the DEM data sets (border area of Portugal and Spain; Deadman's Butte, Lavallee *et. al.* 1993; and Ethiopia, Saudi Arabia, and Somalia, Weissel *et. al.*, 1994). This may be explained by the facts that TM data include both topographic information and non-topographic information high frequencies, such as roads and edges caused by different spectral characteristics of different neighbouring cover types (Lam, 1990).

In summary, the fractal dimensions of TM imagery are controlled by the land types, the bands, and the methodologies used. TM imagery of Qatar have multi-scaling properties.

6.4. FEATURE EXTRACTION (EASTERN COASTLINE)

The TM imagery quadrant of Qatar has 6967 by 5965 pixels has a spatial resolution of 30 m (i.e., each pixel covers a square area of 30^2 m^2. An area of 512 by 512 pixels from the eastern Qatar is taken as an example to demonstrate the way of extracting the coastline. The area covers part land and part sea. The D value of the extracted coastline is determined by the ruler and box-counting methods, and the results are linked with those of topographic contours and coastlines obtained in Chapters 3 and 5.

6.4.1 Extracting coastline from TM data

A FORTRAN program was developed to extract the coastline from the Landsat TM image data which covers the east coast of Qatar. The extraction procedure is briefly described as follows.

Firstly, a criterion is needed to distinguish the land and the sea in the area of the TM imagery. This criterion should be unique to characterize the pixels in which the coastline passes in the whole imagery area. Therefore, the digital numbers (DN) of the adjacent pixels of each band for characterizing the coastal line of the all six bands were carefully studied. It is found that, in a single band, the difference of DN between the adjacent pixels which are located on both the land and sea is not significantly different from that of DN between the pixels of the sea and the land. The combinations of several bands distinguish the boundary between the land and the sea significantly. Among them, the combination of bands 4, 5, and 6 provides the best discrimination of the east coastline boundary of Qatar.

Therefore, bands 4, 5 and 6 are selected, and their DN are added together to be DN3, and used to characterize the coastal boundary. For each pixel, the DN of bands 4, 5, and 6 are recorded as DN_4, DN_5, and DN_6, hence, $DN3 = DN_4 + DN_5 + DN_6$. The subtraction (or differences) of DN3 between the adjacent pixels, which cover the coastline, then become a unique threshold value (DN0) in the whole imagery. In other words, the subtraction values of DN3 between adjacent pixels where coastline passes can only be greater than DN0, otherwise the adjacent pixels are regarded as pixels of inter land or inter sea. Thus, the threshold value DN0 can be used to discriminate the boundary between the sea and the land. The procedure of extracting coastline from TM imagery is similar to that of contouring a topographic surface with a certain elevation level, and the contour elevation level is 0 here.

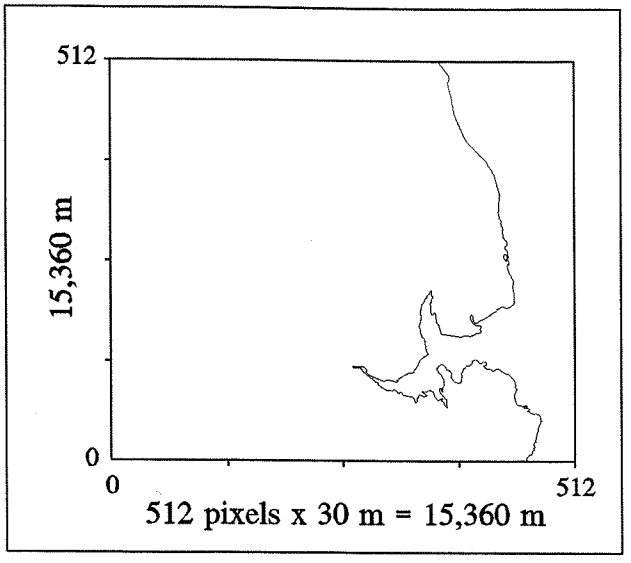

Fig. 6.13. The east coastline segment extracted from Qatar TM imagery.

Thirdly, if the subtraction of DN3 between any adjacent pixels exceeds DN0 in the whole image, the coordinates of the pixel (row and column numbers) is recorded as the boundary point, in which the coastline passes.

Finally, the program scans the whole imagery row by row. As soon as first point (P_1) of the coastline is found, the program starts to trace the coastline by comparing the pixels surrounded the point P_1, and the second point P_2 of the same criterion is found. This process can be carried out until either the last point P_N to be the same as the first point P_1 of the coastline (this is the closed coastline) or the edge of the study area $\begin{bmatrix}(0,512) & (512,512)\\ (0, \ 0) & (512, \ 0)\end{bmatrix}$ had been reached (this is open coastline). Therefore, a series of coordinates can be recorded as the coastline of the imagery area, and form a coastline. Therefore, the extracted coastline has a resolution of 30 m, which is the spatial resolution of the TM data.

Fig. 6.13 shows the extracted coastline of eastern Qatar. The side length of the square is 512 pixels by 30 m = 15,360 m.

6.4.2 Fractal analysis of the extracted coastline

The ruler and box counting methods were used to determine the fractal dimensions of the coastline. The coastline has fractal dimensions of $D_r = 1.25$ and $D_{1b} = 1.23$. They have little difference, they are consistent with each other, and have an average fractal dimension of $D = 1.24$.

The theory of zerosets demonstrates that fractals reduce their dimensions by one

under intersection with a plane (Chapter 2.7.3). A coastline can be regarded as the result of the study area intersecting with the sea level plane. Therefore, the topographic surface of Qatar has the fractal dimension of D = 2.24. This D value is roughly the same as that of Spain DEM (D = 2.23, Chapter 6.2.2), but is different from that of the TM imagery data. This can be explained firstly by the fact that TM data represent the spectral characteristics of the vegetation, land type, road, buildings; secondly that the coastline extraction procedure might have enhanced the coastline information and this is need to be further investigated in the future.

6.4.3 Discussion

The fractal dimension of the east coastline of Qatar (D = 1.24) is roughly the same as that of the coastline of Britain (D = 1.25, Chapter 5; Kaye, 1989; Mandelbrot, 1967). It is also consistent with the fractal dimension of topographic contours (Chapter 3) of different map scales of the border area between Spain and Portugal where D = 1.23. Therefore, the successful extraction of the Qatar TM feature (eastern coastline) and the consistent D value with the coastlines of Britain demonstrate that the TM feature can be used to estimate the D value of topography for the area.

As shown in Table 6.5, the sub-image of band 2 of the coastal area (study area D) has a fractal dimension about D = 2.18 - 2.25 [D_{2f} = 2.25, $D_{2s}(q=1)$ = 2.18, and $D_{2s}(q=2)$ = 2.24], which is reasonably consistent with the D value of the extracted eastern coastline (D = 1.24) based on the zeroset theory. However, the sub-image of band 4 of the coastal area has a fractal dimension about D = 2.64 - 2.90 (D_{2f} = 2.90, $D_{2s}(q=1)$ = 2.64, and $D_{2s}(q=2)$ = 2.88), witch is much higher than the D value of the extracted eastern coastline (D = 1.24). The different behaviours in the fractal dimension D can be explained by observing their TM surfaces as shown in Fig. 6.9(g) and (h). Band 2 (wavelength = 0.52 - 0.60 μm) has distinguished a coastal boundary between the land and the sea [Fig. 6.9(g)], and the coastline of the sub-image coastal area represents a small portion of the extracted eastern coastline, hence they have roughly the same D values. On the other hand, band 5 (wavelength = 0.76 - 0.90 μm) reflects not only the spectral characteristics of the sea but also the similar spectral characteristics of the land [Fig. 6.9(h)]. Therefore, the fractal dimension D characterizes the different spectral features of the TM imagery.

6.5. CONCLUSIONS

The fractal analysis has been successfully conducted on the DEM data digitized from the border area of Spain and Portugal and on the TM data from five study areas (A-Edm2, B-Qmcs, C-Qsb, D-Coast, and E-Urban) of Qatar. The results of the fractal analysis of DEM and TM data in this chapter can be concluded as following.

1. The digitized DEM of the border area of Portugal and Spain, which has a elevation of 10 m and covers an area of 640 m by 640 m, has a fractal dimension of D = 2.23 (Table 6.1). The D value of the DEM data is in the D ranges from 2.1 to 2.5 obtained by Shelberg *et. al.*, (1983); Mark and Aronson, (1984); Roy *et. al.*, (1987); Lavallee, (1993); Weissel *et. al.*, (1994). Based on the zerosets theory, the fractal dimension of the DEM data is consistent with that of the topographic contours from the same area ($D_1 = D_2 - 1 = 1.23$) (Chapter 3). The difference between the D values derived from the 2nd and 1st order structure function methods is $D_{2s}(q=2) - D_{2s}(q=1) = 0.03$, and suggests that the DEM has a multi-scaling property. The difference is consistent with that obtained by Lavalle *et. al.* (1993) and Weissel *et. al.* (1994), they found the difference is 0.03 and 0.06.
2. Five TM sub-images of the Qatar have D values ranging from 2.10 to 2.96 (Table 6.5) derived from the spectral and structure function methods. The D values have a wider range than the results obtained by Lam (1990) based on the TM quadrants of Louisiana, where D ranged from 2.54 to 2.87. The lowest fractal dimension is found in band 2 of the study area B, where $D_{2f} = 2.14$, $D_{2s} = 2.10$ ($q = 1$), and $D_{2s} = 2.12$ ($q = 2$). This is because study area B is covered by a single rock unit (calcareous sand of marine origin including coastal dunes), and band 2 (wavelength 0.52 - 0.60 μm) produced relatively less complexity of the TM surface in spectral characteristics. The highest fractal dimension is found in band 5 of the urban area of Doho (E), where $D_{2f} = 2.96$, $D_{2s} = 2.81$, and $D_{2b} = 2.95$. This may be explained by the sensitivity of band 5 to the existence of different spectral characteristics and linear structures such as roads, vegetation, houses, and land types in urban area.
3. Different land types control the D values. The paired t-test results at a confidence level of 95% shows that the study area B (Qmcs, covers the calcareous sand of marine origin) produces the lowest D value (D is about 2.25) and is significantly different from the other four study areas; study area C (Qsb, covers saline, gypsiferous and silt flats) is

significantly different from the urban area E. The urban area E yields the highest fractal dimension followed by areas D, A, C, and B (Table 6.6).

4. Different bands also contribute to the variations in D values for the same study area and same methodology. Band 3 yields the highest fractal dimensions, followed by bands 4, 5, 1, and 6, and band 2 has the lowest D value (Table 6.7). The paired t-test comparison at a confidential level of 95% (Table 6.7) shows the fractal dimension of band 2 is significantly different from those of bands 1, 3, 4, and 5 at a confidential level of 95%; the significant difference also exists between band 3 and band 6. There is no significant difference found for the other pairs of bands.
5. Different methodologies also cause the changes of D values of the TM imagery. The paired t-test comparison results (Table 6.8), at a confidential level of $\alpha = 0.001$, for all the six bands of the five study areas shows that the 2-d spectral and 2^{nd} order structure function methods resulted in roughly the same fractal dimensions, they have no significant difference. Both of them are significantly higher than the D values determined by the 1^{st} order structure function method. This maybe explained by the TM surfaces have multi-scaling properties.
6. The difference between the D values derived from the 2^{nd} and 1^{st} order structure function methods for all the six bands of five study areas is $D_{2s}(q=2) - D_{2s}(q=1) = 0.16 \pm 0.13$ (the standard deviation), and suggests that the TM imagery has a multi-scaling property.
7. The fractal analysis of the extracted coastline from eastern Qatar TM quadrant shows that TM feature can be extracted to estimate the D value of the topographic surface. The consistent of the D value of the extracted coastline with the coastal sub-image area can be used to verify the efficiency of different bands characterizing the coastal boundary. For example, the sub-image of band 2 of the coastal area [Fig. 6.9(g)] has a clear coastal boundary, and has a close D value about D = 2.18 - 2.25 (Table 6.5) to the extracted coastline D = 1.24 based on zeroset theory, whereas the sub-image of band 4 of the coastal area [Fig. 6.9(h)] has complex spectral features in characterizing the coastal boundary, and has a higher fractal dimension about D = 2.64 - 2.90. Therefore, fractal analysis of the extracted TM feature characterizes different spectral features of the TM image. The extracted coastline has a roughly same D values as the coastline of Britain [D = 1.25; Chapter 5; Kaye (1989), and Mandelbrot (1967)] and the topographic contours of the border area between Spain and Portugal where (D = 1.23, Chapter 3).

CHAPTER 7.

CONCLUSIONS

CHAPTER 7.

CONCLUSIONS

7. CONCLUSIONS

7.1. METHODOLOGIES

Seven methods [the ruler, box-counting, spectral, q^{th} order structure function (i.e., q^{th} order moments) , intersection, cube-counting, and triangular prism methods] for calculating the fractal dimensions of profiles or surfaces have been used in the thesis. The programs and the implementation of these methodologies (including the ruler, box, spectral, and structure function methods) were verified by the comparison the calculated fractal dimensions with the known ones (theoretical D values) of the Koch curve, the Cantor set, and the simulated 1-d and 2-d fBm profiles and surfaces of (Chapter 2). The simulated 1-d and 2-d fBm with different values of H = 0.8, 0.5, and 0.2 were generated by the midpoint displacement and interpolation methods (Barsley *et. al.*, 1988). Based on the analysis results, some conclusions can be drawn;

Fractals or not: Unlike the theoretical fractal models (e.g., the Koch curve and the Cantor set), natural phenomena are characterized by the self-similar or the self-affine fractal models in a statistical sense (Mandelbrot, 1977). The fractal dimension is usually estimated from the slope of the regression line through comparatively few points. In some situations, the points from the log-log plot do not fit a straight line. This may indicate that a line is a non-fractal. On the other side, some studies (e.g., Ringrose, 1994) did show that the D values of the coastline profiles in Fife, eastern Britain, vary with map scales. This is needed

to be investigated further so that proper explanations can be provided.

The application of appropriate methods to self-similar or self-affine fractals is essential. On one side, some methods are not suitable for determining D values of some curves or surfaces due to the data structure and the underlying theory of the methods. For example, the ruler method can be deployed to determine the fractal dimension of the Koch curve (or the topographic contours), whereas the 1-d spectral method can not. This is because the Koch curve (or the topographic contours) has a lot of overhangs motif, i.e., given a certain position x, there might be more than one corresponding height y values. This excludes the applicability of some fractal analysis methods, e.g. the spectral method. On the other side, the assignment of a fractal dimension D determined for a self-similar set to a self-affine set could produce ambiguous results (Mandelbrot, 1985). The ruler and box-counting methods are successful fractal models to describe the self-similar fractals, while the spectral and q^{th} order structure function (i.e., q^{th} moments) methods are suitable to deal with self-affine fractals. Generally, the methods for determining the fractal dimension of a self-similar fractal should not be used for determining the fractal dimension of a self-affine fractal, otherwise, meaningful results would be hardly achieved. For example, the fractal dimensions of 1-d simulated self-affine fBm surfaces of H = 0.8, 0.5 and 0.2 are very close to 1 as they are determined by the ruler or box-counting method (Chapter 2.10.1), and will vary with the vertical scale (i.e., the amplitude of the curve). This is consistent with the results obtained by some previous studies (Mandelbrot, 1985; Brown, 1987; Wong, 1987; Brown, 1987; Fox, 1989; Hough, 1989).

The ruler and spectral dimensions: The ruler dimension (determined by the ruler or box-counting method, the two methods are equivalent) is different from the spectral dimension (determined by the spectral or structure function method, the two methods are equivalent). The former is more or less a roughness descriptor and focuses on the "*area filling capacity*" of a curve in the space at certain range of observation scales and the intercepts depend on the contour length; whereas the latter is to describe how roughness varies within observation scales and the intercept characterizes the amplitude of roughness. Therefore, different methodologies can give different fractal dimensions for a single data set. Fundamentally, there is no reasons why the fractal dimensions should be the same for different methods (Turcotte, 1992). For example, the topographic profiles digitized from the 1:10,000 map of southern England have a fractal dimension of D = 1.03 for the ruler method, whereas of D = 1.13 for the spectral method.

Fractal limits: Natural phenomena are characterized by the self-similar or the self-affine fractal models in a statistical sense over a certain range of fractal limits (Mandelbrot, 1977). Better estimation of fractal dimensions arises: 1) when the map quality is good and the digitizing noise is little (these two factors control the lower fractal limit); and 2) when analyzed contour lengths are large (it controls the upper fractal limit). The fractal limits of the fitted regression line do not always have clear boundaries, and may lead to systematic deviation from the power-law behaviour (Richardson, 1961). In some cases, the plotted points may be fitted by more than one straight lines over more than one range of observation scales. This shows that a line or a surface has multi-scaling behaviours, Kaye (1989) described this phenomenon as "*textural*" and "*structural*" fractals.
A number of studies (Nye, 1973; Bell, 1975 and 1979; Gilbert and Courtillot, 1987; Malinverno, 1988 and 1989; Gilbert, 1989) have noted that the upper fractal limit plays an important role in characterizing surfaces' geography at larger scales. The importance of the lower fractal limit, however, has been little investigated. The study has shown that the lower fractal limits are controlled by the resolution of measurement, such as map scales, map quality, digitizing accuracy etc.

Hanning window: The application of Hanning window on the synthetic fBm samples is essential in order to obtain correct fractal dimensions for the spectral method and structure function methods. This is because the principles of the methods were deduced from the theoretical assumption: the infinite sample size, and the truncation phenomena (Gibbs effects) resulted from applying theory on the data of finite sample size in practice. Table 2.5 and 2.6 show that the D values of 1-d and 2-d fBm can be correctly determined as the fBm were Hanning window weighted for the spectral method. Comparisons between the lower part of Tables 2.5 and 2.7 and between the lower part of Tables 2.6 and 2.8 show the D values of the synthetic fBm are the same as determined by the spectral and structure function methods. They are well consistent with the theoretical D values which are given by H.

Zeroset theory: The zeroset theory relates the fractal dimensions of 1-d profiles to those of 2-d surfaces. The zeroset theory suggests that D values of surfaces (D_2) are reduced by 1 after they are intersected by a plane (Goodchild, 1982; Burrough, 1981; Barnsley *et. al.* 1988), i.e., the resulted curves have a fractal dimension $D_1 = D_2 - 1$. Although this is effective in practice for a crude approximation, care must be taken when this deduction is needed. 1). The WHOLE set of the intersected contours resulted from

intersecting the surface with a horizontal plane has a fractal dimension of its surfaces minus 1. An individual contour of the set of different H values, however, has the same fractal dimension D = 1.24. 2). Only the contour set from intersecting the surface with a horizontal plane is self-similar, the others are self-affine. 3). The spatial location of the intersected contour set (i.e., the spatial locations of different contours of the same elevation) also controls the D value. For example, the intersected contour set only consists of a single coastline for a surface area which covers partly land and partly sea, and it has a fractal dimension of D = 1.2. The deduction of the surface of having D = 2.2 might be not sufficient. The zeroset theory also relates the 2-d self-affine method to the 1-d self-similar method. In a topographic surface (x, y, z), (x, y) are self-similar and z scales differently (hence self-affine). Thus the surface must be analyzed by self-affine method, whereas the contours can be treated by self-similar method (e.g., DEM analysis).

7.2. APPLICATIONS

The fractal concept is a successful model to characterize the spatial variations of the Earth's surface in the form of either 1-dimensional curves (topographic contours and profiles) or 2-dimensional raster data sets (DEM and TM). Based on the analysis results, the conclusions can be reached:

Topographic contours and coastlines: A consistent, reproducible fractal dimension can be estimated from a contour of any elevations (i.e., contour elevation invariant) on any maps (i.e., scale invariant) providing care is taken to define fractal limits. Similar fractal dimensions are obtained from the ruler and box-counting methods at a confidential level of 95%, it shows $D_{1b} = D_r \pm 0.15$. The study of the 132 topographic contours, which were digitized from the different scales (1:200,000, 1:50,000, 1:20,000) of maps from the border area between Spain and Portugal, has shown that topographic contours are self-similar fractals, and have a fractal dimension of about D = 1.23 (ranges from 1.01 to 1.47 and the standard deviation = 0.07) over the fractal limits ranging from 30 m to 13 km (3 orders of magnitude). The analysis result is consistent with previous studies, such as Mandelbrot (1967); Norton and Sorenson (1989).

Geological factors in the variations of D values: The variations in D values of the coastline, topographic contours, and field profiles are controlled by several geological

factors, such as erosive process, lithologies, and fractures. ***Erosive process:*** The dominant control of the D values of the coastlines, contours and profiles is the erosive process. As shown in Table 5.4, coastlines and topographic contours formed by the down-cutting erosion with river net work system and ice have higher D values ($1.1 < D < 1.5$) than those formed by the wave action and cliff retreat process ($1.01 < D < 1.10$) (Feder, 1988; Kaye 1989; and the analysis results of Chapter 3, 4, and 5). ***Lithologies:*** Different lithologies can either result in significant difference or produce more subtle variation in the fractal dimensions of coastlines and contours. For example: The D values of topographic contours from granite areas ($D = 1.25 \pm 0.02$) are higher than those of nearby metamorphic country rocks ($D = 1.20 \pm 0.02$). Although the difference is small, it is statistically significant (Chapter 3); The dolostone layers have higher D values (= 1.13) than the shale layers (D = 1.02) in Kimmeridge Bay (Chapter 4). This corresponds to the geological fact that the shale layer is more easily eroded away, and becomes smoother than the dolostone layer, where fracture joints control its formation; However, the coastlines of Great Britain, which cover different types of lithologies, show little variation in D values (Table 5.6) with lithologies. The variation in D values are dominated by different types of erosive processes, and different lithologies result in subtle variation in D values. ***Fractures:*** Higher D values of topographic surfaces derive from the regions where fractures are abundant (Norton and Sorenson, 1989). High D values also occur as the orientation of the curve cross-out with the structural strike (Power *et. al.*, 1987), whereas fault deformed profile usually leads low D values (Chapter 5.6; Aviles *et. al.*, 1987). It should be pointed out that the erosive processes are often correlated with fractures, and they often compound control the variation in D.

DEM analysis: The DEM data digitized from the 1:20,000 map covering the border area of Spain and Portugal, which has a elevation of 10 m and covers an area of 640 m by 640 m, has a fractal dimension of D = 2.23 (Chapter 6.2). The D value of the DEM data is in the D ranges from 2.1 to 2.5 obtained by Shelberg *et. al.*, (1983); Mark and Aronson, (1984); Roy *et. al.*, (1987); Lavallee, (1993); Weissel *et. al.*, (1994). Based on the zerosets theory, the fractal dimension of the DEM data is consistent with that of the topographic contours from the same area ($D_1 = D_2 - 1 = 1.23$) (Chapter 3). The difference between the D values derived from the 2nd and 1st order structure function methods is $D_{2s}(q=2) - D_{2s}(q=1) = 0.03$, and suggests that the DEM has a multi-scaling property. The difference is consistent with that obtained by Lavalle *et. al.* (1993) and Weissel *et. al.* (1994), they found the difference is 0.04 and 0.05.

TM analysis: The results of the fractal analysis of the five TM sub-image (A-Edm2, B-Qmcs, C-Qsb, D-Coast, and E-Urban) of Qatar have shown that D values of the TM images range from 2.10 to 2.96. The variations in D values are contributed by different types of surface, band variations, and methodologies. ***Types of surfaces:*** Different land types control the D values. The paired t-test results at a confidence level of 95% shows that the study area B has the lowest D value (D is about 2.25) and is significantly different from the other four study areas, whilst the urban area E yields the highest fractal dimension (about D = 2.6) followed by study areas D, A, and C (Chapter 6.3.3.1). This is because the study area B (Qmcs) is covered by a single rock unit (the calcareous sand of marine origin), whereas the urban area E contains much more spectral characteristics, such as buildings, road system etc. ***Band variations:*** Different bands contribute the variations in D values for the same study area and same methodology. Band 3 usually yields the highest fractal dimensions, followed by bands 4, 5, 1, and 6, and band 2 has the lowest D value (Chapter 6.3.3.2). The paired t-test comparison at a confidential level of 95% shows the fractal dimension of band 2 is significantly different from those of bands 1, 3, 4, and 5 at a confidential level of 95%; the significant difference also exists between band 3 and band 6. ***Multi-scaling:*** TM imagery has a multi-scaling property and can cause the variations in D values when it is analyzed by the different methods. The significant difference between the D values derived from the 2nd and 1st order structure function methods for all the six bands of five study areas is $D_{2s}(q=2) - D_{2s}(q=1) = 0.16 \pm 0.13$ (the uncertainty is the standard deviation), and suggests that the TM surfaces exhibit multi-scaling properties (Chapter 6.3.3.3).

7.3. FUTURE WORKS

A number of studies (Nye, 1973; Bell, 1975 and 1979; Gilbert and Courtillot, 1987; Malinverno, 1988 and 1989; Gilbert, 1989) have noted that the upper fractal limit plays an important role in characterizing surfaces' geography at larger scales. The importance of the lower fractal limit, however, has been little investigated. It maybe used to quantify the data sources (e.g., the map quality), data acquiring process (such as the digitizing step and the sampling theory), and the filter designs in the subject of image processing.

Some previous studies (Cox and Sandstrom, 1962; Neidell, 1966; Bretherton, 1969,

Balmino, 1973; Warren, 1973; Bell, 1975; Berry and Hannay, 1978; Sayles and Thomas, 1978; Bell, 1979; Brown and Scholz, 1985; Fox and Hayes, 1985; Power *et. al.*, 1987; Turcotte, 1987; Fox, 1989; Hough, 1989; Malinverno, 1995) have shown that the spectral exponent β of a profile of the Earth varies between 1 and 3, and has an average of $\beta = 2$, hence an average $D = 1.5$. After comparing the synthetic surfaces with actual topography, Mandelbrot (1975, 1983) noted that $D = 1.5$ is too high, and concluded that the topography of the Earth has a fractal dimension $D = 1.2$. The difference in D values is definitely worthwhile further investigating. Ten map and three field profiles described in Chapter 4 show self-similarity, but why their D values determined by the spectral method are not all so near to 1.00 (i.e., the spectral slopes are not 3)? This might provide some information that these profiles behaviour some extent self-affinity.

Gravity provides the fundamental controls on the scaling properties of natural landscapes. This is because the elevations of the Earth's surfaces are biased by tectonic movements and erosive processes. Tectonic forces (especially compresional tectonic movements) bias landscapes towards a greater proportion of areas at higher elevation, whereas the erosive or deposition processes bias landscapes towards a greater proportion of areas at lower elevation. Further study may reveal the scaling properties of the up/down biased effects of the landscape, and the fractal analysis of the real Earth's surface may involve the structure function method at more than 2^{nd} order.

Topography is the representation of the intersection of tectonic and erosive forces at a given time. The continuously observation made for every specific interval for the same objects, such as coastlines, river network, and lake shoreline, may provide the variation of the object. The variation of the scaling properties of the object in the relative age could provide some evolution information of the object, and may have some environmental applications.

The fractal analysis results of the DEMs made of different techniques (e.g., digitization of the existed contour maps, and photogrammetric methods applied to stereo imagery are two examples) could be compared with each other, and used in assessment of the quality of DEMs. In other words, the fractal analysis results (and log-log plot patterns) of the DEM could be used to judge how well the DEM represents the real topography. The fractal analysis method could also be applied to the Radar imagery, and the results could be compared with those of the TM imagery.

The application of the spectral and structure function methods applied on the Hanning window, straight line y = x (or a plane surface z = 2x + 4y + 6), and Hanning window filtered straight line or surface described in Chapter 2.5.1 and 2.5.3 leads to the slope (β) of the regression line on log-log scale and the D values as following:

Table 7.1. D values of the Hanning window, straight line or surface, and Hanning window filtered straight line or surface by the spectral and structure function methods

	1-d spectral method	1-d structure function method	
		q = 1	q = 2
1-d Hanning window (h_1)	β = 4.3; D = 0.35.	β = 1.0; D = 1.0.	β = 2.0; D = 1.0.
straight line y = x	β = 2.0; D = 1.50.	β = 1.0; D = 1.0.	β = 2.0; D = 1.0.
filtered straight line $y_f = y \bullet h_1$	β = 6.2; D = 0.60.	β = 1.0; D = 1.0.	β = 2.0; D = 1.0.
	2-d spectral method	2-d structure function method	
		q = 1	q = 2
2-d Hanning window (h_2)	β = 2.0; D = 2.50.	β = 1.0; D = 2.0.	β = 2.0; D = 2.0.
plain plane z = 2x + 4y + 6	β = 2.0; D = 2.50.	β = 1.0; D = 2.0.	β = 2.0; D = 2.0.
plain plane $z_f = z \bullet h_2$	β = 2.0; D = 2.50.	β = 1.0; D = 2.0.	β = 2.0; D = 2.0.

From the results shown in the above table, it can be seen that structure function method yield reliable D values, whereas the D values determined by the spectral method does lead to expected results. This might need further investigation in the areas of the theoretical theorem between the D value and the regression slope β.

Further investigation is also needed for understanding the problems like :

1. the necessarility of applying the Hanning window to the profiles or surfaces for the structure function method;
2. theoretically the detrending process is necessary for FFT, why the detrending process had no effects on (or distorted) the D values of the simulated theoretical 1-d and 2-d fBm;
3. whether it is possible to obtain better and more reliable D values by using much larger sizes of the simulated 1-d and 2-d fBm;
4. the simulated 1-d and 2-d fBm samples might need to be characterized by other parameters in describing their scaling properties;
5. the effects caused by applying the Hanning window to the unequal intervaled map and field profiles (Chapter 4) needs to be evaluated in quantity, this estimating error also occurred as resampling the filed and map profiles before FFT.

APPENDIXES

APPENDIXES

APPENDIX 1. SIMULATION OF RANDOM FRACTALS

A1.1. INTRODUCTION

The fractal concept can be combined with Brownian motion, and used to simulate the natural realities in the world. The two most important methods to generate fBm are interpolation and spectral synthesis. In this appendix, the principles of the midpoint displacement and interpolation methods will be explained and used to generate 1-d and 2-d fBm.

In Section A1.2, the concept of Brownian motion and its generation by using the integration of white noise and midpoint displacement method are reviewed. 1-d fBm is discussed in Section A1.3. This includes the definition of 1-d fBm and its generation by using the midpoint displacement and interpolation methods. The relationship between the fractal dimension D and the roughness characteristic parameter H of fBm is also investigated. Section A1.4 focuses on the discussion of 2-d fBm. The displacement and bilinear interpolation methods are employed to generate samples of 2-d fBm

All programs of generating Brownian motion, white noise, and fBm are written in VISUAL BASIC and FORTRAN 77 codes.

A1.2. 1-DIMENSIONAL BROWNIAN MOTION

Brownian motion is the name given to the irregular and erratic movement of small particles of solid matter, suspended in a liquid, under microscope by the botanist Robert Brown (1828). Brownian motion is also occasionally either refer to as "brown noise" or "Wiener Process". The mathematical theory of Brownian motion was invented by Wiener (1923). The range of applications of Brownian motion has gone far beyond the study of microscopic suspended pollen, and includes a variety of statistical mechanics, physical, biological, electronics, communications, economic and management systems etc. Furthermore, the concept of fractional Brownian motion (fBm) may be introduced through the integration of Brownian motion with the fractal concept. The theory of fBm is fundamental to the simulation of random fractal profiles and surfaces.

A1.2.1. Definition

Suppose one dimensional Brownian motion is defined as a random process B(t), i.e., a function B(t) of a real variable t (t usually indicates time, or a horizontal position). B(t) has independent increments with t, i.e., the random variable $B(t_2) - B(t_1)$ is independent for any sequence $0 < t_1 < t_2$. Generally it satisfies,

i). $B(t_2) - B(t_1)$ *has a Gaussian distribution* **(A1.1)**

ii). $E\left[B(t_2) - B(t_1)\right]^2 \propto |t_2 - t_1|$ **(A1.2)**

where $B(t_2)$, $B(t_1)$ are two realizations of the random variable at time t_2 and t_1, $\Delta B(t) = B(t_2) - B(t_1)$ is the increment of B(t) from time t_1 to t_2, and E is the mathematical expectation. (A1.1) and (A1.2) indicate that the increment of Brownian motion $\Delta B(t)$ follows the Gaussian distribution and its variance (the mean square increments) is proportional to the time difference Δt. Such a function is said to be both stationary and isotropic.

From equation (A1.2), it is obviously that,

$$B(t_0 + t) - B(t_0) \quad and \quad \frac{1}{\sqrt{r}}\left[B(t_0 + rt) - B(t_0)\right]$$

have the same finite dimensional joint distribution functions for any t_0 and $r > 0$, we may say that the increments of B(t) are statistically self-similar in this sense. The second equation above is just a properly rescaled version of the first with a scaling factor $\sqrt{r}$. In other words, B(t) has a statistical invariant scaling behaviour. If the time t is changed by a factor r (from t to rt), then the increment $\Delta B(t)$ is changed by a factor $\sqrt{r}$. This characterizes Brownian motion as self-affine.

A1.2.2. Construction of Brownian motion

Brownian motion can be constructed using either integration of Gaussian white noise (W) or the midpoint displacement method.

A1.2.2.1. Integrating Gaussian white noise

White noise, W, is the term applied to any zero mean random process whose power spectral density spectrum is a flat line. In other words, all the frequencies have the same amount of energy. The name comes from an analogy to the idealized spectrum of white light (taken as a whole) which would contain power at all frequencies (all visible wave bands) in equal proportions. Therefore, the correlation of a white noise is an impulse. In other words, $W = (W_t)$ is defined as a White noise process if W_t and W_s are independent and have the same distribution whenever $t \neq s$. Especially, it is termed as Gaussian white noise if the random variables have the same Gaussian distribution. Refer to Kallianpur and Karandikar (1988) for more details.

1). Generating Gaussian white noise

Gaussian white noise can be produced by using a pseudo random number generator, i.e., a series of uniformly distributed random numbers over a certain interval. This interval is usually in [0, A], where A will be 1, or 2^{31} - 1 (32-bit), or 2^{15} - 1 (16-bit). The standardisation procedure, which is given by,

$$Z = \frac{Y - E(Y)}{\sqrt{Var(Y)}} \qquad \textbf{(A1.3)}$$

is used to approximate the Gaussian white noise based on the Central Limit Theorem. The Central Limit Theorem states that if Z_n is the standardized sum of any n identically

distributed random variables Y_i (i = 1, 2, ..., n), then the probability distribution of Z_n tends to be normal distribution as n goes to infinity. In practice, n = 3 or n = 4 yields satisfactory results for our purpose (Voss, 1985).

Let us now briefly examine the link between the uniformly distributed random variable Y_i and its standardized sum Z_n. Suppose that Y_i is the i-th uniformly distributed random variable, then its expectation $E(Y_i)$ and variance $Var(Y_i)$ are given respectively by,

$$E(Y_i) = \int_0^A \frac{1}{A} y \, dy = \frac{1}{2}A$$

$$Var(Y_i) = E(Y_i^2) - E(Y_i)^2 = \int_0^A \frac{1}{A} y^2 \, dy - \frac{1}{4}A^2 = \frac{1}{12}A^2$$

Thus,

$$E\left(\sum_{i=1}^{n} Y_i\right) = \sum_{i=1}^{n} E(Y_i) = \frac{n}{2}A$$

$$Var\left(\sum_{i=1}^{n} Y_i\right) = \sum_{i=1}^{n} Var(Y_i) = \frac{n}{12}A^2$$

Therefore,

$$Z_n = \frac{\sum_{i=1}^{n} Y_i - \frac{n}{2}A}{\sqrt{\frac{n}{12}}A} = \frac{1}{A}\sqrt{\frac{12}{n}}\sum_{i=1}^{n} Y_i - \sqrt{3n} \qquad \textbf{(A1.4)}$$

2). Integration of Gaussian white noise

Equation (A1.4) allows white noise to be obtained from uniformly distributed random variables which are generated by a random number generator in most computers. The integration of Gaussian white noise as shown,

$$B(t) = \int_{-\infty}^{t} W(s) \, ds$$

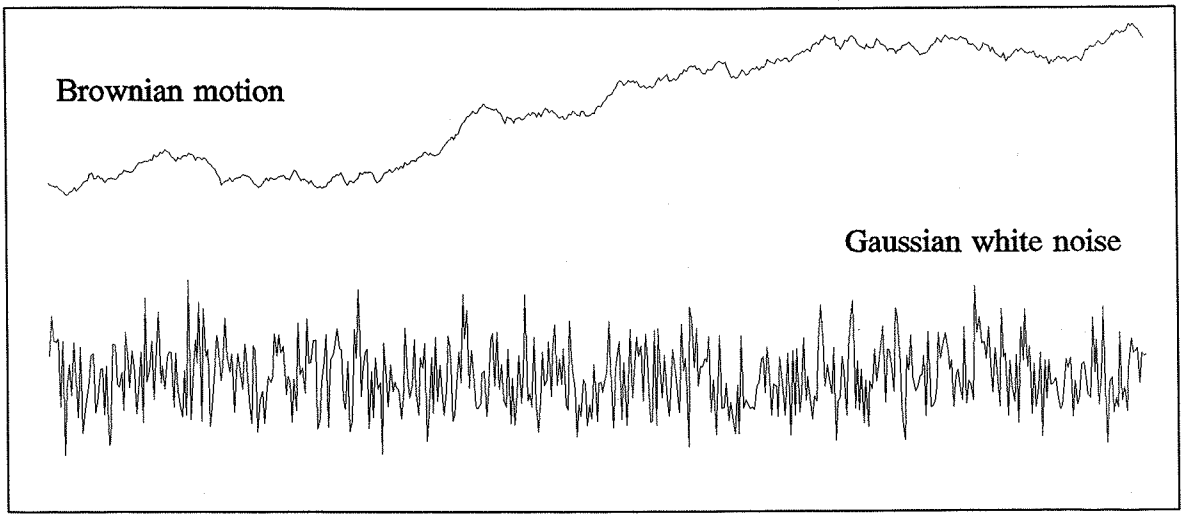

Fig. A1.1. Gaussian white noise and its integration of 1-dimensional Brownian motion.

obviously satisfies (A1.1) and (A1.2), and therefore yields Brownian motion.

A Visual Basic code is written to produce the Gaussian white noise and its integration - Brownian motion traces as shown in Fig. A1.1. Notice that the trace of Brownian motion has a increase trend from the left to right, this is because that the series of generated uniformly distributed random numbers fall over the interval of [0, 1].

A1.2.2.2. The midpoint displacement method

Another straight-forward way to approximate Brownian motion is the midpoint displacement method. This method is a recursive generating, or midpoint interpolating technique, which was firstly used to approximate the normal Brownian motion in 1920's by N. Wiener. Promoted by Carpenter, Fournier, and Fussell (Carpenter,1980; Fournier *et al.*, 1982), it has become widely popular in areas of surfaces simulation and computer graphics (Hearn and Baker, 1986; Harrington, 1987).

Fig. A1.2 demonstrates the principle of the midpoint displacement method for the first two levels. Considering the time interval [0, 1], we select B(0) = 0 and B(1) as a Gaussian random variable with zero mean value and variance σ^2, i.e.,

$$Var[B(1)-B(0)]=\sigma^2 \qquad \textbf{(A1.5)}$$

and we expect,

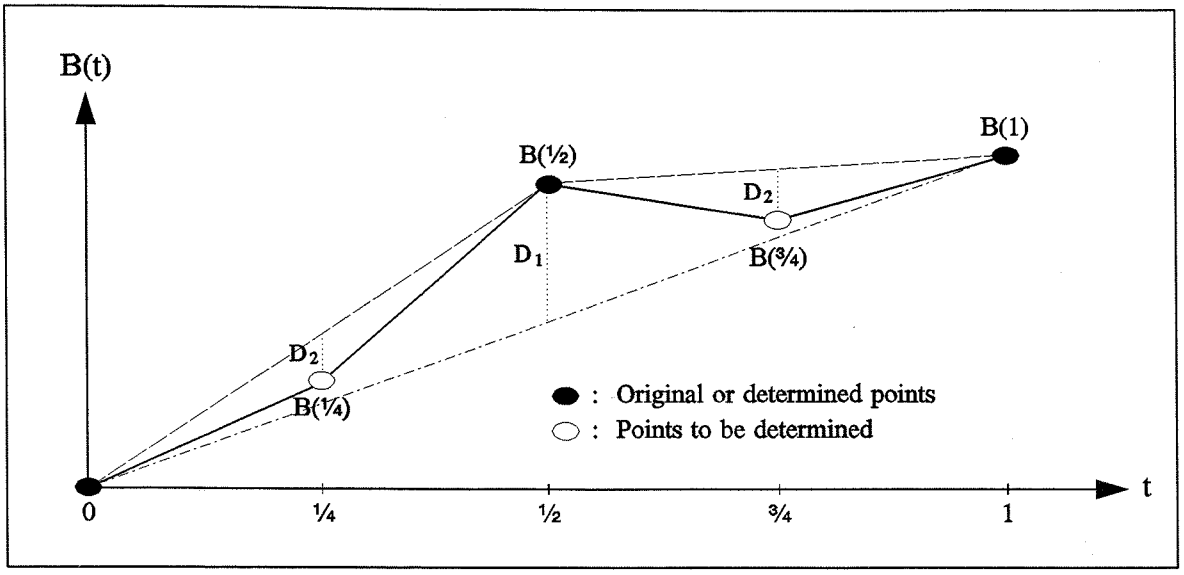

Fig. A1.2. Principles of the 1-dimensional midpoint displacement.

$$Var\left[B(t_2)-B(t_1)\right]=|t_2-t_1|\sigma^2 \qquad \textbf{(A1.6)}$$

to satisfy (A1.2), where t_1 and t_2 two moments in [0, 1], i.e., $0 \le t_1 \le t_2 \le 1$.

Firstly, t is taken as ½, the middle point of 0 and 1; and B(½) is set to be the average of B(0) and B(1) plus some Gaussian random offset D_1 with zero mean and variance Δ_1^2, i.e.,

$$\left[B\left(\frac{1}{2}\right)-B(0)\right]=\frac{1}{2}\left[B(1)-B(0)\right]+D_1$$

and obviously the same holds for B(1) - B(½). Combined with (A1.5) and (A1.6), the variance of the left part of the above equation is given by,

$$Var\left[B\left(\frac{1}{2}\right)-B(0)\right]=\frac{1}{4}Var\left[B(1)-B(0)\right]+Var\left(D_1\right) \overset{Eq(5.5)}{=} \frac{1}{4}\sigma^2+\Delta_1^2 \overset{Eq(5.6)}{=} \frac{1}{2}\sigma^2$$

Therefore,

$$\Delta_1^2=\frac{1}{4}\sigma^2$$

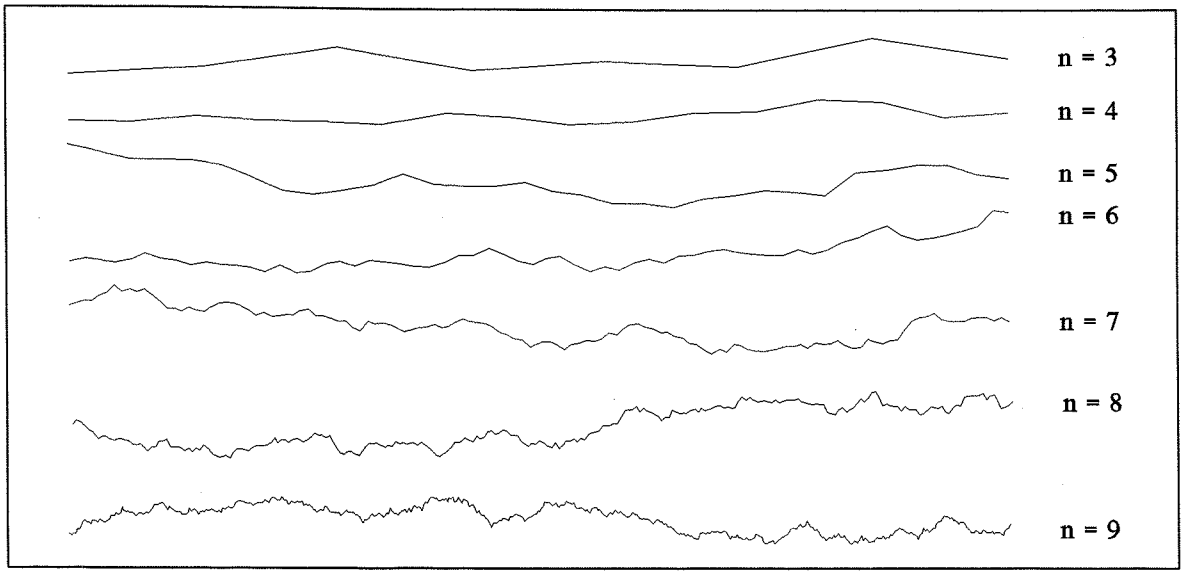

Fig. A1.3. Some samples of 1-dimensional Brownian motion generated by the midpoint displacement technique at different levels. 2^n is the number of points in a single sample profile at level n. The sample profiles have been vertically condensed to fit in the diagram.

Secondly, t is taken as ¼, and B(¼) is set to be the average of B(½) and B(0) plus some Gaussian random offset D_2 with zero mean and variance Δ_2^2. Similarly, we have,

$$\left[B\left(\frac{1}{4}\right) - B(0)\right] = \frac{1}{2}\left[B\left(\frac{1}{2}\right) - B(0)\right] + D_2$$

Thus,

$$Var\left[B\left(\frac{1}{4}\right) - B(0)\right] = \frac{1}{4}Var\left[B\left(\frac{1}{2}\right) - B(0)\right] + \Delta_2^{\,2} = \frac{1}{4}\sigma^2$$

Therefore,

$$\Delta_2^{\,2} = \frac{1}{8}\sigma^2$$

The same procedure can be applied to B(¾) when t is taken as ¾, and furthermore to the finer resolutions. Generally speaking, at level n, the values of midpoints are averaged

by their nearby two points plus a random Gaussian offset D_n with zero mean and variance Δ_n^2 which is given by,

$$\Delta_n^2 = \frac{1}{2^{n+1}}\sigma^2 \qquad \textbf{(A1.7)}$$

Therefore a random element, D_n, of variance $2^{-(n+1)}\sigma^2$, which is proportional and corresponding to the time difference $\Delta t = 2^{-n}$, is added to ALL the midpoints of the displacement procedure at level n, and a Brownian noise of $2^n + 1$ points is obtained.

A Visual Basic code, ***mp1d***, is made to generate 1-d Brownian motion by using the midpoint displacement method. Fig. A1.3 shows some samples of 1-d Brownian motion generated by ***mp1d*** at different levels n, where n = 3, 4, 5, 6, 7, 8, and 9. With the requirement of a task, finer resolution can be reached at deeper level.

A1.3. 1-DIMENSIONAL FRACTIONAL BROWNIAN MOTION

One dimensional fractal Brownian motion, (abbreviated as 1-d fBm in later discussion), combines the concepts of 1-d Brownian motion and fractals, due to the work done by Mandelbrot and Ness (1968). It has become a fundamental mathematical model for the random fractals found in the nature, and in the computer graphics simulations (Voss, 1985).

A1.3.1. Definition of a fractional Brownian motion

1-d fBm is defined as a random process $V_H(t)$, which is a function $V_H(t)$ of a real variable t (t usually denotes time). Its increment $\Delta V_H(t) = V_H(t_2) - V_H(t_1)$ has a Gaussian distribution with a variance $|t_2 - t_1|^{2H}$ for $0 \le t_1 \le t_2 \le 1$ i.e., $\Delta V_H(t)$ satisfies,

i). $V_H(t_2) - V_H(t_1)$ *has a Gaussian distribution* **(A1.8)**

ii). $E\left[V_H(t_2) - V_H(t_1)\right]^2 \propto |t_2 - t_1|^{2H}$ **(A1.9)**

where the parameter H has a value $0 < H < 1$. Therefore H typically relates with ΔV_H by the simple statistical scaling law,

$$\Delta V_H \propto \Delta t^H \qquad \textbf{(A1.10)}$$

where $\Delta V_H = V_H(t_2) - V_H(t_1)$, and $\Delta t = t_2 - t_1 > 0$.

H is a very important parameter to characterizes the behaviour of ΔV_H. It has a relationship with the fractal dimension D of D = 2. Brownian motion discussed in Section A1.2 is the special case of fBm with H = 0.5, and D = 2 - H = 1.5.

A1.3.2. Relationship between H and D

As discussed in Chapter 1, the fractal dimension of a self-similar curve, in terms of box (or interval) dimension, is given by,

$$N_r = r^{-D} \tag{A1.11}$$

where N_r is the number of boxes of size r required to cover the curve, and D is the fractal dimension derived from the box counting method. Mandelbrot (1985) pointed out that the assignment of a fractal dimension D determined by (A1.11) to a self-affine set could produce ambiguous results. The difficulties can be easily explained here by the scaling law (A1.10) of fBm $V_H(t)$. For instance, if the time span [0, 1] is divided into N equal intervals, then for the time increment Δt each of these intervals will contain a rectangle of Δt by ΔV_H. Therefore Δt is given by,

$$\Delta_t = \frac{1}{N} = r$$

From (A1.10), we have,

$$\Delta V_H = \Delta t^H = \frac{1}{N^H}$$

Thus the number of boxes of size r required to cover the sample of fBm over the time span [0, 1] is given by,

$$N_r = \frac{\Delta V_H}{\Delta t} N = N^{2-H} = r^{-(2-H)} \tag{A1.12}$$

Combining this equation with (A1.11) and (A1.12), we can deduce the very important relationship between D and H for 1-d fBm,

$$D = 2 - H \tag{A1.13}$$

For the normal Brownian motion, H = 0.5, and D = 1.5.

A1.3.3. Generating fractional Brownian motion

A variety of techniques and methods have been developed for generating fBm. The

most important two methods are interpolation and spectral methods. The interpolation method is focused on in this discussion since it can be easily extended to 2-d fBm generation and requires less computing time and memory.

A1.3.3.1. The midpoint displacement method

The midpoint displacement technique, discussed in Section A1.2.2.2, is very often used in approximating fBm (Voss, 1985). Combining equations of (A1.6) and (A1.10), we have,

$$Var\left[V_H(t_2 - t_1)\right] = |t_2 - t_1|^{2H}\sigma^2 \qquad \textbf{(A1.14)}$$

where $\Delta V_H = V_H(t_2) - V_H(t_1)$ has a Gaussian distribution over the time span [0, 1], and $Var[V_H(1) - V_H(0)] = \sigma^2$ with $0 \le t_1 \le t_2 \le 1$.

Similarly, $V_H(0)$ is set to be 0, $V_H(1)$ a sample of Gaussian random variable with variance of σ^2, and $V_H(½)$ the average of $V_H(0)$ and $V_H(1)$ plus some Gaussian random offset D_1 with zero mean and variance Δ_1^2, i.e.,

$$V_H\left(\frac{1}{2}\right) - V_H(0) = \frac{1}{2}\left[V_H(1) - V_H(0)\right] + D_1 \qquad \textbf{(A1.15)}$$

Combining (A1.15) with (A1.14) gives,

$$Var\left[V_H\left(\frac{1}{2}\right) - V_H(0)\right] = \frac{1}{4}\sigma^2 + \Delta_1^2 = \left(\frac{1}{2}\right)^{2H}\sigma^2$$

Thus,

$$\Delta_1^2 = \frac{\sigma^2}{2^{2H}}\left[1 - 2^{2H-2}\right] \qquad \textbf{(A1.16)}$$

The same procedure is carried out until level n, then the length scale has decreased to 2^{-n}, and a random Gaussian variable offsets D_n with variance Δ_n^2 is added to the midpoints of

the $(n-1)^{th}$ level. Δ_n^2 is given by,

$$\Delta_n^2 = \frac{1}{(2^n)^{2H}}\left(1-2^{2H-2}\right)\sigma^2 \qquad \textbf{(A1.17)}$$

For H = ½, (A1.17) is equivalent with (A1.7).

Fig. A1.4(a) shows three samples of 1-d fBm generated by the midpoint displacement method with different H values of 0.8, 0.5, 0.2 respectively. The programs used are written in Visual Basic code; ***mp1d*** is for generating samples, and ***profp*** is for plotting the samples.

It has been shown that the midpoint displacement method does not yield the right fBm when H ≠ ½ (Mandelbrot, 1982). In fact, we do have,

$$Var\left[V_H(1)-V_H\left(\frac{1}{2}\right)\right] = Var\left[V_H\left(\frac{1}{2}\right)-V_H(0)\right] = \frac{1}{4}\sigma^2 + \Delta_1^2 = \left(\frac{1}{2}\right)^{2H}\sigma^2$$

but unfortunately,

$$\begin{aligned} Var\left[V_H\left(\frac{3}{4}\right)-V_H\left(\frac{1}{4}\right)\right] &= Var\left[\frac{1}{2}\left(V_H(1)+V_H\left(\frac{1}{2}\right)\right)-\frac{1}{2}\left(V_H\left(\frac{1}{2}\right)+V_H(0)\right)\right] \\ &= Var\left[\frac{1}{2}\left(V_H(1)-V_H(0)\right)\right] = \frac{1}{4}\sigma^2 \neq \left(\frac{1}{2}\right)^{2H}\sigma^2 \end{aligned}$$

This clearly indicates that this process does not have stationary increments ΔV_H over Δt except H = 1, they are not all statistically equivalent, although it does produce a fractal. For example, points generated at different levels have different statistical properties in their neighbourhoods. Actually the values of points remain unchanged once they are determined, and roughly only half points are determined more accurately. For example, at level (n - 1), there are $(2^n - 2^{n-1} + 1)$ points in total, of those there are $(2^{n-1} - 2^{n-2})$ points are newly determined. The concept of the stationary increments demands that ALL the points generated during the displacing procedure should be determined more accurately.

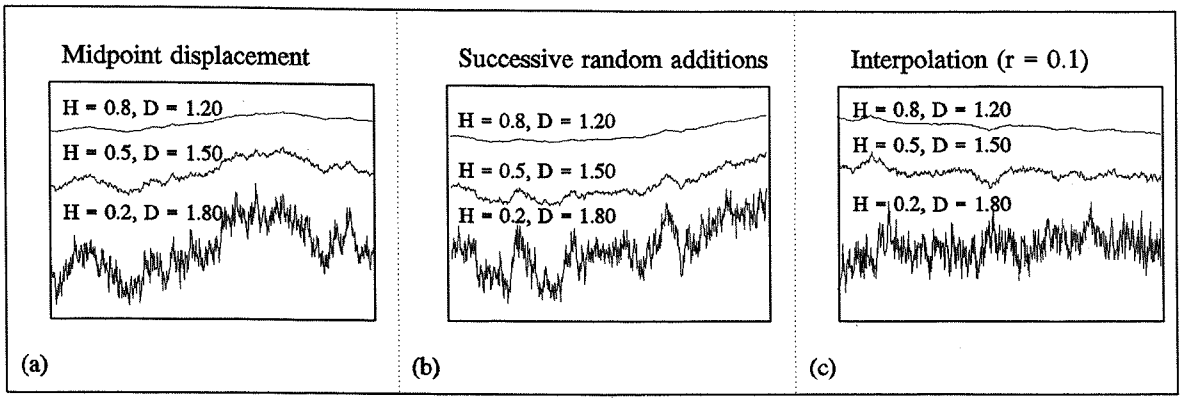

Fig. A1.4. Some samples of 1-dimensional fBm generated by; **(a)** the midpoint displacement, **(b)** the successive random addition, and **(c)** interpolation techniques with H values of 0.8, 0.5, and 0.2 respectively. There are 2^{10} points for a single sample.

From the point of view of the Nyquist sampling theorem, to approximate N real points requires N/2 complex frequencies or N/2 sine and cosine components. The midpoint displacement, however, only adds sine or cosine parts, not both.

One approach to deal with this non-stationary increments caused by the midpoint displacement technique is to add offsets D_n of a suitable variance Δ_n to all points generated during the approximating procedure. This method is termed 'successive random addition' by Voss (1985). All points at each level are treated equivalently and determined more accurately by adding an offset D_n which is a Gaussian random variable with a variance Δ_n^2 at level n, where Δ_n^2 is given by,

$$\Delta_n^2 = \frac{1}{2}\frac{1}{(2^n)^{2H}}\left(1-2^{2H-2}\right)\sigma^2 \qquad \textbf{(A1.18)}$$

Fig. A1.4 (b) shows three samples of 1-d fBm generated by the successive random addition method with different H values of 0.8, 0.5, 0.2 respectively. . The programs written in Visual Basic code; ***mpad1d*** for generating samples, and ***profp*** for plotting the samples.

A1.3.3.2. The interpolation method

The midpoint displacement and successive random additions methods are two special cases of the interpolation method, which interpolate midpoints at each level with an interpolating ratio r = ½, i.e., the resolution is improved by a factor r = ½ each time further.

The interpolation method deals with the situations that different interpolating ratios $0 < r < 1$ are evoked.

If there are N_n points with a resolution of Δt at level n, then there will be $N_{n+1} = N_n / r$ new points with a new resolution of $r\Delta t$ at level $(n + 1)$. The values of these new points are set through using the linear interpolation which is a kind of distance weighted average method. That is, the closer to one end the new point is, the higher weighted index is given to that end point. This can be easily illustrated by the 1-d x-axis situation as shown in Fig. A1.5(a). If the weighted index to the end point x_0, say u, is defined as,

$$u = \frac{(x - x_0)}{(x_1 - x_0)}$$

then the value of the interpolated point at x, $V_H(x)$, is determined by,

$$V_H(x) = (1-u)V_H(x_0) + u\,V_H(x_1) + D_n$$

A random offset D_n of Gaussian random variable with variance of Δ_n^2 is added to all points, including the original and new interpolated points for the purpose of stationary increments. From (A1.9), Δ_n^2 is given by,

$$\Delta_n^2 \propto (r^n)^{2H} \qquad \textbf{(A1.19)}$$

With the same idea of the midpoint displacement method, a similar equation to (A1.18) to determine Δ_n^2 is given by,

$$\Delta_n^2 = \frac{1}{2}(r^n)^{2H}(1 - r^{2-2H})\sigma^2 \qquad \textbf{(A1.20)}$$

where r is a scaling factor $(0 < r < 1)$. Different values r will change the appearance of the generated fractals, but not the fractal dimension D which is only determined by the parameter H. The variation in fractal appearance caused by the changes of r is termed

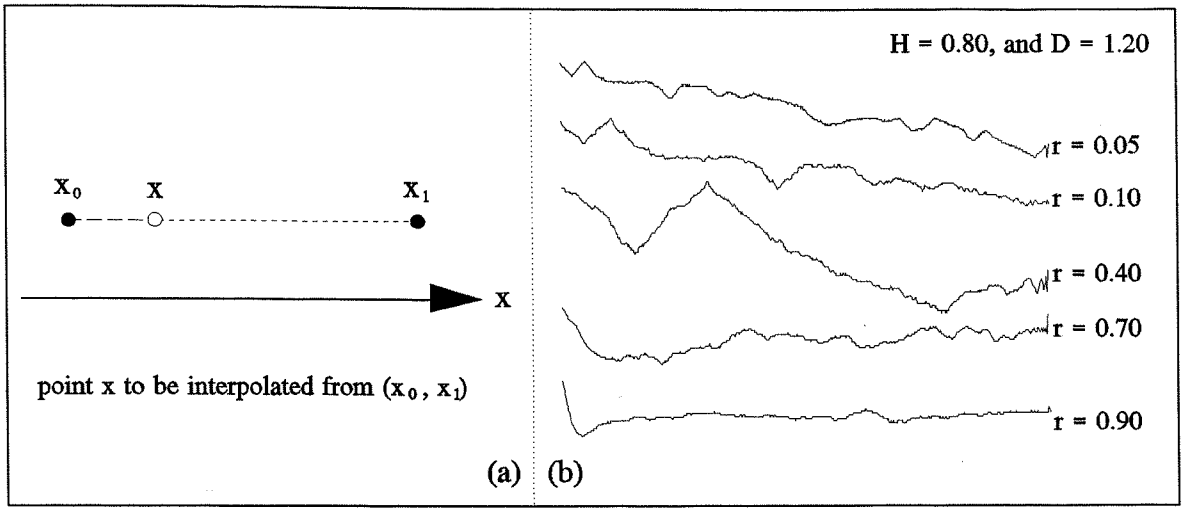

Fig. A1.5. **(a)** Principles of 1-d linear interpolation method; and **(b)** some samples of 1-dimensional fBm generated by interpolation method using different scaling factors r.

lacunarity.

Fig. A1.5(b) shows the changes of fractal appearance using different scaling factors r and a constant H = 0.80.

The linear interpolating technique used here can be easily extending to higher dimensions.

A1.3.4. Discussion

The fBm is self-affine. Fig. A1.4 shows some samples of 1-d fBm generated by the midpoint displacement, the successive random addition, and the interpolation (r = 0.1) methods through using different H-value. As can be seen from (A1.10) and Fig. A1.4, $V_H(t)$ must be magnified by a factor r^H (from $V_H(t)$ to $r^H V_H(t)$) if t is increased by a factor r (from t to rt) to keep the traces statistically invariant in shape. This non-uniform scaling behaviour is known as self-affinity.

H is a very important parameter to characterizes the behaviour of fBm. Generally, a sample of fBm is rough when its H-value is close to 0, while those with H-value close to 1 are relatively smooth. Furthermore, the parameter H describes the "roughness" of samples of fBm at small scales. From Fig. A1.4, the samples of high H values seem to characterize the trends of the samples of low H values. As mentioned that the Brownian motion is one special case of fBm, with H = 0.5, and D = 1.5.

The followings are some general discussion with the variations of H between [0, 1]:

1. **H = 0**. fBm is termed 1/f noise, which is an intermediate type of noise between white noise and Brownian noise. 1/f noise presents one of the most common types of noise found in the nature, and its origin is still a mystery after more than 60 years of investigation (Voss, 1979). The name comes from the special relationship between the power spectral density P(f) and its corresponding frequency f, i.e.,

$$P(f) = C\frac{1}{f}$$

where C is a constant. Thus, the sample of $V_H(t)$ could be expanded in the t-direction by any factors and could densely fill up a region in the plane, and its fractal dimension is 2.

2. **H = 1**. This is the opposite situation of 1/f noise, gives the fractal dimension of a ample of 1-d fBm D = 1, and shows its behaviour as a straight line since $\Delta V_H(t) = \Delta t$.
3. **0 < H < 1**. This is the most important and common case of fBm. The relationship between the fractal dimension of samples of 1-d fBm and the parameter H is D = 2 - H, and hence 1 < D < 2. Taking Brownian motion as a dividing situation, then we can divide the fBm into three categories:
   - **H = ½**. fBm becomes normal Brownian motion, i.e., $1/f^2$ noise, which satisfies,

$$P(f) = C\frac{1}{f^2}$$

   where P(f) is the power spectrum density for the frequency f, and C is again a constant. Its derivative corresponds to the uncorrelated Gaussian white noise (Mandelbrot and Ness, 1968; Mandelbrot, 1982). This indicates that $V_H(t_2) - V_H(t)$ is statistically independent with $t_2 - t_1$ for H = ½, where $t_1 < t < t_2$, and thus D = 1.5.
   - **½ < H < 1**. There is a positive correlation between increments $\Delta V_H(t)$ and Δt from (A1.10). For example, if t is increased by t_0, then $V_H(t + t_0)$ intends to increase for a fBm.
   - **0 < H < ½**. It is an opposite situation to **2)**, and there is a negative correlation between Δt and $\Delta V_H(t)$, and samples of fBm seem to be more erratic than that with ½ < H < 1 as shown in Fig. A1.4.

A1.4. 2-DIMENSIONAL FRACTIONAL BROWNIAN MOTION

A1.4.1. Definition of a 2-dimensional fractional Brownian motion

A 2-dimensional Brownian motion is a two dimensional process B(t, s), taking values in R^2(t, s), that has the following properties,

i). $B(t_1, s_1) - B(t_2, s_2)$ *has a Gaussian distribution, with zero mean*

ii). $E\left[\left|B(t_1, s_1) - B(t_2, s_2)\right|^2\right] \propto \sqrt{(t_2 - t_1)^2 + (s_2 - s_1)^2}$

indicating that the variance of the increments depends only on the distance.

A 2-d fBm is can be similarly defined as a two dimensional random process, V_H(t, s), which satisfies,

i). $V_H(t_2, s_2) - V_H(t_1, s_1)$ *has a Gaussian distribution* **(A1.21)**

ii). $E\left[V_H(t_2, s_2) - V_H(t_1, s_1)\right|^2\right] \propto \left[(t_2 - t_1)^2 + (s_2 - s_1)^2\right]^H$ **(A1.22)**

where the parameter H again satisfies $0 < H < 1$, and characterizes the roughness of the generated 2-d fBm.

A1.4.2. The zeroset theory - relationship between H and D

The relationship between the fractal dimension D and parameter H is given by,

$$D = 3 - H \qquad \textbf{(A1.23)}$$

which can be deduced using the concept of the zeroset. The zeroset theory points out that dimensions of shapes are reduced by 1 after they are intersected with a plane. For example, a cube has a dimension of 3, its intersection with a plane gives a 2-d square. The intersection of this square with another plane produces a 1-d straight line segment, and a 0-d

point will been created if this segment is intersected with yet another plane. This concept is true when applied to the fractals (Voss, 1988).

It is obvious that the zeroset of a self-similar fractal yields another self-similar fractal, however, the zeroset of a self-affine fractal could become either a self-similar or self-affine fractal. For instance, the zeroset of a self-affine1-d fBm is a set of disconnected points obtained from intersecting 1-d fBm ($V_H(t)$, with a fractal dimension D_1) with a plane parallel to the t-axis. This zeroset is a self-similar fractal and has a topological dimension of zero and a fractal dimension of $D_0 = D_1 - 1$. The zerosets of a self-affine 2-d fBm ($V_H(t, s)$, with a fractal dimension D_2) however, could be either self-similar or self-affine since two types of zerosets can be obtained. One is the intersection of 2-d fBm with a horizontal plane witch is parallel to t- and s- coordinates. This zeroset is a series of contours of the same height, and is a self-similar fractal with a fractal dimension $D_1 = D_2 - 1$. The other type of zeroset is a vertical section as the surface is intersected with a plane that parallels to the t- or s-axis. This zeroset (profile) may show mostly self-affinity and has a fractal dimension again $D_1 = D_2 - 1$. Generally, $0 < D_0 < 1$, $1 < D_1 < 2$, and $2 < D_2 < 3$.

A1.4.3. Generating 2-dimensional fractional Brownian motion

The generation of a 2-d fBm can be directly deduced from the definition of 2-d Brownian motion and the midpoint displacement method as well as interpolation method used to generate 1-d fBm in the previous Sections.

A1.4.3.1. The displacement method

The idea of the midpoint displacement discussed in Section A1.3.3.1 can be extended to generate 2-d fBm. Fig. A1.6 illustrates the principles of the methodology.

The initial geometrical shapes can be a unit square, a triangular grid, etc. (Fournier *et. al.*, 1982; Hearn and Baker, 1986; Miller, 1986; Harrington, 1987). In order to extend the displacement method to 2-dimensional space, a initial unit square is used.

Firstly, start with a unit square of four corner points whose values have Gaussian distribution with zero mean and variance σ^2 as shown in Fig. A1.6(a). Hence the resolution now is 1, and the central point is to be generated. The value of the central point is set to be the average of their four corner points plus an offset D_1, which is again a random Gaussian variable with a variance of Δ_1^2 determined by (A1.19). The scaling factor is $r = 1/\sqrt{2}$,

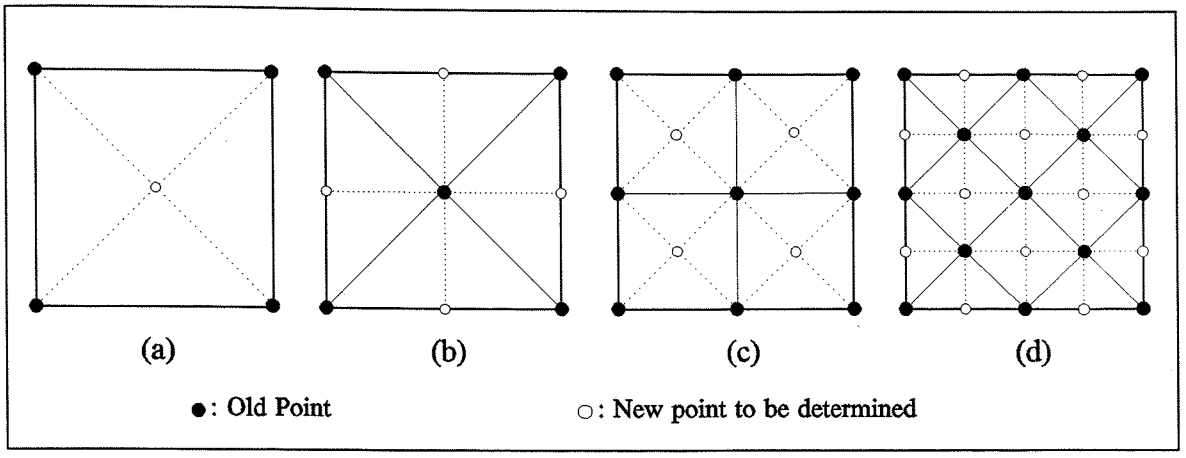

Fig. A1.6. Principles of 2-dimensional midpoint displacement method.

thus,

$$\Delta_1^{\,2} = \left(\frac{1}{\sqrt{2}}\right)^{2H} \sigma^2 = \left(\frac{1}{2}\right)^{H} \sigma^2$$

Secondly, the unit square has become 4 triangles with a resolution of $\frac{1}{\sqrt{2}}$. The four middle points of each side of the original grid are to be determined as shown in Fig. A1.6(b). Their values are set to be the averages of its nearby three points individually plus an offset D_2 with a variance of $\Delta_2^{\,2}$ which is given by,

$$\Delta_2^{\,2} = \left(\frac{1}{2}\right)^{2H} \sigma^2$$

The scaling factor remains fixed, $r = 1/2^{0.5}$. This stage is typically used for displacing those points on the boundary of the original grid.

Thirdly, displacement procedure shown in Fig. A1.6(a) and (b) is repeated, but at finer resolution [$\frac{1}{2}$ in (c), and $\frac{1}{2}\frac{1}{\sqrt{2}}$ in (d)] and 45 degree rotated squares as shown in (d).

Finally, this procedure can be carried out until a satisfactory resolution or number of points is reached.

In general, at stage n, the values of displaced points are set to be the average of their

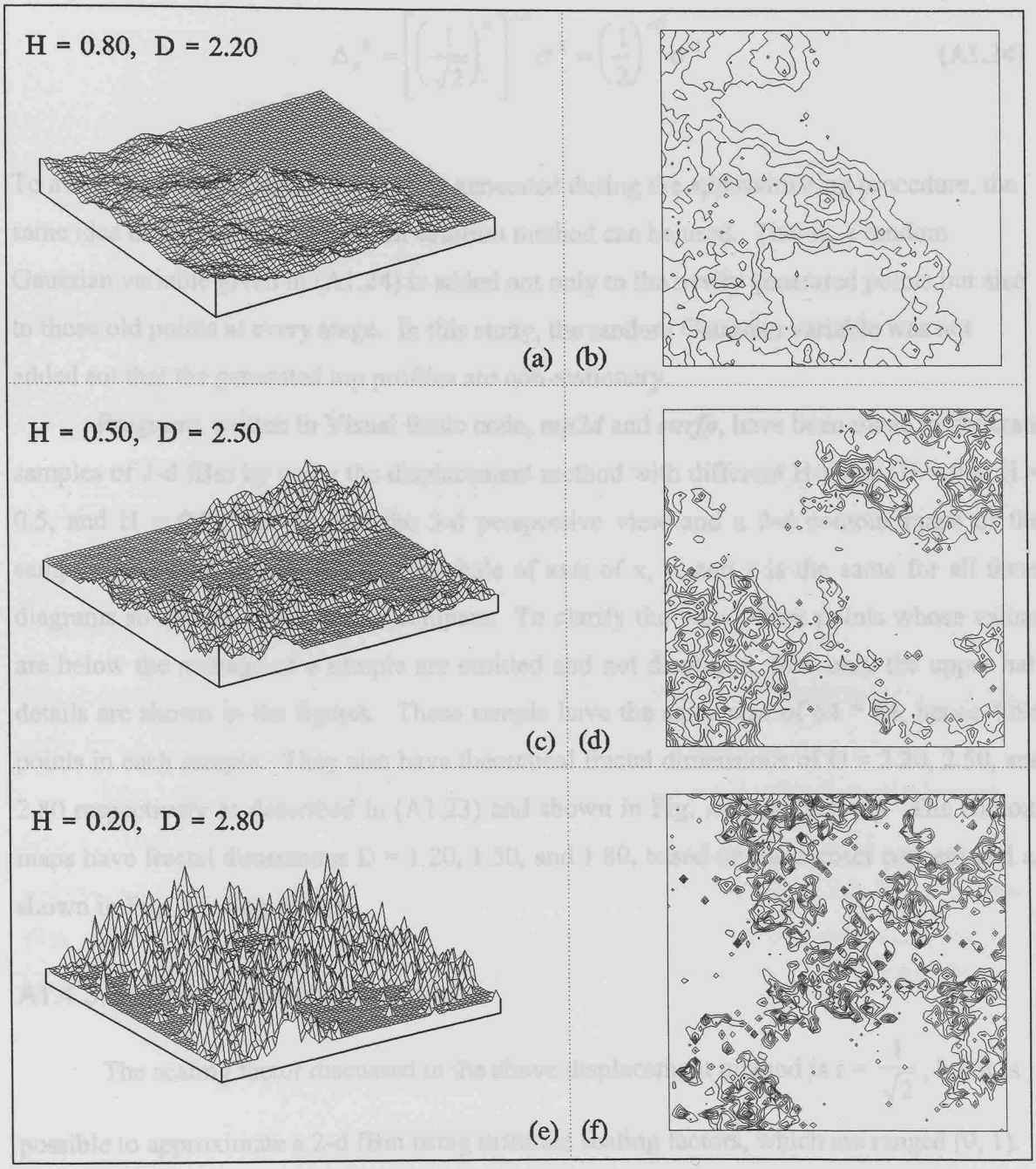

Fig. A1.7. Three 2-d fBm samples generated by the midpoint displacement method with H = 0.8, 0.5, and 0.2.

nearby four (or three) corner points plus an offset D_n, which is again a random Gaussian variable, with a variance of σ_n^2 determined by (A1.19). The scaling factor remains unchanged, $r = \frac{1}{\sqrt{2}}$, at different stages, thus,

$$\Delta_n^{\,2} = \left[\left(\frac{1}{\sqrt{2}}\right)^n\right]^{2H} \sigma^2 = \left(\frac{1}{2}\right)^{nH} \sigma^2 \qquad \textbf{(A1.24)}$$

To avoid the non-stationary increments generated during the approximating procedure, the same idea of the successive random addition method can be used. That is, a random Gaussian variable given in (A1.24) is added not only to the newly generated points but also to those old points at every stage. In this study, the random Gaussian variable was not added sot that the generated mp profiles are non-stationary.

Programs written in Visual Basic code, ***mp2d*** and ***surfp***, have been made to generate samples of 2-d fBm by using the displacement method with different H-value (H = 0.8, H = 0.5, and H = 0.2), and to plot the 3-d perspective view and a 2-d contour maps of the samples as shown in Fig. A1.7. The scale of axis of x, y, and z is the same for all these diagrams so that they are easy to compare. To clarify the view, those points whose values are below the average of a sample are omitted and not displayed, thus only the upper half details are shown in the figures. These sample have the same size of 64 * 64, hence 4096 points in each sample. They also have theoretical fractal dimensions of D = 2.20, 2.50, and 2.80 respectively as described in (A1.23) and shown in Fig. A1.7(a), (c), (e). The contour maps have fractal dimensions D = 1.20, 1.50, and 1.80, based on the zeroset concept and as shown in Fig. A1.7(b), (d), (f).

A1.4.3.2. The interpolation method

The scaling factor discussed in the above displacement method is $r = \frac{1}{\sqrt{2}}$, but it is possible to approximate a 2-d fBm using different scaling factors, which are ranged (0, 1). The idea of the 1-d interpolation method discussed in Section A1.3.3.2 can be further developed for 2-d interpolation (Voss, 1985).

A unit square is again used, with random values of its four corners selected from a Gaussian distribution with variance σ^2. Supposing that the data size is to be N^2, then the final resolution is to be $\frac{1}{N-1}$. As can be deduced easily that there will be $\left[(r)^{-n}+1\right]^2 - 4$ new points to be generated at stage n. The values of these new points are firstly bilinearly interpolated from their nearby four corner points, then an offset D_n is added to ALL the

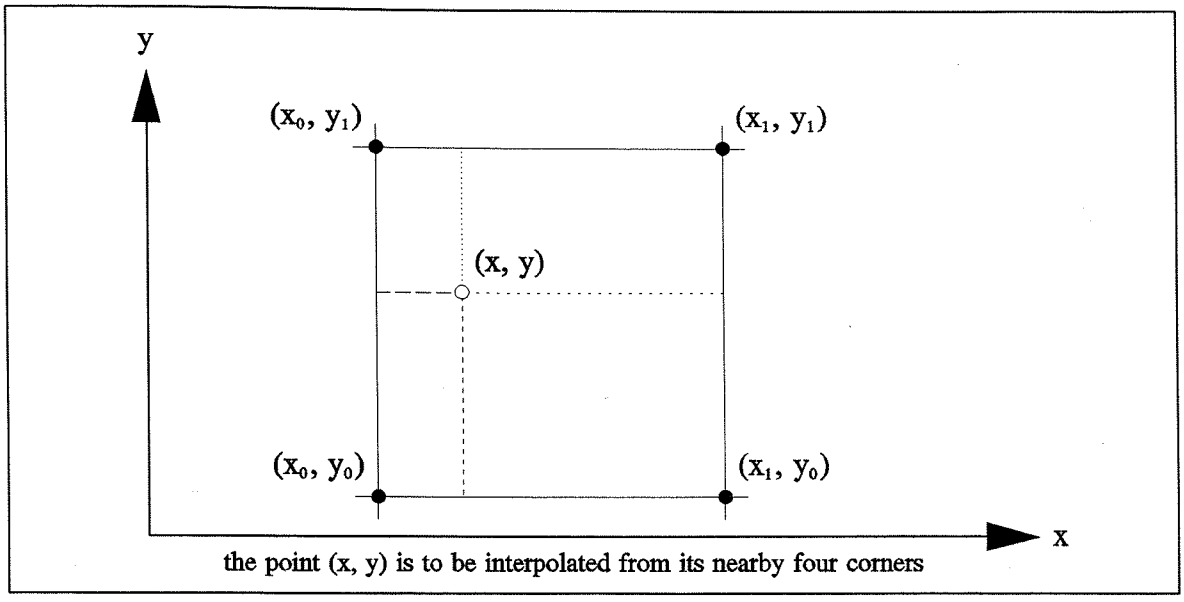

Fig. A1.8. Principles of 2-d linear interpolation method.

new generated points. D_n is, again, a Gaussian random variable with a variance σ_n^2 which is given by (A1.20).

The 2-dimensional linear interpolation method discussed by Press *et. al.* (1986) is demonstrated in Fig. A1.8. The grid square has four corner points (x_0, y_0), (x_1, y_0), (x_1, y_1), and (x_0, y_1), and their corresponding values are given as $V(x_0, y_0)$, $V(x_1, y_0)$, $V(x_1, y_1)$, and $V(x_0, y_1)$. Supposing that a new point V(x, y) falls in the grid square, then the bilinear interpolation gives its value as,

$$V(x,y) = (1-u)(1-v)V(x_0,y_0) + u(1-v)V(x_1,y_0) + (1-u)vV(x_0,y_1) + uvV(x_1,y_1) + D_n$$

if u and v are defined as,

$$u = \frac{(x-x_0)}{(x_1-x_0)} \quad and \quad v = \frac{(y-y_0)}{(y_1-y_0)}$$

where $0 \le u, v \le 1$. A random offset D_n with a variance of Δ_n^2, which is given by (A1.20), is added ALL points to maintain the property of stationary increments.

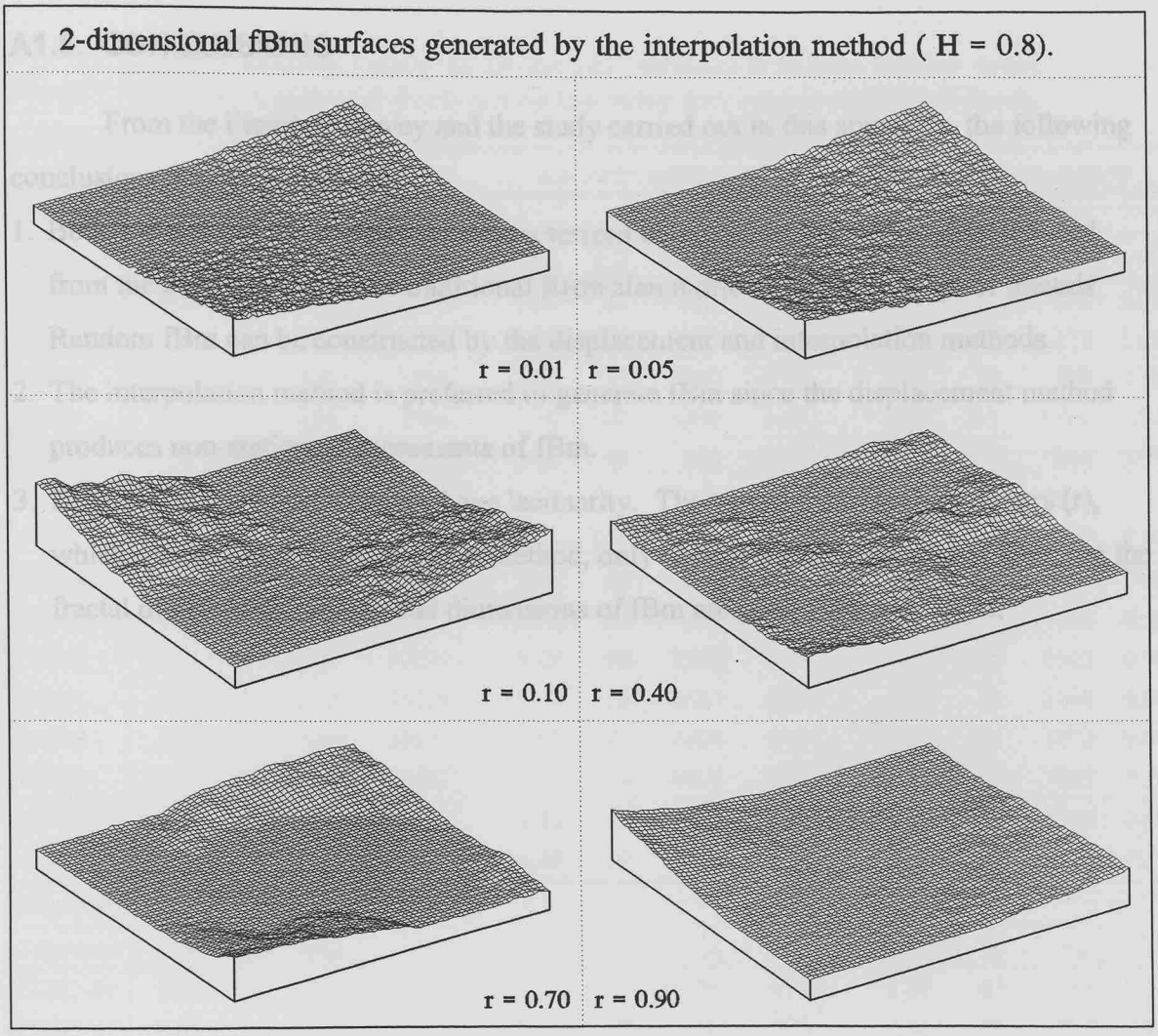

Fig. A1.9. Samples of 2-d fBm generated by the interpolation method using different scaling factor r.

Fig. A1.9 shows the lacunarity of samples of 2-d fBm with a constant H = 0.80 and different scaling factors r (r = 0.05, 0.10, 0.40, 0.70, 0.90 respectively). The variations in r change the appearance of the generated fractals, but not the fractal dimension D which is only determined by the parameter H. All samples have a fractal dimension D = 2.20.

A1.5. CONCLUSIONS

From the literature survey and the study carried out in this appendix, the following conclusions may be concluded;

1. Both 1-d and 2-d fBm, which are characterized by the parameter H, may be deduced from the combination of the traditional Brownian motion and the concept of fractals. Random fBm can be constructed by the displacement and interpolation methods.
2. The interpolation method is preferred to generate fBm since the displacement method produces non-stationary increments of fBm.
3. Both 1-d and 2-d fBm samples have lacunarity. The variations in scaling factors (r), which are used in the interpolation method, only change the appearances of fBm, not the fractal dimensions. The fractal dimensions of fBm are controlled only by H.

APPENDIX 2. FRACTAL ANALYSIS RESULTS OF 132 CONTOURS

Fractal analysis results of all the 132 contours from the border areas between Spain and Portugal by the ruler and box-counting methods.

	Contour features				*The ruler method*				*The box counting method*			
Map scale: 1:20,000 (Total = 13 contours)												
Filename	**E**	**S_0**	**N_{dp}**	**L_0**	**D_r**	**r_{RL}**	**r_{RU}**	**R^2**	**D_{1b}**	**r_{BL}**	**r_{BU}**	**R^2**
D2001	500	9	305	2838	1.07	90	600	0.65	1.08	91	606	0.99
D2002	500	8	252	1913	1.09	30	200	0.83	1.07	11	219	1.00
D2003	500	7	410	2854	1.18	70	600	0.86	1.10	30	298	0.99
D2004	480	12	651	7506	1.18	100	1200	0.80	1.29	213	1280	0.97
D2005	480	7	981	6648	1.15	90	600	0.84	1.31	63	944	0.97
D2006	480	7	476	3150	1.32	100	700	0.91	1.15	49	328	0.97
D2007	460	8	2218	18454	1.30	120	2000	0.93	1.30	114	2270	0.99
D2008	460	6	373	2385	1.10	40	300	0.80	1.21	45	446	0.98
D2009	460	8	996	7607	1.26	80	600	0.94	1.25	100	664	0.98
D2010	440	9	3527	30647	1.27	90	2500	0.96	1.28	91	2113	0.99
D2011	420	7	3663	25528	1.19	60	2500	0.97	1.19	92	2140	0.99
D2012	400	8	3189	26023	1.18	50	2500	0.97	1.18	101	2352	0.99
D2013	380	9	6538	57733	1.27	50	4000	0.98	1.34	80	5096	0.99
AVG		**8**			**1.20**	**75**	**1408**	**0.88**	**1.21**	**83**	**1443**	**0.98**
STD		**1**			**0.08**	**27**	**1172**	**0.10**	**0.09**	**50**	**1367**	**0.00**
Map scale: 1:50,000 (Total = 114 contours)												
Filename	**E**	**S_0**	**N_{dp}**	**L_0**	**D_r**	**r_{RL}**	**r_{RU}**	**R^2**	**D_{1b}**	**r_{BL}**	**r_{BU}**	**R^2**
G-M2-01	360	30	150	4544	1.24	50	1500	0.96	1.20	66	986	0.98
G-M2-02	340	31	116	3600	1.35	70	500	0.94	1.15	55	823	0.98
G-M2-20	320	31	138	4324	1.13	50	700	0.78	1.16	60	905	0.99
G22B002	400	27	207	5567	1.21	50	700	0.92	1.25	51	634	0.98
G22B003	400	22	299	6604	1.26	50	1000	0.92	1.27	38	959	0.98
G22B005	380	23	477	10785	1.30	70	2500	0.96	1.26	73	1466	0.99
G22B006	380	21	218	4526	1.26	80	900	0.90	1.22	85	851	0.97
G22B007	380	24	153	3694	1.29	70	700	0.91	1.21	44	664	0.98
G22B016	400	21	199	4135	1.23	60	400	0.97	1.30	58	387	0.97
G22B017	380	25	790	19896	1.22	50	3000	0.98	1.21	71	3214	0.99
G22B018	360	31	831	25974	1.28	50	3000	0.97	1.23	69	3119	1.00
G22B019	360	24	108	2626	1.24	40	250	0.82	1.20	37	182	0.99
G22B020	340	27	913	24888	1.29	50	1250	0.95	1.27	95	2853	0.99
G22B021	340	27	249	6604	1.22	70	1750	0.97	1.15	58	1451	0.98
G22B022	320	28	502	13960	1.26	70	1250	0.96	1.24	80	2009	0.99
G22B026	370	25	214	5425	1.30	40	500	0.95	1.29	29	389	0.98
G22B027	350	30	246	7492	1.24	50	500	0.92	1.23	49	657	0.99
G22B034	320	24	216	5183	1.29	50	1500	0.97	1.23	80	803	0.98
G22B036	300	28	304	8464	1.23	50	1000	0.94	1.25	77	770	0.98
G22B037	340	29	124	3657	1.31	50	700	0.89	1.18	45	670	0.98

K1022	320	18	112	2027	1.18	40	1000	0.88	1.11	53	532	0.95
K1025	580	21	151	3096	1.20	50	1000	0.76	1.11	77	771	0.99
K1026	560	21	132	2741	1.18	30	700	0.94	1.09	33	658	0.99
K1027	540	28	120	3330	1.16	40	700	0.82	1.15	80	798	0.97
K1028	520	25	116	2937	1.19	30	700	0.87	1.26	63	629	0.97
K1030	480	22	105	2354	1.25	40	600	0.95	1.17	35	520	0.94
K1031	460	24	120	2833	1.32	40	1000	0.94	1.19	54	540	0.99
K1032	440	30	106	3143	1.27	60	400	0.91	1.23	61	324	0.98
K1033	420	24	400	9570	1.27	30	900	0.94	1.25	46	1074	1.00
K1034	400	20	133	2721	1.20	30	350	0.88	1.30	76	454	0.98
K1036	440	21	173	3674	1.25	30	900	0.95	1.19	41	819	0.94
K1039	400	17	215	3666	1.28	40	900	0.93	1.33	62	623	0.94
K1042	360	26	249	6589	1.19	30	500	0.94	1.18	98	979	0.99
K1045	340	23	130	2952	1.25	60	200	0.76	1.23	102	340	0.98
K1046	340	25	113	2782	1.23	60	600	0.90	1.17	99	792	0.95
K1047	320	25	155	3834	1.21	30	600	0.95	1.11	64	958	0.99
K1049	300	26	122	3118	1.14	90	500	0.91	1.16	109	874	0.99
K1052	280	20	142	2824	1.08	50	600	0.97	1.12	175	874	0.97
K2004	380	27	108	2942	1.18	60	400	0.83	1.24	101	606	0.97
K2006	420	23	175	4080	1.20	70	900	0.87	1.23	70	703	0.98
K2011	340	28	110	3072	1.11	50	400	0.92	1.05	115	1146	0.95
K2019	320	26	129	3305	1.11	60	500	0.79	1.20	106	424	0.99
K2027	520	25	267	6679	1.23	40	1000	0.90	1.22	56	1126	0.99
K2028	540	22	154	3313	1.21	50	1000	0.94	1.15	84	672	0.97
K2029	560	19	130	2427	1.18	100	400	0.86	1.05	49	486	0.99
K2031	500	25	340	8464	1.21	70	600	0.90	1.22	101	1009	0.99
K2032	520	22	181	4008	1.26	50	800	0.92	1.21	83	831	0.95
K2035	480	21	274	5815	1.12	80	2000	0.94	1.13	67	1667	0.99
K2037	460	24	116	2747	1.20	60	600	0.96	1.32	70	560	0.96
K2038	440	19	114	2208	1.16	90	600	0.96	1.19	54	542	0.93
K2040	400	22	271	5904	1.15	40	500	0.92	1.15	66	553	0.99
K2042	420	29	250	7199	1.18	70	400	0.88	1.20	82	818	0.97
K2047	380	21	103	2134	1.23	30	600	0.93	1.10	37	549	0.98
K2055	360	15	119	1752	1.17	60	500	0.64	1.11	91	273	0.94
PC2008	420	20	169	3443	1.28	30	400	0.96	1.25	86	516	0.93
PC2010	400	20	257	5026	1.22	40	400	0.92	1.24	68	451	0.99
PC2011	380	21	362	7658	1.24	70	1500	0.97	1.28	89	1339	0.99
PC2012	380	20	324	6493	1.33	40	1000	0.97	1.23	52	1042	0.98
PC2016	360	21	1229	25896	1.33	50	2500	0.99	1.35	73	2183	0.99
PC2025	340	21	1597	34276	1.37	60	4000	0.96	1.39	88	2638	0.99
PC2031	320	22	1277	28651	1.24	50	4000	0.97	1.24	75	3554	1.00
PC2034	300	25	1083	27401	1.31	60	2500	0.95	1.32	76	2648	0.99
PC2043	360	24	141	3390	1.20	60	700	0.94	1.11	122	653	0.95
PC2046	320	28	128	3533	1.06	90	1000	0.87	1.02	134	1335	0.95

PC2047	340	21	103	2130	1.09	60	500	0.78	1.07	55	546	0.98
PC2049	340	18	160	2940	1.15	80	400	0.73	1.12	42	628	0.98
PC2055	340	21	135	2900	1.16	80	600	0.61	1.32	111	555	0.98
PC2056	340	25	184	4572	1.13	90	2000	0.95	1.12	134	1339	0.98
PC2058	340	21	162	3372	1.35	100	1250	0.93	1.23	58	579	0.99
GP005	420	28	146	4031	1.17	80	1250	0.96	1.08	192	1154	0.98
GP006	420	27	242	6574	1.10	50	1000	0.95	1.07	68	1696	0.98
GP007	440	26	222	5850	1.08	60	2000	0.96	1.10	85	2127	0.97
GP010	400	24	371	8751	1.26	50	2000	0.94	1.18	51	1543	0.97
GP012	380	24	598	14571	1.29	60	2000	0.97	1.22	105	2103	0.99
GP014	360	25	980	24399	1.31	60	2500	0.98	1.31	61	2429	0.99
GP017	360	19	100	1876	1.19	30	150	0.92	1.16	26	132	0.98
GP019	340	26	1079	28264	1.32	50	2000	0.98	1.28	60	3010	1.00
GP023	320	22	470	10516	1.34	50	900	0.97	1.33	44	1089	0.99
GP025	340	32	141	4466	1.25	175	600	0.90	1.20	103	548	0.97
GP027	320	31	319	9797	1.19	80	2000	0.91	1.19	101	2029	0.99
GP029	320	23	432	9937	1.24	50	900	0.98	1.27	49	488	0.98
GP030	320	22	175	3819	1.22	40	1000	0.95	1.30	40	404	0.98
GP032	300	27	902	24265	1.30	60	2000	0.97	1.25	68	3079	1.00
GP033	290	30	117	3470	1.21	50	500	0.89	1.37	58	576	0.94
GP036	280	27	158	4338	1.14	70	700	0.77	1.26	53	789	0.98
GP039	300	25	356	8787	1.30	40	1500	0.98	1.26	53	1313	0.98
GP043	400	22	646	14430	1.30	70	2000	0.92	1.28	63	1479	0.99
GP044	400	20	535	10817	1.23	80	1250	0.94	1.25	88	880	0.99
GP045	380	23	1226	28309	1.25	60	3500	0.93	1.28	106	3699	0.98
GP046	360	23	587	13560	1.30	80	1250	0.93	1.26	114	1138	0.98
GP047	300	24	384	9047	1.21	90	800	0.94	1.35	104	694	0.98
GP048	320	25	714	17516	1.28	60	1000	0.98	1.28	62	935	0.99
GP049	340	23	1116	25960	1.32	60	2500	0.94	1.32	65	2584	0.99
GP050	360	23	1615	36988	1.34	70	2000	0.97	1.34	88	2042	0.99
GP051	380	28	915	25270	1.25	60	3500	0.94	1.26	80	3606	0.97
GP052	400	29	984	28643	1.32	100	3000	0.97	1.29	116	1930	0.99
GP053	420	26	267	6825	1.27	80	600	0.96	1.25	53	528	0.99
D1001	500	21	128	2629	1.09	90	250	0.87	1.15	46	304	0.99
D1002	500	22	81	1814	1.14	50	400	0.86	1.17	52	208	0.97
D1003	500	20	142	2791	1.06	60	600	0.60	1.01	149	893	0.98
D1004	480	24	153	3702	1.10	90	1500	0.86	1.01	127	1272	0.98
D1005	480	24	259	6127	1.23	125	900	0.76	1.39	112	899	0.98
D1006	480	24	133	3158	1.22	100	900	0.82	1.17	48	465	0.97
D1007	460	19	385	7458	1.30	125	2000	0.89	1.21	96	1445	0.99
D1008	460	21	827	17580	1.24	100	2000	0.95	1.36	105	2106	0.97
D1009	460	15	118	1720	1.19	50	300	0.80	1.23	34	344	0.97
D1010	440	19	1579	29914	1.28	90	3500	0.96	1.32	77	3078	0.97
D1011	420	20	1368	26693	1.22	70	2500	0.98	1.22	78	2093	0.99

D1012	400	22	1081	24319	1.18	70	2500	0.97	1.21	106	2112	1.00
D1013	380	21	2541	54371	1.26	80	2500	0.99	1.29	78	2489	1.00
L2001	242	21	5078	104951	1.31	100	4000	0.96	1.39	109	4003	0.99
L2002	260	24	8101	197556	1.37	100	4000	0.98	1.43	178	3203	0.99
L2003	280	23	3196	72095	1.30	60	6000	0.98	1.28	114	6273	1.00
L2004	300	25	2476	62064	1.36	100	8000	0.98	1.36	111	3318	0.99
AVG		**24**			**1.23**	**63**	**1368**	**0.91**	**1.22**	**77**	**1287**	**0.98**
STD		**4**			**0.07**	**24**	**1226**	**0.08**	**0.09**	**31**	**1041**	**0.02**
Map scale: 1:200,000 (Total = 5 contours)												
Filename	**E**	**S_0**	**N_{dp}**	**L_0**	**D_r**	**r_{RL}**	**r_{RU}**	**R^2**	**D_{1b}**	**r_{BL}**	**r_{BU}**	**R^2**
L1001	256	85	835	71043	1.33	200	5000	0.97	1.39	177	3548	0.99
L1002	300	89	975	86488	1.31	240	10000	0.98	1.29	267	7112	1.00
L1003	300	86	1964	168110	1.47	300	12000	0.97	1.39	372	13028	0.99
L1004	300	86	369	31861	1.32	400	2500	0.94	1.46	394	2103	0.94
L1005	300	91	1502	137067	1.42	400	12000	0.96	1.32	307	12290	1.00
AVG		**87**			**1.37**	**308**	**8300**	**0.96**	**1.37**	**303**	**7616**	**0.98**
STD		**3**			**0.07**	**91**	**4324**	**0.02**	**0.07**	**87**	**4958**	**0.03**
Totavg					**1.23**			**0.91**	**1.23**			**0.98**

E: Contour elevation (m);

S_0: Average digitized separation (m); $S_0 = \dfrac{L_0}{N_{dp}}$;

N_{dp}: Number of the digitized points used for a contour;

L_0: Digitized contour length (m); $L_0 = \sum_{i=1}^{N-1} \sqrt{(x_{i+1} - x_i)^2 + (y_{i+1} - y_i)^2}$;

D_r: D-value derived from the ruler method;

r_{RL}: Lower fractal limit derived from the ruler method (m);

r_{RU}: Upper fractal limit derived from the ruler method (m);

R^2: The correlation coefficient for the regression line; $r_{xy} = \dfrac{\sum_{i=1}^{N} \sqrt{(x_i - \bar{x})(y_i - \bar{y})}}{\sqrt{\left[\sum_{i=1}^{N} (x_i - \bar{x})^2\right]\left[\sum_{i=1}^{N} (y_i - \bar{y})^2\right]}}$;

D_{1b}: D-value derived from the box counting method;

r_{BL}: Lower fractal limit derived from the box counting method (m);

r_{BU}: Upper fractal limit derived using the box counting method (m);

AVG: Average value;

STD: Standard deviation;

Totavg: Total average for all contours.

REFERENCES

REFERENCES

Aharonov, E. and Rothman, D. H., 1996, Growth of correlated pore-scale structures in sedimentary-rocks - a dynamical model, *J. of Geophys. Res.-Solid Earth, 101*, B2, 2973-2987.

Aki, K., 1984, Asperities, barriers, characteristic earthquakes and strong motion prediction, *J. Geophys. Res., 89*, 5,867 - 5,872.

Allègre, C. J., Le Mouel, J. L., and Provost, A., 1982, Scaling rules in rock fracture and possible implication for earthquake prediction *Nature, 297*, 47 - 49.

An, L J. and Sammis, C. G., 1994, Particle-size distribution of cataclastic fault materials from southern California - a 3-d study, *Pure And Applied Geophysics, 143*, 1-3, 203-227.

Anderson, J. G., 1986, Seismic strains rates in the central and eastern United States, *Seis. Soc. Am. Bull., 76*, 273 - 290.

Arab, N., Kazi, A. and Rieke, H. H., 1994, Fractal geometry of faults in relation to the 12-October-1992 Cairo earthquake, *Natural Hazards, 10*, 3, 221-233.

Atkinson, B. K. (ed.), 1987, *Fracture Mechanics of Rocks*, Academic Press, N.Y.

Aviles, C. A., Scholz, C. H., and Boatwright, J., 1987, Fractal analysis applied to characteristic segments of the San Andreas fault, *J. Geophys. Res. 92*, 331 - 44.

Bak, P. and Tang, C., 1989, Earthquake as a self-organized critical phenomena, *J. Geophys. Res. 94*, 15,635 - 637.

Balmino, G., Lambeck, K., and Kaula, W. M., 1973, A spherical harmonic analysis of the earth's topography, *J. Geophys. Res. 78*, 478 - 481.

Bandrivskii, S. A., Divin, G. D. and Malyshev, I. A., 1995, Mathematical-modelling of

random images with fractal properties, *J. of Optical Technology, 62*, 9, 578-582.

Barenblatt, G. I., Zhivago, A. V., Neprochnov, Y. P., and Ostrovskiy, A. A., 1985, The fractal dimension: A quantitative characteristic of ocean-bottom relief, *Oceanology (USSR), 24*, 695 - 697.

Barnsley, M. F., Devaney, R. L., Mandelbrot, B. B., Peitgen, H. O., Saupe, D., and Voss, R. F., 1988, *The Science of Fractal Images*, 312 pp., Springer-Verlag.

Barton, N. R., 1986, Deformation phenomena in jointed rock, *Geotechnique, 36*, 147 - 167.

Beauvais, A. A. and Montgomery, D. R., 1996, Influence of valley-type on the scaling properties of river planforms, *Water Resources Res., 32*, 5, 1441-1448.

Bell, T. H., 1975, Statistical features of sea-floor topography, *Deep-sea res., 22*, 883 - 892.

Bell, T. H., 1979, Messoscale sea floor roughness, *Deep-sea res., 26A*, 65-76.

Berkson, J. M., and Mathews, J. E., 1983, Statistical properties of sea-floor roughness, in *Acoustics and the sea-bed*, Pace, N. C. ed., 215 - 223.

Bendat, J. S., and Piersol, A. G., 1986, *Random data : Analysis and Measurement Procedure*, 556p, John Wiley, New York.

Berry, M. V. and Hannay, J. H., 1978, Topography of random surfaces, *Nature, 273*, 573.

Berry, M. V. and Lewis, Z. V., 1980, On the Weierstrass-Mandelbrot fractal function, *Proc. R. Soc. London, Ser., A,370*, 459 - 484.

Bevington, P. R., 1969, *Data Reduction and Error Analysis for the Physical*, McGraw-Hill, New York.

Borodich, F. M., 1994, Fracture energy of brittle and quasi-brittle fractal cracks, *IFIP Transactions A-Computer Sci. And Technology, 41*, 61-68.

Bower, C., Washington, C. and Purewal, T. S., 1995, A combined rheometer and image analyzer for characterization of suspensions and aggregates in a shear field, *Measurement Sci. & Technology, 6*, 2, 196-201.

Bracewell, R. N., 1986, *The Fourier Transform and Its Applications*, 474p, McGraw-Hill, New York.

Bretherton, F. P., 1969, Momentum transport by gravity waves, *Q. J. R. Meteorol. Soc.*, 213 - 243.

Brown, R., 1828, A brief account of microscopical observations made in the months of June, July, and August, 1827, on the particles contained in the pollen of plants; and on the general existence of active molecules in organic and inorganic bodies. *Philos. Mag. Ann. of Philos. New ser. 4*, 161 - 178.

Brown, S. R., 1987, A note on the description of surface roughness using fractal dimension, *Geophys. Res. Lett., 14*, 1,095 - 098.

Brown, S. R. and Scholz, C. H., 1985, Broad bandwidth study of the topography of natural rock surfaces, *J. Geophys. Res., 90*, 12,575 - 582.

Brown, S. R. and Scholz, C. H., 1986, Closure of rock joints, *J. Geophys. Res., 91*, 4,939 - 948.

Burrough, P. A., 1981, Fractal dimensions of landscapes and other environmental data, *Nature, 294*, 240 - 242.

Byerlee, J., 1978, Friction of rocks, *Pure Appl. Geophys, 116*, 615 - 626.

Caldarelli, G., Castellano, C. and Vespignani, A., 1994, Fractal and topological properties of directed fractures, *Physical Review E, 49*, 4 Pta, 2673-2679.

Cao, T. and Aki, K, 1984, Seismicity simulation with a mass-spring model and a displacement hardening-softening friction law, *Pure Appl. Geophys, 122*, 10 - 24.

Cao, T. and Aki, K, 1986, Seismicity simulation with a rate-and-state friction law, *Pure Appl. Geophys, 124*, 487 - 513.

Carmichael, D. R., Linnett, L. M., Clarke, S. J. and Calder, B. R., 1996, Seabed classification through multifractal analysis of sidescan sonar imagery, *IEEE Proc.-Radar Sonar And Navigation, 143*, 3, 140-148.

Carpenter, L., 1980, Computer rendering of fractal curves of surfaces, *Computer Graphics*, 109ff.

Carpinteri, A. and Chiaia, B., 1995, Multifractal nature of concrete fracture surfaces and size effects on nominal fracture energy, *Materials And Structures, 28*, 182, 435-443.

Carpinteri, A. and Chiaia, B., 1996, Crack-resistance behavior as a consequence of self-similar fracture topologies, *International J. of Fracture, 76*, 4, 327- 340.

Carter, K. E. and Winter, C. L., 1995, Fractal nature and scaling of normal faults in the Espanola basin, Rio-grande rift, new-Mexico - implications for fault growth and brittle strain, *J. of Structural Geology, 17*, 6, 863-873.

Chan, K. L., 1995, Quantitative characterization of electron micrograph image using fractal feature, *IEEE Transactions On Biomedical Engineering, 42*, 10, 1033-1037.

Chatfield, C., 1983, *Statistics for technology, a course in applied statistics*, 381 pp., London, New York, Chapman and Hall.

C. G. S., S.A., July 1987, 1:20,000, Ministerio De Industria Y Energia, Exploration En El Area De La Codosera (Badajoz) (Au, Sn, W, Sb).

Claps, P. and Oliveto, G., 1996, Reexamining the determination of the fractal dimension of river networks, *Water Resources Res., 32*, 10, 3123-3135.

Clarke, K. C., 1986, Computation of the fractal dimension of topographic surfaces using the triangular prism surface area method, *Comput. Geosci., 12*, 713 - 712.

Costain, J. K. and Bollinger, G. A., 1996, Climatic changes, streamflow, and long-term forecasting of intraplate seismicity, *J. of Geodynamics, 22*, 1-2, 97-117.

Cox, C. and Sandstrom, H., 1962, Coupling of internal and surface waves in water of variable depth, *J. Oceanography. Soc. Jpn.., 20*, 499 - 513.

Dejong, S. M. and Burrough, P. A., 1995, A fractal approach to the classification of Mediterranean vegetation types in remotely-sensed images, *Photogrammetric Engineering And Remote Sensing, 61*, 8, 1041-1053.

Devries, H., Becker, T. and Eckhardt, B., 1994, Power-law distribution of discharge in ideal networks, *Water Resources Res., 30*, 12, 3541-3543.

Dieterich, J. H., 1979, Modelling of rock friction, 1, Experimental results and constitutive equations, *J. Geophys. Res., 84*, 2,161 - 168.

Djordjevic, Z. V., Li, X. F., Shin, W. S., Wunder, S. L. and Baran, G. R., 1995, Fractal and topological characterization of branching patterns on the fracture surface of cross-linked dimethacrylate resins, *J. of Materials Sci., 30*, 11, 2968-2980.

Dolan, S. S., Bean, C. J. and Riollet, B., 1998, The broad-band fractal nature of heterogeneity in the upper crust from petrophysical logs, *Geophys. J. International, 132*, 3, 489-507.

Donnelly, D. P., Wilkins, M. F. and Boddy, L., 1995, An integrated image-analysis approach for determining biomass, radial extent and box-count fractal dimension of macroscopic mycelial systems, *Binary-Computing In Microbiology, 7*, 1, 19-28.

Dubuc, B., Quiniou, J. F., Roques-Carmes, C., Tricot, C., and Zucker, S. W., 1989a, Evaluating the fractal dimension of profiles, *Phys. Rev., A39*, 1,500 - 512.

Dubuc, B., Zucker, S. W., Tricot, C., Quiniou, J. F., and Wehbi, D., 1989b, Evaluating the fractal dimension of surfaces, *Proc. Roy. Soc. London, A425*, 113 - 127.

Feder, J., 1988, *Fractals,* Plenum, New York, 283.

Fournier, A., Fussell, D., and Carpenter, L., 1982, Computer rendering of stochastic models, *Comm. of the ACM, 25*, 371 - 384.

Evans, C. D. R., 1990, *United Kingdom offshore regional report: the geology of the western English Channel and its western approaches.,* London: HMSO for the British Geological

Survey.

Fox, C. G. and Hayes, D. E., 1985, Quantitative methods for analysing the roughness of the sea floor, *Rev. Geophys., 23*, 1 - 48.

Fox, C. G., 1989, Empirically derived relationships between fractal dimension and power law from frequency spectra, *Pure Appl. Geophys., 131*, 307 - 313.

Fox, C. G., 1996, Objective classification of oceanic ridge-crest terrains using 2-dimensional spectral models of bathymetry - application to the juan-de-fuca ridge, *Marine Geophys. Res.es, 18*, 6, 707-728.

Frantziskonis, G., 1995, Heterogeneity and implicated surface effects - statistical, fractal formulation and relevant analytical solution, *ACTA Mechanica, 108*, 1-4, 157-178.

Fyfe, J. A., Long, D., and Evans, C. D. R., 1993, *United Kingdom offshore regional report: the geology of the Malin-Hebrides sea.,* London: HMSO for the British Geological Survey.

Gan, K. C., McMahon, T. A., and Finlayson, B. L., 1992, Fractal dimensions and lengths of rivers in south-east Australia, *Cartographic J., 29*, 31 - 34.

Gilbert, L. E., 1989, Are topographic data sets fractal?, *Pure Appl. Geophys., 131*, 241 - 254.

Gilbert, L. E., and Malinverno, A.,1988, A characterization of the spectral density of residential ocean floor topography, *Geophys. Res. Lett. 15*, 1,401 - 404.

Gilbert, L. E., and Courtillot, V.,1987, Seasat altimetry and the South Atlantic geoid, 1, Spectral analysis, *J. Geophys. Res., 92*, 6,235 - 248.

Gillespie, P. A., Howard, C. B., Walsh, J. J. and Watterson, J., 1993, Measurement and characterization of spatial distributions of fractures, *Tectonophysics, 226*, 1-4, 113-141.

Glover, P. W. J., Meredith, P. G., Sammonds, P. R. and Murrell, S. A. F., 1994, Ionic surface electrical-conductivity in sandstone, *J. of Geophys. Res.-Solid Earth, 99*, B11, 21635-21650.

Godano, C., Alonzo, M. L. and Bottari, A., 1996, Multifractal analysis of the spatial-distribution of earthquakes in southern Italy, *Geophys. J. International, 125*, 3, 901- 911.

Godano, C. and Caruso, V., 1995, Multifractal analysis of earthquake catalogues, *Geophys. J. International, 121*, 2, 385- 392.

Goodchild, M. F., 1980, Fractals and the accuracy of geographical measures, *Math. Geol., 12*, 85 - 98.

Goodchild, M. F., 1982, The fractional Brownian process as a terrain simulation models, *Comm. of the ACM, 25*, 371 - 384.

Goff, J. A. and T. H. Jordan, 1988, Stochastic modelling of sea floor morphology: Inversion of

sea beam data for second-order statistics, *J. Geophys. Res. 93*, 13,589 - 608.

Hamblin, R. J. O., Crosby, A., Balson, P. S., Jones, S. M., Chadwick, R. A., Pene, I. E. and Arthur, M. J., 1992, *United Kingdom offshore regional report: the geology of the English channel.*, London: HMSO for the British Geological Survey.

Hammad, A. M. and Issa, M. A., 1994, Fractal dimension as a measure of roughness of concrete fracture trajectories, *Advanced Cement Based Materials, 1*, 4, 169-177.

Hao, Y., Wang, Z. G. and Kang, Y., 1994, Fractal analysis on the fatigue fracture surface along the crack-propagation direction, *Steel Res., 65*, 7, 305-308.

Harington, S., 1987, *Computer Graphics - A programming Approach*, McGraw Hil, New York.

Hearn, D. and Baker, M. P., 1986, *Computer Graphics*, Prentice-Hall, Englewood Cliffs, N.J.

Hewett, T. A., 1986, Fractal distributions of reservoir heterogeneity and their influence on fluid transport, *Soc. Petrol. Eng. Paper 15386*, 15 pp.

Hirata, T., Satoh, T., and Ito, K., 1987, Fractal structure of spatial distribution of microfracturing in rock, *Geophys. J. Roy. Astron. Soc. 90*, 369 - 374.

Hirata, T., 1989a, Fractal dimension of fault systems in Japan: Fractal structure in rock fracture geometry at various scales, *Pure Appl. Geophys., 131*, 157 - 170.

Hirata, T., 1989b, A correction between the b value and the fractal dimension of earthquakes, *J. Geophys. Res., 94*, 7,507 - 514.

Holliger, K. and Levander, A., 1994, Seismic structure of gneissic/granitic upper crust - geological and petrophysical evidence from the strona-ceneri zone (northern Italy) and implications for crustal seismic exploration, *Geophys. J. International, 119*, 2, 497-510.

Hooke, R. L. and Iverson, N. R., 1995, Grain-size distribution in deforming subglacial tills - role of grain fracture, *Geology, 23*, 1, 57-60.

Hough, S. E., 1989, On the use of spectral methods for the determination of fractal dimensions, *Geophys. Res. Lett., 16*, 673 - 676.

Huang, J. and Turcotte, D. L., 1989, Fractal mapping of digitized images: application to the topography of Arizona and comparisons with synthetic images, *J. Geophys. Res., 94*, 7491 - 5.

Huang, J. and Turcotte, D. L., 1990a, Are earthquakes an example of deterministic chaos?, *Geophys. Res. Lett., 17*, 223 - 226.

Huang, J. and Turcotte, D. L., 1990b, Fractal image analysis: application to the topography of Oregon and synthetic images, *J. Opt. Soc. Am. A7*, 1124 - 30.

Idziak, A. and Teper, L., 1996, Fractal dimension of faults network in the upper Silesian coal basin (Poland) - preliminary studies, *Pure And Applied Geophysics, 147*, 2, 239-247.

Jackson, P. and Sanderson, D. J., 1992, Scaling of fault displacements from the Badajoz-Cordoba shear zone, SW Spain, *Tectonophysics, 210*, 179 - 90.

Jensen, J. R., ed. 1983, *Urban/Suburban Land Use Analysis, Chapter 30 in Manual of Remote Sensing*, edited by Robert N. C., Fall Church, Virginia: American Society of Photogrammetry. .

Journel, A. G., and Huijbregts, C. J., 1978, *Mining Geostatistics*, 600 pp., Academic, San Diego, Calif.

Kallianpur, G. and Karandikar, R. L., 1988, *White Noise of Prediction, Filtering and Smoothing*, Stochastics Monographs, Volume 3, Gordon and Breach Science Publishers.

Katz, A. J. and Thompson, A. H., 1985, Fractal sandstone pores: Implications for conductivity and pore formation, *Phys. Rev. Lett., 54*, 1,325 - 328.

Kaye, H. B., 1989, *A random walk through fractal dimensions.*, ed. Chrisinna Dyllick-Brenzinger, VCH publishers, New York, 421.

Khattri, K. N., 1995, Fractal description of seismicity of India and inferences regarding earthquake hazard, *Current Sci., 69, 4*, 361-366.

King, G., 1983, The accommodation of large strains in the upper lithosphere of the earth and other solids by self-similar fault systems: The geometrical origin of b-value, *Pure Appl. Geophys., 121*, 761 - 815.

King, G. and J. Nabelek, 1985, Role of fault bends in the initiation and termination of earthquake rupture, *Science, 228*, 984 - 987.

Kopaskamerkel, D. C., 1994, Pore-throat morphology in the upper Jurassic smackover formation of Alabama, *J. of Sedimentary Res. Section A-Sedimentary Petrology And Processes, 64*, 3, 524-534.

Kronhn, C. E., and Thompson, A. H., 1986, Fractal sandstone pores: Automated measurements using scanning-electron microscope images, *Phys. Rev., B33*, 6366 - 6374.

Kronhn, C. E., 1988a, Fractal measurements of sandstones, shales, and carbonates, *J. Geophys. Res., 93*, 3297 - 3305.

Kronhn, C. E., 1988b, Sandstone fractal and Euclidean pore volume distributions, *J. Geophys. Res., 93*, 3286 - 3296.

Krueger, W. M., Jost, S. D., Rossi, K. and Axen, U., 1996, On synthesizing discrete fractional Brownian-motion with applications to image-processing, *Graphical Models*

And Image Processing, 58, 4, 334-344.

Kulatilake, P. H. S. W., Shou, G. and Huang, T. H., 1995, Spectral-based peak-shear-strength criterion for rock joints, *J. of Geotechnical Engineering-Asce, 121*, 11, 789-796.

Kulatilake, P. H. S. W., Shou, G., Huang, T. H. and Morgan, R. M., 1995, New peak shear-strength criteria for anisotropic rock joints, *International J. of Rock Mechanics And Mining Sci.s & Geomechanics Abstracts, 32*, 7, 673-697.

Lam, N. S. N., 1990, Description and measurement of Landsat TM images using fractals, *Photographic Engineering and Remote Sensing, 56, 2*, 187 - 195.

Lavallee, D., Lovejoy, S., Schertzer, D., Ladoy, P., 1993, Non-linear variability of landscape topography: Multifractals in analysis and simulation, in *Fractals in geography*, edited by L. De Cola and N. Lam, 158 - 192, Prentice-Hall, Engelwood Cliffs, NJ.

Lawrence, R. L. and Ripple, W. J., 1996, Determining patch perimeters in raster image-processing and geographic information-systems, *International J. of Remote Sensing, 17*, 6, 1255-1259.

Lee, C. H., Lin, B. S. and Yu, J. L., 1994, Dispersion and connectivity in flow-through fractured networks, *J. of The Chinese Institute of Engineers, 17*, 4, 521-535.

Lee, H. K. and Schwarcz, H. P., 1995, Fractal clustering of fault activity in California, *Geology, 23*, 4, 377-380.

Lee, J. J. and Bruhn, R. L., 1996, Structural anisotropy of normal-fault surfaces, *J. of Structural Geology, 18*, 8, 1043-1059.

Leonardi, S., Mulargia, F., and P. M. L., Rossi, 1994, Lithological influence on the fractal dimension of coastal morphology: the volcanic islands of Vulcano, Stromboli and Alicudi in southern Tyrrhenian sea, *Terra Nova, 6,* 246 - 250.

Leonardi, S., Mulargia, F. and Rossi, P. M. L., 1994, Lithological influences on the fractal dimension of coastal morphology - the volcanic islands of vulcano, stromboli and alicudi in the southern Tyrrhenian sea, *TERRA Nova, 6*, 3, 246-250.

Levander, A., England, R. W., Smith, S. K., Hobbs, R. W., Goff, J. A. and Holliger, K., 1994, Stochastic characterization and seismic response of upper and middle crustal rocks based on the Lewisian gneiss complex, Scotland, *Geophys. J. International, 119*, 1, 243-259.

Long, J. C. S., P. Gilmour, and P. A. Witherspoon, 1985, A model for steady fluid flow in random three-dimensional networks of disc-shaped fractures, *Water Resour. Res., 21*, 1,105 - 1,115. .

Lu, C. S., 1995, On the validity of the slit islands analysis in the measure of fractal dimension of fracture surfaces, *International J. of Fracture, 69*, 4, R 77- R 80.

Lyu, S. P., Zhu, X. G. and Qi, Z. N., 1994, Correlation between the fractal dimension of fracture surfaces and fracture-toughness for ductile polymer materials, *J. of Polymer Sci. Part B-Polymer Physics, 32*, 13, 2151-2154.

Madden, T. R., 1983, Microcrack connectivity in rocks: A renormalization group approach to the critical phenomena of conduction and failure in crystalline rocks, *J. Geophys. Res. 88*, 585 - 592.

Magde, L. S., Dick, H. J. B. and Hart, S. R., 1995, Tectonics, alteration and the fractal distribution of hydrothermal veins in the lower ocean crust, *Earth And Planetary Sci. Lett., 129*, 1-4, 103-119.

Main, I. G., and Burton, P. W., 1986, Long-term earthquake recurrence constrained by tectonic seismic moment release rates, *Seis. Soc. Am. Bull., 76*, 297 - 304.

Malinverno, A., 1989b, Testing linear models of sea-floor topography, *Pure Appl. Geophys. 131*, 139 - 155.

Malinverno, A., 1995, *Fractal in the earth science*, ed. Christopher, C. Barton and Paul R. La Pointe, Plenum Press, New York, 107 - 130.

Mandelbrot, B. B., 1967, How long is the coast of Britain? Statistical self-similarity and fractional dimension, *Science 156*, 636 - 638.

Mandelbrot, B. B., and Van Ness, J. W., 1968, Fractional Brownian motion, fractional noises and applications, *SIAW Review 10, 4*, 422 - 437.

Mandelbrot, B. B., and Wallis, J. R., 1969, Some long-run properties of geophysical records, *Water Resour. Res., 5*, 321 - 340.

Mandelbrot, B. B., 1975, Stochastic models for the Earth's relief, the shape and the fractal dimension of the coast lines, and the number area-rule for islands, *Proc. Nat. Acad. Sci USA 72*, 3,825 - 828.

Mandelbrot, B. B., 1977, *Fractals: Form, Chance, and Dimension*, 365 pp., W. H. Freeman, San Francisco.

Mandelbrot, B. B., 1982, Comment on computer rendering of fractal stochastic models, *Comm. of the ACM, 25, 8*, 581 - 583.

Mandelbrot, B. B., 1983, *The Fractal Geometry of Nature*, 468 pp., W. H. Freeman, New York.

Mandelbrot, B. B., 1985, Self-affine fractal and the fractal dimension, *Physica Scripta 32,* 257

- 260.

Mandelbrot, B. B., 1986, Self-affine fractal sets, I: The basic fractal dimensions, in *Fractals in physics,* edited by Pietronero, L. and Tosatti, E., 3 - 15, Elsevier, Amsterdam.

Mandelbrot, B. B., 1989, Multifractal measures, especially for the geophysicist., *Pure Appl. Geophys., 131,* 5 - 42.

Manna, S. S. and Subramanian, B., 1996, Quasi-random spanning tree model for the early river network, *Physical Review Lett., 76,* 18, 3460-3463.

Mareschal, J. C., 1989, Fractal reconstruction of sea-floor topography, *Pure Appl. Geophys., 131,* 197 - 210.

Maritan, A., Rinaldo, A., Rigon, R., Giacometti, A. and Rodrigueziturbe, I., 1996, Scaling laws for river networks, *Physical Review E, 53,* 2, 1510-1515.

Mark, D. M. and Aronson, P. B., 1984, Scaled-dependent fractal dimensions of topographic surfaces: an empirical investigation, with applications in geomorphology and computer mapping, *Mathematical Geology 11,* 671 - 684.

Milne, B. T., 1988, Measuring the fractal geometry of landscapes, *Appl. Math. Comput. 27,* 67 - 79.

Mishnaevsky, L. L., 1994, A new approach to the determination of the crack velocity versus crack length relation, *Fatigue & Fracture of Engineering Materials & Structures, 17,* 10, 1205-1212.

Monin, A. S. and Yaglom, A. M., 1971; *Statistical Fluid Mechanics, II,* MIT Press, Cambridge, Mass.,

Myers, N. O., 1962, Characterization of surface roughness, *Wear, 5,* 182 - 189.

Neidell, N. S., 1966, Spectral studies of marine geophysical profiles, *Geo-physics., 31,* 122 - 134.

Nolte, D. D., Pyrak-Nolte, L. J. and Cook, N. G. W., 1989, The fractal geometry of flow paths in natural fractures in rock and the approach to percolation, *Pure Appl. Geophys., 131,* 111 - 138.

Norton, D., and Sorenson, S., 1989, Variations in geometric of topographic surfaces underlain by fractured granite plutons, *Pure Appl. Geophys., 131,* 77 - 97.

Nye, J. F., 1970, Glacier sliding without cavitation in a linear viscous approximation, *Proc. R. Soc. London, Ser. A, 315,* 381 - 403.

Nye, J. F., 1973, *AIDJEX Bull., 21,* 20.

Odling, N. E., 1994, Natural fracture profiles, fractal dimension and joint roughness

coefficients, Rock Mechanics And Rock Engineering, 27, 3, 135-153.

Okubo, P. G. and K. Aki, 1987, Fractal geometry in the San Andreas fault system, *J. Geophys. Res., 92*, 345 - 355.

Olea, R. Editor, 1991, *Geostatistical Glossary and Multilingual Dictionary*, Oxford University Press, New York.

Oncel, A. O., Main, I., Alptekin, O. and Cowie, P., 1996, Temporal variations in the fractal properties of seismicity in the north Anatolian fault zone between 31-degrees-E and 41-degrees-E, *Pure And Applied Geophysics, 147*, 1, 147-159.

Parisi, G. and Frisch, U., 1985, Fully developed turbulence and intermittency, *Proc. Of the international School on Turbulence and Predictability in Geophysical Fluid Dynamics and Climate Dynamics*, edited by M. Ghil, R. Benzi, and G. Parisi, 84 - 88, North Holland, New York.

Pentland, A. P. 1984, *Fractal-based description of natural scenes*, IEEE Trans. Pattern Analysis and Machine Intelligence, PAMI-6:661-674.

Perfect, E. and Kay, B. D., 1995, Brittle-fracture of fractal cubic aggregates, *Soil Sci. Society of America J., 59*, 4, 969-974.

Pezzotti, G., Sakai, M., Okamoto, Y. and Nishida, T., 1995, Fractal character of fracture surfaces and boundary-values of toughness in a simple ceramic-ceramic system, *Materials Sci. And Engineering A-Structural Materials Properties Microstructure And Processing, 197*, 1, 109-112.

Pfeifer, P., 1984, Fractal dimensions as a working tool for surface roughness problems, *Appl. Surf. Sci., 18*, 146.

Pickering, G., Bull, J. M., Sanderson, D. J., and Harrison, P. V., 1994, Fractal fault displacements: a case study from the Moray Firth, Scotland, *Fractal and Dynamic Systems in Geosciences, Kruhl, J, H. (ed.)*, 105 - 19, Springer-Verlag, Berlin.

Pietronero and Tosatti, E., 1986, 3 - 15, Elsevier, Amsterdam.

Plotnick, R. E., 1986, A fractal model for the distribution of stratigraphic hiatuses, *J. Geol., 95*, 885 - 890.

Podsiadlo, P. and Stachowiak, G. W., 1995, Numerical-analysis of shape of wear particles from arthritic and asymptomatic synovial joints, *J. of Orthopaedic Rheumatology, 8*, 3, 155- 160.

Poliakov, A. N. B. and Herrmann, H. J., 1994, Self-organized criticality of plastic shear bands in rocks, *Geophys. Res. Lett., 21*, 19, 2143-2146.

Priestley, M. B., 1981, *Spectral Analysis and Time Series*, 890p, Academic, San Diego, California.

Polidori, L. Chorowicz, J, and Guillande, R., 1991, Descripsion of terrain as a fractal surface, application to digital elevation model quality assessment, *Photogram Eng. Remote Sensing, 57*, 1329 - 32.

Power, W. L. and Tullis, T. E., Brown, S. R., Boitnott, G. N., and Scholz, C. H., 1987, Roughness of natural fault surfaces, *Geophys. Res. Lett., 14*, 29 - 32.

Power, W. L. and Tullis, T. E., 1991, Euclidean and fractal models for the description of rock surface roughness, *J. Geophys. Res., 96*, 415 - 424.

Press, W. H., Flannery, B. P., Teukolsky, S. A., and Vetterling, W. T, 1986, Numerical recipes, Cambridge University Press, Cambridge.

Press, W. H., Teukolsky, S. A., Flannery, B. P., and Vetterling, W. T, 1992, Numerical recipes in C, Cambridge University Press, Cambridge.

Raizer, V. Y., Novikov, V. M. and Bocharova, T. Y., 1994, The geometrical and fractal properties of visible radiances associated with breaking waves in the ocean, *Annales Geophysicae-Atmospheres Hydrospheres And Space Sci.s, 12*, 12, 1229-1233.

Reeves, M. J., 1985, Rock surface roughness and frictional strength, *Int. J. Rock Mech. Min. Sci. Geomech. Abstr., 22*, 429 - 442.

Richardson, L. F., 1961, The problem of contiguity: An appendix of statistics of deadly quarrels, *General System Yearbook 6*, 139-187.

Ringrose, P. S., 1994, Structural and lithological controls on coastline profiles in fife, eastern Britain, *TERRA Nova, 6*, 3, 251-254.

Robertson, M. C., Sammis, C. G., Sahimi, M. and Martin, A. J., 1995, Fractal analysis of 3-dimensional spatial distributions of earthquakes with a percolation interpretation, *J. of Geophys. Res.-Solid Earth, 100*, B1, 609-620.

Roy, A. G., Gravel, G., and Gauthier, C., 1987, Measuring the fractal dimensions of surfaces: A review and appraisal of different methods, *Proceedings, Eight International Symposium on Computer-Assisted Cartography (Auto-Carto 8)*, 68 - 77, Baltimore.

Saleur, H., Sammis, C. G. and Sornette, D., 1996, Discrete scale-invariance, complex fractal dimensions, and log- periodic fluctuations in seismicity, *J. of Geophys. Res.-Solid Earth, 101*, B8, 17661-17677.

Sammis, C. G. and Biegel, R. L., 1989, Fractals, faults-gauge, and friction, *Pure Appl. Geophys. 131*, 255 - 271.

Saouma, V. E. and Barton, C. C., 1994, Fractals, fractures, and size effects in concrete, *J. of Engineering Mechanics-Asce, 120*, 4, 835-854.

Sarkar, N. and Chaudhuri, B. B., 1994, An efficient differential box-counting approach to compute fractal dimension of image, *IEEE Transactions On Systems Man And Cybernetics, 24*, 1, 115-120.

Sarkar, N. and Chaudhuri, B., B., 1995, Multifractal and generalized dimensions of gray-tone digital images, *Signal Processing, 42*, 2, 181-190.

Sayles, R. S. and Thomas, T. R., 1978, Surface topography as a nonstationary random process, *Nature 271*, 431 - 434.

Sayles, R. S., 1982, The profile as a random process, *Rough surfaces*, 92 - 94, Longman Inc. New York.

Scholz, C. H. and B. B. Mandelbrot (Edited by), 1989, *Fractals in Geophysics*, Birkhauser Verlag, Basel . Boston. Berlin. 313.

Scholz, C. H., 1988, The critical distance for seismic faulting, *Nature, 336*, 761 - 763.

Scholz, C. H., 1990, *The mechanics of earthquakes and faulting*, Cambridge University Press, Cambridge.

Schock, S. G. and LeBlanc, L. R., 1990, Chirp sonar: New technology for sub-bottom profiling, *Sea Technology, 31*, 35 - 39.

Shelberg, M. C., Lam, N. S-N., and Moellering, H., 1983, Measuring the fractal dimensions of surfaces, *Proceedings, Sixth International Symposium on Automated Cartography (Auto-Carto 6), 2*, 319 - 328, Ottawa, Ontario, Canada, 248 - 251.

Silberschmidt, V. V., 1994, Fractal and multifractal characteristics of stochastic brittle-fracture, *IFIP Transactions A-Computer Sci. And Technology, 41*, 385-396.

Sibson, R. H., 1985, Stopping of earthquake ruptures at dilational fault jogs, *Nature, 316*, 248 - 251.

Simonett, D. S., 1983, *The Development and Principles of Remote Sensing, Chapter 1 in Manual of Remote Sensing*, edited by Robert N. C., Fall Church, Virginia: American Society of Photogrammetry.

Smalley, R. F., Chatelain, J. L., Turcotte, D. L., and Prevot, R., 1987, A fractal approach to the clustering of earthquakes: applications to the seismicity of the New Hebrides, *Seis. Soc. Am. Bull. 77*, 1,368 - 381.

Soille, P. and Rivest, J. F., 1996, On the validity of fractal dimension measurements in image- analysis, *J. of Visual Communication And Image Representation, 7*, 3, 217-229.

Srivastava, H. N., Bhattacharya, S. N. and Ray, K. C. S., 1996, Strange attractor characteristics of earthquakes in Shillong plateau and adjoining regions, *Geophys. Res. Lett., 23*, 24, 3519-3522.

Star, J. and Estes. J., 1990, *Geographic Information System: An Introduction*, Englewood Cliffs, N.J.: Prentice-Hall.

Steacy, S. J., Mccloskey, J., Bean, C. J. and Ren, J. W., 1996, Heterogeneity in a self-organized critical earthquake model, *Geophys. Res. Lett., 23*, 4, 383-386.

Steers, J. A., 1948, *The coastline of England and Whales.,* Cambridge University Press.

Subba Rao, T., 1991, Bispectral analysis of nonlinear stationary time series with reference to bilinear time-series models, in *Handbook of statistics Vol. 3*, 293 - 319. edited by D. R. Brillinger and P. R. Krishnaiah, Elsevier Science Publishers B. V., 1983.

Sun, T, Meakin, P. and Jossang, T., 1994, Minimum energy-dissipation model for river basin geometry, *Physical Review E, 49*, 6 Pta, 4865-4872.

Thomas, T. R., 1982, *Rough surfaces*, 261 pp., Longman Inc. New York.

Thompson, J. Y., Anusavice, K. J. and Balasubramaniam, B., 1995a, Effect of microcracking on the fracture-toughness and fracture surface fractal dimension of lithia-based glass-ceramics, *J. of The American Ceramic Society, 78*, 11, 3045-3049.

Thompson, J. Y., Mecholsky, J. J. and Anusavice, K. J., 1995b, Microcrack influence on fracture-toughness and fractal dimension of lithia-based glass-ceramics, *J. of Dental Res., 74*, P.219.

Tullis, T. E., 1986, The relation between surface roughness of laboratory samples and decay distances of friction constitutive laws (abstract), *Eos Trans. AGU, 67*, 1,187.

Turcotte, D. L., 1987, A fractal interpretation of topography and geoid spectra on the Earth, Moon, Venus, and Mars, *J. Geophys. Res., 92*, E597 - E601.

Turcotte, D. L., 1989, A fractal approach to probabilistic seismic hazard assessment, *Tectonophys., 167*, 171 - 177.

Turcotte, D. L., 1992, *Fractals and chaos in geology and geophysics*, 83, Cambridge University Press.

Turcotte, D. L., 1995, Scaling in geology - landforms and earthquakes, *Proc. of The National Academy of Sci.s of The United States of America, 92*, 15, 6697-6704.

Varnes, D. J. and Bufe, C. G., 1996, The cyclic and fractal seismic series preceding an m(b) 4.8 earthquake on 1980 february 14 near the virgin-islands, *Geophys. J. International, 124*, 1, 149- 158.

Vasselle, B. and Giraudon, G., 1994, A multiscale regularity measure as a geometric criterion for image segmentation, *Machine Vision And Applications, 7*, 4, 229-236.

Velde, B., Dubois, J., Touchard, G., and Bardi, A., 1990, Fractal analysis of fractures in rocks: The Cantor's Dust method, *Tectonophysics, 179*, 345 - 52.

Velde, B., Dubois, J., Moore, D., and Touchard, G., 1991, Fractal patterns of fractures in granites, *Earth Planet. Sci. Lett., 104*, 25 - 35.

Volant, P. and Grasso, J. R., 1994, The finite extension of fractal geometry and power-law distribution of shallow earthquakes - a geomechanical effect, *J. of Geophys. Res.-Solid Earth, 99*, B11, 21879-21889.

Voss, R. F., 1979a, I/f (flicker) noise: A brief review, *Proc. 32rd Annual Symposium on Frequency Control, Atlantic City*, 40 - 46.

Voss, R. F., 1985a, Random fractal: characterization and measurement, in *Scaling phenomena in disordered systems*, edited by R. Pynn and A. Skjeltorp, 1 - 11, Plenum, New York.

Voss, R. F., 1985b, Random fractal forgeries, in *Fundamental Algorithms for Computer Graphics*, NATO AS1 Ser., Vol. F17, edited by R. A. Earnshaw, 805 - 835, Springer-Verlag, New York.

Voss, R. F., 1988, Fractals in nature: from characterization to simulation, in *The Science of Fractal Images*, H. O. Peitgen and D. Saupe, eds, 21 - 70, Springer-Verlag, New York.

Wang, J. H., 1993, The source rupture duration of earthquakes synthesized from an one-dimensional dynamic lattice model, *J. of Physics of The Earth, 41*, 6, 391-404.

Wang, J. H., 1995, A study of rupture length vs moment for synthetic earthquakes, *Pure And Applied Geophysics, 144*, 2, 211-228.

Wang, J. H., 1996, Velocity-weakening friction as a factor in controlling the frequency-magnitude relation of earthquakes, *Bulletin of The Seismological Society of America, 86*, 3, 701-713.

Wang, J. H. and Lee, C. W., 1996, Multifractal measures of earthquakes in west Taiwan, *Pure And Applied Geophysics, 146*, 1, 131-145.

Wang, J. S. Y., Narasimhan, T. N., and Scholz, C. H., 1988, Aperture correlation of a fractal fracture, *J. Geophys. Res., 93*, 2,216 - 2,224.

Weissel, J. K., Pratson, L. F., and, Malinverno, A., 1994, The length-scaling property of topography, *J. Geophys. Res., 99, B7*, 13,997 - 14,012.

Ward, H. C., 1982, Profile description, *Rough surfaces*, 82, Longman Inc. New York.

Watanabe, K. and Takahashi, H., 1995, Fractal geometry characterization of geothermal

reservoir fracture networks, *J. of Geophys. Res.-Solid Earth, 100*, B1, 521-528.

Weinstein, R. S. and Majumdar, S., 1994, Fractal geometry and vertebral compression fractures, *J. of Bone And Mineral Res., 9*, 11, 1797-1802.

Wiener, N., 1923, Differential space, *J. Math. and Phys. 2*, 131 - 174.

Wu, Q. L. and Wu, B. M., 1995, Study of membrane morphology by image-analysis of electron- micrographs, *J. of Membrane Sci., 105*, 1-2, 113-120.

Xie, H. P., 1993, *Fractals in rock mechanics*, A. A. Balkema Publishers, Rotterdam.

Xie, H. P. and Pariseau, W. G., 1994, Fractal estimation of joint roughness coefficients. *Science In China Series B-Chemistry Life Sciences & Earth Sciences, 37*, No.12, 1516-1524

Xie, H. P. and Sanderson, D. J., 1994, A fractal model and energy dissipation for en echelon fractures, *Engineering Fracture Mechanics, 48*, 655 - 662.

Xie, H. P. and Sanderson, D. J., 1995, Fractal kinematics of crack propagation in geomaterials, *Engineering Fracture Mechanics, 50*, 529 - 536.

Xu, T. B., Moore, I. D., and Gallant, J. C., 1993, Fractals, fractal dimensions and landscapes - a review, *Geomorphology, 8*, 245 - 262.

Yin, Z. M. and Ranalli, G., 1995, Modelling of earthquake rupturing as a stochastic-process and estimation of its distribution function from earthquake observations, *Geophys. J. International, 123*, 3, 838- 848.

Yokoya, N., Yamamoto, K., and Funakubo, N., 1989, Fractal-based analysis and interpolation of 3D natural surface shapes and their application to terrain modelling, *Comput. Vision Graph. Image Process., 46*, 284 - 302.

Zhang, P., Slemmons, D. B., and Mao, F., 1991, Geometric pattern, rupture termination and fault segmentation of the Dixie valley-Pleasant valley active normal fault system, Nevada, USA, *J. of Struc. Geol., Vol. 13, 2*, 165-176.

Zhang, Y., Wang, Y. B., Qiao, L. J., Chu, W. Y. and Hsiao, C. M., 1994, Investigation of fractal dimensions of hydrogen-induced brittle-fracture of titanium aluminide, *Materials Sci. And Engineering A-Structural Materials Properties Microstructure And Processing, 177*, 1- 2, L 1-L 5.

Zhao, Y. H., Huang, J. F. and Wang, R., 1993, Fractal characteristics of mesofractures in compressed rock specimens, *International J. of Rock Mechanics And Mining Sci. & Geomechanics Abstracts, 30*, 7, 877-882.